



Production of lactobionic acid by oxidation of lactose over gold catalysts supported on mesoporous silicas – Reaction optimization and purification process proposal

Thèse

Luis Felipe Gutiérrez

Doctorat en sciences et technologie des aliments
Philosophiae Doctor (Ph.D)

Québec, Canada

© Luis Felipe Gutiérrez, 2013

Résumé

Le surplus mondial et le faible prix du lactose ont attiré l'attention de chercheurs et de l'industrie pour développer des procédés novateurs pour la production de dérivés du lactose à valeur ajoutée, tels que l'acide lactobionique (ALB), qui est un produit à haute valeur ajoutée obtenu par l'oxydation du lactose, avec d'excellentes propriétés pour des applications dans les industries alimentaire et pharmaceutique.

Des recherches sur la production d'ALB via l'oxydation catalytique du lactose avec des catalyseurs à base de palladium et de palladium-bismuth, ont montré des bonnes conversions et sélectivités envers l'ALB. Cependant, le principal problème de ces catalyseurs est leur instabilité par lixiviation et désactivation par suroxydation au cours de la réaction. Les catalyseurs à base d'or ont montré une meilleure performance que les catalyseurs de bismuth-palladium pour l'oxydation de glucides. Cependant, trouver un catalyseur robuste pour l'oxydation du lactose est encore un grand défi. Dans cette dissertation, des nouveaux catalyseurs à base d'or supportés sur des matériaux mésostructurés de silicium (Au/MSM) ont été synthétisés par deux méthodes différentes, et évalués comme catalyseurs pour l'oxydation du lactose. Les catalyseurs ont été caractérisés à l'aide de la physisorption de l'azote, DRX, FTIR, TEM et XPS. Les effets des conditions d'opération, telles que la température, le pH, la charge d'or et le ratio catalyseur/lactose, sur la conversion du lactose ont été étudiés. Finalement, le procédé de déminéralisation de la solution de lactobionate de sodium à la sortie du réacteur a été étudié à l'aide de deux approches: l'électrodialyse avec des membranes bipolaires (EDMB) et la technologie d'échange d'ions.

Des catalyseurs Au/MSM hautement actifs ont été synthétisés avec succès par la co-condensation d'un mélange de *bis* [3-(triéthoxysilyl) propyle] tétrasulfide (BTESPTS), tétra-éthyle ortho-silicate (TEOS) et le précurseur d'or (HAuCl_4) en milieu acide, avec le tribloc co-polymère $\text{EO}_{20}\text{PO}_{70}\text{EO}_{20}$ utilisé comme agent structurant. Il a été trouvé que l'augmentation du ratio molaire BTESPTS/TEOS provoque un changement dans la structure des matériaux, laquelle passe d'une structure 2D-hexagonal très ordonnée à une structure mixte de type hexagonal-vésicule et mousse cellulaire. Dans les conditions opératoires optimales (charge d'or = 0.7% en poids, $T = 65^\circ\text{C}$, catalyseur/lactose ratio = 0.2, pH = 8-9, débit d'air = $40 \text{ mL} \cdot \text{min}^{-1}$), le lactose a été complètement converti en ALB après 80-100 min de réaction, lorsqu'on a utilisé les catalyseurs synthétisés à partir des mélanges contenant une concentration molaire de BTESPTS entre 6-10%. Ces catalyseurs ont été caractérisés

par une structure de type « wormhole-like », favorable pour l'accessibilité des réactifs aux nanoparticules d'or (AuNPs) d'environ 8 nm intercalées dans les murs de la silice.

AuNPs d'environ 5-6 nm ont été aussi chargées avec succès sur les matériaux mésoporeux SBA-15 et SBA-15-CeO₂, par l'adsorption du complexe [Au(en)₂]³⁺ (en=éthylènediamine) en milieu alcalin. Ces catalyseurs ont conservé la structure hexagonale 2D très ordonnée typique de la SBA-15, et ils ont présenté une grande activité pour l'oxydation du lactose. Après 60 min de réaction, les catalyseurs Au/SBA-15-CeO₂ (ratio molaire Ce/Si = 0.2) ont présenté l'activité catalytique la plus élevée (100% conversion du lactose) et 100% de sélectivité envers l'ALB, lorsqu'ils ont été utilisés dans les conditions optimales décrites ci-dessus. Ces résultats suggèrent que l'oxyde de cérium joue un rôle dans l'augmentation de l'activité catalytique, où la coordination et les états d'agglomération des atomes du Ce pourraient avoir un effet important.

En général, les résultats des analyses XPS sur les états d'oxydation de l'or à la surface des Au/MSM, ont montré la coexistence d'espèces d'or métalliques et oxydées, avec une abondance relative suivant l'ordre Au⁰ >>>Au⁺¹ > Au⁺³. Dans le cas des catalyseurs Au/SBA-15-CeO₂, la présence des deux états d'oxydation Ce³⁺ et Ce⁴⁺ a été aussi observée.

Les expériences de recyclage des catalyseurs ont montré que l'activité des échantillons Au/SBA-15 et Au/SBA-15-CeO₂ a été significativement réduite (40-65%) après des cycles de réaction d'oxydation consécutifs, lorsque le lavage avec de l'eau a été utilisé comme procédé de régénération. Par contre, les catalyseurs ont conservé leur activité catalytique, en utilisant la calcination comme méthode de régénération, ce qui indique qu'une des causes de désactivation des catalyseurs Au/MSM pourrait être due à une forte adsorption d'espèces organiques sur la surface des catalyseurs. De plus des quantités significatives d'or ont été trouvées dans la solution après des cycles de réaction consécutifs, ce qui démontre la désactivation est aussi due à la lixiviation de la phase active dans la solution de réaction.

Les données expérimentales ont révélé que tant l'EDMB que la technologie d'échange d'ions pourraient être utilisées pour produire l'ALB à partir de son sel de sodium. Cependant, en tenant compte du fait que l'EDMB a été utilisée pour la première fois pour cette application, ce procédé a donc besoin d'une amélioration pour des applications industrielles. En effet, une déminéralisation de 50% a été atteinte après l'application d'une différence de potentiel de 5.0-5.5 V pendant 100-180 min

aux bornes d'une cellule d'électrodialyse à trois compartiments, tandis que la solution de lactobionate de sodium a été complètement dépourvue de sodium après 10-30 min, lorsqu'on a utilisé une résine échangeuse de cations commerciale fortement acide (Amberlite™ FPC23 H).

Abstract

The worldwide surplus and low cost of lactose have drawn the attention of researchers and industry to develop innovative processes for the production of value-added lactose derivatives, such as lactobionic acid (LBA), which is a high value-added product obtained from lactose oxidation, with excellent properties for applications in the food and pharmaceutical industries.

Investigations on LBA production by means of catalytic oxidation of lactose over palladium and bismuth-palladium supported catalysts have shown good conversion rates and selectivities towards LBA, but the main problem of these catalysts is their instability by leaching and deactivation by over-oxidation during the reaction. Supported gold catalysts have shown to outperform palladium and bismuth-palladium catalysts for the oxidation of carbohydrates. However, there is still a big challenge in finding a robust catalyst for the lactose oxidation. In this dissertation, new gold catalysts supported on mesoporous silica materials (Au/MSM) have been synthesized by two different methods, and evaluated as catalysts in the oxidation of lactose. The catalytic materials were characterized by nitrogen physisorption, XRD, FTIR, TEM and XPS. The effects of the operating conditions such as temperature, pH, gold loading and catalyst/lactose ratio on the lactose conversion were investigated. Finally, the demineralization process of the sodium lactobionate solution obtained at the reactor outlet has been studied using two approaches: bipolar membrane electrodialysis (BMED) and ion-exchange technology.

Highly active Au/MSM were successfully formulated by the co-condensation of a mixture of *bis* [3-(triethoxysilyl) propyl] tetrasulfide (BTESPTS), tetraethyl orthosilicate (TEOS) and the gold precursor (HAuCl₄) in acidic media, using the triblock co-polymer EO₂₀PO₇₀EO₂₀ as template. It was found that by increasing the BTESPTS/TEOS molar ratio, the structure of the synthesized materials changed from a highly ordered 2D hexagonal structure to a mixed hexagonal-vesicle and cellular foam structure. Under the optimal operating conditions (gold loading = 0.7%wt, T = 65°C, catalyst/lactose ratio = 0.2, pH = 8-9, air flow = 40 mL·min⁻¹), the lactose was completely converted into LBA after 80-100 min reaction, when using the catalysts synthesized from mixtures containing 6-10% molar concentration of BTESPTS. These catalytic materials were characterized by the predominance of a wormhole-like structure, favorable for the reagent accessibility to the gold nanoparticles (AuNPs) of about 8 nm intercalated in the silica walls.

AuNPs of about 5-6 nm were also successfully loaded of mesoporous SBA-15 and SBA-15-CeO₂ materials, by the wet adsorption of the gold cationic complex [Au(en)₂]³⁺ (en=ethylenediamine) in alkaline media. These catalysts retained the well-ordered 2D hexagonal structure typical of SBA-15, and showed high activity to lactose oxidation. After 60 min of reaction, the Au/SBA-15-CeO₂ catalysts (Ce/Si = 0.2) showed the highest catalytic activity (100% lactose conversion) and 100% selectivity towards LBA, when used at the optimal operating reaction conditions described above. These results suggest that ceria plays a role in the enhancement of the catalytic activity, where the coordination and agglomeration states of Ce atoms could have an important effect.

In general, the XPS study on the oxidation states of gold on the Au/MSM surfaces revealed the coexistence of metallic and oxidized Au species, whose relative abundance followed the order Au⁰ >>>Au⁺¹ > Au⁺³. In the case of Au/SBA-15-CeO₂ catalysts, the presence of both Ce³⁺ and Ce⁴⁺ oxidation states was also observed.

Catalysts' recycling experiments showed that the activity of Au/SBA-15 and Au/SBA-15-CeO₂ was significantly reduced (40-65%) after consecutive oxidation reaction cycles, when washing with water was used as regeneration process. On the contrary, these catalytic samples conserved their catalytic activity when calcination was used as regeneration method, indicating that one of the causes of deactivation of Au/MSM might be the strong adsorption of organic species on the catalyst surface. Moreover, significant amounts of Au were found in the solution after consecutive reaction cycles, demonstrating that the leaching of the active phase into the reaction solution is another important cause of the catalyst' deactivation.

Experimental data showed that both BMED and ion exchange technology might be used for producing LBA from its sodium salt. However, taking into account that it is the first time that BMED is used for this application, this process still needs further improvement for industrial applications, since a demineralization rate of 50% was achieved after applying a voltage difference of 5.0-5.5 V during 100-180 min to a three-compartment electrodialysis stack, while a complete sodium removal was achieved after 10-30 min when using a commercial strong cation exchange resin (Amberlite™ FPC23 H).

Table of contents

Résumé.....	iii
Abstract.....	vii
Table of contents.....	ix
Index of tables.....	xiii
Index of figures.....	xv
List of abbreviations.....	xix
Acknowledgements.....	xxiii
Preface.....	xxvii
Introduction.....	1
Chapter 1. Literature Review.....	7
1.1. Lactobionic acid: A high value-added lactose derivative for food and pharmaceutical applications.....	7
1.1.1. Abstract.....	7
1.1.2. Introduction.....	7
1.1.3. Lactobionic acid: general characteristics.....	8
1.1.4. Lactobionic acid production.....	8
1.1.5. Commercial and proposed applications of lactobionic acid.....	16
1.1.6. Physiological effects of lactobionic acid.....	18
1.1.7. Conclusions.....	19
1.2. Mesoporous silica materials: General characteristics and synthesis methods.....	21
1.2.1. General characteristics.....	21
1.2.2. Synthesis methods.....	22
1.2.3. Mesoporous silica SBA-15.....	24
1.3. Synthesis of gold catalysts supported on mesoporous silica materials: Recent developments.....	29
1.3.1. Abstract.....	29
1.3.2. Introduction.....	29
1.3.3. Methods to synthesize active gold catalyst supported on MSM.....	32
1.3.4. Conclusions and outlook.....	80
Chapter 2. Hypotheses and objectives.....	85
2.1. Hypotheses.....	85
2.2. Objectives.....	85
2.2.1. General objective.....	85
2.2.2. Specific objectives.....	85
Chapter 3. Selective production of lactobionic acid by aerobic oxidation of lactose over gold crystallites supported on mesoporous silica.....	87
3.1. Abstract.....	87
3.2. Introduction.....	87
3.3. Experimental.....	90
3.3.1. Materials.....	90
3.3.2. Catalyst preparation.....	90
3.3.3. Characterization.....	90
3.3.4. Lactose oxidation experiments.....	91
3.3.5. Reaction sample analysis.....	92

3.4. Results and discussion	92
3.4.1. Material characterization	92
3.4.2. Catalyst activity	100
3.5. Conclusions.....	106
Chapter 4. Characteristics and lactose oxidation activity of gold catalysts supported on mesoporous silica synthesized in the presence of thioether functional groups.....	107
4.1. Abstract.....	107
4.2. Introduction	107
4.3. Materials and methods.....	109
4.3.1. Materials	109
4.3.2. Catalysts preparation.....	109
4.3.3. Catalysts characterization.....	110
4.3.4. Lactose oxidation experiments	111
4.3.5. Reaction sample analysis	111
4.4. Results and discussion	112
4.4.1. Catalysts characterization.....	112
4.4.2. Catalytic activity	122
4.5. Conclusion	124
Chapter 5. Effective gold catalyst supported on mesoporous silica decorated by ceria for the synthesis of high value lactobionic acid	125
5.1. Abstract.....	125
5.2. Introduction	126
5.3. Experimental	128
5.3.1. Materials	128
5.3.2. Synthesis of mesoporous SBA-15 and SBA-15-CeO ₂	128
5.3.3. Synthesis of Au(en) ₂ Cl ₃	129
5.3.4. Catalyst preparation.....	129
5.3.5. Catalyst characterization.....	129
5.3.6. Lactose oxidation experiments	130
5.3.7. Reaction sample analysis	131
5.4. Results and discussion	132
5.4.1. Catalyst characterization.....	132
5.4.2. Catalytic activity	141
5.5. Conclusions.....	148
Chapter 6. Synthesis of high value lactobionic acid by aerobic oxidation of lactose on Au/SiO ₂ catalysts.....	151
6.1. Abstract.....	151
6.2. Introduction	151
6.3. Experimental details.....	154
6.3.1. Materials	154
6.3.2. Synthesis of mesoporous SBA-15	154
6.3.3. Synthesis of Au(en) ₂ Cl ₃	154
6.3.4. Catalyst preparation.....	154
6.3.5. Catalysts characterization.....	155
6.3.6. Lactose oxidation experiments	156

6.3.7. Reaction sample analysis	157
6.4. Results and discussion	157
6.4.1. Catalyst characterization	157
6.5. Conclusions	169
Chapter 7. Catalysts recycle and deactivation	171
7.1. Experimental methodology	171
7.1.1. Catalysts synthesis	171
7.1.2. Lactose oxidation reactions	171
7.1.3. Catalyst deactivation study	171
7.1.4. Catalyst regeneration procedures	172
7.2. Results and discussion	172
7.2.1. Catalysts activity and selectivity after consecutive reactions	172
7.2.2. Catalysts deactivation	173
7.3. Conclusions	180
Chapter 8. Production of lactobionic acid by means of a process comprising the catalytic oxidation of lactose and bipolar membrane electro dialysis	181
8.1. Abstract	181
8.2. Introduction	181
8.3. Experimental details	183
8.3.1. Materials	183
8.3.2. BMED cell and protocol	184
8.3.3. Analysis methods and calculations	186
8.4. Results and discussion	190
8.4.1. Process parameters	190
8.4.2. Membrane parameters	195
8.5. Conclusions	198
Chapter 9. Production of lactobionic acid from sodium lactobionate solution by ion exchange on a commercial strong acid resin: Kinetic data and modeling	199
9.1. Abstract	199
9.2. Introduction	199
9.2. Experimental details	201
9.2.1. Materials	201
9.2.2. LBNA production	202
9.2.3. Ion-exchange experiments	203
9.2.4. Analysis methods and calculations	203
9.3. Results and discussion	205
9.3.1 LBNA production	205
9.3.2 LBA production by adsorption exchange	205
9.4. Conclusion	217
General conclusions	219
Recommendations for future work	223
References	225
Appendix 1: List of contributions	245

Appendix 2: Poster presented at 22nd North American Catalysis Society Meeting (June 5-10, 2011, Detroit, MI, USA).....	247
Appendix 3: Poster presented at 22nd Canadian Symposium on Catalysis (May 13-16, 2012, Quebec City, QC, Canada)	249

Index of tables

Table 1.1. Production of lactobionic acid by biocatalytic oxidation of lactose.	10
Table 1.2. Production of lactobionic acid by heterogeneous catalytic oxidation of lactose.	14
Table 1.3. Main commercial and proposed applications of lactobionic acid and/or its salts.	18
Table 1.4. Textural properties of some mesoporous silica materials	22
Table 1.5. Characteristics and catalytic applications of the Au/MSM catalysts synthesized by postsynthetic modification of MSM before gold loading.	33
Table 1.6. Characteristics and catalytic applications of the Au/MSM catalysts synthesized by self-assembly functionalization of MSM before gold loading.....	42
Table 1.7. Characteristics and catalytic applications of the Au/MSM catalysts prepared by direct synthesis. ...	47
Table 1.8. Characteristics and catalytic applications of the Au/MSM catalysts synthesized using cationic gold complex $[\text{Au}(\text{en})_2]\text{Cl}_3$ (en = ethylenediamine).....	56
Table 1.9. Characteristics and catalytic applications of the Au/MSM catalysts synthesized by deposition-precipitation.....	65
Table 1.10. Characteristics and catalytic applications of the mesoporous SiO_2 -based gold catalysts.	71
Table 3.1. The textural parameters of the mesoporous silica support as well as Au catalyst samples prepared at different Au loadings.....	94
Table 3.2. Average crystallite size of Au catalyst samples obtained with TEM and XRD analysis of catalyst samples prepared at different Au loadings.....	98
Table 3.3. Binding energies of Au $4f_{7/2}$ and $4f_{5/2}$ deconvoluted peaks of catalyst samples prepared at different Au loadings.	99
Table 4.1. Textural parameters of the mesoporous SBA-15 and Au/MSM synthesized in the presence of different amounts of BTESPTS.	117
Table 4.2. Binding energies (BE) of Au $4f_{7/2}$ and $4f_{5/2}$ deconvoluted peaks and its relative surface distribution in Au/MSM catalysts.	120
Table 5.1. Textural parameters of the mesoporous SBA-15- CeO_2 support and 0.7%Au/SBA-15- CeO_2 catalyst (Ce/Si molar ratio 0.1).	132
Table 5.2. Binding energies of Au $4f_{7/2}$ and $4f_{5/2}$ deconvoluted peaks and its relative surface distribution in 0.7%Au/SBA-15- CeO_2 (Ce/Si = 0.1 M).	140
Table 5.3. Comparative preponderance of Au species in Au/SBA-15, Au/SBA-15- CeO_2 , and Au/ SiO_2 -meso [11].	143
Table 5.4. Au speciation changes as determined by XPS characterization for fresh and spent Au/SBA15 and Au/SBA-15- CeO_2 catalysts at different pH and Ce/Si molar ratios.....	147
Table 6.1. Textural parameters of silica supports and gold on silica catalysts.....	158
Table 6.2. Binding energies (BE) of Au $4f_{7/2}$ and $4f_{5/2}$ deconvoluted peaks and its relative surface distribution in 0.7%Au/ SiO_2 catalysts.	166
Table 7.1. Effect of catalyst reuse on the lactose conversion (X) and selectivity (S) towards lactobionic acid ^a	173
Table 7.2. Binding energies (BE) of Au $4f_{7/2}$ and $4f_{5/2}$ deconvoluted peaks and its relative surface distribution in fresh and spent Au/SBA-15 and Au/SBA-15- CeO_2 catalysts.	177
Table 7.3. Comparative preponderance of gold species in fresh and spent Au/SBA-15 and Au/SBA-15- CeO_2 catalysts.....	178
Table 7.4. Gold content in the reaction solutions after consecutive oxidation cycles.....	180

Table 8.1. Main properties of the cationic, anionic and bipolar membranes used in the stack..... 184
Table 9.1. Physical and chemical properties of the Amberlite FPC23 H^a202
Table 9.2. Exchange capacity and ion exchange efficiency as a function of temperature during the adsorption exchange of sodium from LBNa on Amberlite FPC23 H208
Table 9.3. Kinetic model parameters of sodium exchange on AmberliteTM FPC23 H at different temperatures.210

Index of figures

Figure 1. Usage of lactose in the EU and USA in 2005.....	2
Figure 2. Scheme for the production processes of lactose derivatives.....	2
Figure 1.1. Schematic oxidation of lactose to lactobionic acid.	9
Figure 1.2. Schematic biocatalytic oxidation of lactose to lactobionic acid.....	9
Figure 1.3. Schematic catalytic oxidation of lactose to lactobionic acid under alkaline conditions.	14
Figure 1.4. General scheme of the formation of MSM by structure-directing agents: a) true liquid-crystal template mechanism, b) cooperative liquid crystal template mechanism.....	24
Figure 1.5. Typical XRD pattern for SBA-15 materials. The corresponding d-spacings: (100) = 9.80 nm; (110) = 5.45 nm and (200) = 4.74 nm.....	25
Figure 1.6. TEM images and diffraction pattern showing the hexagonal ordering of SBA-15 and the curved pores.	26
Figure 1.7. Typical nitrogen adsorption (●) – desorption (×) isotherm of calcined (500°C, 6h) mesoporous silica SBA-15 synthesized with the amphiphilic triblock copolymer Pluronic P123. (STP: standard temperature and pressure).....	26
Figure 1.8. Variation of the unit cell parameter <i>a</i> (●) and pore size (○) for calcined SBA-15 as a function of the TMB: surfactant ratio (g/g).....	28
Figure 1.9. Published papers on the topic of gold catalysts. Source: Web of Science, Thomson Reuters.....	31
Figure 1.10. General procedure to synthesize gold catalysts by post-synthetic functionalization of the MSM before gold loading.....	33
Figure 1.11. TEM (a,b,c) and HAADF STEM (d,e,f) images of gold catalysts supported on different MSM prepared by using the postsynthetic functionalization of MSM before gold loading. (a) Au/SBA-15 modified with APS; (b) Au/SBA-16 modified with APTS; (c) Au/MCM-41 modified with APTS; (d) Au/HMM-2 modified with APS; (e) Au/SBA-12 modified with APS; (f) Au/SBA-11 modified with APS; (g) Au/SBA-15 modified with PANAM; (h) Au/SBA-15 modified with TPED; (i) Au/SBA-15 modified with Py.....	37
Figure 1.12. General procedure to synthesize gold catalysts by self-assembly functionalization of MSM before gold loading.....	41
Figure 1.13. TEM images of gold catalysts supported on different MSM prepared by using the self-assembly functionalization of MSM before gold loading. (a) Au/MCM-41 modified with OBSQ; (b) Au/MSU modified with OBSQ; (c) Au/SBA-15 modified with OBSQ; (d) Au/MCM-41 modified with APS; (e) Au/HMS modified with hydrophilic bis-silylated precursor containing disulfide; (f) Au/SBA-15 modified with MPS.	46
Figure 1.14. TEM images of gold catalysts supported on different MSM prepared by direct synthesis. (a) Au/SBA-15 using MPS; (b) Au/SBA-15 using VTES; (c) Au/MCM-41 using APTS; (d) Au/MS using BTESPTS; (e) Au/HMS using TMPTA; (f) Au/PMOs using TMPTA; (g) Au/MS using BTESPTS 7% molar concentration; (h) Au/MS using BTESPTS 2% molar concentration	53
Figure 1.15. TEM micrographs of Au/MSM using Au(en) ₂ Cl ₃ as gold precursor. (a) Au/SBA-15; (b) Au/SBA-15; (c) Au/MCM-41; (d) Mesoporous SBA-15-CeO ₂ (Ce/Si molar ratio = 0.1); (e) 0.7% Au/SBA-15-CeO ₂	57
Figure 1.16. TEM micrographs of Au/MSM prepared by deposition-precipitation. (a) Au/SBA-15; (b) Au/SBA-15; (c) Au/SBA-15; (d) Au/SBA-15; (e) Au/HMM-2	66
Figure 1.17. TEM micrographs of mesoporous SiO ₂ -based gold catalysts. (a) Au/Ti-MCM-41; (b) Au/Al ₂ O ₃ -SiO ₂ ; (c) Au/Ti-HMS; (d) Au/Co-SBA-15; (e) Au/Ti-SBA-15; (f) Au/Ti-MCM-48; (g) Au/Fe-MCM-41; (h) Au/Al-MCM-41; (i) Au/Co-MCM-41; (j) Au/Ce-HMS; (k) Au/Fe-HMS; (l) Au/Co-UVM-7.....	75

Figure 3.1. Nitrogen adsorption/desorption of mesoporous silica material and Au on mesoporous silica at different Au loadings.....	93
Figure 3.2. Pore size distributions of mesoporous silica material and Au/SiO ₂ -meso at different Au loadings.	94
Figure 3.3. Low angle XRD profiles of mesoporous silica material and Au/SiO ₂ -meso at different Au loadings.	95
Figure 3.4. Wide angle XRD profiles of Au on mesoporous silica at different Au loadings.....	96
Figure 3.5. (a) TEM micrographs of mesoporous silica material; (b) 0.4% Au/SiO ₂ -meso; (c) 0.5% Au/SiO ₂ -meso; (d) 0.7% Au/SiO ₂ -meso; (e) 0.8% Au/SiO ₂ -meso; (f) 1.0% Au/SiO ₂ -meso.	97
Figure 3.6. XPS-spectra of Au 4f photoelectron peak for: (a) 0.4% Au/SiO ₂ -meso; (b) 0.7% Au/SiO ₂ -meso; (c) 1.0% Au/SiO ₂ -meso.....	99
Figure 3.7. Kinetic profiles of lactose uptake and LBA production during lactose oxidation over 0.7% Au/SiO ₂ -meso catalyst. Conditions: T = 65°C; pH 9; Catalyst to lactose ratio R = 0.2. Bares stand for the standard deviation for two repetitions.	100
Figure 3.8. Trends of the initial rate and the Au crystallite size versus Au loading. Bares stand for the standard deviation for two repetitions for each catalyst synthesis.	102
Figure 3.9. Trend of the initial rate versus the Au crystallite size. The vertical bares stand for the standard deviation in the initial rate while horizontal bares stand for the standard deviation in the crystallite size for two repetitions for each catalyst synthesis. Dashed line represents only a general tendency.	102
Figure 3.10. Effect of the catalyst/lactose ratio, R, on the initial reaction rate, <i>r</i> ₀ during the partial oxidation of lactose to LBA over 0.7% Au/SiO ₂ -meso catalyst. Conditions: T=65°C; pH 9.0. Bares stand for the standard deviation for two repetitions of the catalyst synthesis.....	103
Figure 3.11. Effect of the pH on the initial reaction rate, <i>r</i> ₀ during the partial oxidation of lactose to LBA over 0.7% Au/SiO ₂ -meso catalyst. Conditions: T = 65°C; R = 0.2. Bares stand for the standard deviation for two repetitions of the catalyst synthesis.	104
Figure 3.12. Effect of the reaction temperature on the initial reaction rate, <i>r</i> ₀ during the partial oxidation of lactose to LBA over 0.7% Au/SiO ₂ -meso catalyst. Conditions: pH 9.0; R = 0.2. Bares stand for the standard deviation for two repetitions of the catalyst synthesis.....	106
Figure 4.1. Low-angle XRD patterns of mesoporous silica SBA-15 and Au/MSM catalysts synthesized with different BTESPTS/TEOS molar ratios.....	112
Figure 4.2. Wide-angle XRD patterns of Au/MSM catalysts synthesized with different BTESPTS/TEOS molar ratios.....	113
Figure 4.3. TEM micrographs of mesoporous silica SBA-15 and Au/MSM catalysts synthesized with different BTESPTS/TEOS molar ratios.....	115
Figure 4.4. Nitrogen adsorption/desorption isotherms of mesoporous silica SBA-15 and Au/MSM catalysts synthesized with different BTESPTS/TEOS molar ratios.	118
Figure 4.5. XPS-spectra of the Au 4f core-level of Au/MSM catalysts synthesized with different BTESPTS/TEOS molar ratios.....	121
Figure 4.6. Images of mesoporous silica SBA-15 and Au/MSM catalysts synthesized with different BTESPTS/TEOS molar ratios.....	122
Figure 4.7. Kinetics profiles of lactose oxidation to LBA over Au/MSM catalysts synthesized with different BTESPTS/TEOS molar ratios.....	124
Figure 5.1. Nitrogen adsorption/desorption isotherms (a) and pore size distributions (b) of SBA-15, SBA-15-CeO ₂ and 0.7%Au/SBA-15-CeO ₂ materials (Ce/Si molar ratio 0.1).....	133

Figure 5.2. Low angle XRD patterns of SBA-15, SBA-15-CeO ₂ and Au/SBA-15-CeO ₂ materials. Inset: Wide angle XRD pattern of 0.7%Au/SBA-15-CeO ₂ catalyst (Ce/Si molar ratio 0.1).....	135
Figure 5.3. TEM micrographs of (a) mesoporous SBA-15; (b) SBA-15-CeO ₂ (Ce/Si molar ratio 0.1); (c) 0.7%Au/SBA and (d) 0.7%Au/SBA-15-CeO ₂	136
Figure 5.4. FTIR spectra of mesoporous SBA-15, SBA-15-CeO ₂ (molar ratio Ce/Si = 0.1) and 0.7%Au/SBA-15-CeO ₂ (molar ratio Ce/Si = 0.1).	137
Figure 5.5. XPS-spectra of (a) O 1s, (b) Si 2p, (c) Au 4f and (d) Ce 3d core-level photoelectron spectra of the 0.7%Au/SBA-15-CeO ₂ catalyst (molar ratio Ce/Si = 0.1).	139
Figure 5.6. Effect of the pH on the kinetics of lactose oxidation to LBA acid over 0.7%Au/SBA-15-CeO ₂ catalyst (Ce/Si=0.1 M). (a) pH 7; (b) pH 8; (c) pH 9 and 0.7%Au/SBA-15 catalysts (d) pH 8; (e) pH 9. Conditions: T=65°C; catalyst/lactose ratio 0.2, air flow=40 mL/min, agitation = 900 rpm.	142
Figure 5.7. Activity comparison of the catalysts at pH 8 and pH 9. Conditions: T = 65°C; catalyst/lactose ratio 0.2, air flow = 40 mL/min, agitation = 900 rpm.	145
Figure 5.8. Initial rate of LBA formation vs. Ce/Si molar ratio for 0.7%Au/SBA-15-CeO ₂ catalysts.....	146
Figure 5.9. Au crystallite size vs. Ce/Si molar ratio for 0.7%Au/SBA-15-CeO ₂ catalysts.....	146
Figure 6.1. (a) Au/SBA-15 (b) Au/Cab-O-Sil.....	155
Figure 6.2. Nitrogen adsorption/desorption isotherms (a) and pore size distributions (b) of SBA-15, 0.7%Au/SBA-15, Cab-O-Sil and 0.7%Au/Cab-O-Sil materials (for clarity, the isotherms of SBA-15, 0.7%Au/SBA-15 and Cab-O-Sil were up-shifted by 500, 450 and 300 cm ³ .g ⁻¹ , respectively).	159
Figure 6.3. (a) Low angle XRD patterns of SBA-15 and 0.7%Au/SBA-15 materials. (b) Low angle XRD patterns of Cab-O-Sil and 0.7%Au/Cab-O-Sil materials. (c) Low angle XRD patterns of SiO ₂ -meso and 0.7%Au/ SiO ₂ -meso materials. (d) Wide angle XRD patterns of 0.7%Au/SBA-15, 0.7%Au/Cab-O-Sil and 0.7%Au/ SiO ₂ -meso catalysts.....	161
Figure 6.4. Representative transmission electron micrographs and gold particle size distributions of (a) 0.7%Au/SBA-15, (b) 0.7%Au/Cab-O-Sil and (c) 0.7%Au/SiO ₂ -meso (Reproduced by permission of Elsevier from Reference [11]).....	162
Figure 6.5 FTIR spectra at the Si–O vibration region of SBA-15, 0.7%Au/SBA-15, Cab-O-Sil and 0.7%Au/Cab-O-Sil samples.	164
Figure 6.6. XPS-spectra of Au 4f core-level of (a) 0.7%Au/SBA-15 and (b) 0.7%Au/Cab-O-Sil catalysts.	165
Figure 6.7 Effect of the pH on the kinetics of lactose oxidation to LBA acid over Au/SiO ₂ catalysts. (a) 0.7%Au/SBA-15 at pH=8.0; (b) 0.7%Au/SBA-15 at pH=9.0; (c) 0.7%Au/Cab-O-Sil at pH=8.0; and (d) 0.7%Au/Cab-O-Sil at pH=9.0. Reaction conditions: T=65°C; Catalyst/Lactose ratio 0.2, air flow = 40 mL/min, agitation=900 rpm.	167
Figure 6.8 Initial rate of LBA synthesis by aerobic oxidation of lactose on Au/SiO ₂ catalysts. Reaction conditions: T=65°C; Catalyst/Lactose ratio 0.2, air flow = 40 mL/min, agitation=900 rpm.....	169
Figure 7.1. TEM images and particle size distribution Au/SBA-15 catalysts. (a) Before the reaction. (b) After two reactions. (c) After three reactions.	174
Figure 7.2. TEM images and particle size distribution Au/SBA-15-CeO ₂ catalysts. (a) Before the reaction. (b) After two reactions. (c) After two reactions and calcination at 400°C during 4h. (d) After three reactions.	175
Figure 7.3. Typical XPS-spectra of Au 4f core-level photoelectron spectra of fresh and spent Au/SBA-15 and Au/SBA-15-CeO ₂ catalysts.....	176
Figure 7.4. XPS-spectra of Au 4f core-level photoelectron spectra of spent Au/SBA-15-CeO ₂ catalyst regenerated by calcination at 400°C for 4h.	179

Figure 8.1. Configuration of the BMED cell. AEM: anion-exchange membrane; BM: bipolar membrane, CEM: cation-exchange membrane.	185
Figure 8.2. Variation of the pH values in the diluate, base and acid compartments during the recovery of LBA from LBNa by means of BMED.	190
Figure 8.3. Variation of the electrical conductivity in the diluate, base and acid compartments during the recovery of LBA from LBNa by means of BMED.	191
Figure 8.4. Effect of voltage on the number of charges transported during the recovery of LBA from LBNa by means of BMED.	192
Figure 8.5. (a) LBA concentration in the diluate and acid compartments, and sodium concentration in the diluate (b) and acid (c) compartments during the recovery of LBA from LBNa by means of BMED.	193
Figure 8.6. Scanning electron micrographs of the surface of (a) BM, (b) CEM and (c) AEM before and after the BMED process.	196
Figure 8.7. X-ray elemental analyses of the AEM surface before (a) and after (b) the BMED process.	197
Figure 9.1. Experimental kinetic profiles of lactose oxidation over gold catalysts supported on mesoporous silica. Lines stand for experimental tendency.	205
Figure 9.2. Sodium concentration kinetic profiles in LBNa solution during the exchange adsorption process of sodium on Amberlite™ FPC23 H at different resin/solution (mg/mL) ratios.	206
Figure 9.3. Kinetic profiles of sodium adsorption exchange on Amberlite™ FPC23 H at different temperatures.	207
Figure 9.4. Modeling of sodium ion-exchange curves calculated by different kinetic model approaches: (a) Pseudo-first order model, (b) Pseudo-second-order model, (c) Intra-particle diffusion model, and (d) Reversible reaction model.	211
Figure 9.5. Intra-particle diffusion plots of sodium adsorption exchange on Amberlite™ FPC23 H at different temperatures.	213
Figure 9.6. SEM micrographs and X-ray elemental analyses of the Amberlite™ FPC23 H before (a) and after (b) the adsorption exchange of Na ⁺ from LBNa.	216

List of abbreviations

a.u.	Arbitrary units
AAPTS	3-(2-Aminoethylamino) Propyltrimethoxysilane
AEM	Anion exchange membrane
ALB	Acide lactobionique
APS	3-Aminopropyltrimethoxysilane
APTS	3-Aminopropyltriethoxysilane
AuCl(THT)	Chloro-(thiophene)gold(I)
AuMe ₂ (HFA)	Dimethyl(hexafluoroacetylacetoato) gold(III)
Au/MSM	Gold catalysts supported on mesoporous silica materials
AuNPs	Gold nanoparticles
BE	Binding energy
BET	Brunauer-Emmett-Teller
BMED	Bipolar membrane electro dialysis
BOD	Biological oxygen demand
BTESPTS	<i>bis</i> -[3-(triethoxysilyl) propyl] tetrasulfide
C ₁₀ H ₂₃ ClSi	Chlorodimethyloctylsilane
C ₁₈ TMS	<i>n</i> -Octadecyltrimethoxysilane
CDH	Cellobiose dehydrogenase
CEM	Cation exchange membrane
COD	Chemical oxygen demand
CTABr	Cetyltrimethylammonium bromide
CTACl	Cetyltrimethylammonium chloride
CVD	Chemical vapor deposition
DBTA	Dibenzoyl tartaric acid
DDA	Dodecylamine
DP	Deposition-precipitation
<i>en</i>	Ethylenediamine
EO	Polyethyleneoxide
EtOH	Ethanol
F127	Pluronic block copolymer surfactant
FDU	Fudan University in Shanghai Marerials
FT-IR	Fourier transform infrared spectroscopy
FW	Formula weight
G4-PANAM	Polyamidoamine dendrimers fourth generation
GFOR	Glucosee fructose oxidoreductase
GFOR/GL	Glucosee fructose oxidoreductase and glucono- δ -lactonase
HAADF STEM	Higher angle annular dark field scanning transmission electron microscopy
HMM	Hiroshima mesoporous material
HMS	Hexagonal mesoporous silica
HSN	Hollow silica nanospheres
ICP-OES	Inductively coupled plasma optical emission spectrometry
IEP	Isoelectric point
IUPAC	International union of pure and applied chemistry
IWI	Incipient wet impregnation

KIT-5	Large mesopore <i>Fm3m</i> silica
LBA	Lactobionic acid
LBNa	Sodium lactobionate
LB ⁻	Lactobionate anion
MCF	Mesostructured cellular foam
MCM	Mobile crystalline material
Me ₂ Au(acac)	Dimethyl Gold Acetylacetonate
MPS	3-Mercaptopropyltrimethoxysilane
MPTS	3-Mercaptopropyltriethoxysilane
MS	Mesoporous silica
MSM	Mesoporous silica materials
MSS	Mesoporous silica spheres
MSTF	Mesoporous silica thin films
MSU	Michigan State University materials
MTFs	Mesoporous thin films
OBSQ	Organic bridged silsesquioxane
OFL	Organic functional ligand
P123	Pluronic acid block copolymer
PAMAM	Polyamidoamine dendrimers
PDH	Pyranose dehydrogenase
PLL	Poly(L-lysine)
PLT	Poly(L-tyrosine)
PMOs	Periodic mesoporous organosilica
PO	Polypropyleneoxide
PROX	Preferential oxidation of CO in the presence of H ₂
PrTMS	Propyl trimethoxysilane
Py	(s)-(-)-2-Pyrrolidinone-5-carboxylic acid (Py)
r_0	Initial reaction rate of lactose conversion to LBA
RxN	Reaction
SBA	Santa Barbara amorphous
SDA	Structure-directing agent
SDS	Sodium dodecyl sulfate
TEM	Transmission electron microscopy
TEOS	Tetraethoxysilane
THF	Tetrahydrofuran
TMOS	Tetramethoxysilane
TMPDA	3-(Trimethoxysilyl)propyl]diethylenediamine
TMPTA	3-(Trimethoxysilyl)propyl]diethylenetriamine
TPED	<i>N</i> -[3-(Trimethoxysilyl)propyl]ethylenediamine
TPO	Temperature Programmed Oxidation
TPTAC	<i>N</i> -Trimethoxysilylpropyl- <i>N,N,N</i> -trimethylammonium chloride
VTES	Vinyl triethoxysilane
WSS	Wormhole silica support
XANES	X-ray absorption near-edge spectroscopy
XPS	X-ray photoelectron spectroscopy
XRD	Powder X-ray diffraction

In the memory of my Father died in February 2013. This thesis is for you Dad, thanks for all.

With love to my Mother, example of faith, strength and tenacity. I will always love you mom!

To my daughter Dana: The light of my eyes and my reason to live.

To my wife Sandra Dalila: always there for supporting me.

I would like also to dedicate the effort I made during all my PhD studies to all cancer victims. I know how painful is the life after getting cancer, and I hope that scientists can find soon a real cure to this terrible illness.

Acknowledgements

The submission of a PhD thesis is the result of various years of hard work, and the longed-for light at the “end” of a way full of hurdles and joyous moments. This dissertation has been my priority since three years. However, it is true that life doesn’t stand still, nor wait until you have finished and have time to manage it. Unfortunately, due to life’s challenges and the changes that followed, my thesis could not always be the number one priority. In any case, now, while I’m writing these final words of my dissertation, I’m proud of this work and I feel that I have finished, but not alone. During this long journey, the invaluable support of the people who contributed me in one way or another for accomplishing this goal deserves special mention. Without these supporters, I could not have succeeded.

Of all thanks I must render, my Parents Stella and Jorge get the first. Without them, I may not have gotten to where I am today. Thank you so much mom and dad for your wise advices and words, for your prayers, for your unconditional support, for teaching me that our dreams can come true if we have the courage to pursue them with discipline and persistence. Thank you both for being a model of strength, resilience and character. Thank you because all these things have made me the man that I am today. How happy I would be if you could be here seeing how I’m still trying to reach all the things that you wanted me to be.

I am deeply grateful to my advisor, Professor Khaled Belkacemi, for giving me the opportunity to follow this doctoral formation, as well as for his patience, flexibility, guidance and constructive criticism. We have shared long time in a good working relationship, and I will always be thankful for the trust he deposited in me. Moreover, above the academic field, I would like to thank his understanding during the difficult moments I had in my personal life during these years. He has never judged nor pushed when he knew I needed to manage priorities.

I do gratefully acknowledge my co-advisor, Professor Safia Hamoudi, for her collaboration in the XRD analysis, and for her gentle availability for explaining and discussing.

I would like to give special thanks to Professor Laurent Bazinet for his collaboration and for lending me his lab equipments and instruments to carry out the electro dialysis experiments. I could never

have realized this part of my thesis without his support. Moreover, I appreciated the opportunities he gave me to teach part of his course during my PhD studies.

I also want to thank Professor Maria-Cornélia Iliuta, for doing the pre-reading of this thesis and for her valuable comments.

I am deeply grateful to Dr. Catherine Louis, the external examiner of this thesis. I was very fortunate to get the precious and helpful comments from one of the most important researchers worldwide on gold catalysts, in order to improve this dissertation.

Thanks very much to the technicians who assisted me in the especial analyses. Alain Adnot, Alain Brousseau, André Ferland, Daniel Marcotte, Richard Janvier and Diane Gagnon, your collaboration was crucial to complete this thesis.

I am also grateful to the Universidad Nacional de Colombia for granting study leave for getting my PhD. My colleagues at the Instituto de Ciencia y Tecnología de Alimentos are acknowledged for their collaboration during my absence. Special mention deserves Professors William Albarracín, Carlos Fernando Novoa and Anibal Orlando Herrera, as well as Carmen Elisa Scarpeta and Margarita Díaz, who helped me in the administrative procedures all these years.

I would like to thank to my wife, for always being by my side, loving, supporting and believing in me. Her encouraging words when the way seemed to be dark and without exit were the support for do not lose heart and keep trying.

To my lovely daughter Dana, thank you for the happiness you brought into my life and for reminding me the important things in life. She gives me the strength and courage to continue and press forward.

Thanks so much to my brother Jorge Enrique Gutiérrez, for taking care of our mom during my absence. Otherwise I could not have finished this PhD.

My gratitude is also extended to my family in law, Nancy, Germán, Lina Marcela and Germán Andrés. Thank you for your silent but unconditional support.

My deep appreciation must also be expressed to my friends and colleagues Mónica Araya-Farías, Nicolás Cifuentes-Araya, Romuald Babou, Abdou Dioum, Subha Kumaraswamy, Elodie Rozoy,

Fatoumata Diarrassouba, Shyam Suwal, Juan Li, Sergei Mikhailyn, Luca Lo Verso, Pedro Álvarez, Marina Bergoli and Sébastien Goumon. Thank you for friendship, and for lending a sympathetic ear and giving useful advice. Thank you for the parties, for the discussions and for enriching my culture all these years.

Finally, these acknowledgements would not be complete if I did not mention my dog Pepón, died in November 2012. He was part of my life's projects almost 13 years. He waited for me at home every night until I came back from the university to go outside. How I miss you my friend, and how I remember our walks, which always brought peace, solutions and new research ideas.

Preface

This doctoral thesis is written in the form of a compilation of scientific papers, which at the time of the thesis submission, have been mostly published or submitted for publication. In all cases, the first author of these papers is the submitter of this Ph.D. thesis, who was in charge of the conception, planning and execution of the practical works, as well as of the articles' writing.

The thesis is divided into nine chapters. Firstly, the general introduction presents the generalities and uses of lactose, as well as the identification of the main research problems related to the selective production of LBA by aerobic oxidation of lactose over supported-metal catalysts, and the recovery of LBA from its sodium salt.

The literature review is presented in Chapter 1. In the first part of this chapter, the main characteristics, manufacturing methods, applications and physiological effects of lactobionic acid are presented in the form of an article review, published in the *International Dairy Journal* 2012, 26(2), 103-111. In the second part, the principal aspects of the mesoporous silica materials, with special emphasis on the mesoporous SBA-15, are described and discussed. Finally, the third part of this chapter consists in a complete review on the synthesis of gold catalysts supported on mesoporous silica materials, which was a contribution to the special issue Gold Catalysts of the journal *Catalysts* 2011, 1(1), 97-154.

Chapter 2 presents the hypotheses and objectives of this research project, while the results are described in Chapters 3 to 9.

Chapter 3 reports the synthesis and characterization of gold catalysts supported on mesoporous silica (Au/MSM), as well as the influence of the reaction conditions on the lactose oxidation to LBA. Various Au/MSM catalysts with nominal gold loadings varying between 0.4 and 1.0%wt were synthesized by co-condensation of a mixture of *bis* [3-(triethoxysilyl)propyl] tetrasulfide (BTESPTS), tetraethyl orthosilicate (TEOS) and the gold precursor (HAuCl₄) in acidic media, using the triblock copolymer EO₂₀PO₇₀EO₂₀ (P123) as template. This method led to obtain well dispersed gold nanoparticles highly active and 100% selective towards LBA. The results of this work were published in *Applied Catalysis A: General* 2011, 402, 94- 103.

In Chapter 4, the effect of different concentrations of BTESPTS in the synthesis of various Au/MSM catalysts, with a nominal gold loading of 0.7%wt, on their characteristics and lactose oxidation activity is presented. The characterization analysis and the lactose oxidation experiments indicated that samples synthesized with BTESPTS molar concentrations of 6-10% showed the highest catalytic activity, because their wormhole-like structure facilitate the access of the substrate to the active sites. This article is still under revision and it will be submitted to an appropriate journal when considered opportune.

Chapter 5 report the synthesis and characterization of gold catalyst supported on mesoporous silica decorated by ceria by means of a chemical process using a gold cationic complex precursor $Au(en)_2Cl_3$ (en = ethylenediamine). Various Au/SBA-15 and Au/SBA-15-CeO₂ with nominal gold loading of 0.7%wt and different Ce/Si molar ratios were synthesized and evaluated as catalysts for the selective production of LBA from lactose. It was found that ceria plays a role in the enhancement of the catalytic activity. At the optimized conditions, the Au/SBA-15-CeO₂ catalysts synthesized with Ce/Si molar ratios of 0.1 and 0.2 showed the highest catalytic activity. These results were published in *Applied Catalysis A: General* 2012, 425-426, 213-223.

In Chapter 6 gold catalysts supported on mesoporous SBA-15 and amorphous fumed silica (Cab-O-Sil) synthesized by cation adsorption of $Au(en)_2Cl_3$ (en = ethylenediamine) are compared in terms of their general characteristics and their catalytic activity on the lactose oxidation. Although both catalysts exhibited high activity and 100% selectivity towards LBA, the Au/SBA-15 samples showed better performance. This article was submitted to *Catalysis Science & Technology*.

Chapter 7 consists in a brief study on the catalysts recycle and deactivation. The characteristics and catalytic activity of two catalysts (Au/SBA-15 and Au/SBA-15-CeO₂ molar ratio Ce/Si of 0.2) were investigated after consecutive reaction cycles. It was found that the main causes of deactivation could be the strong adsorption of organic species on the catalyst surface and the leaching of the active phase into the reaction solution. Calcination was found to be an effective method for the catalysts' regeneration.

In Chapter 8, bipolar membrane electrodialysis was investigated for the demineralization of the sodium lactobionate solution obtained after lactose oxidation over Au/MSM. Using a three-compartment bipolar membrane electrodialysis stack, a demineralization rate of 50% was achieved

after applying a voltage difference of 5.0-5.5 V during 100-180 min. The results of this work were published in *Separation and Purification Technology* 2013, 109, 23-32.

Chapter 9 describes the production of LBA from sodium lactobionate (LBNa) by ion exchange technology. A commercial cation exchange resin (Amberlite™ FPC23 H) was used for this purpose. A complete sodium removal was achieved after 10-30 min at the investigated conditions. The results of these experiments were submitted to the journal *Solvent Extraction and Ion Exchange*.

Finally, the general conclusions section and some recommendations for future work are presented to complete the thesis.

Introduction

In recent years, the use of biomass as raw material for the production of energy, bulk chemicals and value-added chemicals has shown remarkable increase, because of its abundance, renewability and worldwide distribution, as well as for diminishing the current dependence on nonrenewable energy sources. From the five categories of biomass materials (virgin wood, energy crops, agricultural residues, food waste, industrial waste and co-products), carbohydrates are the most abundant renewable resources available, and they are currently viewed as a feedstock for the green chemistry of the future, since sugars are one of the foremost natural sources of potentially relevant chemicals [1].

The dairy industry generates huge amounts of stream wastewaters characterized by high biological oxygen demand (BOD) and chemical oxygen demand (COD) concentrations. For example, the BOD of whey, the greenish translucent liquid obtained from milk after precipitation of caseins, is very high ($\geq 40000 \text{ mg}\cdot\text{kg}^{-1}$), constituting a major environmental problem if disposed off as a waste material [2]. The cheese production worldwide generates more than 145 million tons of liquid whey per year, which is mainly used for animal feeding or discarded without treatment [3], even if over the last years numerous processes for whey processing have been developed for the manufacture of functional foods and nutraceutical products.

Although the composition of whey varies depending on the milk source and the casein precipitation process, it contains about 65 grams of solids per kg, comprising approximately 50 g of lactose, 6 g protein, 6 g ash, 2 g non-protein nitrogen, and 0.5 g fat [2]. Thus, taking into account that the main component of whey is lactose (70-75% of the total solids), the increasing in value of whey is closely related to the effective use of lactose, whose production and global market have been estimated to about 1.2 million tons per year [4], and to reach US\$1.4 billion by 2015 [5], respectively.

Lactose can find many applications in the food and pharmaceutical industries. As depicted in Figure 1, lactose is mainly used as an ingredient in foods, infant formula, bakery and confectionery products, and it has been extensively employed as diluent in tablets and carrier of medicines in the pharmaceutical industry. Nevertheless, the use of lactose is limited in many applications, because of its low sweetness and solubility, as well as due to the intolerance of some population segments, and only a small amount of lactose is employed as a raw material for producing fine chemicals [6].

However, the worldwide surplus and low cost of lactose have heightened interest in the development of innovative processes for producing valuable lactose derivatives, and expanding their applications in the food, pharmaceutical and chemical industries. Some significant developments include the manufacture of epilactose, galacto-oligosaccharides, lactitol, lactobionic acid, lactosucrose, lactulose, sialyllactose and tagatose, which can be produced by enzymatic, microbial or chemical modification of lactose, as shown in Figure 2.

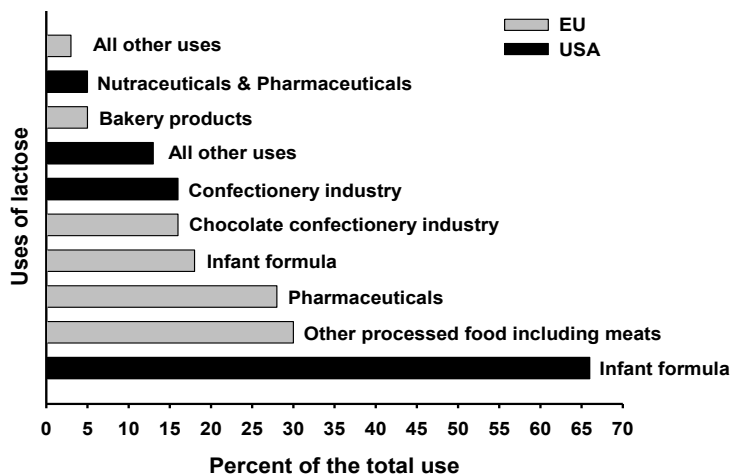


Figure 1. Usage of lactose in the EU and USA in 2005 (Adapted from [7]).

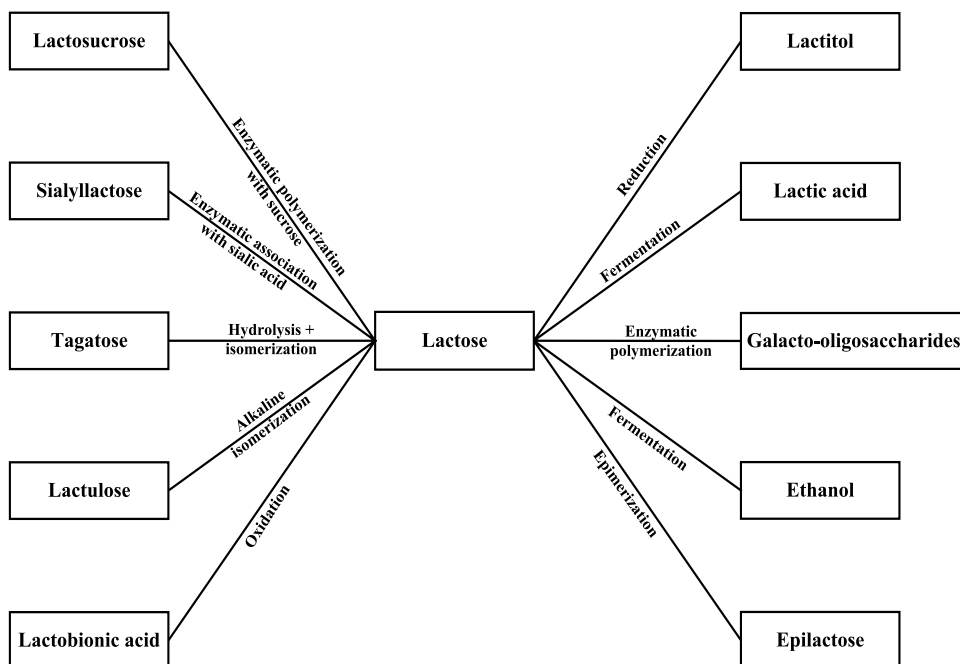


Figure 2. Scheme for the production processes of lactose derivatives.

Lactobionic acid (LBA) (4-O- β -D-galactopyranosyl-D-gluconic acid) is a high value-added product obtained from the oxidation of lactose, with high potential applications as ingredient in foods, pharmaceutical and cosmetic products, because of its antioxidant, chelating and humectant properties. LBA and its mineral salts (mainly Na-, Ca and K-lactobionate) are commercially produced in small quantities for industrial and medical applications, as well as for research use. The most important producers are Solvay (Germany) and FrieslandCampina Domo (The Netherlands) [8]. According to Affertsholt-Allen [7], the market for LBA is between 15000 and 17000 tons per year, with an expected annual growth rate of 5%.

Although LBA can be manufactured by chemical, electrochemical, biocatalytic and heterogeneous catalytic oxidations, the heterogeneous catalytic processes using air or molecular oxygen as eco-friendly oxidizing agents are considered as an environmentally friendly alternative, presenting faster conversions and fewer amounts of effluents and side-products than the biocatalytic reactions. Moreover, the benefits in using heterogeneous catalysts are associated with the ease of their recovery from the reaction media, their potential for recyclability, and the relatively low prices compared to homogeneous catalysts. In addition, the heterogeneous catalytic process can easily be integrated into other lactose transformation technologies [9].

Similar to other carbohydrates, the oxidation of lactose in aqueous media using supported-metal catalysts has undergone considerable development since the decade of the 1990s. LBA production by means of heterogeneous catalytic oxidation of lactose on palladium and bismuth-palladium supported catalysts was first successfully performed by Hendriks et al. [10]. Since then, this reaction has been mainly evaluated over platinum, palladium, **Mx**-promoted platinum and **My**-promoted palladium supported catalysts (**Mx** = Bi, Cu, V, Fe, and **My** = Bi, V, Tl, Pb) [6]. The reaction should be carried out at atmospheric pressure in alkaline media (pH between 8.0 and 9.0), with temperatures in the range of 50-70°C. Higher pH values have an important influence on selectivity, since isomerization of lactose to lactulose is favored. On the other hand, low pH values promote the catalyst deactivation by the strong adsorption of the reaction products, which occupy the active sites of the catalyst, reducing significantly the lactose conversion rate [11]. Although high conversions and selectivities have been achieved with platinum and palladium catalysts, the main problem of these catalysts is their instability by leaching and deactivation by over-oxidation during the reaction. Moreover, since bismuth is prone to leaching from the catalyst surface, applications of catalysts

containing bismuth are not appropriate for production of chemicals for the food and pharmaceutical industries [9]. Thus, as in the case of glucose and other carbohydrates, the challenge in the catalyst selection for lactose oxidation is in finding a catalyst that is less prone to deactivation.

Supported gold catalysts have shown to outperform palladium and platinum catalysts for the oxidation of carbohydrates, because they are less prone to overoxidation, and they exhibit high activity and selectivity towards aldonic acids [12]. However, the oxidation of lactose using gold catalysts has been scarcely investigated. Lactose oxidation reactions over gold on Al_2O_3 , TiO_2 , SiO_2 , Fe_2O_3 , Fe_3O_4 , ZrO_2 , ZnO_2 and CeO_2 , indicated that supported AuNPs on Al_2O_3 , TiO_2 , and CeO_2 allowed to achieve moderate to high conversions (>80%) and selectivities (up to 95%), using Au loadings in the range of 0.4-2.0% [13-16]. Even though these relatively high conversions and selectivities have been reached, the selective oxidation of lactose to LBA over gold catalysts still needs further improvement of conversion and selectivity, for achieving the goal of eventually commercial applications.

It is worth mentioning that taking into account that the main product of selective oxidation of lactose to LBA over gold catalysts is a lactobionate salt solution rather than the protonated acid form, given that the pH must be kept in alkaline conditions during reaction by adequate addition of a Na-, Ca- or K-base. Thus, if the desired product is LBA, the demineralization of the salt solution obtained at the reactor outlet is indispensable. However, there are no available data for this demineralization step in the open literature. From the three existing processes for industrial acidification of organic salts (adding inorganic acids, ion-exchange technology and demineralization using bipolar membrane electrodialysis), the latter is particularly interesting because it can be considered as a “green” process to achieve the conversion of the acid salts into their acidic forms, without the generation of large volumes of chemical effluents, thus avoiding a cumbersome regeneration step required in the ion-exchange technologies [17]. However, the recovery of large size organic acids such as LBA (358.3 Da) using electrodialysis processes is a challenging task, because of the difficulties for their migration across the anion-exchange membranes, which normally show high resistances to the transport of larger compounds.

Mesoporous silica materials (MSM) are very suitable as catalyst supports, since they provide high dispersion of metal nanoparticles and facilitate the access of the substrates to the active sites [18]. However, due to the low isoelectric point of silica (~ 2), the common deposition-precipitation method

is not appropriate for the synthesis of gold catalysts supported on MSM (Au/MSM), because under the high pH conditions required to hydrolyze the most commonly used gold precursor (HAuCl_4), the weak interaction between the negatively charged silica surface and the $[\text{Au}(\text{OH})_n\text{Cl}_{4-n}]^-$ species hinders the gold adsorption and facilitates the mobility of AuNPs, which can sinter easily during the synthesis process, yielding low gold loadings and inactive catalysts with aggregated-Au clusters [19].

Taking into account that Au/MSM catalysts have not been investigated in the oxidation of lactose, and that studies on the recovery of LBA from its sodium salt are lacking in the open literature, the main objectives of this work include: (*i*) The synthesis and characterization of Au/MSM catalysts, and the application of these catalytic materials in the oxidation of lactose to selectively produce LBA; and (*ii*) the investigation of the recovery of LBA from its sodium salt obtained at the reactor outlet, by means of bipolar membrane electrodialysis and ion exchange technology.

Chapter 1. Literature Review

1.1. Lactobionic acid: A high value-added lactose derivative for food and pharmaceutical applications

Published in *International Dairy Journal* 2012, 26(2), 103-111 by **Luis-Felipe Gutiérrez, Safia Hamoudi and Khaled Belkacemi**.

1.1.1. Abstract

Lactose has long been used as a precursor for the production of high-value derivatives with emerging applications in the food and pharmaceutical industries. Some significant developments include the manufacture of epilactose, galacto-oligosaccharides, lactitol, lactobionic acid, lactosucrose, lactulose, sialyllactose and tagatose, which are obtained by enzymatic, microbial or chemical modification of lactose. This review focuses on the main characteristics, manufacturing methods, applications and physiological effects of lactobionic acid, a relatively new product derived from lactose oxidation, with high potential applications as a bioactive compound.

1.1.2. Introduction

Carbohydrates have long been used in the manufacture of bulk and fine chemicals, and are viewed as a renewable feedstock for the “green chemistry” of the future. Lactose, the main carbohydrate of milk, is an important cheese and casein manufacturing by-product, whose production and global market have been estimated at about 1.2 million tons per year [4], and to reach US\$1.4 billion by 2015, respectively [5].

Lactose is mainly used as an ingredient in foods, beverages and confectionery products, and it has been extensively employed as diluent in tablets and carrier of medicines in the pharmaceutical industry. Nevertheless, the use of lactose is limited in many applications, because of its low sweetness and solubility, as well as due to the intolerance of some population segments, and only a small amount of lactose is employed as a raw material for producing fine chemicals [11]. However, the worldwide surplus and low cost of lactose have motivated research on innovative processes for producing valuable lactose derivatives, and expanding their applications in the food, pharmaceutical and chemical industries. Significant developments include the production of highly valued pharmaceutical products and functional food ingredients, such as lactitol, lactobionic acid (LBA), lactosucrose, lactulose and galacto-oligosaccharides, some of which have become commercially

successful [20]. Owing to their emerging applications, various reviews on galacto-oligosaccharides, lactulose and lactitol have been recently published [21-26]. However, although the research on LBA has been extensive in recent years due to its high potential applications, this lactose derivative has hardly been reviewed. This work aims to provide a complete review of the main characteristics, manufacturing methods, applications and physiological effects of LBA, an oxidation product of lactose, with excellent properties for food, pharmaceutical and chemical applications.

1.1.3. Lactobionic acid: general characteristics

LBA (4-O- β -D-galactopyranosyl-D-gluconic acid; C₁₂H₂₂O₁₂; MW 358.30 Da; pKa 3.8) is an aldonic acid obtained from the oxidation of lactose, with high potential applications as an ingredient in foods and pharmaceutical products, because of its antioxidant, chelating and humectant properties. The chemical structure of LBA comprises a galactose moiety linked to a gluconic acid molecule via an etherlike linkage. Owing to the high number of hydroxyl groups, LBA is very hygroscopic and forms gels containing about 14% water with atmospheric moisture. LBA and its mineral salts (mainly Na-, Ca and K-lactobionate) are commercially produced in small quantities for industrial and medical applications, as well as for research use. The most important producers are Solvay (Germany) and FrieslandCampina Domo (The Netherlands) [8]. According to Affertsholt-Allen [7], the market for LBA is between 15000 and 17000 tons per year, with an expected annual growth rate of 5%.

1.1.4. Lactobionic acid production

The selective conversion of lactose to LBA consists of the oxidation of the free aldehyde group of glucose on the lactose molecule to the carboxyl group, according to the scheme presented in Figure 1.1 LBA was first synthesized by Fischer and Meyer [27], by oxidizing lactose with bromine. Since then, several processes including chemical, electrochemical, biocatalytic and heterogeneous catalytic oxidations have been investigated for the production of LBA. Taking into account that for industrial applications only the latter three oxidation processes are economically feasible, the chemical oxidation of lactose using halogens will not be discussed in this document.

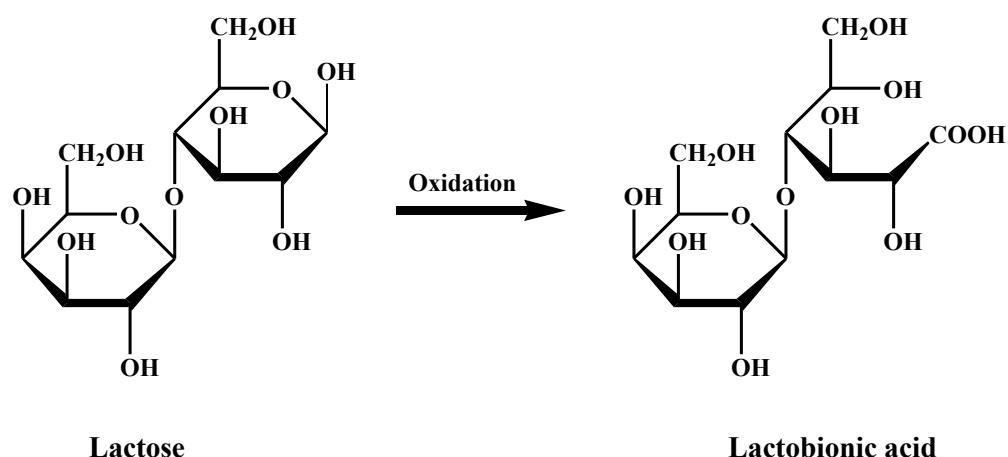


Figure 1.1. Schematic oxidation of lactose to lactobionic acid.

1.1.4.1. Biocatalytic oxidation

The biocatalytic production of LBA comprises the oxidation of lactose by means of specific enzymes or by using microorganisms as biocatalysts. The general reaction mechanism, presented in Figure 1.2, involves the formation of lactobiono- δ -lactone as an intermediate product, which is subsequently hydrolyzed to LBA [28]. The process is generally carried out at mild temperature conditions (25-50°C), and, because the pH must be kept constant during reaction by adequate addition of a Na-, Ca- or K-base, the product can be LBA or its salts. When lactobionate salts are produced, the solution can be passed through cation exchange resins to obtain an LBA solution, which can be further concentrated and crystallized to produce pure LBA. Table 1.1 summarizes the main biocatalysts used in LBA production from lactose.

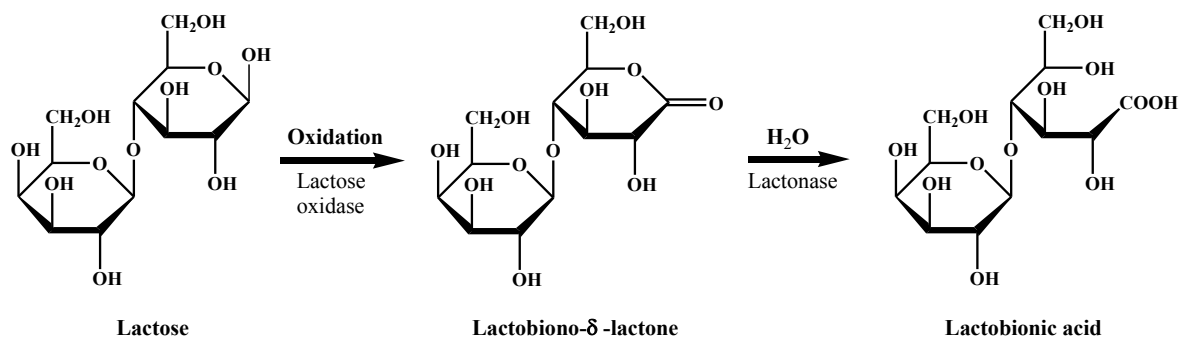


Figure 1.2. Schematic biocatalytic oxidation of lactose to lactobionic acid.

Stodola and Lockwood [29] reported for the first time the ability of various species of *Pseudomonas* for the oxidation of lactose. They obtained a LBA yield of 75%, after a 165 h reaction using

Pseudomonas graveolens 14. Since then, several microorganisms have been investigated for LBA production. As shown in Table 1.1, the lactose-oxidizing activity has also been confirmed in other microorganisms such as *Acetobacter orientalis*, *Burkholderia cepacia*, *Halobacterium saccharovorum*, *Paraconiothyrium* sp., *Penicillium chrysogenum*, *Pseudomonas* sp. LS13-1, *Sporotrichum thermophile* and *Zymomonas mobilis*. Recently, Alonso et al. [30-31] reported a LBA production of 42.4 g L⁻¹ after 32 h of incubation of sterilized sweet whey with *Pseudomonas taetrolens*, indicating that cheese whey can be an inexpensive alternative media for the synthesis of LBA.

Table 1.1. Production of lactobionic acid by biocatalytic oxidation of lactose.

Biocatalyst ^a	Conversion yield (%)	Selectivity LBA (%)	Reaction time (min)	Space-time yield for LBA (g L ⁻¹ h ⁻¹)	Ref.
GFOR/GL enzymes from <i>Zymomonas mobilis</i> ATCC 29191	~85	100	1500-4500	5.6	[32-33]
GFOR from permeabilized cells of <i>Zymomonas mobilis</i> CP4 (ATCC 31821)	~90-95	100	3600	0.8-2.3	[34]
GFOR from <i>Zymomonas mobilis</i> DSM 473	90-95	100	4200	2.6-4.6	[35]
GFOR from <i>Zymomonas mobilis</i> DSM 3580					
CDH (EC 1.1.99.18) from <i>Sclerotium rolfsii</i> (SrCDH, 420UL ⁻¹) + Laccase (EC 1.10.3.2, 2030UL ⁻¹)	95-98	100	720	3.1	[36]
CDH (EC 1.1.99.18) from <i>Sclerotium rolfsii</i> CBS 191.62 + Laccase (EC 1.10.3.2) from <i>Trametes pubescens</i> MB 89	100	~100	360	-	[37]
CDH from <i>Sclerotium (Athelia) rolfsii</i>	~100	100	600	-	[38]
CDH from <i>Sclerotium rolfsii</i> CBS 191.62 + Laccase from <i>Trametes pubescens</i> MB 89	99	100	150	15.9 ^b	[39]
CDH (EC 1.1.99.18) from the basidiomycete <i>S. rolfsii</i> CBS 191.62	100	100	420	3.0	[40]
CDH from <i>Athelia (Sclerotium) rolfsii</i> CBS 191.62 + Laccase from <i>Trametes pubescens</i> MB 89	~100	100	300-1350	3.0-21.0	[41]
CDH from <i>Athelia (Sclerotium) rolfsii</i> CBS 191.62 + Laccase from <i>Trametes pubescens</i> MB 89	100	100	150-250	7.2-27.0	[42]

Table 1.1. Cont.

Biocatalyst ^a	Conversion yield (%)	Selectivity LBA (%)	Reaction time (min)	Space-time yield for LBA (g L ⁻¹ h ⁻¹)	Ref.
CDH from the ascomycete <i>M. thermophilum</i>	100	100	420	3.3	[40]
CDH from <i>Myriococcum thermophilum</i>	~100	100	600	-	[38]
CDH from <i>Microdochium nivale</i> + Catalase (Catazyme® 25 L from Novozymes A/S)	98	-	~600	-	[43]
CDH from <i>Microdochium nivale</i> + Catalase (Catazyme® 25 L from Novozymes A/S)	100	100	300-380	7.9-11.5	[44]
CDH from <i>Termitomyces clypeatus</i>	~100	100	300	0.01	[45]
CDH from <i>Sporotrichum-thermophile</i>	-	-	-	-	[46]
CDH from white mould + Laccase from <i>Trametes versicolor</i>	-	-	-	1.8	[47]
Carbohydrate oxidase from <i>Microdochium nivale</i> + Catalase (Catazyme® 25 L from Novozymes A/S)	>98	100	720	~4.0	[48]
Carbohydrate acceptor oxidoreductase from <i>Paraconiothyrium</i> sp.	100	100	420-900	14.3	[49]
Cellooligosaccharide oxidase from <i>Sarocladium oryzae</i> F137 + Catalase	90	100	720	2.1	[50]
PDH from various <i>Agaricus</i> species	-	83-95	960-2880	-	[51]
Hexose oxidase from <i>Chondrus crispus</i>	-	-	-	-	[52]
Glucooligosaccharide oxidase from <i>Acremonium strictum</i> T1-38 + Catalase	98	100	240	6.7	[53]
Lactose-oxidizing enzyme from <i>Paraconiothyrium</i> sp. KD-3 + Catalase	75-100	100	600-3000	7.4-11.5	[54]
Lactose dehydrogenase from <i>Pseudomonas graveolens</i> ATCC-4683 + Lactonase	100	100	-	-	[55]
<i>Pseudomonas graveolens</i> ATCC-4683	-	-	-	-	[56]
<i>Pseudomonas graveolans</i> 14	100	96	9900	~0.5	[29]
<i>Pseudomonas taetrolens</i> LMG 2336	66-100	100	2880-4800	0.59-1.12 ^c	[30]
<i>Pseudomonas taetrolens</i> LMG 2336	6-100	100	3600	0.04-1.3 ^c	[31]
<i>Pseudomonas</i> sp. LS13-1	>90	100	10800	0.46-1.0 ^c	[57]

Table 1.1. Cont.

Biocatalyst ^a	Conversion yield (%)	Selectivity LBA (%)	Reaction time (min)	Space-time yield for LBA (g L⁻¹ h⁻¹)	Ref.
<i>Pseudomonas</i> sp. LS13-1	>90	100	7200	1.5-1.9	[57]
<i>Pseudomonas calco-acetica</i>	85-90	-	11520	~0.5	[58]
<i>Pseudomonas quercito-pyrogallica</i>	~90	-	~46000	~0.5	
<i>Burkholderia cepacia</i> No.24	~100	100	900-1620	5.6-10.0	[59-60]
<i>Burkholderia cepacia</i> No. 216	100	100	3000	0.2	[61]
<i>Acetobacter orientalis</i> KYG22	36	-	4320	0.1	[62]
<i>Acetobacter orientalis</i> KYG22	~100	-	4320	~0.4	[63]
<i>Paraconiothyrium</i> sp.	-	-	-	-	[64]
<i>Halobacterium saccharovorom</i>	97	100	2880	-	[65]
Paracolon bacteria B1x urease-positive and C6 urease-negative	100	100	2880	~0.4	[66]
<i>Penicillium chrysogenum</i>	~6	-	7200	0.04-0.07	[67]

^a CDH, cellobiose dehydrogenase; GFOR, glucose/fructose oxidoreductase; GFOR/GL, glucose/fructose oxidoreductase and glucono- δ -lactonase; PDH, pyranose dehydrogenase. ^b The substrate solution contained lactose, monosaccharides and galacto-oligosaccharides. ^c Sterilized sweet whey as substrate.

Similarly, numerous lactose-oxidizing enzymes (glucose–fructose dehydrogenases or cellobiose dehydrogenase) from microorganisms and plants have been used for the production of LBA. The first study, carried out by Lin et al. [53], revealed a lactose conversion of 98% after 4 h of incubation with a glucooligosaccharide oxidase from *Acremonium strictum*. Some years later, Baminger et al. [42] reported 100% lactose conversion after only 150 min of incubation with a cellobiose dehydrogenase from *Athelia (Sclerotium) rolfsii* CBS 191.62. Recently, Budtz et al. [44] demonstrated that the enzyme inactivation caused by the hydrogen peroxide generated when a carbohydrate oxidase converts lactose to LBA, can be avoided by simultaneous addition of catalase to the substrate, in order to convert the H₂O₂ produced to O₂, and reduce significantly (up to 50%) the oxygen supply required for the system. Using this approach, Van Hecke et al. [36] obtained a LBA production of 74.4 g L⁻¹ d⁻¹ with a degree of conversion higher than 97%, using a combination of cellobiose dehydrogenase (EC 1.1.99.18) from *Sclerotiumrolfsii* (SrCDH, 420 UL⁻¹) and laccase (EC 1.10.3.2, 2030 UL⁻¹). Other hexose oxidases derived from *Microdochium nivale*, *Chondrus crispus*,

Zymomonas mobilis and *Sarocladium oryzae*, among others, have been investigated for producing LBA from lactose, and high conversions (close to 100%) have been reported.

From the data presented in Table 1.1, one can conclude that biocatalytic oxidation of lactose is an interesting “green” method to produce LBA, because of the high selectivity of biocatalysts. However, the main drawbacks of this approach lie in the long time required for reaching high conversions, the cofactor dependency of some enzymes, the formation of H₂O₂ as a second product, which inactivates enzymes, and the enzyme inactivation by the dispersive methods used for oxygen delivery. Moreover, some of the redox mediators investigated for the biocatalytic production of LBA are not appropriate for the food industry.

1.1.4.2. Electrochemical oxidation

LBA has been also prepared by electrolytic oxidation processes. Isbell [68] produced calcium lactobionate by electrochemical oxidation of lactose in the presence of bromine and calcium carbonate, using graphite electrodes. This process was improved by Magariello and Islip [69], who patented a method for the production of large quantities of LBA (yield ~98%) by means of electrolytic oxidation of lactose, using graphite electrodes, iodine or bromine as catalysts, and an alkaline solution to maintain the pH above 5.2. Since then, investigation on electrochemical production of LBA has been scarce, and only a few works have been published [70-73]. The studies carried out by Druliolle’s group [74-76] demonstrated that high yields (>90%) and selectivities (~100%) toward LBA can be obtained by means of the electro-catalytic oxidation of lactose on noble metal electrodes (platinum, platinum-modified and gold electrodes) in alkaline media. These authors also proposed that gold electrodes could be the best catalyst for the oxidation of sugars, and that lactone is the primary product of the electrochemical oxidation of lactose, which is hydrolyzed in a subsequent step to produce LBA, following a similar mechanism to that of glucose.

1.1.4.3. Heterogeneous catalytic oxidation

Heterogeneous catalytic oxidation of lactose is a very promising field, because such a process can easily be integrated into other lactose transformation technologies. During this reaction, the desired LBA is normally obtained as the main product, as shown in Figure 1.3. However, lactulose and 2-keto LBA are undesirable co-products that can be produced depending on the catalyst activity and selectivity, and on the reaction operation conditions. In order to selectively produce LBA, the reaction

should be carried out at atmospheric pressure in alkaline media (pH between 8.0 and 9.0), at a temperature in the range of 50-70°C, using air or oxygen as eco-friendly oxidizing agents. Higher pH values have an important influence on selectivity, since isomerization of lactose to lactulose is favored. On the other hand, low pH values promote the catalyst deactivation by the strong adsorption of the reaction products, which occupy the active sites of the catalyst surface [11]. Table 1.2 presents the main catalysts used in LBA production from lactose.

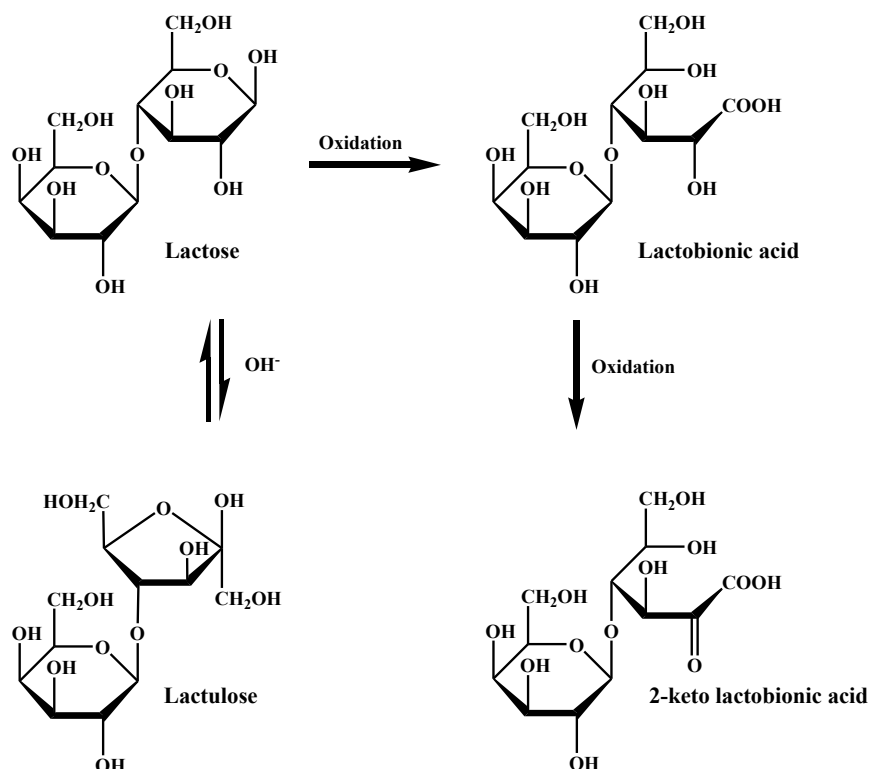


Figure 1.3. Schematic catalytic oxidation of lactose to lactobionic acid under alkaline conditions.

Table 1.2. Production of lactobionic acid by heterogeneous catalytic oxidation of lactose.

Catalyst	Conversion yield (%)	Selectivity LBA (%)	Reaction time (min)	Space-time yield for LBA (g L ⁻¹ h ⁻¹)	Ref.
Pd/C	29-97	46-95.8	67-200	1.4-136.1	[13, 77-80]
Pd/SiO ₂	16.3-27	30-80	120-200	2.0-7.3	[81-83]
Pd/Al ₂ O ₃	54-99	63-97	200	5.8-5.9	[16, 79, 83]
Pd/Beta zeolites	34.3-47.9	76-80	200	4.1-4.8	[83]
Pd/MCM-22 zeolites	8.4-82.7	80-97	200	0.9-12.5	[83]

Table 1.2. Cont.

Catalyst	Conversion yield (%)	Selectivity LBA (%)	Reaction time (min)	Space-time yield for LBA (g L⁻¹ h⁻¹)	Ref.
Pd-Bi/C	95-100	95-100	67-300	6.1-145.1	[77, 84]
Pd-V/C	30	57	200	~1.6	[78]
Pd-Pt-Bi/C	93	83	200	~7.1	[78]
Pd-Bi/SiO ₂	40-100	23-100	120-180	0.5-89.6	[81, 85-87]
Pd-Ti/SiO ₂	25-30	10-82	120	2.2-22.0	[82]
Pd-Pb/CaCO ₃	92	83	200	-	[78]
Pt/C	87-94	54-75	200	5.4-11.8	[88]
Pt/Sibunit	35-66	-	200	-	[13]
Pt/Al ₂ O ₃	67-100	0-44	150-300	1.6-3.6	[84, 88]
Pt/CeMn	100	0	150-300	-	[84]
Pt-Bi/C	80	72.5	300	~15.5	[89]
Pt-Cu/C	93	74	200	~8.5	[88]
Pt-V/C	55-82	70	200	~4.7-7.1	[88]
Pt-Fe/C	50	68	200	~4.2	[88]
Ru/C	33-34	14-38	200	~0.6-1.6	[88]
Ru/Al ₂ O ₃	29	6	200	~0.2	[88]
Au/Al ₂ O ₃	82.6-100	80-100	200	1.7-11.5	[13-16]
Au/TiO ₂	34.5-100	90.4-100	200	2.0-8.8	[14-15]
Au/SiO ₂	100	95.2-100	120-200	3.2-5.9	[11, 15, 90]
Au/Fe ₂ O ₃	-	-	-	-	[15]
Au/Fe ₃ O ₄	46.5	90.3	200	4.3	[15]
Au/ZrO ₂	40.5	91.2	200	2.9	[15]
Au/ZnO	83.3	93.9	200	7.3	[15]
Au/CeO ₂	100	99.1	200	~15.3	[13]
Au/SiO ₂ -CeO ₂	80-100	100	100	3.2-7.2	[90]

LBA production by means of heterogeneous catalytic oxidation of lactose on palladium and bismuth-palladium supported catalysts was first successfully performed by Hendriks et al. [10]. Since then, the oxidation of lactose over platinum, palladium and bismuth-promoted palladium supported catalysts has been largely investigated, as summarized in Table 1.2. Taking into account that the main problem of the latter catalysts is their poisoning and deactivation by over-oxidation during the reaction, the control of the oxygen concentration in the reaction media is of extreme importance, in order to avoid deactivation of the catalysts [85, 91]. Periodic bubbling of air and nitrogen has been successfully used to strip off the dissolved oxygen, and maintain the overall reaction kinetics [86]. However, since bismuth is prone to leaching, applications of catalysts containing bismuth are not appropriate for production of chemicals for the food and pharmaceutical industries [9]. On the contrary, gold catalysts have shown high stability against overoxidation, and supported gold nanoparticles have demonstrated exceptional activity and selectivity in the oxidation of carbohydrates, outperforming other metal catalysts such as palladium and platinum, with no need for promoters. However, the oxidation of lactose over gold catalysts has been scarcely investigated. Studies indicate that supporting gold nanoparticles on Al_2O_3 , TiO_2 , and CeO_2 allowed to achieve moderate to high conversions (>80%) and selectivities (up to 95%), using Au loadings in the range of 0.4-2.0% [13-16]. Recently, we have synthesized gold catalysts supported on mesoporous silica materials (meso- SiO_2 and SBA-15- CeO_2), with which 100% lactose conversion and 100% selectivity toward LBA were obtained after only 100 min of reaction [11, 90]. Due to the rapid and simple method of synthesis, as well as because of its excellent catalytic performance, these catalysts could be regarded as a major breakthrough on the way to an industrial process of catalytic oxidation of lactose.

1.1.5. Commercial and proposed applications of lactobionic acid

The main commercial and proposed applications of LBA, summarized in Table 1.3, derive from its antioxidant, chelating and emulsifying properties. The most important commercial use of LBA is as a major ingredient of the cold-storage solutions employed for stabilizing organs prior to transplantation, such as the University of Wisconsin (UW) solution. The metal-chelating properties of LBA have been reported to reduce the oxidative damage to tissues during storage and preservation of organs caused by some metal ions, such as iron [92]. Moreover, LBA has been shown to suppress the hypothermally induced cell swelling in various tissues, and it does not permeate cell membranes at

low temperature, due to its size and three dimensional structure [93-94]. LBA is commercially used to enhance the solubility of antibiotics such as erythromycin and clarithromycin [28].

LBA is an excellent carrier for calcium supplementation [95]. Recently, it has been employed in the design of some carrier-nanomaterials of drugs and functional nanoparticles. The carboxylic group of the gluconic acid moiety of LBA can be used to react with other active groups, such as amino groups, whereas the galactose molecule acts as specific targeting ligand of drugs and genes to specific cells, such as human liver cancer cells [96-98]. LBA has been also employed to synthesize receptor targeted radiopharmaceutical agents for hepatocyte imaging [99], and receptor-mediated gene transfer material to target DNA to specific cellular receptors and/or tissues [100]. Moreover, LBA has been used in the preparation of virus-like particles, a kind of biological nanoparticle with excellent biocompatibility and biodegradability, for specific targeting for hepatocytes or hepatoma cells bearing asialoglycoprotein receptors [101]. Recently, LBA has been employed for designing new magnetic resonance imaging contrast agents [102], for preparing a glycoconjugated chitosan functional polymer to modify the surface of iron nanoparticles and enhance their colloidal stability [103], and as a weak capping ligand in the synthesis of semiconductor nanocrystalline networks [104].

In the cosmetic industry, LBA has been also extensively employed. LBA is currently contained in some skin care products available on the market, because it represents a new ingredient featuring potent antioxidant, wound healing, humectant anti-aging and keratinizing properties [105-106].

LBA has been approved as a food additive by the US FDA, and it has promising applications in the food industry as an acidulant with a sweet taste, a filler in cheese production, a firming agent, and to fortify functional drinks with essential minerals such as Fe and Cu [30, 107]. Nielsen [108] proposed LBA as an ingredient to produce a meat-based food product with a reduced water loss upon freezing and subsequent thawing, and/or upon cooking. Furthermore, the biodegradable, biocompatible and chelating properties of LBA make this product useful in biomaterials, biodegradable detergents, anti-corrosive coatings and sugar-based bio-surfactants, as proposed by Gerling [95] and Oskarsson et al. [109].

Table 1.3. Main commercial and proposed applications of lactobionic acid and/or its salts.

Industry	Applications	Ref.
Pharmaceutical	<ul style="list-style-type: none"> • Enhance the solubility of macrolide antibiotics such as erythromycin and clarithromycin • Anti-aging and keratinizing ingredient of skin care cosmetics • Calcium supplementation • Metal-chelating agent in organ preservation solutions • Ingredient in chlorohexidine-based disinfectant • Bio-surfactant in its fatty acid derivatives forms • Inducer for cellulase production by <i>Trichoderma reesei</i> • Functional molecule in the synthesis of polymeric nanoparticles for liver-specific drug deliver 	[8, 36, 105, 110-113]
Food	<ul style="list-style-type: none"> • Acidulant with a sweet taste • Filler in cheese production • Firming agent • Calcium carrier in functional drinks • Reduction of souring and ripening time for the production of cheese and yogurt • Enhancement of flavors • Improvement of bitter or sour taste of foods • Preservation of aroma freshness • Preparation of dairy products with reduced lactose content 	[8, 28, 43, 95, 114]
Chemical	<ul style="list-style-type: none"> • Ion sequestrant in detergent solutions • Biodegradable cobuilder in washing powder • Anti-corrosive coatings • Chiral selector for enantiomeric separation of basic drugs in capillary electrophoresis (clarithromycin lactobionate) • Reactant for synthetic amides 	[95, 115]
Nanotechnology	<ul style="list-style-type: none"> • Part of biocompatible scaffolds for tissue engineering • Part of nanoplatfoms for new bioimaging applications • Ingredient of galactose-conjugated fluorescent nanoparticles for immunofluorescence assays 	[116-118]

1.1.6. Physiological effects of lactobionic acid

Although LBA is not normally found in nature, according to Kiryu et al. [62], the occurrence of LBA in foods and beverages indicates that people have unknowingly consumed LBA for a long time. These authors estimated the annual LBA intake to be 760 mg, after they found more than 10 mg of LBA per 100 g in a Caucasian traditional yogurt.

The most important physiological effect of LBA is the anticoagulant and antithrombotic activity of its sulfated derivative *bis*-lactobionic acid amides, which have been studied as potential anticoagulant

and antithrombotic agents, without a risk of bleeding [119-120]. This compound, also known as Aprosulat sodium, stimulated HCII activity in vitro [121] and has been found to delay the activation of factor X and prothrombin in plasma and to inhibit factor IXa/VIIIa complex (Xase) [122-123].

LBA is a strong humectant, showing anti-aging effects, including skin plumping and smoothing of surface topography with diminished appearance of fine lines and wrinkles. LBA containing samples (6% w/w) produced better skin performance than glycolic acid, providing skin exfoliation and improving skin moisture level without irritation, when it was used on healthy volunteers periodically over two weeks [124]. LBA could increase the synthesis of glycosaminoglycans in the skin, and it has been shown to enhance cell turnover in vitro [125]. Significant improvements in the signs of photo ageing were observed by Green et al. [126] after women aged between 35 and 60 years used an 8% LBA cream for 6 and 12 weeks. The maintenance of a low pH by topical applications of LBA (60 μ L of 10% LBA) inhibited the development of induced atopic dermatitis in mice [127]. Moreover, LBA has been reported to suppress tissue damage caused by oxygen radicals and is used to assist wound healing [128].

LBA has also revealed antioxidant properties in tissues, by inhibiting the production of hydroxyl radicals as a result of its iron chelating properties [92]. Furthermore, it has prevented oxidation of other substances such as anthralin, hydroquinone and banana peel [129]. LBA also promotes wound healing, and it is useful for general care of skin, hair, nail, oral and vaginal mucosa, and oral and gum diseases [106].

One of the latest emerging applications of LBA derives from its galactose group, which can act as a specific targeting ligand. In consequence, LBA has been recently used in the fabrication of lactobionic-modified materials for carrying drugs for the treatment of liver and breast cancer [130-133].

1.1.7. Conclusions

One of the most exciting contributions to dairy by-products has been the development of transformation processes for producing high-value lactose derivatives. The design of new processes for the profitable utilization of lactose has been a big challenge, owing to its worldwide surplus and low cost. LBA, an oxidation product of lactose, is a relatively new lactose derivative with potential applications in the food, pharmaceutical and chemical industries, owing to its antioxidant, chelating,

humectant and emulsifying properties. Moreover, due to the remarkable growth of nanotechnology, the applications of LBA can be expanded as a functional molecule for carrying drugs. Although LBA can be obtained by chemical, electrochemical, biocatalytic and heterogeneous catalytic oxidations, the production of LBA by means of lactose oxidation on gold supported catalysts, using air or oxygen as eco-friendly oxidants, offers an attractive alternative for industrial applications, because of their high activity and selectivity. Moreover, the reaction time of catalytic processes using gold is lower in comparison to the biocatalytic reactions using microorganisms or enzymes, and the reaction control is easier.

1.2. Mesoporous silica materials: General characteristics and synthesis methods

Taking into account that in this study lactose was oxidized using gold catalysts supported on mesoporous silica materials (MSM), a brief description of the general characteristics and synthesis principles of this kind of materials is presented below, making special emphasis on the mesoporous SBA-15, since it was the support of the most of the catalysts used in this project.

1.2.1. General characteristics

According to the IUPAC definition, mesoporous materials with ordered or disordered mesostructure are materials containing pores with diameters ranging between 2 and 50 nm [134].

Mesoporous silica materials with hexagonal and cubic mesostructure order were discovered by scientists of the Mobil Oil Corporation in the early of 1990's, who published a new class of mesostructured silicas known as M41S family [135-136]. The most well-known representatives of this materials family includes the MCM-41 (with a hexagonal arrangement of the mesopores, space group $p6mm$), the MCM-48 (with a cubic arrangement of the mesopores, space group $la3d$), and the MCM-50 (with a laminar structure, space group $p2$) [137].

After this breakthrough in the materials engineering science, MSM have attracted great scientific and industrial interest. As a consequence of the incredible expanded research on this topic, numerous new silica mesophases have been invented. Some of them are FDU-1, FDU-12, FSM-16, HMM-2, HMM-33, HMS, HUM-1, KIT-1, KIT-5, MSU-J, MSU- n , MSU-V, PCH, TUD-1 and the SBA family materials, which includes SBA-1, SBA-2, SBA-3, SBA-6, SBA-8, SBA-11, SBA-12, SBA-14, SBA-15, SBA-16. These mesoporous materials may present different structural characteristics (hexagonal, cubic, laminar or wormhole mesostructure), and their pore size may vary since few nanometers until up to 30 nm, as presented in Table 1.4. Although the investigation on mesoporous materials is a very dynamic field, the most well known and studied mesoporous silica materials are MCM-41, MCM-48 and SBA-15 [138]. They are usually used as models to compare with other materials or to study fundamental aspects of the MSM applications.

Owing to their physicochemical and mechanical properties (unique mesoporous structure, well defined radius distribution, large specific volume, high surface area, well defined connectivity, thermal stability, low mass density, easy functionalization, tunable pore size, and good biocompatibility), MSM

have found numerous applications many fields, such as catalysis, adsorption, chromatography, drug delivery, encapsulation, gas storage, biotechnological and biomedical systems, as well as in optical, electrical and electronic devices.

Table 1.4. Textural properties of some mesoporous silica materials

Material	BET surface area (m²·g⁻¹)	Pore size (nm)	Wall thickness (nm)	Total pore volume (cm³·g⁻¹)	Ref.
FDU-12	281-712	10.0-12.3	-	0.66-0.86	[139]
HMS	740-1200	1.6-3.1	1.7-3.0	0.73-1.75	[140]
HUM-1	472	4.2	-	1.25	[141]
MCM-41	> 1000	1.5-10	0.97-1.10	0.7-1.2	[136]
MCM-48	986-1056	2.4-2.9	1.5	0.86-0.98	[142]
MSU-J	408-1127	4.9-14.3	0.4-1.7	1.37-2.29	[143]
SBA-11	910-1070	2.5-3-5	-	0.68-1.02	[144]
SBA-12	910-1150	3.1-4-0	-	0.83-0.92	[144]
SBA-14	610-670	2.2-2.4	-	0.38-0.39	[144]
SBA-15	630-1040	4.6-30	3.1-6.4	0.56-1.26	[145]
SBA-16	740	5.4	-	0.45	[144]

Particularly, in catalytic applications MSM are not often used as catalysts as such. However, MSM are very suitable catalysts supports, because they provide high dispersion of metal nanoparticles and facilitate the access of the substrates to the active sites. Moreover, the relatively large pores facilitate the mass transfer, while the very high surface area allows high concentrations of active sites per mass of material [146]. The catalytic functions can be introduced into MSM by direct incorporation of active sites in the silica walls, by deposition of active species on their inner surface, or after a surface modification with organic functional groups, which will facilitate the incorporation of active sites [147]. Many reviews covering different aspects of the catalysts supported on MSM, such as their synthesis and catalytic applications have been published [137, 147-157].

1.2.2. Synthesis methods

Mesoporous silica materials can be synthesized under conditions where a silica-surfactant self-assembly occurs simultaneously with condensation of the inorganic species, which yields

mesoscopically ordered composites, after the surfactant removal by extraction or calcination [145]. In general, one can say that the synthesis of MSM includes the following steps:

- (i) The dissolution of the surfactant in the appropriate solvent, paying special attention to the temperature and pH;
- (ii) The addition of the silica source (tetraethyl orthosilicate (TEOS), tetramethylorthosilicate (TMOS), fumed silica, sodium silicate, etc.);
- (iii) The hydrolysis and pre-condensation by means of one stirring period at a certain temperature;
- (iv) The ageing at high temperature in order to direct the condensation process;
- (v) The recovery, washing and drying of the solids; and
- (vi) The surfactant removal by calcination procedures or extraction methods.

The operating conditions (pH and temperature) depend on the type of material, but normally they include a wide range of pHs from strongly acidic to highly basic conditions, and from subambient temperatures to $\sim 150^{\circ}\text{C}$. Cationic, anionic, neutral, zwitterionic, bolaamphiphile, gemini and divalent surfactants can be used as structure-directing agents, as well as a variety of commercially available polymers (*i.e.* Brij 52, Triton X-100, Tween 60, Tergitol TMN 6, Pluronic P123, Pluronic F127, etc.) [156].

Nowadays, it is well accepted that two different mechanisms are involved in the formation of MSM, as illustrated in Figure 1.4 [137]: (i) The true liquid-crystal template mechanism, in which the concentration of the surfactant is so high that under the synthesis conditions (temperature, pH) a lyotropic liquid-crystalline phase is formed without requiring the presence of the silica precursors. (ii) The liquid-crystalline phase (hexagonal, cubic, or laminar arrangement) is formed even at lower concentrations of surfactant molecules, when there is cooperative self-assembly of the structure-directing agent and the added silica species.

One important advantage of MSM is that the pore size of their mesopores can be easily tuned in the range of 2–30 nm by controlling the synthesis conditions (*i.e.* choosing a proper surfactant, adding controllable amounts of additives, such as co-solvents, inorganic salts or swelling agents, modifying

the temperature and time of ageing, etc.) [158]. A complete review covering verified synthesis methods for a large number of selected relevant MSM, including the synthesis recipes for the most well-known MSM has been compiled by Meynen et al. [159].

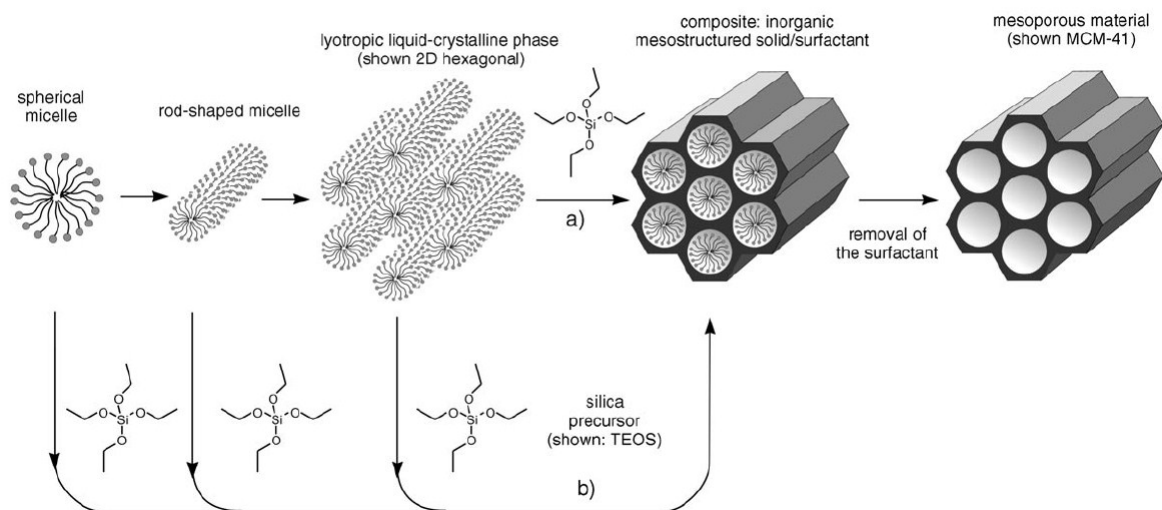


Figure 1.4. General scheme of the formation of MSM by structure-directing agents: a) true liquid-crystal template mechanism, b) cooperative liquid crystal template mechanism. [137].

On the other hand, the need of incorporating functionalities for different applications, including catalysis, can be easily achieved by means of the following procedures [137]: (i) the subsequent modification of the silica surface with organic functional groups (grafting); (ii) the simultaneous reaction of condensable inorganic silica species with silylated organic compounds (co-condensation); and (iii) the use of bis-silylated organic precursors to produce periodic mesoporous organosilicas.

1.2.3. Mesoporous silica SBA-15

1.2.3.1. General characteristics

SBA materials (the acronym for Santa Barbara acids) were synthesized in 1998 by using non-ionic triblock copolymers ($\text{EO}_n\text{PO}_m\text{EO}_n$) with large polyethyleneoxide (EO)_n and polypropyleneoxide (PO)_m blocks. This kind of surfactants interact through an indirect reaction with the positively charged silica source in acid medium by a hydrogen bonding ($\text{S}^0\text{H}^+(\text{X}^-)\text{I}^+$) pathway, where S^0 is the nonionic surfactant, X^- is the halide anion, and I^+ is a protonated $\text{Si}-\text{OH}$ moiety [144-145]. Moreover, they display excellent interfacial stabilization properties, and are commercially available, nontoxic, biodegradable and low-cost [144].

The SBA family includes a wide variety of materials with different mesostructures, such as cubic (SBA-1, SBA-11), 3D hexagonal network (SBA-12), lamellar (SBA-14), 2D hexagonal (SBA-3, SBA-15), and cubic cage-structured (SBA-16) [144]. However, because of its attractive characteristics, the mesoporous SBA-15 has been the most intensely studied SBA material [159].

SBA-15 can be defined as a combined micro- and mesoporous material with uniform hexagonal mesopores ranging from 5 to 30 nm, and micropores varying between 0.5 and 3.0 nm in size, depending on the synthesis conditions [144, 160]. The micropores in the walls of the SBA-15 derive from the polyethyleneoxide blocks in the triblock copolymers that are directed to the aqueous solution, whereas the polypropyleneoxide are more hydrophobic and give rise to the internal structure of the mesopore [159].

The thick walls of the SBA-15 (3.1–6.4 nm), gives to this material higher hydrothermal stability, compared to other MSM such as MCM-41, MCM-48 and HMS [161-162].

As far as the structure is concerned, mesoporous silica SBA-15 shows three well-defined peaks at low XRD angles, which can be indexed as (100), (110), and (200) Bragg reflections, and are associated with 2D hexagonally structured pores ($p6mm$ space group), as depicted in the typical XRD pattern presented in Figure 1.5. No diffraction peaks are observed at high XRD angles due to the amorphous nature of the pore walls [159]. TEM images of the SBA-15 (Figure 1.6) have confirmed that this material has a two-dimensional $p6mm$ hexagonal structure, with well ordered hexagonal array and one-dimensional channel structure [145]. Moreover, they have revealed the curved nature of its pores, which has been claimed to be important for adsorption capacity, and for the diffusion of molecules through its structure [163-164].

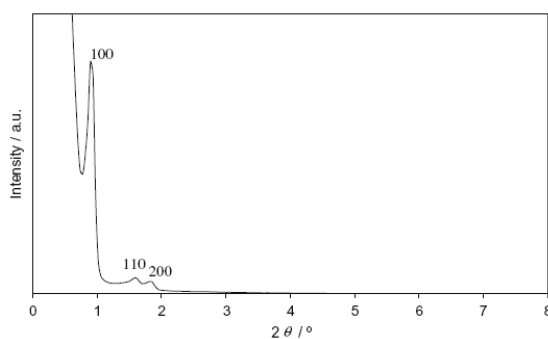


Figure 1.5. Typical XRD pattern for SBA-15 materials. The corresponding d-spacings: (100) = 9.80 nm; (110) = 5.45 nm and (200) = 4.74 nm. [159].

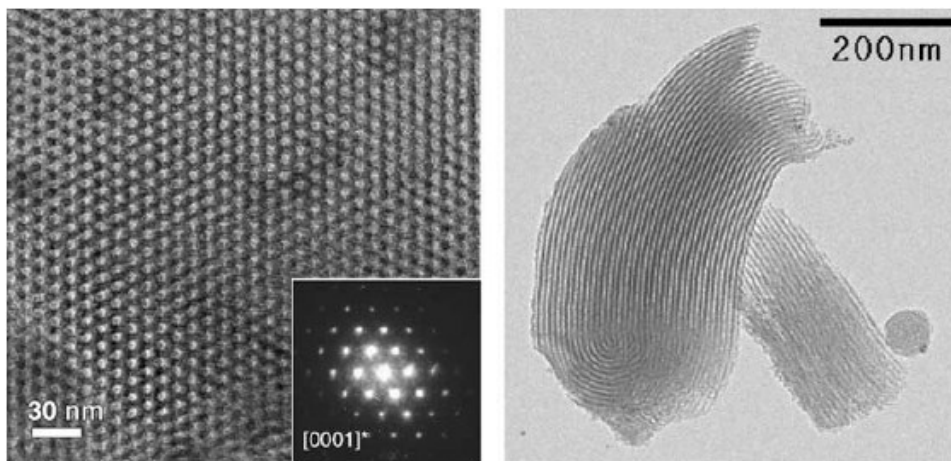


Figure 1.6. TEM images and diffraction pattern showing the hexagonal ordering of SBA-15 and the curved pores. [159, 163]

The typical adsorption isotherm of SBA-15 (Figure 1.7) corresponds to type IV according to the IUPAC classification [165], and displays a clear type-H1 hysteresis loop characteristic of large mesoporous solids. It shows three well distinguished regions: (i) monolayer multilayer adsorption, (ii) capillary condensation at high relative pressure ($P/P_0 \sim 0.75$), and (iii) multilayer adsorption on the outer particle surfaces.

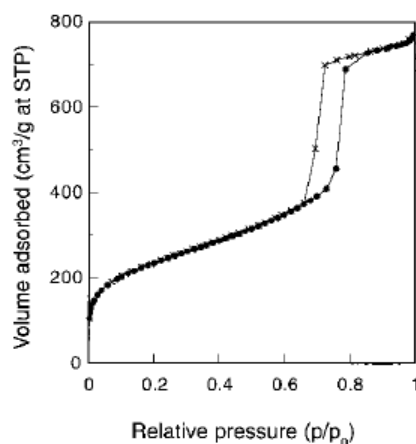


Figure 1.7. Typical nitrogen adsorption (●) – desorption (×) isotherm of calcined (500°C, 6h) mesoporous silica SBA-15 synthesized with the amphiphilic triblock copolymer Pluronic P123. (STP: standard temperature and pressure) [145].

1.2.3.2. Synthesis methods

The synthesis of SBA-15 follows the same steps described above for MSM (see 1.2.2.). However, high quality SBA-15 can be obtained only in acid media ($\text{pH} < 1$) [145]. If the acid concentration is in the range of $\text{pH} 2\text{-}6$ (above the isoelectric point of silica, $\text{pH} \sim 2$), no precipitation or formation of

silica gel occurs. In a neutral conditions (pH ~ 7), only disordered or amorphous silica are obtained [144-145].

Although SBA-15 can be synthesized over a range of reaction mixture compositions and conditions, the most usual synthesis method uses a poly(alkylene oxide) triblock copolymer (poly(ethylene oxide)-poly(propylene oxide)-poly(ethylene oxide), (EO₂₀PO₇₀EO₂₀)), known as Pluronic P123, and TEOS as silica source, according to the following chemical composition of the reaction mixture [145]: 4 g copolymer: 0.041 mol TEOS: 0.24 mol HCl: 6.67 mol H₂O. In a typical preparation of mesoporous silica SBA-15, 4.0 g of Pluronic P123 are dissolved in 30 g of water and 120 g of 2 M HCl solution with stirring at 35°C. Then 8.5 g of TEOS are added into that solution with stirring at 35°C for 20 h. Subsequently, the mixture is transferred in an autoclave and aged at 100°C for 24 h under static conditions. The solid product is recovered by filtration, washed thoroughly with deionized water, and dried at room temperature. To remove the surfactant, the as-synthesized material is calcined at 500°C for 6 hours. Alternatively, the surfactant may be removed by solvent extraction with ethanol at 78°C, which allows the organic copolymer to be completely removed without decomposition, permitting its recovery and reuse [144-145]. According to these authors, the recycled copolymer can be used to synthesize highly ordered hexagonal SBA-15 with identical characteristics and properties to the initial SBA-15.

As mentioned above for MSM, the pore size of the SBA-15 mesopores can be easily tuned the by the modification of the synthesis conditions. For example, an increase in the gel aging temperature or in the reaction time leads to a larger pore diameter and pore volume, and to a thinner silica walls, possibly due to the protonation or temperature-dependent hydrophilicity of the EO block of the copolymer under the acidic synthesis conditions, or a combination of both [145]. Moreover, the pore size of SBA-15 can be expanded up to 30 nm by changing the copolymer composition or block sizes, or by the addition of organic swelling agents, such as 1,3,5-trimethylbenzene (TMB), without changes in the wall thickness, as presented in Figure 1.8 [144].

1.2.3.3. Synthesis mechanism

The synthesis mechanism of the mesoporous silica SBA-15 has been studied by Zhao et al. [144]. According to these authors, the assembly of the mesoporous silicas organized by nonionic poly(alkylene oxide) triblock copolymer species in acid media occurs through an (S⁰H⁺)(X⁻) pathway.

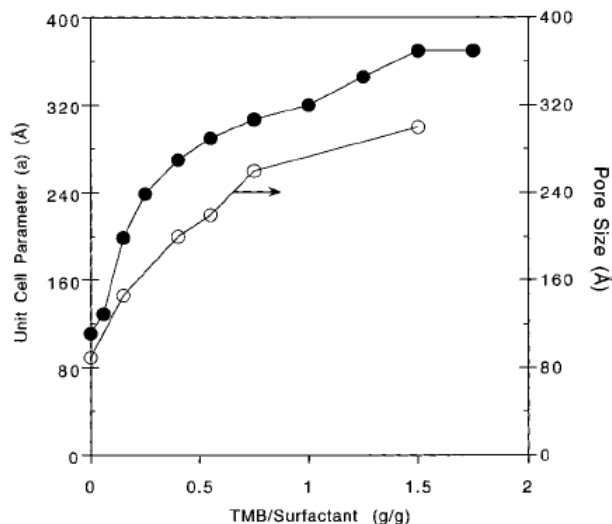


Figure 1.8. Variation of the unit cell parameter a (●) and pore size (○) for calcined SBA-15 as a function of the TMB: surfactant ratio (g/g) [144].

In strong acid media the EO moieties of the surfactant are associated with hydronium ions (reaction 1), while the alkoxy silane species are hydrolyzed and positively charged (reaction 2), which is followed by partial oligomerization at the silica:



where R is the poly(propylene oxide).

These charge-associated EO units and the cationic silica species formed by the reactions represented in equations (1) and (2) are subsequently assembled together by a combination of electrostatic, hydrogen bonding, and Van der Waals interactions, through an $(\text{S}^0\text{H}^+)(\text{X}^-\text{I}^+)$ pathway, as follows:



In this mechanism it has been proposed that the acid anion (Cl^-) might mediate the coordination sphere expansion around the silicon atom, in the form $\text{X}^- \bullet \text{Si} - \text{OH}_2^+$.

1.3. Synthesis of gold catalysts supported on mesoporous silica materials: Recent developments

Published in *Catalysts* 2011, 1(1), 97-154 by Luis-Felipe Gutiérrez, Safia Hamoudi and Khaled Belkacemi.

1.3.1. Abstract

Mesoporous silica materials (MSM) with ordered and controllable porous structure, high surface area, pore volume and thermal stability are very suitable catalyst supports, because they provide high dispersion of metal nanoparticles and facilitate the access of the substrates to the active sites. Since the conventional wet-impregnation and deposition-precipitation methods are not appropriate for the incorporation of gold nanoparticles (AuNPs) into MSM, considerable efforts have been made to develop suitable methods to synthesize Au/MSM catalysts, because the incorporation of AuNPs into the channel system can prevent their agglomeration and leaching. In this review, we summarize the main methods to synthesize active gold catalysts supported on MSM. Examples and details of the preparative methods, as well as selected applications are provided. We expect this article to be interesting to researchers due to the wide variety of chemical reactions that can be catalyzed by gold supported catalysts.

1.3.2. Introduction

After the pioneering works of Hutchings [166] and Haruta *et al.* [167], the high activity of gold catalysts has demonstrated that gold can be the catalyst of choice for an important number of chemical reactions such as selective oxidations and hydrogenations of organic substrates [11, 167-170] water-gas shift reaction [171-173], acetylene hydro-chlorination [174-175], direct synthesis of hydrogen peroxide [176], reduction of NO to N₂ [177-178] and the addition of nucleophiles to acetylenes [179], among others [180-181]. Although gold has been sometimes alloyed with other metals such as Pd, Cu and Ag, in most cases, gold alone exhibits high and exceptional catalytic activity.

Notwithstanding the origin of the active sites associated to the supported gold catalysts is still under debate because of their very complex nature, and still remains challenging for the homogeneous control of particle size distribution of the supported gold nanoparticles, heterogeneous gold catalysis can be currently considered as a mature topic. As illustrated in Figure 1.9, the published papers on

the topic of gold catalysis have augmented exponentially in the last 20 years, and the rate of publication shows no declining signs. Moreover, the numerous reviews covering a wide range of applications of gold catalysts and the most relevant aspects of gold chemistry [181-194] have provided a huge and fascinating understanding of catalysis by gold. From all this available literature, nowadays it is well known that the catalytic activity of gold catalysts is highly influenced by [195-197]: (i) the size and shape of gold particles; (ii) the catalyst synthesis methods; (iii) the nature of support; (iv) the gold-support interface interactions; and (v) the oxidation state(s) of gold in the synthesized catalysts. Furthermore, it has been reported that the synthesis of gold catalysis by the conventional incipient wetness impregnation method yields AuNPs larger than 30 nm, due to the weak interaction of the most commonly used gold precursor (HAuCl_4) with the metal oxide support. The chloride remaining on the support promotes the aggregation of AuNPs and may poison the active sites of the catalyst [182, 186, 198]. Consequently, numerous papers describing different methods to incorporate AuNPs on a variety of metal oxides, including TiO_2 , Al_2O_3 , Fe_2O_3 , CeO_2 , Co_3O_4 , ZrO_2 , MgO and SiO_2 have been published by different research groups to overcome this problem [182, 199-200]. Depending on the metal oxide support, gold catalysts can be synthesized mainly by deposition-precipitation, co-precipitation, colloidal dispersion and gas- and liquid-phase grafting of organo-gold complexes. Deposition-precipitation has been the most used method for the preparation of gold catalysts supported on metal oxides having high isoelectric points (IEP), such as TiO_2 , Fe_2O_3 , Al_2O_3 , ZrO_2 and CeO_2 [200]. However, in the case of supports having low IEP, such as SiO_2 (IEP ~ 2), the deposition-precipitation method is not appropriate for the incorporation of AuNPs, because under the high pH conditions required to hydrolyze the HAuCl_4 , commonly used as gold precursor, the weak interaction between the negatively charged silica surface and the $[\text{Au}(\text{OH})_n\text{Cl}_{4-n}]^-$ species hinders the gold adsorption and facilitates the mobility of AuNPs, which can sinter easily during the synthesis process, especially during the calcination step, yielding low gold loadings and inactive catalysts [19].

Mesoporous silica materials with ordered and controllable porous structure, excellent mechanical properties, high surface area, pore volume and thermal stability are very suitable catalyst supports, because they provide high dispersion of metal nanoparticles and facilitate the access of the substrates to the active sites [18]. Consequently, considerable efforts have been made for developing suitable methods to synthesize gold catalysts supported on these materials, because the incorporation of AuNPs into the channel system can prevent their agglomeration and leaching.

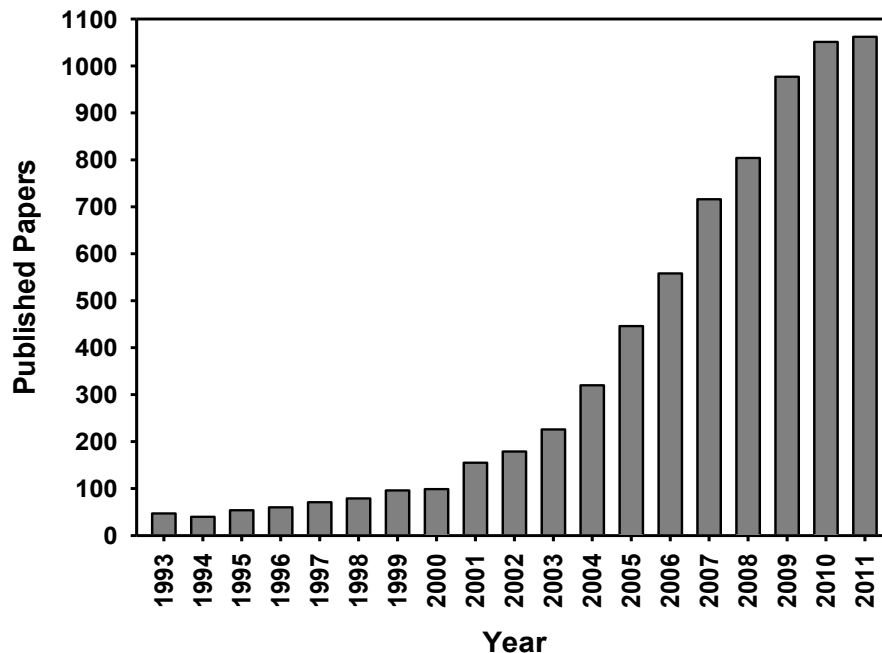


Figure 1.9. Published papers on the topic of gold catalysts. Source: Web of Science, Thomson Reuters. Consulted: 23 November 2011 [201].

In principle, gold can be loaded into MSM during or after the synthesis of the mesoporous silica support [202]. The most used methods for preparing Au/MSM catalysts include the modification of the MSM support with organic functional groups by post-grafting or co-condensation before gold loading [203-204], one-pot synthesis by the incorporation of both gold and the coupling agent containing functional groups into the MSM synthesis [205], the use of cationic gold complexes such as $[\text{Au}(\text{en})_2]\text{Cl}_3$ (en = ethylenediamine) [206], chemical vapor deposition using expensive organometallic gold precursors [207], synthesis of the MSM in the presence of gold colloids [208-209], dispersion of gold colloids protected by ligands or polymers onto SiO_2 [208-209], and modification of the mesoporous SiO_2 supports with other metal oxides, such as TiO_2 , Al_2O_3 and CeO_2 to prepare SiO_2 -based gold catalysts [210-211].

Although there are several published reviews on different aspects of gold catalysis [181-194], as mentioned previously, to the best of our knowledge the synthesis of gold catalysts supported on MSM have not been extensively reviewed. Only two interesting contributions focusing on the preparation of Au/ SiO_2 catalysts, mainly for CO oxidation, have been published by Ma and Dai [199] and Ma *et al.* [200]. Herein we reviewed the main methods to synthesize gold catalysts supported on MSM, as well

as some selected examples of their catalytic applications, in order to contribute to the fascinating topic of catalysis by gold. Because of the large number of available literature and applications, neither the characterization methods of the synthesized gold catalysts nor the physical chemistry of the catalytic reactions is covered in this review. Readers interested on these topics can find useful information in this special issue of Catalysts, in the recent thematic issue of the Chemical Society Reviews (2008 Gold: Chemistry, Materials and Catalysis issue), and in the current specific literature [169, 199, 202, 212].

1.3.3. Methods to synthesize active gold catalyst supported on MSM

1.3.3.1. Post-synthetic functionalization of MSM (grafting) before gold loading

The subsequent modification of the silica surface with organic functional groups (commonly named grafting [213]) prior to the gold loading, has been a surface-engineering strategy to promote the interaction between the frequently used HAuCl_4 gold precursor and the mesoporous silica support, which lead to avoid the mobility and aggregation of the AuNPs on the silica surfaces. After functionalization, the MSM adsorb easily the AuCl_4^- ions, by the formation of a monolayer of positively charged groups on the pore surface. Upon calcination or chemical reduction with NaBH_4 , the metallic gold precursor evolves in highly dispersed metal AuNPs. The general procedure to synthesize gold catalysts following this approach, summarized in Figure 1.10, normally consists of two general steps: (i) the grafting of the stabilizing ligands into the inner surfaces of the mesoporous silica material; and (ii) the gold loading. The first step consists in the reaction of a suitable organic functional group (usually organosilanes containing amine or thiol groups) with the mesoporous silica support using an appropriate solvent (normally toluene or ethanol) in a refluxing system under nitrogen [156, 184, 214]. The resulting solids are subsequently recovered by filtration, washed with the solvent and dried. In the second step, the functionalized MSM are dispersed in a yellow solution of the gold precursor (commonly HAuCl_4) under vigorous stirring. Then, the solution turns colorless, while the solids become yellow, indicating that the ion-exchange between the gold precursor solution and the functionalized MSM support has been attained. After filtration, the gold catalysts are washed with abundant deionized water to remove the residual chloride ions, dried and subsequently calcined to remove the functional ligands, and to reduce the oxidized Au^{3+} species to metallic Au^0 gold particles strongly attached to the support [182]. The catalysts prepared under this approach can also be reduced in H_2 or chemically using NaBH_4 solution [215].

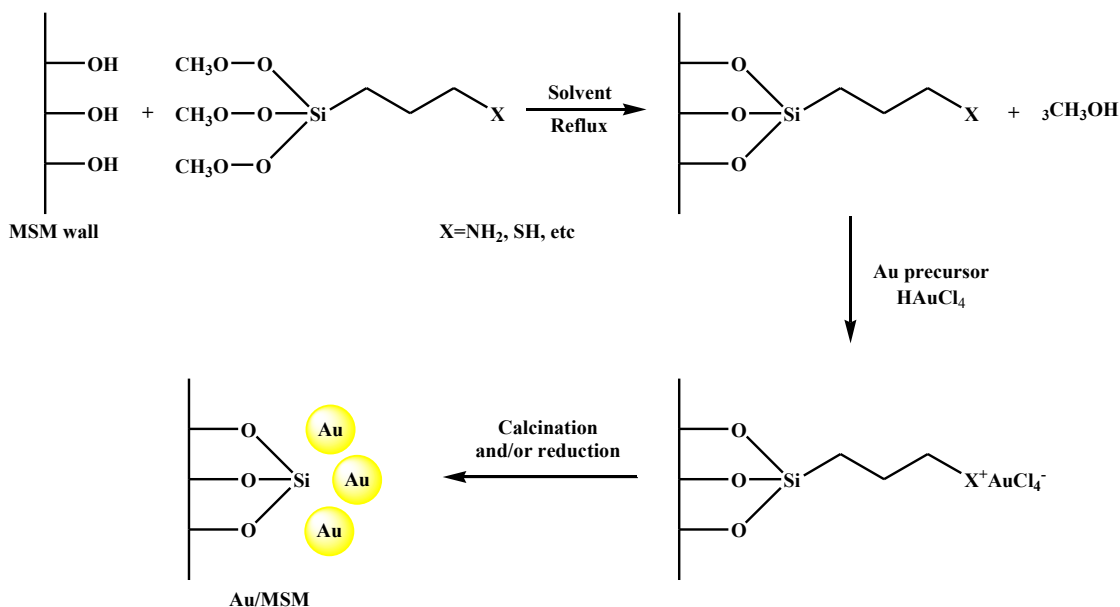


Figure 1.10. General procedure to synthesize gold catalysts by post-synthetic functionalization of the MSM before gold loading.

This method has been used for the synthesis of numerous gold catalysts supported on different mesoporous silicas such as MCM-41, MCM-48, SBA-11, SBA-12, SBA-15, SBA-16, HMM-2 and HMS, as summarized in Table 1.5 and illustrated in Figure 1.11. Some relevant catalysts synthesized by this method and their catalytic applications are highlighted below.

Table 1.5. Characteristics and catalytic applications of the Au/MSM catalysts synthesized by postsynthetic modification of MSM before gold loading.

Support	Functional ligand	Au Precursor	Au loading (%wt)	Au size (nm)	Catalytic application	Ref.
SBA-11	APS	HAuCl ₄	5.0	6.0±1.9	CO oxidation	[216-217]
SBA-12	APS	HAuCl ₄	5.0	4.2±0.8	CO oxidation	[216-217]
SBA-15	OBSQ	HAuCl ₄	1.4	1.6	Epoxidation of olefins	[18]
SBA-15	APS	HAuCl ₄	5.0	4.1±0.8	CO oxidation	[216-217]
SBA-15	APS	HAuCl ₄	4.0	5.8	CO oxidation	[215]
SBA-15	APS	HAuCl ₄	3.86	2.8	Cyclohexane oxidation	[218]
SBA-15	MPTS	HAuCl ₄	4.53	6.5	Cyclohexane oxidation	[218]
SBA-15	TPTAC	HAuCl ₄	4.8	4.5	CO oxidation	[219]

Table 1.5. Cont.

Support	Functional ligand	Au Precursor	Au loading (%wt)	Au size (nm)	Catalytic application	Ref.
SBA-15	MPS and APTS	HAuCl ₄	4.0	10.0		[220]
SBA-15	MPS and APTS	HAuCl ₄ Pd(NO ₃) ₂	4.0 0.5	5.0	Benzyl alcohol oxidation	[220]
SBA-15	APS	HAuCl ₄	5.0	1.0-4.0		[221]
SBA-15	APS	HAuCl ₄ In(NO ₃) ₃	4.6-4.9 0.5-1.5	1.0-5.0	Hydrogenation of crotonaldehyde	[221]
SBA-15	MPS	HAuCl ₄	2.0	3.4-6.6	CO oxidation	[222]
SBA-15	VTES	HAuCl ₄	1.0	9.0	Cyclohexane oxidation	[223]
SBA-15	APS	HAuCl ₄	0.5-1.5	3.0-8.0	Cyclohexane oxidation	[224]
SBA-15	MPTS	HAuCl ₄	4.53	5.0-8.0	<i>n</i> -Hexadecane oxidation	[225]
SBA-15	APTS	HAuCl ₄	1.0	4.0-13.0	Benzyl alcohol oxidation	[226]
SBA-15	PAMAM	HAuCl ₄	10.83-12.51	1.0-6.0	Oxidation of alcohols	[227]
SBA-15	APS	HAuCl ₄	18.0	3.0-5.0	Glucose oxidation	[228]
SBA-15	TPED	HAuCl ₄	2.6	2.0-3.0	Cyclohexene oxidation	[229]
SBA-15	Py	HAuCl ₄	2.7	2.0-3.0	Cyclohexene oxidation	[229]
SBA-15	MPS	HAuCl ₄	3.0	2.7-6.4	CO oxidation	[230]
SBA-15	APTS	HAuCl ₄	-	2.1-10.3	-	[231]
SBA-15	APTS	HAuCl ₄ ^a	-	4.5-19.4	-	[231]
SBA-15	TPED	HAuCl ₄	-	5.8-11.7	-	[231]
SBA-15	TPED	HAuCl ₄ ^a	-	4.5-23.3	-	[231]
SBA-15	TPTAC	HAuCl ₄	1.7	3.0	-	[232]
SBA-15	MPS	Au colloids	2.1	5.0-7.0	-	[233]
SBA-15	APS and Glycidol	HAuCl ₄	9.0	5.0-10.0	-	[234]
SBA-15	NH ₃	HAuCl ₄	-	-	-	[235]
SBA-15	TPTAC	HAuCl ₄	4.0-9.0	1.0-5.0	-	[236]
SBA-15	APTS	HAuCl ₄	6.0	3.0-5.0	-	[237]
SBA-15	TPTAC	HAuCl ₄	2.7-3.0	< 7.0	-	[238]

Table 1.5. *Cont.*

Support	Functional ligand	Au Precursor	Au loading (%wt)	Au size (nm)	Catalytic application	Ref.
SBA-15	G4-PAMAM	HAuCl ₄ K ₂ PdCl ₄	0.5% mol	1.5	Microwave-assisted Suzuki-Miyaura coupling reaction	[239]
SBA-15	APTS	HAuCl ₄ AgNO ₃	6.0	2.9	CO oxidation	[240]
SBA-16	APTS	HAuCl ₄	1.0	2.0-9.0	Benzyl alcohol oxidation	[226]
SBA-16	APTS	HAuCl ₄	0.89	3.0-11.0	Benzyl alcohol oxidation	[241]
SBA-16	APTS	HAuCl ₄ PdCl ₂	0.24-1-15 0.24-0.55	2.0-12.0	Benzyl alcohol oxidation	[241]
SBA-16	APTS	HAuCl ₄	-	2.4-11.4	-	[231]
MCM-41	APS	HAuCl ₄	4.0	5.1	CO oxidation	[215]
MCM-41	APS	HAuCl ₄	-	3.5±0.5	Styrene hydrogenation	[242]
MCM-41	APS	HAuCl ₄	5.0	3.9±0.7	CO oxidation	[216-217]
MCM-41	APTS	HAuCl ₄	1.0	2.0-11.0	Benzyl alcohol oxidation	[226]
MCM-41	APS	HAuCl ₄	5.0	3.9±0.9	CO oxidation	[243]
MCM-41	MPTS	Au colloids	-	52.4	-	[244]
MCM-41	APTS	HAuCl ₄	-	1.9-21.0	-	[231]
MCM-48	APS	HAuCl ₄	4.0	6.9	CO oxidation	[215]
MCM-48	APTS	HAuCl ₄	-	1.4-27.2	-	[231]
HMM-2	APS	HAuCl ₄	5.0	4.7±0.7	CO oxidation	[216-217]
PMOs	APS	HAuCl ₄	-	50.0	Reduction of methylene blue	[245]
PMOs	C ₁₈ TMS - APS	HAuCl ₄	-	3.0-5.0		[245]
Aerosol derived SiO ₂	APS	HAuCl ₄	5.0	1.4±0.2	CO oxidation	[216]
Aerosol silica	APS	HAuCl ₄	5.0	1.4±0.2	CO oxidation	[243]
Nanosilica	MPS	Au colloids	1.0-5.0	6.3	Cyclohexane oxidation	[246]
HMS	APS	HAuCl ₄	-	80.0	Glucose oxidation	[247]
HMS	MPS	HAuCl ₄	-	80.0	Glucose oxidation	[247]
FDU-12	APTS	Au nanocrystals	15.0	4.0	-	[248]

Table 1.5. Cont.

Support	Functional ligand	Au Precursor	Au loading (%wt)	Au size (nm)	Catalytic application	Ref.
MCF	C ₁₀ H ₂₃ ClSi	Au nanocrystals	15.0	4.0	-	[248]
MTFs	APS or TPED	HAuCl ₄	16.2	7.0	-	[249]
HMS	APTS	HAuCl ₄	-	2.1-22.4	-	[231]
HMS	APTS	HAuCl ₄ ^a	-	2.3-18.3	-	[231]
HMS	TPED	HAuCl ₄	-	8.7-20.8	-	[231]
HMS	TPED	HAuCl ₄ ^a	-	4.7-22.3	-	[231]

Chi *et al.* [215] synthesized AuNPs confined in the channels of MCM-41, MCM-48 and SBA-15 by previous modification of their surface with APS. To do this, the as-synthesized MCM-41 and MCM-48 materials were first acidified with nitric acid solution (pH < 1.0), and then, the as-synthesized SBA-15 and the acidified MCM-41 and MCM-48 silicas were modified with APS in a reflux system for 3–6 h at about 70°C, using ethanol as solvent. After filtration, washing and drying, the resulting surface-functionalized solids were mixed with HAuCl₄ aqueous solution, and the slurry was chemically reduced with NaBH₄ solution. The catalysts (Au-loading of 4%wt), activated by calcination at 560°C with subsequent heating to 600°C under H₂/N₂ flow for 1 h, were active for CO oxidation, and showed an average Au particle size of 5.1, 6.9 and 5.5 nm on MCM-41, MCM-48 and SBA-15 supports, respectively. The smaller the Au particle size, the higher the catalyst activity. Moreover, the XPS analysis revealed that AuNPs were present on the catalysts in the metallic Au⁰ state.

Richards group [218] used APS and MPTS as stabilizing ligands, to immobilize AuNPs into mesoporous SBA-15. The resulting gold catalysts (Au-loading ~4%wt) were highly active for the aerobic oxidation of cyclohexane, and conversions ranging between 21 and 32% after 6 h reaction at 150°C and 1.5 MPa of oxygen pressure were attained. Although the synthesized Au/SBA-15 catalysts showed smaller surface area and pore size than pure SBA-15, they retained the characteristic isotherm shape of the mesoporous materials, demonstrating that SBA-15 support was stable to the surface modification and gold loading. AuNPs along the channels of the silica walls with mean particle sizes of 2.8 and 6.5 nm were obtained when using APS and MPTS, respectively.

According to these authors, the smallest AuNPs were obtained using APS, because the aqueous solution precursor AuCl_3OH^- can interact strongly with the amine groups, preventing the agglomeration of particles during the synthesis process.

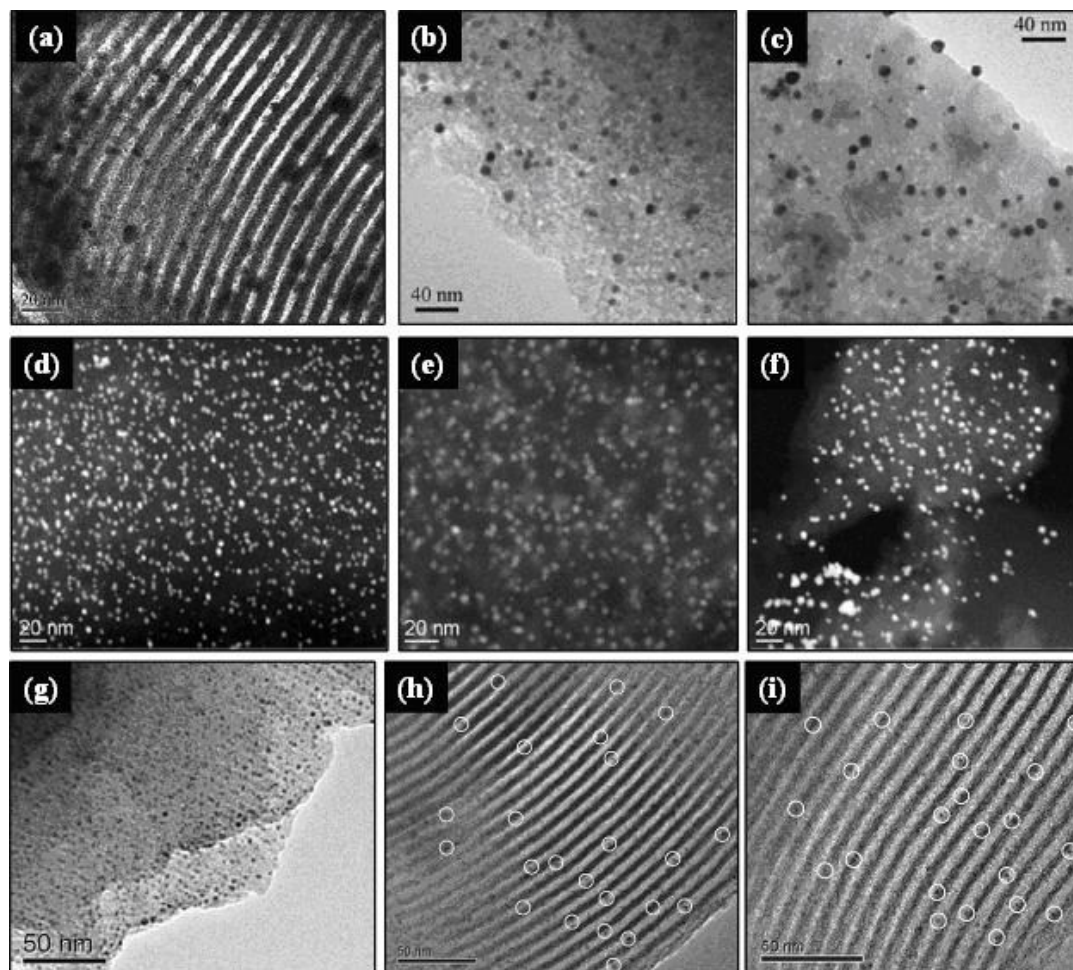


Figure 1.11. TEM (a,b,c) and HAADF STEM (d,e,f) images of gold catalysts supported on different MSM prepared by using the postsynthetic functionalization of MSM before gold loading. (a) Au/SBA-15 modified with APS (Reproduced by permission of Elsevier from Reference [215]); (b) Au/SBA-16 modified with APTS (Reproduced by permission of Elsevier from Reference [226]); (c) Au/MCM-41 modified with APTS (Reproduced by permission of Elsevier from Reference [226]); (d) Au/HMM-2 modified with APS (Reproduced by permission of ACS Publications from Reference [217]); (e) Au/SBA-12 modified with APS (Reproduced by permission of ACS Publications from Reference [217]); (f) Au/SBA-11 modified with APS (Reproduced by permission of ACS Publications from Reference [217]); (g) Au/SBA-15 modified with PANAM (Reproduced by permission of Elsevier from Reference [227]); (h) Au/SBA-15 modified with TPED (Reproduced by permission of Elsevier from Reference [229]); (i) Au/SBA-15 modified with Py (Reproduced by permission of Elsevier from Reference [229]).

Recently, Wei *et al.* [245] developed a modified external passivation route to control the location and the distribution of AuNPs in periodic mesoporous organosilica. In this approach, the catalysts synthesis method consisted in three main steps: (i) one external passivation of the PMOs with a long chain of hydrophobic *n*-octadecyltrimethoxysilane, to obtain C₁₈TMS-PMOs material; (ii) the internal amino-functionalization of the C₁₈TMS-PMOs material with aminopropyl groups (APS); and (iii) the Au impregnation of the obtained NH₂-C₁₈TMS-PMOs support using HAuCl₄, followed by reduction under H₂ at 100°C for 2 h. The synthesized catalysts displayed the typical mesoporous structure and narrow pore size distribution of the PMOs, and were active for the reduction of methylene blue. In this interesting method of synthesis, to avoid the adsorption of AuNPs onto the PMOs external surface, the functionalization with C₁₈TMS was made, because it has no affinity for gold complex. However, to introduce AuNPs into the channels of the PMOs, the internal surface was modified with APS, which significantly enhanced the adsorption of AuNPs with particle sizes between 3 and 5 nm inside the pores of the silica material. This approach is a good example of how the surface-engineering can be used in order to control the location of the AuNPs into MSM.

Since the MSM do not have the same structural properties, the Dai's group [231] evaluated the influences of the synthesis conditions and mesoporous structures on the AuNPs supported on different mesoporous silicas (HMS, MCM-41, MCM-48, SBA-15 and SBA-16). The MSM were modified with two different amine ligands (APTS and TPED) using toluene as solvent. The functionalized silica materials were washed several times with a large quantity of ethanol and toluene, and then vacuum-dried at 80°C for 6 h. Gold was incorporated into the mesopores by mixing HAuCl₄ dissolved in water or ethanol with the silica hosts, followed by sonication for 30 min. The resulting materials were finally filtered, vacuum-dried at room temperature and calcined at 200 or 550°C for 1 h. On the basis of the obtained materials characterization, the following conclusions were drawn: (i) Bigger AuNPs were generated when using diamine instead of monoamine ligand, and when ethanol was used as solvent. Although the explanation of this behavior was related to the fact that the use of diamine ligand could have facilitated a higher uptake of gold and that ethanol could have facilitated the reduction of gold cations, unfortunately the amount of loaded gold on the synthesized materials was not reported. (ii) The gold particle size increases with the calcination temperature, but the extent of sintering is different with different mesoporous hosts. (iii) The size of nanopores may play a role in determining the thermal stability of AuNPs against sintering. (iv) Bicontinuous pore structures such as HMS, MCM-48 and SBA-16 materials could lead to the

sintering of gold nanoparticles, whereas one-dimensional pore channels such as MCM-41 and SBA-15 materials could mitigate the sintering of AuNPs. These results were in agreement with the previous works carried out by Bore *et al.* [217] and Gabaldon *et al.* [216], who studied the incorporation of gold on a variety of mesoporous silica materials (MCM-48, SBA-11, SBA-12, SBA-15 and HMM-2) with different mesoporous architectures, and concluded that 1-D mesoporous architectures were most effective for controlling Au sizes, than cubic and 3-D mesoporous architectures, because the easier access and connectivity of the 3-D structures facilitates the particle growth, while when using 1-D mesoporous silicas, the amount of free gold that can participate in Ostwald ripening is limited. Moreover, these authors pointed out that among the 1-D pores, the curved pores were better for confining Au particles than the 1-D straight pores, and that small pore sizes are not sufficient to control the Au particle size.

The post grafting functionalization has been also used for the synthesis of supported bimetallic gold catalysts. For example, a four step grafting method was used by Ma *et al.* [220] to modify mesoporous SBA-15 before gold loading. Firstly, the as-synthesized SBA-15 was grafted with MPS, and after removing the surfactant template by ethanol extraction and subsequent calcination at 300°C for 4 h, the MPS functionalized SBA-15 was grafted again with APTS. This double modified material was loaded with both Au and Au-Pd particles, using HAuCl_4 and $\text{Pd}(\text{NO}_3)_2$ aqueous solutions, respectively, and calcined at 200°C for 2 h. Gold and palladium particles penetrate into the pores of SBA-15 owing to the high affinity of the $-\text{NH}$ groups to the binding metals [220]. The resulting Au/SBA-15 and Au-Pd/SBA-15 catalysts conserved the mesoporous structure of the support, and were active for the oxidation of benzyl alcohol under air flow at 80°C in alkaline media. According to these authors, the addition of Pd to Au/SBA-15 catalyst decreased the size of AuNPs from 10 to 5 nm, contributed to their uniform dispersion, increased the activity and retained high selectivity towards benzaldehyde. Yang *et al.* [221] immobilized Au and Au-In nanoparticles on SBA-15 using APS as functionalizing agent. The spherical Au and Au-In particles with average size of around 2 nm were homogeneously dispersed on the mesopore walls of SBA-15, and were highly active and selective for the hydrogenation of crotonaldehyde to crotyl alcohol in liquid phase. Yen *et al.* [250] used APS to functionalize the surface of mesoporous MCM-41 for the synthesis of bimetallic Au-Ag/MCM-41 catalysts. The catalysts, activated by calcination with subsequent hydrogen reduction at 600°C, showed Au-Ag bimetallic nanoparticles with sizes ranging between 4 to 6 nm, and exhibited high activity in catalysis for low-temperature CO oxidation with high stability. Moreover,

these catalysts were resistant to moisture over a long storage time. Liu *et al.* [251] prepared Au-Cu alloy nanoparticles with sizes of around 3 nm in the confined space of mesoporous SBA-15 using APTS to functionalize the support surface. The calcined (at 500°C for 6 h) and subsequently reduced under H₂ (at 550°C for 2 h) catalysts, showed much better performance than monometallic gold particles in catalyzing CO oxidation. Recently Chen *et al.* [241] modified the SBA-16 surface with APTS to prepare Au-Pd/SBA-16 catalysts. The highly dispersed Au-Pd bimetallic nanoparticles with a mean diameter ~6 nm were active for the selective solvent-free oxidation of a variety of aromatic alcohols and maintained good catalytic stability after recycling.

The above mentioned examples demonstrate that the post-synthetic functionalization of MSM with organic moieties containing polar groups such as -NH₂, -SH, *etc.* before gold loading, may be a good way to synthesize Au/MSM catalysts. However, this method does not allow the homogeneous distribution of the organic functional groups in the pore surface, because it depends on numerous parameters, such as the number of the surface silanol residual groups, the diffusion of reagents through the pores channels and steric factors [252]. Consequently the AuNPs are not homogeneously distributed after gold loading [253]. Moreover, the grafting procedure leads to a reduction of the specific surface area and the pore volume of the MSM [252] which are normally further reduced after gold incorporation.

1.3.3.2. Self-assembly functionalization of MSM before gold loading

The self-assembly functionalization of MSM before gold loading consists in the co-hydrolysis and poly-condensation of the silica source with the organic functional groups (mainly organosilanes, RSi(OR')₃) in the presence of a structure-directing agent. This method of synthesis enables the functional groups to be anchored covalently with regular distribution inside the pore walls of the MSM [213, 252]. Moreover, pore blocking is not a problem, because the functional organic groups are direct components of the silica matrix [213, 252]. The gold loading is carried out in a subsequent step, mainly by deposition-precipitation, using HAuCl₄ as gold precursor. After filtration, the synthesized gold catalysts are washed with abundant deionized water to remove the residual chloride ions, dried and subsequently calcined to remove the functional ligands and to reduce the oxidized Au³⁺ species to metallic Au⁰ gold particles. The catalysts prepared following this approach can also be reduced in H₂ or chemically using NaBH₄ solution [215]. Figure 1.12 presents a general scheme of this synthesis procedure. In Table 1.6 we present the characteristics of the Au/MSM catalysis

prepared following this method of synthesis, whereas some interesting papers are briefly discussed below.

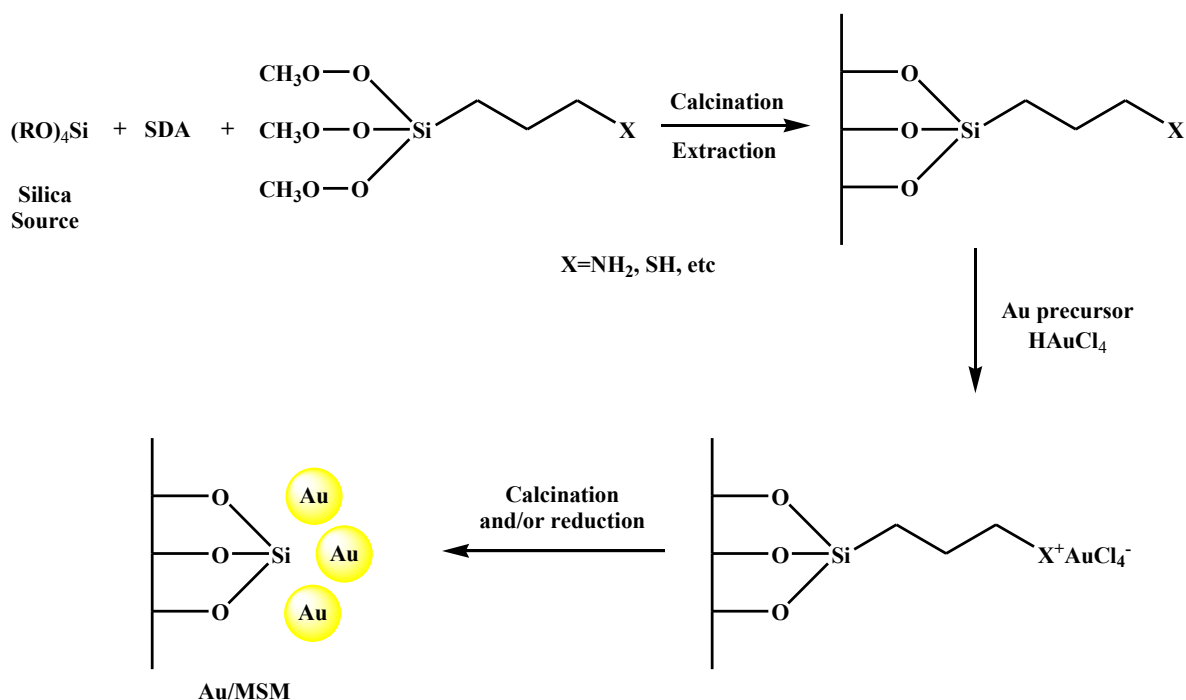


Figure 1.12. General procedure to synthesize gold catalysts by self-assembly functionalization of MSM before gold loading.

Ghosh *et al.* [254] synthesized Au/MCM-41 hybrid materials by direct functionalization of the silica material with APS and MPS in a one-pot process. The surfactant of the functionalized MCM-41- NH_2 and MCM-41-SH supports was removed by solvent extraction under reflux for 24 h, with a mixture of solvents containing 85 g of methanol and 2 g of HCl (35.5%). Subsequently, gold (3.0–3.5%) was loaded by mixing the aforementioned supports with $H Au Cl_4$ aqueous solution for 96 h. After filtration, washing and vacuum drying at room temperature, the resulting catalysts retained the ordered mesoporous structure characteristic of the pristine MCM-41, but a decrease of approximately 20% and 22% in the surface areas of Au/MCM-41- NH_2 and Au/MCM-41-SH, respectively, was observed. Although the pore volumes of the catalysts also decreased as a consequence of the guest species incorporation, the average pore diameters of samples did not change considerably after gold loading. The mean diameters of the AuNPs were approximately 3.4 ± 0.5 and 3.2 ± 0.5 nm for Au/MCM-41- NH_2 and Au/MCM-41-SH, respectively. The synthesized catalysts were active and completely selective for the hydrogenation of different olefinic substrates (cyclohexene, 1-hexene and 1-octene),

and fairly comparable catalytic activity was found for both Au/MCM-41-NH₂ and Au/MCM-41-SH samples.

Table 1.6. Characteristics and catalytic applications of the Au/MSM catalysts synthesized by self-assembly functionalization of MSM before gold loading.

Support	Functional ligand	Au Precursor	Au loading (%wt)	Au size (nm)	Catalytic application	Ref.
MCM-41	APS	HAuCl ₄	3.1–3.2	3.4 ± 0.5	Hydrogenation of olefinic substrates	[254]
MCM-41	MPS	HAuCl ₄	3.2–3.5	3.2 ± 0.5	-	[254]
MCM-41	OBSQ	HAuCl ₄	2.1	2.1	Epoxidation of olefins	[18]
SBA-15	MPS	HAuCl ₄	1.05–16.1	2.5	-	[204, 255]
SBA-15	MPS	AuCl(THT)	1.05–16.1	4.5	-	[204, 255]
SBA-15	Mannitol derivative	HAuCl ₄	-	3.0–6.0	-	[256]
SBA-15	MPS	HAuCl ₄	3.0	2.0–6.5	CO oxidation	[222]
SBA-15	OBSQ	HAuCl ₄	1.0–5.5	1.8	Styrene epoxidation	[253, 257]
SBA-15	OBSQ	HAuCl ₄	1.0–5.5	2.2 ± 0.5	Benzyl alcohol oxidation	[253, 257]
SBA-15	OBSQ	HAuCl ₄	1.4–2.1	2.0	Epoxidation of olefins	[18]
PMOs	Bis-silylated with disulfide unit	AuCl(THT)	5.0–20.0 ^a	2.0	-	[258]
MSS	MPS and PrTMS	HAuCl ₄	1.0	1.0–15.0	-	[259]
MSS	MPS	HAuCl ₄	14.0	4.8	-	[260]
MSU	OBSQ	HAuCl ₄	2.0	4.7	Epoxidation of olefins	[18]
KIT-5	APS	HAuCl ₄	~10.0	2.0–5.0	-	[261]

^a Au/S molar ratio × 100.

Guari *et al.* [204, 255] described a methodology to synthesize Au/SBA-15, preparing first the support by co-condensation of MPS with TEOS in the presence of Pluronic 123. After surfactant removal by Soxhlet extraction, the functionalized support was vacuum dried at 120°C. The gold loading was performed by using two gold precursors: HAuCl₄ and [AuCl(THT)]. When HAuCl₄ was employed, the functionalized support was suspended in water and heated under reflux in the presence of the gold precursor. Once the yellowish solution color was transferred onto the solid, sodium citrate was

added. When $[\text{AuCl}(\text{THT})]$ was utilized, the functionalized support was suspended in tetrahydrofuran, and sodium acetylacetonate hydrate was added after the gold precursor addition. According to these authors, upon chemical reduction with NaBH_4 ethanolic solution at 60°C , metallic AuNPs (2.5 and 4.5 nm, respectively) were formed within the channels of the silica matrix. However, the typical ordered SBA-15 pore channels cannot be identified from the published TEM images, and unfortunately the catalytic activity of the synthesized materials was not evaluated.

Rombi *et al.* [222] functionalized SBA-15 with MPS by co-condensation using a TEOS:MPS molar ratio of 10, and after surfactant removal by Soxhlet extraction with a mixture of ethanol and HCl, gold (3%wt) was loaded using HAuCl_4 as precursor. Once the solution became colorless, indicating the deposition of gold on the SBA-15 surface, sodium citrate was poured into the mixture to reduce the Au^{3+} to Au^+ species. Then, the solid was recovered by filtration and dried at 120°C for 12 h. Subsequently, NaBH_4 1%wt ethanol solution was mixed with the solid during 18 h at 60°C in order to obtain metallic gold. Finally, the suspension was filtered and the solid was dried at 120°C overnight. Calcination of the catalysts in air at 300 and 560°C led to the formation of small Au spherical nanocrystals homogeneously dispersed inside the SBA-15 channels with average sizes of about 2–3 and ca. 5 nm, respectively. Subsequent reduction under H_2/He 600°C led to an increase in the size of AuNPs up to ca. 6.5 nm. However, despite their large particle size, remarkable catalytic activity for CO oxidation was observed for the catalysts that were first calcined at 560°C and then reduced under H_2/He 600°C , whereas the as-made catalysts were not active for CO oxidation at low temperatures. Moreover, gold was found mainly in metallic Au^0 state, although because of the strong interaction between the mercapto functional groups and gold, positive Au^{5+} species were also present.

Besson *et al.* [258] described a soft method allowing the incorporation of monodisperse AuNPs with average sizes of about 2–3 nm within the framework of 2D-hexagonal mesoporous silicas without any thermal treatment. In this approach, the framework of the silica material was functionalized by co-condensation of a hydrophilic *bis*-silylated precursor containing disulfide (prepared by reaction between 3-isocyanatopropyltriethoxysilane and 2,2'-diaminediethylidisulfide in THF) and TEOS in the presence of pluronic acid (P123) as template. After reduction of disulfide groups into thiol groups with a solution of triphenylphosphine, AuNPs were anchored in the support by impregnation and subsequent reduction of the organometallic gold precursor $[\text{AuCl}(\text{THT})]$ with ethanolic NaBH_4 . The

XRD analysis revealed that the ordered structure of the host materials was preserved after the gold loading. Moreover, the observed broad diffraction peaks at 38.24, 43.81, 64.41 and 78.05° in the XRD high-angle region ($2\theta = 20 - 90^\circ$) confirmed the presence of metallic Au⁰ nanoparticles. In addition, the size of AuNPs was found to depend slightly on the percentage of organic groups in the framework. The AuNPs were very small (<2 nm) in materials containing low quantities of SH groups, while for the more concentrated material in SH groups the AuNPs size was no more monodisperse. Although this method seems to be interesting for the incorporation of AuNPs into MSM, the catalytic activity of the synthesized materials was not evaluated. Moreover, the authors pointed out that AuNPs were stable as long as the organic groups remained intact (up to about 200°C). Beyond this temperature, there was a significant loss of organic moieties which involved the sintering of AuNPs. However, the presence of both the organic moieties and large AuNPs could have a negative effect on the catalytic activity of these composite materials.

Kumagi and Yano [259] prepared functionalized core/shell monodispersed mesoporous silica spheres, by the co-condensation of the silica source (TMOS) with MPS and propyl trimethoxysilane in the presence of CTACl in alkaline media. After the surfactant removal by acid extraction performed in an ethanol mixture of concentrated hydrochloric acid, the samples were filtered off, washed with ethanol, and dried in air. This resulting material was impregnated with a solution of HAuCl₄ in hydrochloric acid to obtain gold-loaded core/shell mesoporous silica spheres containing propyl group in the shell. AuNPs with particle size distributions ranging from 1 to ca. 15 nm were formed, but no catalytic activity was reported. A similar method of synthesis, without the addition of propyl trimethoxysilane had been previously reported by Nakamura *et al.* [260] for the preparation of gold-containing nanoporous silica spheres, with AuNPs sizes in the range of 4.8 nm. However, the catalytic performance of this material was not reported either.

Hérault *et al.* [256] recently obtained SBA-15 mesoporous organosilicas containing mannitol derivative in the framework, by co-hydrolysis and poly-condensation of a *bis*-silylated mannitol precursor (3,4-Di-O-[3-(triethoxysilylpropyl)carbamate]-1,2:5,6-di-O-isopropylidene-D-mannitol, prepared by coupling of 1,2:5,6-di-O-isopropylidene-D-mannitol with 3-(triethoxysilylpropyl)isocyanate) with TEOS in the presence of triblock co-polymer P123 as structure-directing agent in acidic media. After stirring for 24 h at 30°C, the mixture was heated at 110°C for 24 h. Then, the temperature was diminished to room temperature and the reaction mixture was left

without stirring for 3 days. The resulting solids were filtered and washed with ethanol, followed by Soxhlet extractions with ethanol (15 h) and then with acetone (15 h), prior to drying under vacuum. From the three different TEOS: *bis*-silylated mannitol precursor ratios studied (R_9 , R_{19} and R_{39}), it was found that: (i) the highest polycondensation degree (80%) was obtained in the case of R_{39} ; (ii) only the R_{39} sample exhibit the three low-angle XRD diffraction peaks, characteristic of well ordered SBA-15 type materials; (iii) the BET surface areas, the total pore volumes and the pore size distributions ranged from 530 to 630 m²/g, 0.60 to 1.40 cm³/g and 4.4 to 9.0 nm, respectively. On the other hand, during the hydrolysis and poly-condensation processes, some OH functional groups were released, which were used for the stabilization of AuNPs using H₂AuCl₄ or [AuCl(THT)] as gold precursors, involving or not the use of reducing (NaBH₄) and destabilizing (trisodium citrate and sodium acetylacetonate monohydrate) agents. From the characterization analysis it was pointed out that: (i) AuNPs were not formed when using the organogold precursor [AuCl(THT)]; (ii) the absence of destabilizing agent and reducing agent led to the formation of large AuNPs (15–20 nm) overlapping several channels of mesostructured material; (iii) the presence of reducing agent (NaBH₄) allowed the formation of small AuNPs (average size of 6 nm); (iv) the best results, in terms of dispersion, size (3 nm) and location of AuNPs within the walls of the 2D-hexagonal structure of the MSM, were obtained when using trisodium citrate and NaBH₄ as destabilizing and reducing agents, respectively. Unfortunately the catalytic activity of the catalysts synthesized under this approach was not evaluated.

Yu *et al.* [18] functionalized different periodic mesoporous organosilicas (MCM-41, MSU and SBA-15) with an organic bridged silsesquioxane precursor containing disulfide-ionic liquid moieties in one-pot synthesis procedure. Subsequently AuNPs were loaded using aqueous H₂AuCl₄ solution at pH values of 7.0–8.0. The resulting Au/MCM-41, Au/MSU and Au/SBA-15 catalysts showed well dispersed AuNPs, as presented in Figure 1.13(a–c), with mean particle sizes of 2.1, 4.7 and 2.0 nm, respectively, indicating that porous supports with higher pore connectivity, such as MSU with 3-D worm-like pore structure, should be more vulnerable to the aggregation of AuNPs. The catalytic activity, evaluated for the epoxidation of various olefins (α -pinene, cyclohexene, 4-chlorostyrene, α -methylstyrene, 1-hexene and 1-octene) using H₂O₂ as oxidant, was inversely related to the Au particle size, following the order Au/SBA-15 > Au/MCM-41 > Au/MSU. Moreover, after eight consecutive runs, all catalysts showed quite good reusability with no significant losses in both α -pinene conversion and α -pinene oxide selectivity.

Despite the fact that the self-assemble functionalization of MSM before gold loading has permitted the synthesis of Au/MSM materials having well dispersed AuNPs within the channels, as presented in Figure 1.13, the main disadvantages of this method lie in the care that must be taken to avoid the destruction of the functional groups during the surfactant removal and in the difficulty of maintaining the mesostructure of the functionalized silica materials, because the degree of their mesoscopic order decreases with increasing the concentration of functional groups [200, 213]. Moreover, given that the functional group is quite hydrophilic, the functionalization could occur partially within the framework. Then, the organic functional groups have to be sufficiently lipophilic to enter in the core micelle and not too bulky to avoid bursting [262-263].

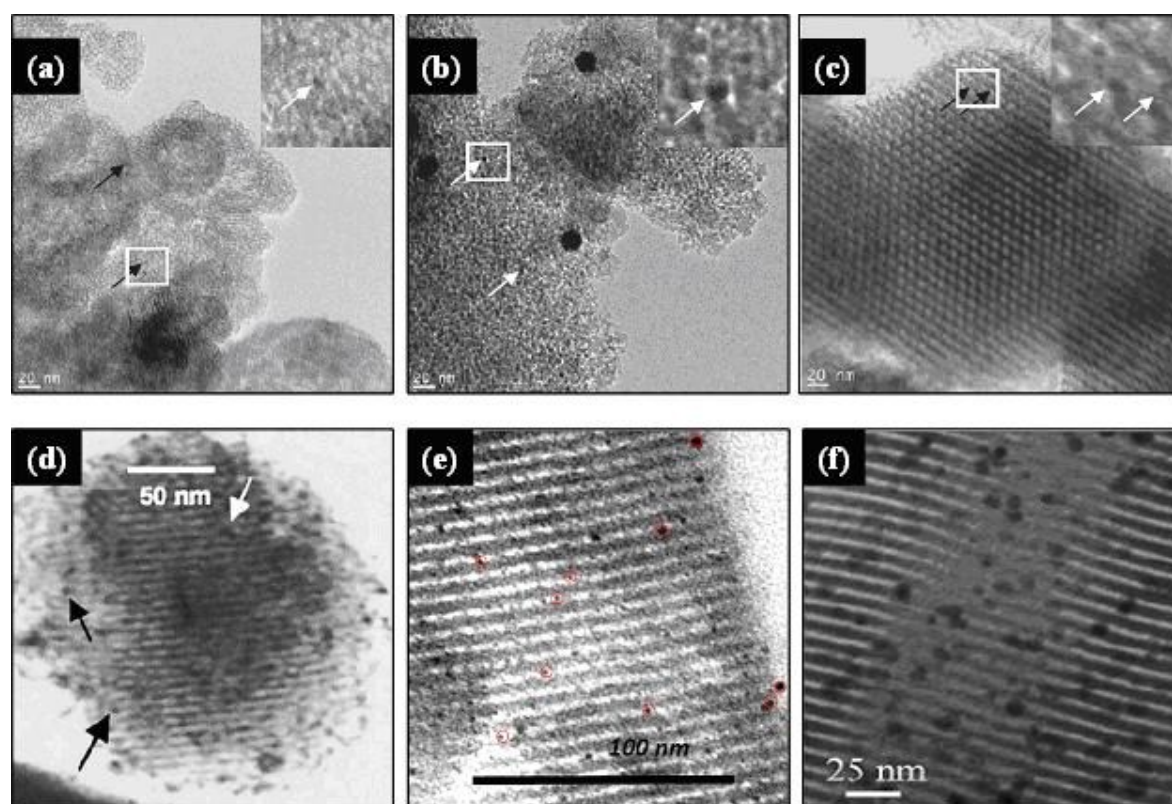


Figure 1.13. TEM images of gold catalysts supported on different MSM prepared by using the self-assembly functionalization of MSM before gold loading. (a) Au/MCM-41 modified with OBSQ (Reproduced by permission of Elsevier from Reference [18]); (b) Au/MSU modified with OBSQ (Reproduced by permission of Elsevier from Reference [18]); (c) Au/SBA-15 modified with OBSQ (Reproduced by permission of Elsevier from Reference [18]); (d) Au/MCM-41 modified with APS (Reproduced by permission of Elsevier from Reference [254]); (e) Au/HMS modified with hydrophilic bis-silylated precursor containing disulfide (Reproduced by permission of RSC Publishing from Reference [258]); (f) Au/SBA-15 modified with MPS (Reproduced by permission of RSC Publishing from Reference [222]).

1.3.3.3. Direct synthesis

This method of synthesis, also called co-condensation or one-pot synthesis, is a simple procedure to introduce AuNPs in MSM, but not necessarily placed within the pores. It consists in the copolymerization of the silica source with the gold precursor in the presence of a structure-directing agent, so that the formation of mesostructures and the gold anchoring occur simultaneously. Organosilane coupling agents (RSi(OR')_3) are frequently added into the gel synthesis in order to functionalize the silica surface for enhancing the gold adsorption. This approach is often preferred, because as mentioned in Section 1.3.3.2., it allows regular distribution of the functional groups inside the channel pores, and therefore uniform distribution of gold, as well as a loading control within the limits of the content supported by the micelle [262]. Although this procedure presents similar shortcomings than the self-assembly functionalization of MSM before gold loading, the direct synthesis method has been largely employed for the preparation of gold catalysts supported on different MSM, as summarized in Table 1.7. Some relevant applications are discussed below.

Table 1.7. Characteristics and catalytic applications of the Au/MSM catalysts prepared by direct synthesis.

Support	Functional ligand	Au Precursor	Au loading (%wt)	Au size (nm)	Catalytic application	Ref.
MCM-41	-	HAuCl ₄	0.13–1.21	-	Cyclohexane oxidation	[264-265]
MCM-41	-	HAuCl ₄	1.0	3.0–18.0	Acetylacetone cyclization	[266]
MCM-41	-	HAuCl ₄	1.0	-	Methanol oxidation	[267]
MCM-41	-	HAuCl ₄ C ₂ NbO ₄	1.0	-	Methanol oxidation	[267]
MCM-41	-	HAuCl ₄ C ₂ NbO ₄	1.0	-	Methanol oxidation	[268]
MCM-41	-	HAuCl ₄	0.386–2.02	3.0–6.0	-	[269-270]
MCM-41	-	HAuCl ₄	1.0	-	Acetylacetone cyclization and methanol oxidation	[271]
MCM-41	-	HAuCl ₄	1.3	20.0	CO oxidation	[272]
MCM-41	-	HAuCl ₄ VO ₂ SO ₄	1.0	-	Methanol oxidation	[273]

Table 1.7. Cont.

Support	Functional ligand	Au Precursor	Au loading (%wt)	Au size (nm)	Catalytic application	Ref.
MCM-41	-	HAuCl ₄ VO ₂ SO ₄ C ₄ H ₄ NNbO ₉	1.0	-	Methanol oxidation	[273]
MCM-41	AAPTS	HAuCl ₄	0.7–7.0	2.0–5.0	-	[205]
MCM-41	TMPTA	HAuCl ₄	-	-	-	[274]
MCM-41	TMPTA	HAuCl ₄	2.2	2.0–3.0	CO oxidation	[275]
MCM-48	TMPDA	HAuCl ₄	-	5.0–20.0	-	[202]
MCM	-	HAuCl ₄	8.0	6.7	CO oxidation	[195]
MCM	-	HAuCl ₄ AgNO ₃	8.0 0/1–1/0 ^b	20.0– 30.0	CO oxidation	[195, 276]
SBA-15	-	HAuCl ₄	0.77	-	Cyclohexane oxidation	[264-265]
SBA-15	-	HAuCl ₄	1.0	3.0–8.0	Cyclohexane oxidation	[224]
SBA-15	TMPDA	HAuCl ₄	-	5.0–50.0	-	[202]
SBA-15	MPS	HAuCl ₄	1.0	2.0–4.0	Cyclohexane oxidation	[277]
SBA-15	VTES	HAuCl ₄	1.0	5.0	Cyclohexane oxidation	[223]
SBA-16	TMPDA	HAuCl ₄	-	10–100	-	[202]
ZSM-5	-	HAuCl ₄	0.51–1.30	-	Cyclohexane oxidation	[278]
ZSM-5	-	HAuCl ₄	0.17–1.16	2.0–5.0	-	[270]
MS	BTESPTS	HAuCl ₄	0.4–1.0	3.0–14.0	Lactose oxidation	[11]
MS	BTESPTS (0.625)	HAuCl ₄	0.75	4.0–15.0	Cyclohexane oxidation	[279]
MS	BTESPTS (1.25)	HAuCl ₄	0.94	3.0–8.0	Cyclohexane oxidation	[279]
MS	BTESPTS (2.5)	HAuCl ₄	1.07	3.0–8.0	Cyclohexane oxidation	[279]
MS	BTESPTS (5.0)	HAuCl ₄	1.10	4.0–12.0	Cyclohexane oxidation	[279]
MS	BTESPTS	HAuCl ₄	0.25–10.0	~3.0	Oxidation of benzyl alcohol	[280]
MS	BTESPTS	HAuCl ₄	2.0–10.0	~2.0	n-hexadecane oxidation	[225, 281]
MS	BTESPTS	HAuCl ₄	0.5–10.0	-	Trichloroethylene oxidation	[282-283]

Table 1.7. Cont.

Support	Functional ligand	Au Precursor	Au loading (%wt)	Au size (nm)	Catalytic application	Ref.
MS	MPS	HAuCl ₄		1.5–5.0	CO oxidation	[284]
MSTF	BTESPTS	Au(en)2Cl ₃	2.1–5.1	3.0–7.0	-	[285]
LSX	-	Au salt	0.646	~3.0	-	[270]
HSN	APS	HAuCl ₄	1.7	2.8–4.5	4-nitrophenol reduction	[286]
WSS	TMPTA	HAuCl ₄	1.6	2.6 ± 0.8	CO oxidation	[275]
HMS	TMPTA	HAuCl ₄	0.5–1.0 ^a	1.7–5.0	-	[287]
PMOs	TMPTA	HAuCl ₄	0.5–1.1 ^a	1.5–2.5	-	[287]
MSU	TMPDA	HAuCl ₄	0.4 [*]	1.7–5.0	-	[287]

^a Au/Si molar ratio × 100; ^b Au/Ag molar ratio.

Lu *et al.* [264–265] synthesized Au/MCM-41 and Au/SBA-15 catalysts by using a direct synthesis process in which the silica and gold precursors (TEOS and aqueous HAuCl₄, respectively) were added to the dissolved surfactants (cetylpyridinium bromide for MCM-41, and P123 for SBA-15) in acidic media. After the hydrothermal treatments, the solids were filtered, washed with deionized water, dried and calcined in air at 550°C for 4.5 h. The gold loading (0.13–1.21%wt) had only a modest effect on the surface area of the supports, and the synthesized catalysts maintained the typical structure of mesoporous materials. Gold was anchored both inside the channels and deposited on the external surface of the mesoporous structures, and it was mainly present in the metallic Au⁰ state. These catalysts were active for the oxidation of cyclohexane, but unfortunately the size of AuNPs was not reported.

Wu *et al.* [277] recently synthesized SBA-15-supported AuNPs (2–4 nm) by means of a one-pot synthesis method in the presence of different amounts of MPS as functionalizing agent. Subsequent to dissolution of the surfactant (P123) in acidic media, different mixtures of TEOS:MPS were slowly added prior the introduction of HAuCl₄ solution (gold loading of 1%wt). After stirring (40°C for 24 h) and hydrothermal treatment (100°C for 24 h), the resulting solids were filtered, washed, dried under vacuum and calcined at 500°C during 8 h, to remove the surfactant and the organic functional group, and to decompose the gold species into metallic Au⁰. From the analysis performed in this study, it can be highlighted that: (i) The functionalizing agent contributed to coordinate the gold precursor via

thiol ligands, and to form covalent bonds with the silica matrix. During the synthesis, the silane moiety co-condensed with the silicon precursor to form the silica framework, and the alkanethiol end interacted with AuCl_4^- to form Au (I)—thiolate complexes, which firmly attached the gold species on the silica framework. (ii) The amount of MPS played a critical role in the loading and dispersion of AuNPs. The larger the amounts of MPS introduced, the higher the Au loading efficiency and dispersion. However, the AuNPs began to aggregate and unevenly distribute with the decrease of added MPS. Withal, when the concentration of MPS in the gel increased up to 20% (molar ratio TEOS:MPS is 32:8), the 2D hexagonal ordered structure decreased significantly, indicating that high concentrations of MPS hindered the TEOS condensation to form an ordered framework. (iii) Because of the formation of void defects on the pore walls after removal of functional groups by calcination, AuNPs were partially intercalated in the pore walls of the mesoporous SBA-15, and the catalysts showed values of surface area higher than the pure SBA-15. (iv) The catalysts were active for the selective oxidation of cyclohexane with molecular oxygen, and the increase of MPS led to an increase on the conversion of cyclohexane up to 21.5% with selectivities towards cyclohexanone and cyclohexanol of up to ~95%. Moreover, the catalyst containing 10%MPS exhibited no obvious activity loss after six runs, demonstrating its good stability. (v) Au^0 was designed as the active site for the cyclohexane oxidation.

In a previous study, Wu *et al.* [223] employed VTES as functionalizing agent to prepare Au/SBA-15 catalysts by a one-pot method, using a TEOS:VTES molar ratio of 20, and HAuCl_4 solution as gold precursor. After stirring for 24 h at 40°C and hydrothermal treatment at 100°C for 24 h, the solid was filtered, washed and dried, prior to template removal by extraction with ethanol at 70°C for 6 h and reduction under H_2 at 250°C for 2 h. The resulting catalyst (Au loading of 1%wt) retained the ordered mesostructure of SBA-15, and the AuNPs (~5 nm) present as metallic Au^0 , were anchored and evenly dispersed in the functionalized SBA-15. The high activity and selectivity for the solvent-free selective oxidation of cyclohexane using this catalyst indicated that VTES may be a good functional group to prepare Au/MSM catalysts by direct synthesis. Moreover, the catalytic activity and selectivity of this catalyst was much better than the Au/SBA-15 catalyst prepared by post-grafting with the same functional group, whose average Au particle size was about 9 nm.

Glomm *et al.* [202] prepared Au/MCM-48, Au/SBA-15 and Au/SBA-16 materials by one-pot process using a gold-modified precursor (HAuCl_4 functionalized with TMPDA), which was added to the

synthesis solutions after precipitation of each MSM. The resulting gold-containing MSM were recovered after stirring for 24 h, and were subsequently filtered, washed and calcined in air at 550°C for 5 h. Although the catalytic activity was not evaluated, the following conclusions were highlighted from the characterization analysis: (i) This *in situ* method resulted in high retention of gold species in all MSM, indicating the important role of the amine functionalizing agent. (ii) The surface areas of the mesoporous SBA-15 and SBA-16 materials were significantly reduced after incorporation of gold, whereas the Au loading did not significantly affect the surface area of the MCM-48. (iii) The three MSM retained their long-range order upon incorporation of gold. (iv) AuNPs ranging between 5 to 20, 5 to 50 and 10 to 100 nm, were present on the synthesized materials supported on MCM-48, SBA-15 and SBA-16, respectively. (v) Even though a significant fraction of the particles was incorporated within the pores, the majority of AuNPs were found to reside on the external surface of the silica materials.

The feasibility of other MSM for retaining AuNPs using amine functionalizing agents has been also evaluated. For example, Lee *et al.* [287] prepared gold-containing HMS, MSU and PMOs materials by a co-synthesis sol-gel method, using HAuCl₄ as gold precursor, and TMPTA and TMPDA as bifunctional silane ligands for HMS and PMOs, and MSU materials, respectively. The structure-directing templates (DDA for HMS and PMOs, and Triton X-100 for MSU) were removed by ethanol extraction at room temperature for 6 h, and the Au(III) precursor was reduced to metallic AuNPs by heating in Ar/H₂ atmosphere (4% H₂), or by calcination. The resulting materials displayed AuNPs uniformly distributed inside the mesopores, with sizes smaller than 5 nm. Although the authors mentioned that this synthesis procedure may be used to prepare AuNPs supported on other mesoporous materials, except for those formed in acidic media due to the protonation of the amine functional groups, the catalytic activity of the synthesized materials was not reported.

Recently, we have used BTESPTS to synthesize active gold crystallites (3–14 nm) dispersed on mesoporous silica, which were mainly present in the metallic Au⁰ state, and displayed high catalytic activity (100% lactose conversion after 100 min reaction) and 100% selectivity towards lactobionic acid, when a catalyst containing 0.7% Au was used at a catalyst/lactose ratio of 0.2 under alkaline (pH 9.0) and mild reaction temperature (65°C) [11]. In general, as indicated by Wu *et al.* [279], during the synthesis procedure the thioether groups incorporated into the silica walls by co-condensation in the presence of the surfactant (P123), form a complex with the tetrachloroauric anions (AuCl₄⁻)

leading to a good dispersion of gold on the MSM. Under the hydrothermal treatment, part of AuCl_4^- —thioether complexes decomposed to form Au clusters stabilized by thioether groups. The subsequent calcination of the resulting solids at high temperature (500°C for 5 h) allows the removal of the template and functional groups, at the same time that gold species are reduced to AuNPs. This simple procedure has been also employed to immobilize gold within mesoporous silica thin films [285] and mesoporous silica [225, 279-283]. The resulting composite materials have shown high activity and selectivity in the oxidation of benzyl alcohol [280], *n*-hexadecane [225, 281] and cyclohexane [279], as well as in the plasma-assisted total oxidation of trichloroethylene [282-283]. However, the main drawback of this method lies to the fact that the structural ordering of the mesoporous material suffers from disturbance at high BTESPTS loading levels. Therefore catalysts show irregular shapes and pores. When using a BTESPTS molar concentration of about 7%, we found that gold catalysts with Au loading of 0.4, 0.5, 0.7, 0.8 and 1.0% presented a wormhole-like framework structure containing interconnected 3D-mesopores (Figure 1.14(g)), suitable for the minimization of diffusion limitation phenomena often encountered in adsorption and catalytic reactions [11]. Conversely, when the molar concentration of BTESPTS was decreased to 2%, ordered mesoporous silica was obtained, but the gold loading was significantly reduced, the size of AuNPs increased as illustrated in Figure 1.14(h), and the catalyst became inactive. These results were in agreement with the recent findings of Wu *et al.* [279] who reported that molar concentrations of BTESPTS higher than 2.5% led to a decrease in the regularity of the 2D hexagonal ordered structure of SBA-15, but lowering this concentration the AuNPs exhibited average sizes up to 24.4 nm.

The direct synthesis has been also carried out to synthesize bimetallic gold catalysts. Sobczak *et al.* prepared Au/MCM-41 [266] and Au/Nb-MCM-41 [267-268] catalysts (Au loading 1%wt) by co-precipitation, adding the gold precursor (HAuCl_4) into the gel containing the Si source (sodium silicate) and the template (CTACl) following the conventional method of synthesis of the MCM-41. The template was removed by calcination at 550°C for 2 h under He, and in air under static conditions for 14 h. The resulting gold catalysts exhibited hexagonally ordered mesopores and Au crystallites in the range of 3–18 nm. Moreover, this approach allowed the formation of gold in two forms: metallic and surrounded (bonded) by chloride. These chloride ions served as a catalytically active basic species in the acetonylacetone (AcAc) cyclization/dehydration in the gas phase, and took

part as promoters in the electron transfer to oxygen in the NO reduction with propene in presence of oxygen.

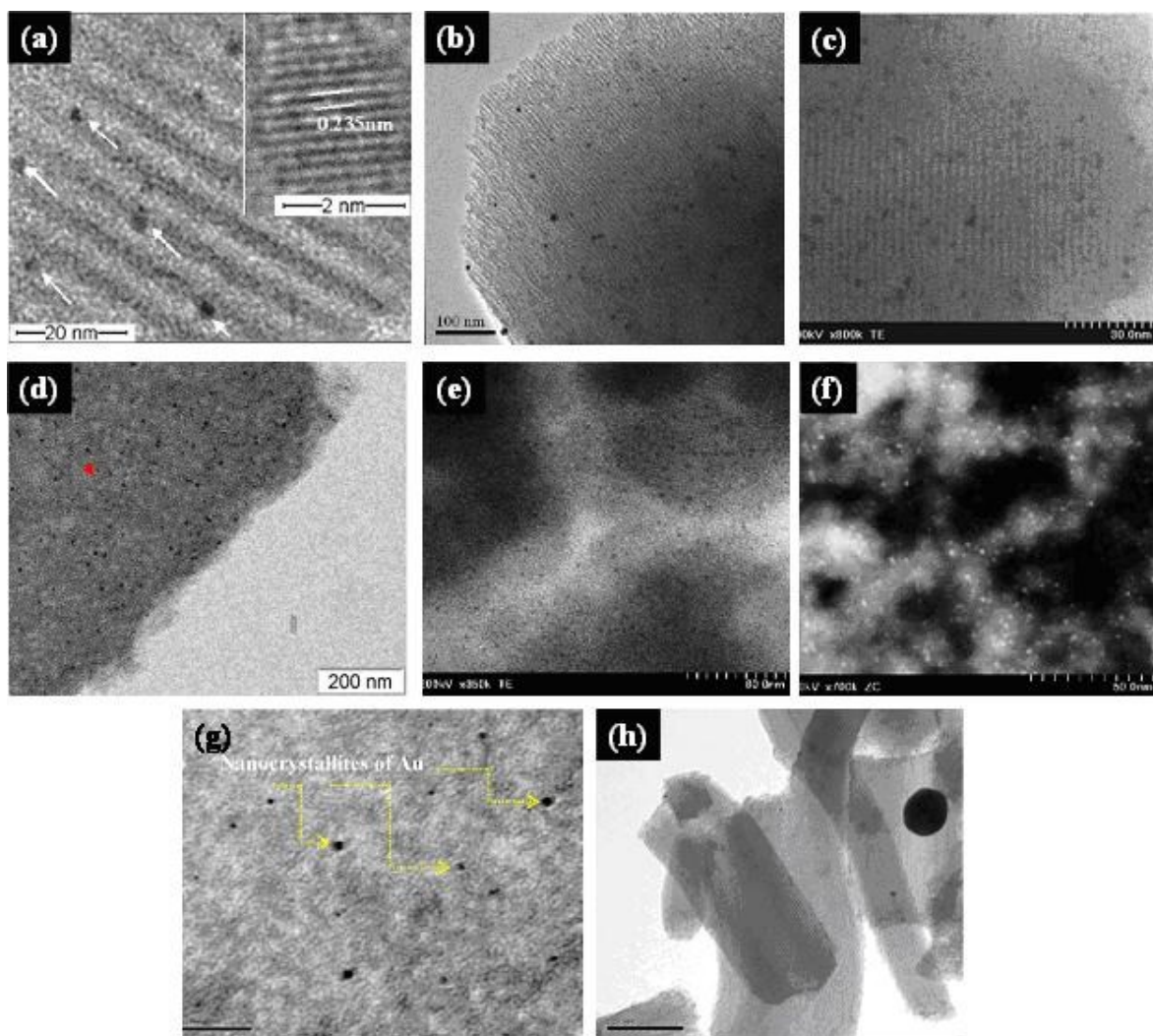


Figure 1.14. TEM images of gold catalysts supported on different MSM prepared by direct synthesis. (a) Au/SBA-15 using MPS (Reproduced by permission of Elsevier from Reference [277]); (b) Au/SBA-15 using VTES (Reproduced by permission of Elsevier from Reference [223]); (c) Au/MCM-41 using APTS (Reproduced by permission of ACS Publications from Reference [205]); (d) Au/MS using BTESPTS (Reproduced by permission of ACS Publications from Reference [281]); (e) Au/HMS using TMPTA (Reproduced by permission of Elsevier from Reference [287]); (f) Au/PMOs using TMPTA (Reproduced by permission of Elsevier from Reference [287]); (g) Au/MS using BTESPTS 7% molar concentration (Reproduced by permission of Elsevier from Reference [11]); (h) Au/MS using BTESPTS 2% molar concentration (TEM picture from our Laboratory, Université Laval, Quebec, Canada).

As discussed above, the direct synthesis provides a simple pathway to prepare stable Au/MSM catalysts using different functional moieties, which, as briefly mentioned by Ma *et al.* [200] can be employed to synthesize gold onto other mesoporous supports such as mesoporous TiO₂, for example. Although the gold loading and Au particle size are correlated with the amount of organic functional ligand, special care must be taken in order to find the optimal conditions of the ratio silica precursor/OFL to obtain ordered structures and well distributed small AuNPs.

1.3.3.4. Synthesis of Au/MSM using cationic gold complex [Au(en)₂]Cl₃ (en = ethylenediamine)

The synthesis procedures mentioned above normally imply the addition of organic functional ligands to incorporate the AuNPs within MSM, when tetrachloroauric acid is used as gold precursor. Although these approaches have allowed the preparation of active Au/MSM catalysts, the grafting of OFL may generate some defects on the mesoporous structure, and the ligands removal at high temperatures may conduce to a decrease in the catalytic activity because of the increase of the gold particle size.

In the early 50's, Block and Bailar [288] found that tetrachloroauric acid reacts with ethylenediamine (en) to form the gold complex [Au(en)₂]Cl₃ after precipitation with ethanol. This complex may act as acid by losing a proton from the coordinated amine group, under basic conditions. Based on this principle, the synthesis of Au/MSM catalysts becomes easier by deposition-precipitation of this gold complex, given that in alkaline media the negative-charged surface of the MSM can readily adsorb the [Au(en)₂]³⁺ cations, by deprotonation reaction of ethylenediamine ligands [289].

Dai and coworkers [206, 290] synthesized gold catalysts supported on mesoporous SBA-15 by mixing the support with an aqueous solution of [Au(en)₂]Cl₃ in alkaline media (pH range between 6.0 and 10.0). After agitation of the slurry for 2 h, the yellowish solid was filtrated, vacuum dried and reduced under H₂/Ar (4%) at 150°C for 1 h. This procedure led to obtain small (~4.9 nm) and uniform AuNPs confined within the SBA-15 mesopores. Moreover, when the pH increased up to ~10, the gold loading increased (2.70 to 9.08%wt) and the gold particle size decreased (from 5.4 to 4.9 nm). However, only the catalysts synthesized at pH value higher than 8 exhibited high catalytic activity for low-temperature CO oxidation (below 0°C), prior to their activation by calcination in air at 400°C for 1 h. From these results, it can be concluded that the pH of synthesis plays an important role on the catalyst activity, and that ethylenediamine moieties may form a strong bond with the surface of AuNPs, interfering with the catalytic activity. This work was a valuable reference for other groups for

synthesizing gold catalysts supported on mesoporous silicas, as presented in Table 1.8. For example, Guan and Hensen [291] prepared gold supported on different MSM (SBA-15, SBA-16 MCM-41) using this approach. After adding the supports to an aqueous solution of $[\text{Au}(\text{en})_2]\text{Cl}_3$, the pH was adjusted to a constant value of 12. The suspension was stirred for 2 h, followed by filtration, washing with deionized water, drying at 110°C overnight and calcination at 400°C for 4 h. The resulting catalysts, showing average Au particle sizes of 4.9 ± 1.3 , 7.3 ± 1.6 and 6.7 ± 2.1 nm for SBA-15, SBA-16 and MCM-41 materials, respectively, were active for ethanol oxidation. Parreira *et al.* [292] synthesized gold catalysts supported on pure and metal-modified hexagonal mesoporous silica (HMS, HMS-M, where M = Ce, Ti, Fe), using $[\text{Au}(\text{en})_2]\text{Cl}_3$ as gold precursor. The HMS and the metal-modified HMS, synthesized by direct synthesis via co-precipitation using appropriate metal salts, were mixed with an aqueous solution of $[\text{Au}(\text{en})_2]\text{Cl}_3$ maintaining the pH value at *ca.* 10. The catalysts were calcined at 300°C for 1.5 h, and subsequently reduced in hydrogen for 1.5 h. The resulting AuNPs with average Au particle sizes ranging between 4.1 and 5.9 nm were active for the aerobic oxidative esterification of benzyl alcohol, and displayed gold in metallic Au^0 and $\text{Au}^{\delta+}$ and Au^+ oxidation states. Recently, we have used $[\text{Au}(\text{en})_2]\text{Cl}_3$ to synthesize gold clusters supported on mesoporous silica decorated by ceria (SBA-15- CeO_2) [90, 293]. The support and the gold precursor were mixed in alkaline media (pH 10), and after vacuum filtration, the solid was thoroughly washed with deionized water, vacuum dried overnight at 100°C , and calcined at 500°C for 5 h. The resulting catalysts showed a regular array of mesopores, as well as well dispersed and not aggregated spherical AuNPs of about 5 nm. However, in agreement with the low-angle XRD analysis, the hexagonal order of the mesoporous SBA-15- CeO_2 support was somewhat affected after gold loading, as it can be depicted in Figure 1.15(d,e). The N_2 physisorption and XRD analysis revealed that support possess ordered hexagonal mesoporous structure, high surface area and large pore volume, similar to SBA-15, whereas BET surface area and pore volume of catalysts were significantly decreased upon impregnation. Moreover, XPS analysis revealed the coexistence of metallic and oxidized species on the catalyst, with relative surface concentrations of Au^0 (78.17%) > Au^+ (13.08%) > Au^{3+} (8.76%), and the presence of both Ce^{3+} and Ce^{4+} oxidation states. The catalytic activity of the synthesized catalysts was evaluated on the partial oxidation of lactose for selective synthesis of lactobionic acid (LBA) for therapeutic, pharmaceutical and food grade applications. After 100 min of reaction, the 0.7% Au/SBA-15- CeO_2 catalyst showed high catalytic activity (100% lactose conversion)

and a 100% selectivity towards LBA, when it was used at a catalyst/lactose ratio of 0.2 under alkaline (pH 9.0) and mild reaction temperature (65°C).

Table 1.8. Characteristics and catalytic applications of the Au/MSM catalysts synthesized using cationic gold complex $[\text{Au}(\text{en})_2]\text{Cl}_3$ (*en* = ethylenediamine).

Support	pH of synthesis	Au loading (%wt)	Au size (nm)	Catalytic application	Ref.
SBA-15	6.0	2.70	5.4	CO oxidation	[206, 290]
SBA-15	7.4	5.98	5.2	CO oxidation	[206, 290]
SBA-15	8.5	6.90	4.9	CO oxidation	[206, 290]
SBA-15	9.6	9.08	4.9	CO oxidation	[206, 290]
SBA-15	~10.0	2.20	2.0–8.0	CO oxidation	[206, 290]
SBA-15	12.0	2.00	4.9 ± 1.3	Ethanol oxidation	[291]
SBA-16	12.0	2.00	7.3 ± 1.6	Ethanol oxidation	[291]
MCM-41	12.0	2.00	6.7 ± 2.1	Ethanol oxidation	[291]
HMS	~10.0	2.19	5.4 ± 0.2		[292]
HMS-Ce	~10.0	2.94	5.9 ± 0.5	Aerobic oxidative esterification of benzyl alcohol	[292]
HMS-Ti	~10.0	2.96	4.8 ± 0.3		[292]
HMS-Fe	~10.0	2.87	4.1 ± 0.4		[292]
SBA-15-CeO ₂	10.0	0.7	~5.0	Lactose oxidation	[90, 293]

The use of the cationic gold complex $[\text{Au}(\text{en})_2]\text{Cl}_3$ as precursor for the synthesis of monometallic [290, 294-300] and bimetallic [301-304] gold catalysts supported amorphous SiO_2 , as well as for the preparation of Au/ SiO_2 -based catalysts [297], has demonstrated that amorphous silica can be also employed as a support to prepare active Au/ SiO_2 catalysts. Although this synthesis method has not been intensively investigated, it can be regarded as highly efficient for the preparation of gold catalysts supported on MSM. However, it should be noted that the $[\text{Au}(\text{en})_2]\text{Cl}_3$ precursor must be kept protected from light to prevent its decomposition [290, 294-300].

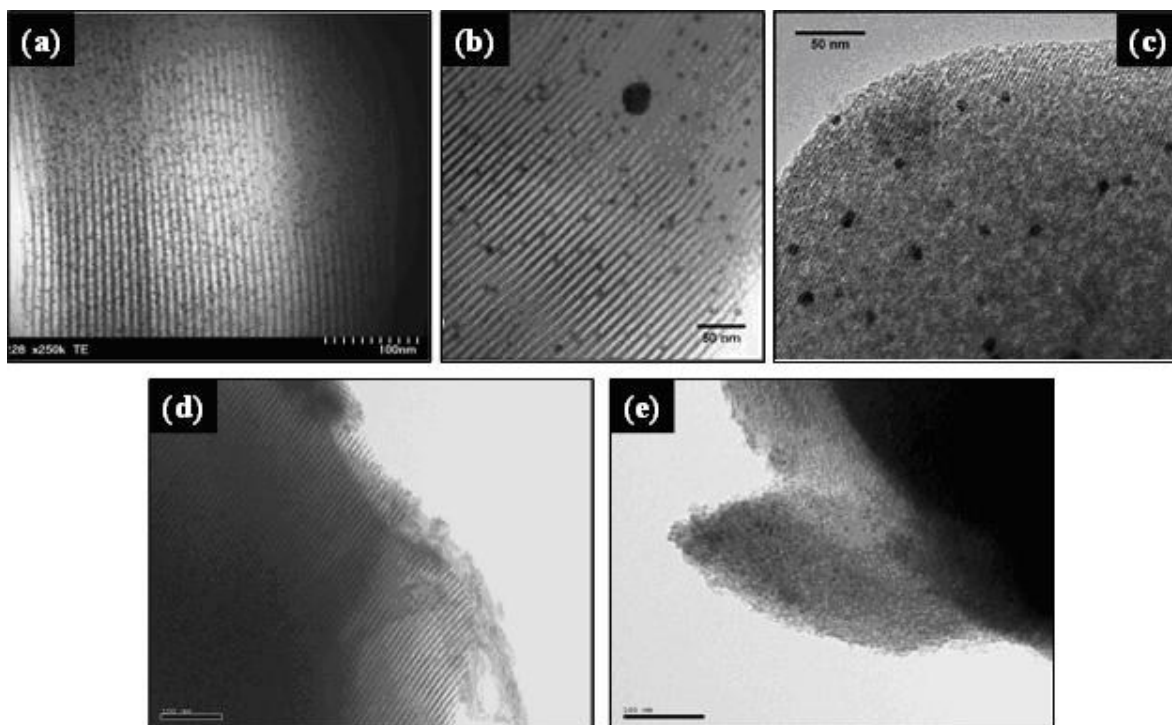


Figure 1.15. TEM micrographs of Au/MSM using $Au(en)_2Cl_3$ as gold precursor. (a) Au/SBA-15 (Reproduced by permission of ACS Publications from Reference [206]); (b) Au/SBA-15 (Reproduced by permission of Elsevier from Reference [291]); (c) Au/MCM-41 (Reproduced by permission of Elsevier from Reference [291]); (d) Mesoporous SBA-15-CeO₂ (Ce/Si molar ratio = 0.1) (Reproduced by permission of NAM 22, NACS from Reference [293]); (e) 0.7% Au/SBA-15-CeO₂ (Reproduced by permission of NAM 22, NACS from Reference [293]).

1.3.3.5. Chemical vapor deposition

Chemical vapor deposition of dimethyl gold acetylacetonate was first used by Okumura *et al.* [19, 207, 305-306] to deposit AuNPs on SiO₂ and MCM-41, demonstrating that silica may be a suitable support for the preparation of active gold catalysts. To do this, the supports were first evacuated in vacuum at 200°C for 4 h to remove the adsorbed water, and then treated with O₂ at 200°C for 30 min to remove organic residue from the surface by oxidation. Subsequently, the gold precursor was gradually evaporated at 33°C on the supports. The resulting materials were calcined in air for 4 h at high temperature (200–500°C) to decompose the gold precursor into metallic AuNPs on the support surface. The synthesized catalysts exhibited remarkably catalytic activities for the oxidation of CO and H₂, and showed a large number of gold particles smaller than 10 nm (mean diameters of 6.6 and 4.2 nm for SiO₂ and MCM-41, respectively), which were three times smaller than those of Au/SiO₂ prepared by impregnation method. From the characterization analysis, it was concluded that the interaction between the gold precursor and the support surface occurred mainly between the oxygen

atoms of Me₂Au(acac) and the OH groups of the SiO₂ surface; and that temperatures above 300°C are needed to prepare highly active Au catalysts following this preparation method.

Schimpf *et al.* [307] synthesized Au/SiO₂ (Au loading of 2.4%wt) by CVD of Me₂Au(acac), following the method proposed by Okumura *et al.* [308]. Highly dispersed AuNPs with mean value of 1.4 nm were obtained. Moreover, the synthesized catalysts were active for the low-temperature oxidation of CO. Araki *et al.* [309] prepared Au/FSM-16 by CVD of AuMe₂(HFA). The gold precursor was adsorbed on the support under reduced pressure at room temperature for 4 h. The resulting white powder turned to pale purple after UV irradiation under reduced pressure for 4 h, indicating the formation of metallic gold. The obtained Au nano-wires (2.5 × 17.1 nm) in the mesopores of FSM-16 were active in the oxidation of CO.

Notwithstanding the CVD allowed the synthesis of highly active Au/SiO₂ and Au/MSM catalysts, the main drawbacks of this preparation method relate to the high cost of the organometallic gold precursor, and to the requirements of special equipments for the catalysts synthesis. Moreover, the amount of metal that can be incorporated following this approach is limited by the pore volume of the support [209, 215].

1.3.3.6. Synthesis by dispersion of gold colloids or pre-synthesized AuNPs

Gold colloids and gold nanoparticles have been prepared by different procedures and used as precursors to prepare gold supported on TiO₂, ZnO, ZrO₂, Al₂O₃, carbon and SiO₂ materials [196, 310-318]. The synthesis of gold supported on MSM using gold colloids or pre-synthesized AuNPs can be achieved by using two different strategies: (i) dispersing the pre-synthesized gold precursors on the MSM support and (ii) synthesizing the MSM in the presence of pre-synthesized gold colloids or AuNPs. Even though suitable, this Au/MSM catalyst synthesis procedure has not been extensively applied in catalytic applications. The main advantage of this method lies to the easy control of AuNPs size throughout the gold sol synthesis, and therefore it offers the possibility to tailor the size of gold particles before their deposition on the support. This could be also attractive to control the AuNP aggregation, because the particle size is normally preserved during the immobilization step [311, 319]. Some relevant applications are presented below.

Ma *et al.* [320] recently reported the synthesis of gold catalysts supported on extra-large mesoporous silica material (EP-FDU-12), which were active and highly selective in the gas-phase oxidation of

benzyl alcohol to benzaldehyde. The EP-FDU-12 support was prepared using Pluronic F127 as template agent and TEOS as silica precursor, in the presence of 1,3,5-trimethylbenzene and KCl. After stirring at 15°C during 24 h, the mixture was hydrothermally treated for 24 h at temperatures ranging between 100 and 220°C. The solids were filtered and dried at room temperature, prior to the template removal by microwave digestion using 30% H₂O₂ and 15 M HNO₃. The Au catalysts (Au loading of 0.5%wt) were obtained by adding the EP-FDU-12 support to a chloroform solution of AuNPs, prepared from AuPPh₃Cl as described by Zheng *et al.* [321]. Subsequent to stirring, the solid product was centrifuged, dried in air and calcined at 350°C for 5 h. From this method of synthesis, it is interesting to pull out these two observations: (i) though the Au particle size was almost the same (11.3±2.7 nm vs. 10.3±2.7 nm) after reaction, carbon deposition was at least 10-fold less on catalysts with pore size of 36 nm than on those with pore size of 23 nm, suggesting that large pores facilitate the diffusion of organic products and therefore diminishing the coke formation; (ii) The pore size can be tuned by modifying the KCl:F127 concentration and the hydrothermal temperature, allowing different applications to these materials.

Tai *et al.* [322] prepared dodecanethiol-capped AuNPs following the method proposed by Brust *et al.* [323], which were adsorbed on a mesoporous silica wet-gel (size of mesopores of maximum 15 nm), synthesized by hydrolysis and subsequent condensation of TMOS in methanol using ammonia as catalyst. The gel was immersed in the AuNPs solution using different solvents (toluene, THF and toluene:THF 1:1). After sufficient contact (more than one day), supercritical CO₂ was used for drying the wet-gel gold containing silica. In the resulting material, the Au particle size distribution was almost identical to that of the original dodecanethiol-capped AuNPs (average 2.4 nm vs. average 2.6 nm, respectively). Moreover, AuNPs were homogeneously distributed in the gel formed in THF, whereas when using toluene the AuNPs were present only in the peripheral part of the gel, indicating that the spatial distribution of the AuNPs inside the gels can be controlled by changing the polarity of the solvents. Nevertheless, the catalytic activity of this composite aerogel was not evaluated. A similar method for synthesizing mesoporous colloidal gold aerogels, using AuNPs (sized at either 5 to 28 nm) prepared by citrate reduction of HAuCl₄ has been reported by Anderson *et al.* [324], but the catalytic behavior was not evaluated.

Glomm *et al.* [202] used citrate-coated AuNPs of 5 and 10 nm for the synthesis of Au/MCM-48, Au/SBA-15 and Au/SBA-16. To do this, the as-synthesized silica supports were first suspended in

water, followed by pH adjustment to 9.0 using 2 M NaOH. Then, the AuNPs were added, and after 24 h stirring at room temperature, the gold-containing materials were filtrated, washed, dried and calcined at 550°C in air during 5 h. Although the three mesoporous structures retained their long-range order upon incorporation of AuNPs, their surface area was significantly reduced after Au loading. Moreover, most of the AuNPs were found on the external surface of the silica materials, regardless a significant fraction of the particles was incorporated within the pores. Unfortunately, no data of catalytic activity of these materials were reported.

The second strategy to prepare Au/MSM using gold colloids or presynthesized AuNPs involves mainly two steps: the synthesis of AuNPs in the presence of a block copolymer, and the synthesis of the MSM using the gold-nanoparticle copolymer unit as template [46]. Notwithstanding the catalytic activity was not evaluated, from the interesting works of the Somorjai group [208-209, 325], who have used this approach to encapsulate AuNPs of different sizes (2, 5, 10 and 20 nm) into the channels of SBA-15, MCM-41 and MCM 48 using P123, hexadecylamine and cetylbenzyltrimethylammonium chloride as templates, respectively, it can be highlighted that: (i) the presence of small Au nanocrystals (2–10 nm) influences only slightly the well-ordered structure but changes the lattice spacing of the MSM; (ii) although the mesopore channels of the MSM expand when small AuNPs are included, the narrow pore size distribution is preserved; (iii) when high amounts of AuNPs or large AuNPs (20 nm) are used, the structure of the materials remains porous, but their crystallinity decreases and a worm like structure appears, instead the hexagonal arrangement; (iv) after calcination, the small AuNPs are incorporated within the channels of the mesoporous host matrixes, but nanoparticles whose diameter is larger than the MSM pore size (20 nm for SBA-15 and 10 nm for MCM-41 and MCM-48), cannot be inserted and they remain exclusively outside of the channels; (v) when using bimodal AuNPs (2 and 5 nm, or 2 and 10 nm), the resultant pore size of the SBA-15 material is controlled by the larger size of nanoparticles; (vi) the AuNPs incorporated inside the pores are accessible to reactant molecules, as confirmed by XANES used in combination with the adsorption of thiols.

Lin *et al.* [326] prepared AuNPs by mixing H₂AuCl₄ aqueous solution with CTABr, followed by chemical reduction with aqueous NaBH₄. The silica precursors (sodium silicate and sodium aluminates) were added into the Au-surfactant solution, and after neutralization (pH value of the gel solution ~8–10), the gel solution was hydrothermally treated at 100°C for 2 days. The solids were

then filtrated, washed, dried and calcined at 560°C. The resulting catalysts with Au loadings of 4 to 12%wt, showing less ordered pore structure than pure MCM-41, and the AuNPs sized between 5 and 15 nm displayed relatively low reactivity (less than 16% conversion) in CO oxidation, probably due to the large size of Au nanoparticles.

Employing the conventional conditions for the synthesis of MCM-41, Aprile *et al.* [327] prepared Au/meso-SiO₂ catalysts using colloidal AuNPs (2–5 nm) stabilized with a quaternary ammonium ion ligand having at one end a long alkyl chain (*N*-[3-(triethoxysilyl)propyl] O-2(dicetylmethylammonium)ethyl urethane) and TEOS as gold and silica precursors, respectively, in the presence of CTABr as structure directing agent. The resulting catalysts, calcined at 500°C for 5 h, were active for the oxidation of primary and secondary alcohols (3,4-dimethoxybenzyl alcohol and 1-phenylethanol) at atmospheric pressure. Moreover, these catalysts showed higher activity than those prepared by IWI of the tetraoctylammonium stabilized colloidal AuNPs in a pre-formed SBA-15. However, in aqueous media, the Au/meso-SiO₂ catalysts were completely deactivated by collapse of the mesoporous structure.

The encapsulation of metal nanoparticles (Au and Ag) during the growth of an organic-inorganic hybrid gel was recently reported by Wichner *et al.* [328], using phenylethylthiol-coated metal nanoparticles dissolved in THF, which were added to a sol-gel mixture of phenyltriethoxysilane, water and THF in acidic media (pH 1.2). The suspension was stirred for 1 h, and then TMOS was added. After 3 h, the pH was increased with NH₃(aq) to 6.0–7.0 to accelerate the condensation. Once the gelation was complete, the organic components were removed by calcination at 600°C in air for 6 h. When the synthesis pH value was raised to 7.0 mesopores were formed with mesopore diameter of about 3.5 nm, whereas at lower pH values the gel matrices were microporous. The resulting catalysts with average diameter of metal particles of 6 nm were catalytically active in CO oxidation, although relatively high activation temperatures of at least 330°C were needed.

Ferrara *et al.* [329] synthesized mesoporous silica films doped with gold, by the dispersion of stable AuNPs (8–9 nm) functionalized by dodecanethiol chains in an acid-catalyzed sol-gel silica solution. Even though the size, shape and crystalline domains of the AuNPs remain unchanged during the synthesis process, the catalytic activity was not evaluated. Cheng *et al.* [330] prepared mesoporous gold-silica nanocomposites (Au loading from 6.9 to 11.4%wt) using a simple one-step method involving the sol-gel reaction of the silica precursor (TEOS) with a gold sol (Liquid Bright Gold 5154,

containing 5%wt metallo-organic gold compound in cyclohexanone) in the presence of DBTA as a nonsurfactant template. After removal of DBTA by calcination at 550°C during 16 h, the mesoporous worm-hole-like structure of the gold-silica nanocomposites, with AuNPs ranging between 2 and 8 nm dispersed throughout the silica porous matrix, showed high surface area (up to 630 m²/g), large pore volume (~0.5 cm³/g) and pore diameters of 3–5 nm with relatively narrow pore size distributions. However, the catalytic activity of this material was not reported.

Bönnemann *et al.* [331] prepared monometallic Au and bimetallic Au-Pd catalyst by embedding pre-synthesized tetraalkylammonium bromide-stabilized Au and Pd-Au alloy particles in a solid silica matrix, following a modified sol-gel process. The colloidal Au and Pd-Au particles were prepared by the co-reduction of Pd and Au salts (palladium acetate and gold chloride) with tetraoctylammonium triethylhydroborate in dry THF under argon at ambient temperature during 16 h. After solvent removal by evaporation under vacuum, the surfactant was removed by dipping the colloidal powder in diethyl ether followed by precipitation with an ethanol/methanol mixture. The embedding of the resulting Au and Pd-Au colloids was carried out in THF using TEOS as silica precursor. The sol was stirred at 70°C under reflux until the gelification was complete (2 days). The resulting gel was dried at 110°C, calcined in air at 450°C, and subsequently reduced in H₂ at 450°C. The resulting materials showed mesoporous structure with a sharp pore diameter distribution and channels randomly distributed and no tubes. Particle sizes ranging between 3.0 and 4.9 nm for both Au and Pd-Au catalysts were observed. The monometallic Au catalyst displayed very low activity in the selective semi-hydrogenation of 3-hexyn-1-ol, whereas the bimetallic Au-Pd catalyst exhibited high activity and was remarkably resistant to deactivation. Some years later, Parvulescu *et al.* [332] evaluated the catalytic activity of the before mentioned catalysts in the selective hydrogenation of 3-hexyn-1-ol, cinnamaldehyde, and styrene. Their results showed that alloying Pd with Au in bimetallic colloids led to enhanced activity and improved selectivity. Moreover, the bimetallic Au-Pd catalysts were very stable against poisoning, as was evidenced for the hydrogenation of styrene in the presence of thiophene.

Liu *et al.* [333] prepared Au-Ag alloy particles (<10 nm) supported on mesoporous MCM-41 which were synthesized by one-pot approach using CTABr both as a stabilizing agent for AuNPs and as a template for assembling the MCM-41 structure. After template removal by calcination at 560°C and subsequent reduction at 600°C with 10% H₂/N₂ the alloy nanoparticles were uniformly dispersed on

the silica support, but their size was enlarged (>30 nm). Moreover, the increase of Ag concentration led to a bigger size of the alloy particles, suggesting that the presence of Ag provokes the aggregation more severely, because of the Ag lower melting point. Besides, mesoporous silica particles were very disordered. However, the bimetallic Au-Ag/MCM-41 catalysts (Au/Ag molar ratios of 3/1, 5/1 and 10/1) were active for CO oxidation at 25°C, while pure Ag/MCM-41 did not exhibit any catalytic activity, and Au/MCM-41 catalyst only had a low CO conversion. These results indicate that the size of bimetallic Au-Ag nanoparticles is not a critical factor in the CO conversion.

1.3.3.7. Deposition-precipitation

As mentioned above (Section 1.3.3), the deposition-precipitation method requires the pH adjustment of the gold precursor solution to high values in order to generate $[\text{Au}(\text{OH})_n\text{Cl}_{4-n}]^-$ species with little chloride as possible. However, under alkaline conditions the surface of the MSM becomes negatively charged and the interaction between the gold and the silica surface is very weak, hindering the gold adsorption and facilitating the mobility and sintering of AuNPs [19, 186]. For this reason, it has been reported that DP is not a suitable method for the incorporation of gold on silica materials, and other strategies have been attempted, as it was described in the preceding sections. However, some gold catalysts supported on MSM have been synthesized using this approach, as summarized in Table 1.9. For example, Hereijgers and Weckhuysen [334] prepared Au/SBA-15 by DP from a dilute solution of HAuCl_4 in HCl at pH of 9.5 using ammonia solution. After calcination, AuNPs with average value of 4.0 nm were obtained, but the structure of the SBA-15 support was slightly damaged because of the high pH effect. This catalyst did not show good catalytic performance in the selective oxidation of cyclohexane to cyclohexanone. Ma *et al.* [220] synthesized monometallic Au/SBA-15 and bimetallic Au-Pd/SBA-15 by DP using chloroauric acid solution and 1 M NaOH solution for adjusting the solution pH to 7.0. After adding the SBA-15 support, the slurry was aged at room temperature for 12 h, followed by washing, drying at 70°C for 5 h and calcination at 200°C for 2 h. The surface area and the pore size of the resulting catalysts were reduced two folds, in comparison with the SBA-15 support, but the pore volume and the adsorption isotherms of both catalysts were almost identical to those of SBA-15. Moreover, the Au/SBA-15 catalyst showed well-developed parallel pore channels with well dispersed AuNPs (in the range of 10–50 nm) on the intra-surface of SBA-15, as illustrated in Figure 1.16(c), while the Au-Pd nanoparticles dispersed better compared to Au/SBA-15 catalyst but did not enter into the channels of SBA-15 as depicted in Figure 1.16 (d). Albeit both catalysts were active for the oxidation of benzyl alcohol, the Au-Pd/SBA-15 was more active than the Au/SBA-15,

but its selectivity towards benzaldehyde was slightly smaller (99 vs. 96%). However, in comparison with bimetallic Au-Pd/SBA-15 catalysts prepared by post-grafting modification of SBA-15 with MPS and APTS, the activity of the bimetallic catalysts synthesized by DP was smaller and decreased with time, indicating that the interaction between Au-Pd nanoparticles could be weaker when using the DP method. Zhou *et al.* [232] synthesized Au/SBA-15 by DP using HAuCl₄ aqueous solution whose pH was adjusted to 7.0. After filtration, washing, freeze-drying and calcination in air at 200°C for 4 h, the pink colored catalyst conserved the 2D hexagonal ordered structure of the SBA-15, but most of the AuNPs (average size ranging between 10 to 15 nm) formed spherical aggregates outside the channels of SBA-15, as it can be depicted in Figure 1.16(a). Li *et al.* [224] prepared Au/MCM-41 (Au loading 1%wt) by pouring the as-synthesized support into a HAuCl₄ solution. After mixing the slurry for 24 h at 80°C, the solids were filtered, washed repeatedly in cycles of water and ethanol, and dried at room temperature. Then, the template was removed by refluxing the solid in HCl/EtOH solution at 78°C for 24 h. The resulting material was reduced in a flow of 5% H₂/Ar at 200°C for 4 h. This catalyst displayed poor dispersion of AuNPs (particle size approximately in the range of 60–100 nm), which were located on the external surface of the MCM-41 support. Moreover, the catalyst showed low activity for the cyclohexane oxidation. Under comparable reaction conditions, cyclohexane conversion was less than that obtained with the 1%Au/SBA-15 catalysts prepared by post-grafting of the SBA-15 support with APS (<1% vs. 15.5%). Liu *et al.* [335] synthesized Au/SBA-15 by DP, by the addition of the SBA-15 support to an aqueous solution of HAuCl₄ whose pH was adjusted to 10 by adding ammonia solution. After stirring for 2 h at room temperature, the water was evaporated, and the sample was freeze dried for more than 24 h, and finally the solids were calcined at 200°C for 2 h in vacuum. The resulting catalyst, with AuNPs of about 10 nm, was active for the oxidation of benzyl alcohol.

Mokhonoana *et al.* [272] incorporated AuNPs into MCM-41, using ethylenediamine which served as both a base and complexing agent for the Au(III) species, through a modified DP method. An aqueous solution of HAuCl₄ was mixed separately with both the as-synthesized MCM-41 (still containing CTABr) and the calcined MCM-41 for 1 h, and then the pH was adjusted to 10 using 1M ethylenediamine solution. The slurry was stirred at room temperature for 13 h, and the recovered solids were washed with warm water to remove the chloride ions, dried and calcined at 500°C during 12 h (for the as-synthesized MCM-41) or 400°C during 4 h (for the calcined MCM-41). The resulting catalysts (4 and 5% nominal Au loading, respectively), containing average AuNPs of 12 and 10 nm,

respectively, retained the ordered structure and high surface area of the MCM-41 material. However, upon calcination at 500°C, the AuNPs aggregated and migrated to the surface. Nevertheless, both catalysts were active in the CO oxidation at $T > 250^\circ\text{C}$.

Table 1.9. Characteristics and catalytic applications of the Au/MSM catalysts synthesized by deposition-precipitation.

Support	pH of synthesis	Au Precursor	Au loading (%wt)	AuNP size (nm)	Catalytic application	Ref.
SBA-15	9.5	HAuCl ₄	1.0	2.0–12.0	Cyclohexane oxidation	[334]
SBA-15	7.0	HAuCl ₄	4.0	10.0–50.0	Benzyl alcohol Oxidation	[220]
SBA-15	7.0	HAuCl ₄ Pd(NO ₃) ₂	4.0 0.5	-		[220]
SBA-15	7.0	HAuCl ₄	0.39	10.0–15.0	-	[232]
SBA-15	-	HAuCl ₄	2.0	4.0–9.0	Ethylacetate combustion	[336]
SBA-15	-	HAuCl ₄ Fe(NO ₃) ₃	2.0 12.0	-		[336]
SBA-15	10.0	HAuCl ₄	0.16–0.20	-	Benzyl alcohol Oxidation	[335]
MCM-41	-	HAuCl ₄	1.0	60.0–100.0	Cyclohexane oxidation	[224]
MCM-41	10.0	HAuCl ₄	5.0	9.0–13.0	CO oxidation	[272]
MCM-41	10.0 *	HAuCl ₄	3.7	11.0–15.0	CO oxidation	[272]
MCM-41	6.4	HAuCl ₄	1.312	2.0–3.0	-	[269]
HMM-2	11.7	HAuCl ₄	2.0	3.2 ± 0.5	-	[337]

* pH adjusted using ethylenediamine.

Au/HMM-2 (Au 2%wt) was prepared by DP of HAuCl₄ aqueous solution in alkaline conditions (pH 11.7) and the resulting solid sample was reduced under H₂ at 200°C for 2 h [337]. The obtained purple powder with homogeneously dispersed AuNPs (mean diameter of 3.2 ± 0.5 nm) retained the 3D-hexagonal structure of the HMM-2 after gold loading. However, the catalytic activity of this material was not evaluated.

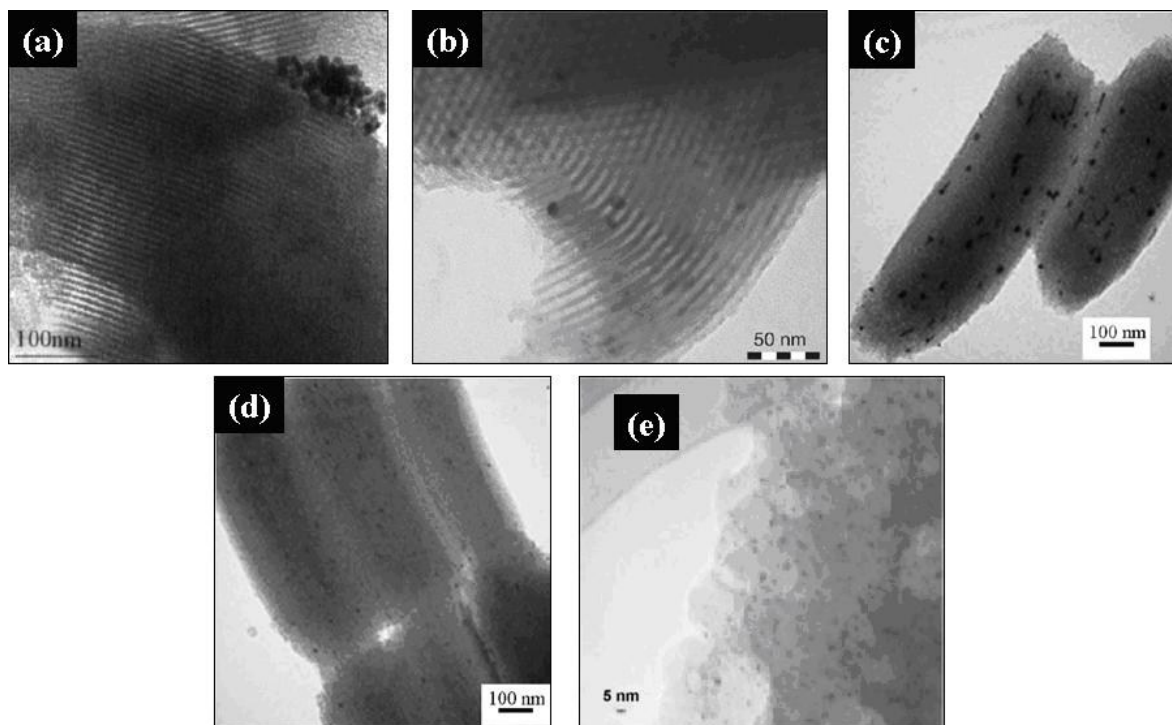


Figure 1.16. TEM micrographs of Au/MSM prepared by deposition-precipitation. (a) Au/SBA-15 (Reproduced by permission of Elsevier from Reference [232]); (b) Au/SBA-15 (Reproduced by permission of Elsevier from Reference [336]); (c) Au/SBA-15 (Reproduced by permission of Elsevier from Reference [220]); (d) Au/SBA-15 (Reproduced by permission of Elsevier from Reference [220]); (e) Au/HMM-2 (Reproduced by permission of RSC Publishing from Reference [337]).

1.3.3.8. Incipient wetness impregnation

Incipient wetness impregnation with HAuCl_4 solution has been considered as an inappropriate method for the synthesis of gold catalysts because it yields larger AuNPs (>30 nm), and for the reason that the residual chloride present on the surface may poison the active sites of the catalysts [182, 186, 198, 200]. To circumvent this problem, Delannoy *et al.* [338] proposed a modified IWI method for the synthesis of gold catalysts supported on different oxides, including silica, involving a washing step with ammonia 1M or with ammonium chloride 0.25 M, followed by calcination at high temperature (300°C). The ammonia washing removes the chloride ligands responsible for the aggregation of AuNPs, and leads to the formation of an amino-hydroxo-aquo cationic gold complex $[\text{Au}(\text{NH}_3)_2(\text{H}_2\text{O})_{2-x}(\text{OH})_x]^{(3-x)+}$, which interacts with the support surface either electrostatically or through grafting, preventing the gold leaching. Moreover, during calcinations, small AuNPs are formed. Nevertheless, this method has been hardly exploited for the Au/MSM catalyst formulation. On the other hand, it is important to underline that after the washing step with ammonia, some

fulminating gold can be formed, and since it violently decomposes around 210°C, a drying pretreatment must be introduced before calcination [339].

Gold catalysts supported on MCM-41 (Au loading of 1%wt) were prepared by Grams and Sobczak [266-267] by IWI of the support with HAuCl₄. After mixing, the solids were dried at 100°C for 5 h followed by calcination in air at 550°C for 3 h. The resulting catalysts exhibited hexagonally ordered mesopores, as well as surface area, pore diameter and pore volume almost identical to the pristine MCM-41 support. However, the metallic AuNPs showed lower dispersion in comparison to the same catalysts prepared by co-precipitation in the presence of CTACl, and displayed diverse dimensions and shapes, making the estimation of their size difficult to carry out. Moreover, it was found that the presence of chloride ions in the surrounding of gold centers was approximately one order of magnitude lower for the catalysts synthesized by IWI than for those prepared by co-precipitation. This was attributed to the interaction of the gold precursor with the CTACl, leading to the formation of Au-Cl species incorporated into the walls of the MCM-41 material. Although both catalysts showed similar activity in the acetylacetone (AcAc) cyclization (35 vs. 38% conversion), the selectivity towards methylcyclopentenone was higher for the catalysts prepared by co-precipitation, which was attributed to the presence of the chloride ions.

Liu *et al.* [335] prepared Au/SBA-15 by impregnation of the support with an aqueous solution of HAuCl₄. The slurry was stirred for 2 h at room temperature, and after evaporating water; the solids were dried for more than 24 h using a freeze drier, and then calcined under vacuum at 200°C for 2 h. The resulting catalyst containing AuNPs of about 10 nm was active for the oxidation of benzyl alcohol, but its activity was slightly lower than that obtained with the Au/SBA-15 synthesized by deposition-precipitation, which displayed similar AuNPs size.

Araki *et al.* [309] impregnated FSM-16 with HAuCl₄ in aqueous solutions at various pH values (5, 7 and 10). The FSM-16 was added to the HAuCl₄ solution, and the mixture was stirred at room temperature for 24 h. After evaporation and washing with water, the Au³⁺/FSM-16 (Au loading of 2.5%wt) samples were reduced with H₂ at 400°C for 2 h or by photo-reduction by irradiation with UV light for 24 h after exposition to water vapor (20 Torr) for 2 h and then to methanol vapor (100 Torr) for 2 h. After reduction in H₂, the samples impregnated at pH 5 gave a mixture of Au nano-wires (mean diameter of 2.5 nm and a mean length of 18.1 nm) and nanoparticles (10 nm). However, only AuNPs (mean diameter of 19.2 nm) were obtained on the external surface of the FSM-16 support,

when UV was used. Moreover, as the pH value increased, only small AuNPs were formed, for both reduction methods. For example, after reduction in H₂, the samples impregnated at pH 10 gave homogeneously dispersed AuNPs in the mesopores with mean diameter of 1.7 nm, whereas the photoreduction of the samples prepared at pH 10 gave AuNPs with a mean diameter of 2.5 nm in the mesopores. Although these AuNPs showed high catalytic activity in the CO oxidation reaction, the rate constant of the Au/FSM-16 synthesized at pH 10 was 40–80 times higher than those of other Au/FSM-16 catalysts, because of the high dispersion of small AuNPs.

The IWI method was used recently by Wu *et al.* [223] to prepare gold catalysts supported on SBA-15 and organically functionalized SBA-15 with VTES. The supports were dispersed in HAuCl₄ solution after stirring for 2 h at room temperature; the slurries were sonicated for 20 min. The resulting products were then evaporated, dried at 60°C for 48 h, and reduced under H₂ at 250°C for 2 h. From the characterization analysis it was found that: (i) the structure of the catalyst prepared with the functionalized SBA-15 collapsed during the impregnation process, while the catalyst synthesized using the unmodified SBA-15 as support exhibited the small-angle XRD profile typical of the well ordered mesostructures; (ii) the XPS analysis revealed that both catalysts presented AuNPs as metallic gold (Au⁰); (iii) the average diameters of the AuNPs were 8 and 9 nm for the catalysts synthesized using the unmodified and the functionalized SBA-15, respectively. These AuNPs were larger than those present on the catalysts prepared by one-pot synthesis process (~5 nm), indicating that during the direct synthesis, the VTES led to the evenly dispersion of the AuNPs in the mesoporous silica support; (iv) both catalysts displayed almost the same activity and selectivity in the oxidation of cyclohexane, with a conversion of about 8% after 2 h of reaction. However, this activity was practically doubled when the catalyst prepared by one-pot synthesis process was used, due to the presence of smaller AuNPs.

Metallic AuNPs uniformly dispersed inside the pores of monolithic porous silica with average diameter of about 4 nm were obtained by Shi *et al.* [340] and Cai *et al.* [341] after more than two weeks of soaking the mesoporous support into HAuCl₄ solution (0.03–0.05 M) at room temperature, followed by reduction in H₂ at 700°C for 1 h. However, the catalytic activity of this material was not evaluated.

Tsung *et al.* [342] incorporated AuNPs with diameters in the range of 5–25 nm within the mesoporous silica nanofibers, by impregnation overnight with HAuCl₄ and subsequent reduction with H₂ at

temperatures ranging between 55 and 100°C. In this procedure, dichloromethane was added before the reduction step, to induce the gold precursor adsorbed on the outer surfaces of the nanofibers to move into the pore channels. However, no catalytic activity was reported.

Lotz and Fröba [343] incorporated AuNPs into the mesopores of SBA-15 using the cluster compound $\text{Au}_{55}(\text{PPh}_3)_{12}\text{Cl}_6$ (diameter of 2.1 nm) as gold precursor. The cluster was dissolved in dichloromethane. After addition of the SBA-15 support, the slurry was stirred for 30 min at room temperature, the solvent was evaporated and the solids were dried under vacuum, followed by annealing in air at 150–250°C. The resulting material retained the structure of the SBA-15, and the Au_{55} clusters decomposed to metallic gold within the pores by annealing. However, the catalytic activity was not given.

AuNPs (2.5 ± 0.3 nm) closely packed in the mesopores of MCM-41-type mesoporous silica films were prepared by impregnation with HAuCl_4 by Fukuoka *et al.* [337, 344]. The silica materials were immersed in aqueous solution of HAuCl_4 . The mixtures were irradiated with ultrasonic wave for 30 s under reduced pressure, and the samples were left in the solution for additional 24 h. After washing with deionized water and drying under vacuum for 24 h, the resulting solids were reduced by H_2 at 400°C for 2 h or by UV-visible irradiation. With both reduction methods, the samples retained the structure of the original supports. However, the catalytic activity of these materials was not investigated.

The IWI method has been also employed for the synthesis of bimetallic Au catalysts. For example, Venezia *et al.* [345] prepared bimetallic AuPd/HMS catalyst by co-impregnating the HMS support with aqueous solutions of the two metal chlorides, PdCl_2 and AuCl_3 , followed by a drying step at 120°C and calcination at 400°C for 2 h. The resulting catalysts, containing PdO nanoparticles (7 nm) and large AuNPs (18 nm), were active for methane oxidation. Li *et al.* [346] dispersed bimetallic Au-Pd nanoparticles within monolithic mesoporous silica by immersion of the silica host into HAuCl_4 solution at room temperature. After soaking for two weeks, the samples were annealed in $\text{N}_2\text{-H}_2$ mixed gas at 500°C for 2 h to reduce gold ions and form AuNPs within the pores of the silica host. The Au/silica samples were then immersed into a PdCl_2 solution at room temperature for two weeks, and subsequently they were taken out and washed with deionized water, before annealing in the $\text{N}_2\text{-H}_2$ mixed gas starting at 500°C for 1 h. With this method, an assembly of $\text{Au}_{\text{core}}\text{Pd}_{\text{shell}}$ nanoparticles into

monolithic mesoporous silica was obtained, with an Au_{core} of about 4 nm. However, the catalytic activity of this material was not reported.

Tsoncheva *et al.* [336] used $H AuCl_4$ and $AuCl(PPh_3)$, and Fe_2O_3 as gold and iron precursors, respectively, to synthesize Au/SBA-15 and AuFe/SBA-15 materials. After impregnation of the support with the gold and iron precursors, the solids were calcined in air at 200–400°C for 2 h, and the resulting solids contained 2% Au and 12% Fe. From the analysis performed in this work, it was pointed out that: (i) The monometallic Au materials showed similar surface area than the pristine SBA-15, but the surface area of the bimetallic materials was reduced about 50% after the metals loading. A similar tendency was observed for the total pore volume of the synthesized materials; (ii) The low angle XRD patterns of the SBA-15-based materials were typical for SBA-15 structure and no substantial changes were observed after the modification with Au and Fe; (iii) The temperature of calcination had a significant effect on the AuNPs size. A broad size distribution of the AuNPs (small, about 6–9 nm and larger ones, 20–50 nm) was observed after calcination 200°C, whereas predominantly larger particles (50–70 nm) were found after calcination at higher temperatures (300–400°C). On the other hand, no reflections of Fe_2O_3 crystalline phase were observed by XRD analysis, indicating the formation of highly dispersed iron oxide phase; (iv) The monometallic and bimetallic catalysts were active for the ethylacetate combustion. However, the catalytic activity of monometallic catalysts was higher when $AuCl(PPh_3)$ was used as gold precursor, whereas the catalytic activity of bimetallic catalysts was higher when $H AuCl_4$ was used as gold precursor. Unfortunately, neither the role of the different gold precursors nor the comparison of the catalytic activity of monometallic and bimetallic catalysts was discussed.

1.3.3.9. SiO₂-based gold catalysts

Another strategy to incorporate AuNPs into mesoporous silica is to modify the SiO_2 materials with inorganic additives and synthesize SiO_2 -based gold catalysts. This approach allows the increase of the isoelectric point of the support, which facilitates the deposition of the $Au(OH)_xCl_{4-x}^-$ species under alkaline conditions required for DP method. At the same time, the sintering is minimized by the separation of AuNPs from one another. Moreover, when adding inorganic additives, such as metal “active” oxides for example, they can also work as co-catalysts taking part in the reaction [347]. Furthermore, the “active” oxides may be responsible of the electronic interactions and structural defects, factors that could represent the key issues in the formation and stabilization of small AuNPs,

which may enhance the catalysts activity [348]. Therefore, silica-based materials have been largely employed as supports for AuNPs, as summarized in Table 1.10. In Figure 1.17 the distribution of AuNPs on different mesoporous SiO₂-based supports is depicted, while some synthesis procedures and catalytic applications are briefly discussed below.

In the late of 90, the Haruta's group initiated the investigation of the catalytic activity of gold deposited on titanium-containing mesoporous MCM-41 and MCM-48 materials, for the partial oxidation of propylene to propylene oxide, in the presence of oxygen and hydrogen [349-361]. They prepared Ti-doped MCM-41 and MCM-48 by means of a sol-gel process using tetrabutylorthotitanate [Ti(OC₄H₉)₄] as titanium source, and then gold (4–12%wt) was loaded on these supports by DP (T = 70°C, pH = 6.5–7.0) or by liquid grafting methods using HAuCl₄ or (CH₃)₂Au(O₂C₅H₇) as gold precursors, respectively. After calcination at 300°C for 4 h, AuNPs with diameters ranging between 2.0 and 5.0 nm, were homogeneously dispersed on the Ti-modified MCM supports. Although these catalysts showed low propylene conversion (~5%), their selectivity towards propylene oxide was very high (>90%). Moreover, Au/Ti-MCM-48 catalysts showed better performance in comparison with the Au/Ti-MCM-41 catalyst, due to the three-dimensional pore system of the MCM-48 material. On the other hand, it was pointed out that under the same reaction conditions, catalysts with the same gold loading on pure MCM silica, and samples of Ti-MCM without gold loading were catalytically inactive, indicating the existence of synergetic effects between gold and titanium in these catalysts.

Table 1.10. Characteristics and catalytic applications of the mesoporous SiO₂-based gold catalysts.

Support	pH of synthesis	Au Precursor	Au loading (%wt)	AuNP size (nm)	Catalytic application	Ref.
Ti-MCM-41	7.0	HAuCl ₄ ^a	-	2.8 ± 1.0	CO oxidation	[216]
Co-MCM-41 ⁱ	7.0	HAuCl ₄ ^a	-	3.9 ± 0.8	CO oxidation	[216]
Al-MCM-41 ⁱ	7.0	HAuCl ₄ ^a	-	1.7 ± 0.2	CO oxidation	[216]
Nb-MCM-41	-	HAuCl ₄ ^b	1.0	-	Methanol oxidation and acetylacetone cyclization	[268]
Ti-MCM-41	7.0	HAuCl ₄ ^a	4.0–12.0	2.0	Propylene oxidation	[349]
Ti-MCM-41	7.0	HAuCl ₄ ^a	1.0	2.2 ± 0.5	Propylene oxidation	[350]
Ti-MCM-41	7.0	HAuCl ₄ ^a	0.015–0.021	-	Propylene oxidation	[351]
Ti-MCM-41	7.0	HAuCl ₄ ^a	0.19–0.37	2.8–3.8	Propylene oxidation	[352]

Table 1.10. Cont.

Support	pH of synthesis	Au Precursor	Au loading (%wt)	AuNP size (nm)	Catalytic application	Ref.
Ti-MCM-41	7.0	HAuCl ₄ ^a	0.42	2.1	Propylene oxidation	[353]
Ti-MCM-41	6.5	HAuCl ₄ ^a	0.36	3.0 ± 1.0	Propylene oxidation	[354]
Ti-MCM-41	7.0	HAuCl ₄ ^a	0.3 ± 1.0	2.0–5.0	Propylene oxidation	[355]
Fe-MCM-41 ⁱ	7.0	HAuCl ₄ ^a	5.0	<2.0	CO oxidation	[362]
Co-MCM-41 ⁱ	7.0	HAuCl ₄ ^a	5.0	>2.0	CO oxidation	[362]
Al-MCM-41 ⁱ	7.0	HAuCl ₄ ^a	5.0	<2.0	CO oxidation	[362]
Ti-MCM-48	7.0	(CH ₃) ₂ Au(O ₂ C ₅ H ₇) ^c	0.37–0.57	3.3–5.2	Propylene oxidation	[351]
Ti-MCM-48	7.0	HAuCl ₄ ^a	0.01–0.32	2.0–2.6	Propylene oxidation	[353]
Ti-MCM-48	6.5	HAuCl ₄ ^a	0.32	3.0 ± 1.0	Propylene oxidation	[354]
Ti-MCM-48	7.0	HAuCl ₄ ^a	0.3 ± 1.0	2.0–5.0	Propylene oxidation	[355]
Ti-MCM-48	7.0	HAuCl ₄ ^a	~3.0	~3.0	CO oxidation	[211]
Ti-MCM-48	7.0	HAuCl ₄ ^a	3.0–7.5	<1.0	CO oxidation	[363–364]
Ti-SBA-15	-	HAuCl ₄ ^a	0.62	5.1 ± 2.9	CO oxidation	[289]
Ti-SBA-15	1.5	Au colloids ^d	2.47	2.7	CO oxidation	[289]
Ti-SBA-15	-	AuNPs ^e	1.47	5.7 ± 2.1	CO oxidation	[289]
Ti-SBA-15	9.5–10.0	AuCl ₃ ^a	1.0	1.0–8.0	CO oxidation	[365]
Ti-SBA-15	~10.0	HAuCl ₄ ^a	-	0.8–1.0	CO oxidation	[366]
Ti-SBA-15	~10.0	HAuCl ₄ ^a	-	0.8–1.0	CO oxidation	[367]
Al-SBA-15 ^g	-	HAuCl ₄	16.22–19.83	2.6–3.0	CO oxidation	[368]
Al-SBA-15 ^g	-	HAuCl ₄	17.97	3.0 ± 0.8	CO oxidation	[369]
Al-SBA-15 ^h	-	HAuCl ₄	17.61	3.0 ± 1.0	CO oxidation	[369]
Al-SBA-15 ⁱ	-	HAuCl ₄	17.73	3.2 ± 0.7	CO oxidation	[369]
Al-SBA-15 ^j	-	HAuCl ₄	17.07	2.6 ± 0.4	CO oxidation	[369]
Ti-SBA-15	~10.0	HAuCl ₄ ^a	-	0.8–1.0	CO oxidation	[370]
Co-SBA-15	7.0	HAuCl ₄ ^a	1.0–4.0	~5.0	CO oxidation	[371]
Ti-SBA-15 ^k	9.5	HAuCl ₄ ^a	1.0	2.0–9.0	Propene epoxidation	[372]
Ti-SBA-15 ^l	9.5	HAuCl ₄ ^a	1.0	3.0–12.0	Propene epoxidation	[372]
Ti-SBA-15	10.0	HAuCl ₄ ^a	5.0–10.0	1.9–2.9	-	[373]

Table 1.10. Cont.

Support	pH of synthesis	Au Precursor	Au loading (%wt)	AuNP size (nm)	Catalytic application	Ref.
Ti ₍₁₀₎ -SBA-15	11.0	HAuCl ₄ ^a	3.6	4.0 ± 1.5	CO oxidation	[374]
Ti ₍₂₀₎ -SBA-15	11.0	HAuCl ₄ ^a	1.7	4.3 ± 1.5	CO oxidation	[374]
Ti ₍₄₀₎ -SBA-15	11.0	HAuCl ₄ ^a	3.0	7.2 ± 3.2	CO oxidation	[374]
Ti-SBA-15	9.0	HAuCl ₄ ^a	1.0	2.0–15.0	Propene oxidation	[375]
SBA-15-CeO ₂	-	Au colloids ^d	1.76	2.7	CO oxidation	[289]
SBA-15-CeO ₂	10.0	[Au(en) ₂]Cl ₃	0.7	~5.0	Lactose oxidation	[90, 293]
Ce-HMS	~10.0	[Au(en) ₂]Cl ₃	2.94	5.9 ± 0.5	Aerobic oxidative esterification of benzyl alcohol	[292]
Ti-HMS	~10.0	[Au(en) ₂]Cl ₃	2.96	4.8 ± 0.3		[292]
Fe-HMS	~10.0	[Au(en) ₂]Cl ₃	2.87	4.1 ± 0.4		[292]
Ti-HMS	-	HAuCl ₄ ^f	3.9	<20	Direct synthesis of H ₂ O ₂ and <i>in situ</i> -H ₂ O ₂ -ODS	[376]
Ti-HMS	-	HAuCl ₄ ^a	4.6	-		[376]
Fe-HMS	9.0	HAuCl ₄ ^a	2.84	4.6	CO oxidation	[377]
Ce-HMS	9.0	HAuCl ₄ ^a	3.44	7.4	CO oxidation	[377]
Ti-HMS	9.0	HAuCl ₄ ^a	3.02	5.2	CO oxidation	[377]
Ti-HMS	-	HAuCl ₄ ^f	2.3–2.4	4.5–12.6	Direct synthesis of H ₂ O ₂ and <i>in situ</i> -H ₂ O ₂ -ODS	[378]
Co-UVM-7	9.0	HAuCl ₄ ^a	1.07–1.21	3.0–4.0	CO and propane oxidations	[379]
Fe-AerosolSi ⁱ	7.0	HAuCl ₄ ^a	5.0	>2.0	CO oxidation	[362]
Co-AerosolSi ⁱ	7.0	HAuCl ₄ ^a	5.0	<2.0	CO oxidation	[362]
Al-AerosolSi ⁱ	7.0	HAuCl ₄ ^a	5.0	<2.0	CO oxidation	[362]
Co-AerosolSi ⁱ	7.0	HAuCl ₄ ^a	-	<2.0	CO oxidation	[216]
Al-AerosolSi ⁱ	7.0	HAuCl ₄ ^a	-	<2.0	CO oxidation	[216]
Ti-Silica Aerogel	-	Thiol-capped AuNPs	0.14–20.0	1.0–4.0	CO oxidation	[380]
Ti-Silica Aerogel	-	Thiol-capped AuNPs	3.4–6.6	1.4–6.4	CO oxidation	[381]
TiO ₂ -SiO ₂	5.0–5.5	HAuCl ₄ ^a	0.2–3.2	2.1–3.2	CO oxidation	[382]
TiO ₂ -SiO ₂	7.0	HAuCl ₄ ^a	5.0–10.0	1.8–1.9	-	[373]
TiO ₂ -SiO ₂	7.0	HAuCl ₄ ^a	-	1.8–6.4	CO oxidation	[383]

Table 1.10. *Cont.*

Support	pH of synthesis	Au Precursor	Au loading (%wt)	AuNP size (nm)	Catalytic application	Ref.
SiO ₂ -Al ₂ O ₃	-	HAuCl ₄ ^b	2.05	~4.5		[384]
SiO ₂ -Al ₂ O ₃	-	HAuCl ₄ ^b -AgNO ₃	0.88–1.32	~4.5	Oxidation and hydrogenation of CO	[384]
SiO ₂ -Al ₂ O ₃	9.0	HAuCl ₄ ^a	2.5	-		[384]

^a Deposition-Precipitation; ^b IWI; ^c Liquid grafting method; ^d In presence of polyvinylalcohol (PVA) as stabilizer; ^e In presence of poly(diallyldimethylammonium) chloride (PDDA); ^f One-pot synthesis; ^g Thin film functionalized with APS; ^h Thin film functionalized with MPS; ⁱ Functionalized with APS; ^j Functionalized with MPS; ^k Ti incorporated by direct synthesis (Si/Ti molar ratio: 20); ^l Ti incorporated by post-grafting (Si/Ti molar ratio: 20).

Ruszel *et al.* [365] synthesized Au/Ti-SBA-15 catalysts (1%wt Au) impregnating first the mesoporous SBA-15 with titanium isopropoxide in isopropanol, followed by filtration, drying, and calcination at 400°C. The modified Ti-SBA-15 support was loaded with gold by DP at room temperature and pH values of 9.5–10, using an aqueous solution of AuCl₃ as gold precursor. After filtration, washing and drying, the solids were calcined at 350°C for 4 h. The catalytic activity of the resulting catalysts was evaluated in the CO oxidation of at low temperature, including “preferential” oxidation of CO in the presence of H₂ (PROX). From the analysis carried out in this study, it was concluded that the increase of the Ti content, leads to the decrease of the amount of the smallest AuNPs (1–2 nm), and simultaneously contributes to the formation of large AuNPs (5–8 nm). Consequently, the Ti content had a major influence on the catalytic activity. The high activity was observed for the catalysts containing 0.13–1.32%wt of Ti, for which AuNPs of sizes between 1 and 4 nm were dominating. However, catalysts without Ti were inactive. Moreover, these authors reported that the performance of the best Au/Ti-SBA-15 catalyst in the PROX CO oxidation was better than that of the Au/TiO₂ reference catalyst, distributed by World Gold Council.

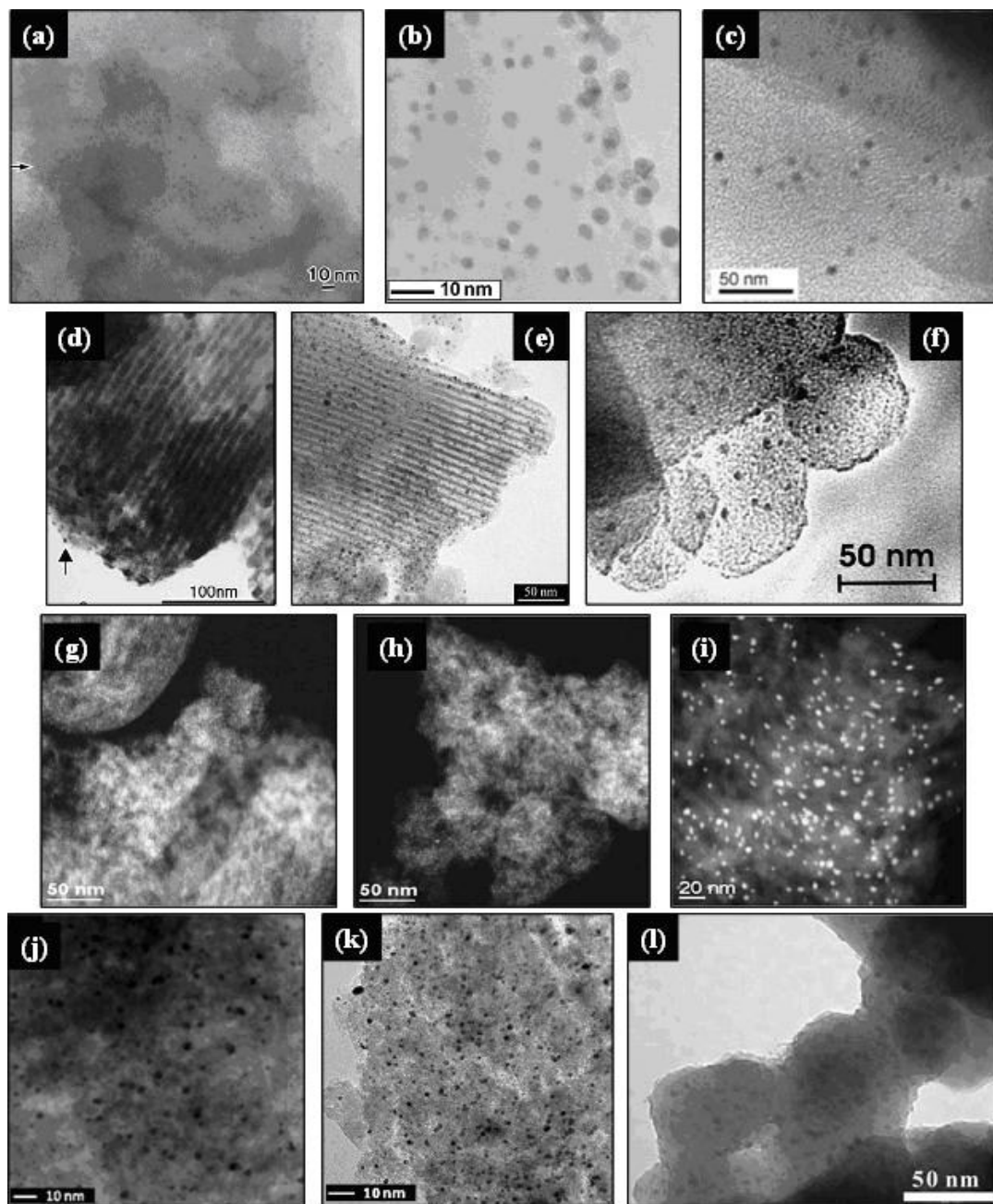


Figure 1.17. TEM micrographs of mesoporous SiO₂-based gold catalysts. (a) Au/Ti-MCM-41 (Reproduced by permission of Elsevier from Reference [350]); (b) Au/Al₂O₃-SiO₂ (Reproduced by permission of Elsevier from Reference [384]); (c) Au/Ti-HMS (Reproduced by permission of Elsevier from Reference [378]); (d) Au/Co-SBA-15 (Reproduced by permission of Elsevier from Reference [371]); (e) Au/Ti-SBA-15 (Reproduced by permission of Elsevier from Reference [289]); (f) Au/Ti-MCM-48 (Reproduced by permission of Elsevier from Reference [211]); (g) Au/Fe-MCM-41 (Reproduced by permission of Elsevier from Reference [362]); (h) Au/Al-MCM-41 (Reproduced by permission of Elsevier from Reference [362]); (i) Au/Co-MCM-41 (Reproduced by permission of Elsevier from Reference [362]); (j) Au/Ce-HMS (Reproduced by permission of Elsevier from Reference [377]); (k) Au/Fe-HMS (Reproduced by permission of Elsevier from Reference [377]); (l) Au/Co-UVM-7 (Reproduced by permission of RSC Publishing from Reference [379]).

A layer-by-layer approach was reported by Yan *et al.* [366-367], who modified the surface of mesoporous SBA-15 with TiO₂ via hydrolytic surface sol-gel process, by mixing the SBA-15 with proper amounts of titanium (IV) butoxide in a mixture of anhydrous toluene and anhydrous methanol. After vacuum filtration, washing with anhydrous methanol and vacuum drying, the monolayer of titanium oxide was hydrolyzed with an excess of deionized water. A second TiO₂ layer was coated following the same procedure, after washing thoroughly with anhydrous methanol and drying. Subsequently gold was loaded on the surface of the modified support using the DP method at pH 10 and 60°C with HAuCl₄ solution. After stirring for 2 h, the precipitates were separated by centrifugation, washed with deionized water and dried at 40°C overnight. The resulting catalysts showed uniform ultra small AuNPs (0.8–1.0 nm) assembled inside the ordered mesopores. These AuNPs, present as oxidized (Au³⁺) and metallic (Au⁰) gold species, displayed high catalytic activity for low-temperature CO oxidation.

Titania has been also used to modify the surface of HMS before the loading of AuNPs through an *in situ* process, using DDA as template, TEOS, tetrabutylorthotitanate as silica and titanium sources, and HAuCl₄ as gold source [376]. After template removal by ethanol extraction at room temperature, the dried powder was calcined at 400°C. The resulting Au/Ti-HMS catalyst (Au loading of 3.9%wt), containing AuNPs of sizes <20 nm, showed high activity in the direct synthesis of H₂O₂ from H₂ and O₂ in methanol solvent. Additionally, high removal rates of bulky sulfur compounds were obtained using the *in situ* generated H₂O₂ over the synthesized Au/Ti-HMS catalyst.

Chiang *et al.* [368-369] incorporated AuNPs over an acidic Al-SBA-15 thin film supports, prepared by mixing pluronic P123 with sodium aluminate in water, followed by the addition of a surfactant mixture solution including CTABr and SDS. The pH and temperature of this mixture were adjusted in the range of 5–6, and 40–50°C, respectively. The as-synthesized Al-SBA-15 materials were functionalized with APS by ethanol refluxing for 12–24 h at 80–90°C. Subsequently, gold was loaded using HAuCl₄ aqueous solution as gold precursor. After stirring, the solids were filtered and dried at room temperature. Finally, the oxidized Au³⁺ species were chemically reduced by means of NaBH₄ aqueous solution. Before the catalytic tests in CO oxidation, the catalyst were activated by heating to 600°C under 10% H₂/N₂ flow for 1 h, followed by cooling step to room temperature under N₂. The resulting catalysts (Au loading of 16.22–19.83%wt), containing AuNPs of about 2.7 nm uniformly distributed within the channels of the support, exhibited high activity for CO oxidation at 80°C, and

this activity attained the highest value of ca. 97% CO conversion when using a Si/Al molar ratio of 39. Moreover, it was reported that most of the Al was present in the tetrahedral framework well-dispersed site, which contributed not only to generate acidity, but also to limit the Au particle size. In an attempt to elucidate the effects of different aluminosilicate supports, the same authors prepared Au supported on Al-SBA-15 thin films and on Al-SBA-15 normal form (Au loading of ~17%wt), using APS and MPS as functionalizing agents [369]. After H₂ reduction at 600°C, the size of AuNPs was almost similar for all the supports (~3.0 nm). However, they found that hydrogen reduction is necessary to activate the catalysts supported on Al-SBA-15 thin films, whereas for the normal Al-SBA-15 support the activation must include a previous calcination step at 560°C for 6 h before reduction under H₂, to obtain good catalytic performance of CO oxidation at 80°C.

Mixed mesoporous silica samples (MCM-41 and aerosol-derived silica) with Co, Al and Fe as heteroelements (Si/heteroelement molar ratio of 30) were synthesized by Datye *et al.* [362]. These modified materials were subsequently functionalized with amine groups (APS) before gold loading (5%wt) with H₂AuCl₄ at neutral pH. After reduction under H₂ at 200°C for 2 h, the resulting SiO₂-based gold catalysts were active for CO oxidation. The size of the AuNPs of these catalysts was less than 2 nm for all samples, except for Au/Co-MCM-41 and Au/Fe-Aerosol silica. These authors concluded that the addition of heteroelements did not lead to a significant improvement in the thermal stability of catalysts, but contributed to increase the catalyst activity compared to the pure silica support. Among the evaluated catalysts, the Au/Co-doped aerosol silica and the Au/Co-MCM-41 showed the highest and lowest reactivity for CO oxidation, respectively.

Zepeda *et al.* [377] modified hexagonal mesoporous silica (HMS) with Fe³⁺, Ce⁴⁺ and Ti⁴⁺ ions prior to the incorporation of Au species by deposition-precipitation (nominal Au loading of 3.5%wt). The added heteroatoms were incorporated principally into the HMS framework, and contributed to the stabilization of AuNPs, which were located mainly in the internal pore network of the support. Gold particle sizes of 4.6, 5.2 and 7.4 nm were obtained for Au/HMS-Fe, Au/HMS-Ti and Au/HMS-Ce, respectively. The catalytic activity of the H₂ reduced samples (300°C, 2 h) for total and preferential CO oxidation followed the trend: Au/HMS-Fe > Au/HMS-Ce > Au/HMS-Ti.

Recently, Zepeda's group [384] proposed a "green-synthesis" process for the synthesis of monometallic Au (Au loading of 2.05%wt) and bimetallic Au-Ag (Au and Ag loadings of 0.88 and 1.32%wt, respectively) catalysts supported on commercial mesoporous SiO₂-Al₂O₃. In their approach,

Camellia sinensis plant extract was used as biological reducing agent. The catalysts were synthesized by IWI of the support with HAuCl_4 and AgNO_3 . After addition of each one of metal precursor solutions, *Camellia sinensis* extract (2 mL) was added to the slurry, followed by vigorous stirring for 48 h at room temperature. Then, the samples were dried at 100°C in air flow. For both catalysts, it was observed that after few minutes of the *Camellia sinensis* extract addition, the color of the solutions changed drastically, indicating the reduction of both Au^{3+} and Ag^{1+} ions. The resulting catalysts preserved the structural parameters of the $\text{SiO}_2\text{-Al}_2\text{O}_3$ support. Moreover, from TEM images, it was observed that in both catalysts the metallic particle sizes varied between 1.5 and 6.5 nm, with a mean value of about 4.5 nm. However, the bimetallic catalyst presented higher amounts of AuNPs of size lower than 4.5 nm, in comparison with the monometallic catalyst, indicating that the presence of Ag contributes to the regular morphology and dispersion of metallic particles. On the other hand, metallic Au^0 (81%) and oxidized Au^{+1} (19%) species were found in the monometallic catalysts, whereas only metallic Au^0 species were present in the bimetallic catalyst, which also contained metallic Ag^0 (93%) and oxidized Ag^{+1} (7%) species, demonstrating that the use of *Camellia sinensis* led to the formation of metallic nanoparticles. After catalytic activity evaluation in CO oxidation, it was found that bimetallic catalyst displayed higher activity than the monometallic sample. At a reaction temperature of 270°C , 100% CO conversion was obtained with the bimetallic Au-Ag catalyst, whereas the CO conversion for the monometallic sample was 85%. Moreover, both catalysts were more active than the monometallic catalyst synthesized by DP and calcined at 473°C for 3 h. Conversely, the activity of the monometallic Au catalyst in the CO hydrogenation was 1.6 times more active than the bimetallic catalyst, and 2 times more active than the monometallic catalyst synthesized by DP. In this interesting “green” approach study, the high activity of the bio-reduced catalysts was mainly attributed to the small metallic particles obtained, because of the absence of calcination or reduction steps at high temperature. Moreover, it was hypothesized that hydroxyl and carboxylic acid functional groups present in the *Camellia sinensis* extract, could be responsible for the bio-reduction process and the stabilization and protection as capping agent of the AuNPs, respectively.

1.3.3.10. Other methods of synthesis

In the previous sections we presented the main methods for the synthesis of gold catalysts supported on MSM. However, because of the advances in nanotechnology, other less-conventional methods, using different technologies and gold precursors, have been published. Although these methods have

not been largely employed, and the catalytic activity of the synthesized materials has not always been investigated, it is worth to mention some of them.

Chatterjee *et al.* [385] deposited gold into the channels of MCM-48 (Au loading of ca. 5%wt) through a process involving H₂-assisted reduction of HAuCl₄ (aqueous solution) in supercritical CO₂. The resulting catalysts, containing AuNPs varying between 2 and 25 nm, were active for the selective hydrogenation of crotonaldehyde. Moreover, it was reported that the size of AuNPs can be controlled by tuning the CO₂ pressure, without disturbing the mesoporous structure. Similarly, Gupta *et al.* [386] loaded pre-synthesized Au nanocrystals (mean diameter of 2.2 ± 0.3 nm) dispersed in toluene into mesoporous SBA-15 and MCM-41 (2%wt), using supercritical CO₂ as antisolvent. It was estimated that approximately 10–100 Au nanocrystals per pore were infused inside the mesoporous silica. However, the catalytic activity of these materials was not evaluated.

Campelo *et al.* [387] synthesized Au/SBA-12 catalyst (Au loading of 1.2%wt) in a conventional microwave oven, using gold bromide dissolved in ethanol-acetone mixture (1:1v/v), as Au precursor. They obtained well and homogeneously dispersed AuNPs of ca. 1.9 nm, highly active for styrene oxidation.

Corma *et al.* [388] prepared Au/MCM-41 (loading of 0.20–30 mmol-Au/g support) using a gold-carbene complex [(carbene)AuCl] as Au precursor. The resulting catalysts were active for the hydrogenation of alkenes and the Suzuki cross-coupling reaction between halobenzene and arylboronic acids.

Small Au clusters (~1 nm) have been deposited on mesoporous SBA-15, MCF and HMS using triphenylphosphine-protected Au₁₁ (Au₁₁:TPP) clusters as gold precursor [335, 389]. To do this, the Au₁₁:TPP clusters and the support were dispersed in CH₂Cl₂/C₂H₅OH (80/20) and stirred for 2 h. After filtration, the resulting solids were calcined at 200°C for 2 h under vacuum. The resulting catalysts were active, highly selective and reusable for the oxidation of various alcohols with H₂O₂, such as benzyl alcohol, under microwave heating.

Silver-catalyzed electroless deposition was used to incorporate AuNPs with sizes of 5.0 to 9.0 [390] and ca. 6.4 nm [391] within the channels of mesoporous SBA-15, but the catalytic activity of the obtained materials was not reported.

Chen *et al.* [392-396] and Sun *et al.* [397] have reported a sonochemical method for the incorporation of AuNPs into mesoporous silica at room temperature. The AuNPs ranging from 2 to 9 nm were dispersed uniformly within the pores of the silica support by the immersion of the host material into a chloroauric acid solution (0.8 mmol/L) containing 0.2 mol/L of isopropanol during 2 to 3 weeks. The mixture was subsequently irradiated for various periods from 600 to 7200 s with 40 kHz ultrasonic waves at 100 W output power. The filtered solid was washed with distilled water and dried at 120°C for 30 min. After ultrasonic irradiation, the AuNPs were formed within pores of the mesoporous silica. However, no catalytic activity was reported.

The bio-assisted synthesis of AuNPs supported on mesoporous silica tubes was recently reported by Jan *et al.* [398], who deposited synthetic polypeptides (PLL and PLT) on the walls of polycarbonate membrane pores to form multilayer films for *in-situ* mediating the formation of AuNPs embedded in porous silica nanostructures. After calcination at 400–500°C for 3–10 h, the resulting materials having AuNPs of ~6.5 nm, displayed promising catalytic activity for the reduction of *p*-nitrophenol.

Recently, Deng *et al.* [399] prepared multifunctional microspheres with a core of nonporous silica-protected magnetite particles, a transition layer of active gold nanoparticles, and an outer shell of ordered mesoporous silica with perpendicularly aligned pore channels. These catalytic materials showed excellent catalytic activity for the reduction of 4-nitrophenol as well as highly selective epoxidation of styrene using *t*-butyl hydroperoxide as oxidant. Moreover, the resulting catalysts containing nanocrystals of 12.2 and 8.3 nm for Au and magnetite nanoparticles, respectively, presented the surface evenly covered by AuNPs and displayed the three low-angle XRD diffraction peaks typical of 2-D hexagonal mesostructures.

Lee *et al.* [400] fabricated a nanoreactor framework of a Au/SiO₂ yolk/shell structure through selective etching of metal cores from Au/SiO₂ by treatment with KCN. Although gold core diameters showed high values (43–104 nm) depending on the added amount of KCN, these Au/SiO₂ yolk/shell particles were active for the catalytic reduction of *p*-nitrophenol by NaBH₄.

1.3.4. Conclusions and outlook

The high catalytic activity of gold at the nanoscale discovered in the late 1980s has been one of the most exciting discoveries in the field of catalysis and, since then, gold catalysts have been synthesized on a variety of metal oxides supports. Particularly, silica was considered an inappropriate

support for AuNPs, until the revolutionary work of Haruta's group [19, 207, 305-306] confirmed that silica materials could be suitable supports for AuNPs using appropriate synthesis methods. Since the chemical vapor deposition approach employed in those studies requires special equipment and expensive gold precursors, extensive research has been developed to synthesize gold catalysts supported on mesoporous silicas, such as MCM-41, MCM-48, SBA-15 and SBA-16, because of the excellent properties of these materials as catalytic supports. Mesoporous SBA-15 has proven to be a better support for gold catalyst in comparison with other mesoporous silica materials, including HMS, MCM-41, MCM-48, SBA-16, because it has a two-dimensional (2D) hexagonal pore structure, large pore size and strong pore wall, allowing the immobilization and stability of AuNPs inside the pores [217, 222, 231].

Although the catalytic activity of Au/MSM catalysts has been evaluated in numerous catalytic reactions, as illustrated in Tables 1.5–1.10, from the published results one can say that gold catalysts supported on mesoporous silicas would have a significant impact on the redox type reactions in liquid phase, in which the mesoporous architecture could enhance the diffusivity of bulky reactants and products, while the AuNPs are kept inside the pores. However, the main problem of the synthesis of Au/MSM catalysts lies in obtaining very small (about 2 nm) and well dispersed AuNPs. To overcome these problems, the main strategies and their related drawbacks can be summarized as follows:

Because of the low isoelectric point of silica (~2.0), the conventional IWI and DP methods are not appropriate for the incorporation of gold nanoparticles (AuNPs) into MSM, although some strategies such as washing with a base or reduction under hydrogen at high temperatures have been employed to synthesize active gold catalysts following these procedures. However, these approaches have not been largely employed, because the AuNPs are usually formed both inside and outside the channels, and the control of shape and particle size is not possible. Despite the fact that the use of pre-synthesized capped AuNPs contributes to circumvent this problem, and seems to be a promising approach in which the size and shape of gold particles can be controlled before the gold loading, this strategy has not been extensively applied in catalytic applications.

A general trend consists then in the modification of the silica materials either by direct or post-grafting functionalization with amine or thiol groups. These groups can act not only as ligands enhancing the interaction between the metal precursors and the silica surface, but also as mild reductants under basic conditions for *in situ* reduction of Au(III). Even if several active Au/MSM have been prepared

using functionalized mesoporous silicas by direct or subsequent incorporation of the gold precursor, as summarized in Tables 1.5 to 1.7, the main problems related to these procedures lie in the followings facts: (i) The gold loading and particle size are correlated with the amount of organic functional ligands, but high concentrations of organic functional groups may hinder the condensation of silica precursors to form an ordered framework, when using direct functionalization, or significantly reduced surface area, pore diameter and pore volume, when using the post-grafting functionalization; (ii) The post-synthetic functionalization of MSM does not allow the homogeneous distribution of the organic functional groups on the pore surface, and consequently, the AuNPs are not homogeneously distributed after gold loading; (iii) The calcination step required for the removal of functional groups, may contribute to the formation of large AuNPs, with the inherent negative effect on the catalytic activity; (iv) When using the simple way of direct incorporation of the gold precursor during the mesoporous silica synthesis, the AuNPs are not necessarily placed within the pores, which can lead to metal leaching and poor life of catalysts.

The modification of silica supports with other metal oxides to produce SiO₂-based gold catalysts, is also an interesting approach, because it allows modifying the isoelectric point of the silica, facilitating the incorporation and dispersion of the AuNPs by simple deposition-precipitation of gold precursor, as summarized in Table 1.10, while simultaneously the functionalizing oxides may take part in the reaction as co-catalysts for the enhancement of the catalytic activity.

Despite the fact that rapid advances in nanotechnology have allowed the emergence of new sophisticated methods for preparing Au/MSM catalysts, it is worth considering the feasibility of the synthesis procedures for applications other than at a laboratory scale. Some disadvantages of various preparation methods lie in the fact that the experimental procedures are not suitable for general applications because of the requirements of special equipment and/or expensive or complicated synthesis of the gold precursors. Moreover, in many cases, the catalytic activity of such catalysts has unfortunately not always been evaluated.

Thus, considering that the success of the introduction of AuNPs into MSM requires the fulfillment of three criteria [205]: (i) retaining the order structure of the MSM; (ii) achieving very small uniform and well dispersed AuNPs; and (iii) attaining high and controlled gold loading; the use of gold complex Au(en)₂Cl₃ (en = ethylenediamine) can be regarded as a promising precursor for the synthesis of not only Au/MSM, but also of gold supported on amorphous silicas. Although this precursor has not been

widely used, the catalysts prepared using $Au(en)_2Cl_3$ have displayed not only small and well dispersed AuNPs, but also high catalytic activities in both gas and liquid phase oxidation reactions [90, 206].

Finally, it is true to say that gold catalyst has become a hot topic for chemical reactions; however, there are still challenges ahead for the development of Au/MSM satisfying the main requirements of any catalyst: a synthesis method as easy and inexpensive as possible with high activity, selectivity and stability. Moreover, the identification of the active gold species is still a challenging task for most of the chemical reactions catalyzed by gold.

Chapter 2. Hypotheses and objectives

2.1. Hypotheses

According to the literature review, the catalytic oxidation of lactose is a good alternative for producing lactobionic acid. Although palladium and bismuth promoted palladium have showed high activity and selectivity for this process, the synthesis of robust catalysts for making the catalytic process more competitive, is still a challenge. In this context, the following hypotheses were proposed in this project:

- Gold catalysts supported on mesoporous silica materials (Au/MSM) would be robust catalysts for the oxidation of lactose to lactobionic acid, and the reaction control would be easier in comparison to the oxidation over palladium and bismuth promoted palladium catalysts, since gold is not prone to oxidation.
- The modification of the mesoporous silica support with ceria could enhance the catalytic activity of the Au/MSM, because of its favorable oxidation activity.
- Lactobionic acid could be produced successfully by a demineralization step using bipolar membrane electro dialysis and/or ion-exchange technology.

2.2. Objectives

In order to verify the research hypotheses, the following objectives were formulated:

2.2.1. General objective

The main objective of this project is to selectively produce lactobionic acid by a two step process comprising the oxidation of lactose over Au/MSM and the demineralization of the salt solution at the reactor outlet.

2.2.2. Specific objectives

- Optimize the formulation of gold catalysts supported on mesoporous silica and on mesoporous silica decorated by ceria.
- Characterize the synthesized catalytic materials, and evaluate their catalytic activity on the oxidation of lactose to lactobionic acid.

- Optimize the operating reaction conditions, using a thermostated magnetically stirred glass reactor.
- Investigate the catalyst stability after consecutive oxidation reaction cycles.
- Study the feasibility of bipolar membrane electro dialysis and ion exchange technology for recovering lactobionic acid from its salt solution obtained after lactose oxidation.

Chapter 3. Selective production of lactobionic acid by aerobic oxidation of lactose over gold crystallites supported on mesoporous silica

This chapter reports the synthesis and characterization of gold catalysts supported on mesoporous silica (Au/MSM) by co-condensation of a mixture of *bis* [3-(triethoxysilyl)propyl] tetrasulfide (BTESPTS), tetraethyl orthosilicate (TEOS) and the gold precursor (HAuCl₄) in acidic media, using the triblock co-polymer EO₂₀PO₇₀EO₂₀ (P123) as template. The influence of the reaction conditions on the lactose oxidation to LBA is also presented and discussed.

Published in *Applied Catalysis A: General* 2011, 402(1–2), 94-103 by **Luis-Felipe Gutiérrez, Safia Hamoudi, Khaled Belkacemi**

3.1. Abstract

Partial oxidation of lactose over Au-based catalyst system using nanostructured silica materials with improved activity, selectivity and stability was investigated as a novel chemo-catalytic approach for selective synthesis of lactobionic acid (LBA) for therapeutic, pharmaceutical and food grade applications.

Highly active gold crystallites dispersed on mesoporous silica (SiO₂-meso) using *bis*-[3-(triethoxysilyl)propyl] tetrasulfide (BTESPTS), a silane coupling agent to immobilize gold, were successfully formulated, and their catalytic activity was evaluated in an agitated semi-batch reactor. The catalysts were characterized by N₂ physisorption, XRD, XPS and TEM. The influence of the reaction conditions, i.e., temperature, pH value, metal loading and catalyst/lactose ratio on lactose conversion were investigated. After 100 min of reaction, the catalyst containing 0.7% Au showed the highest catalytic activity (100% lactose conversion) and a 100% selectivity towards LBA, when it was used at a catalyst/lactose ratio of 0.2 under alkaline (pH 9.0) and mild reaction temperature (65°C).

3.2. Introduction

Lactose is an important by-product of the cheese and casein manufacture, whose production is estimated to about 1.2 million tons per year [4]. Because of its low solubility and sweetness, as well as a certain intolerance of some population segment, the use of lactose is limited in many applications. However, as a consequence of its worldwide surplus and low cost, there is a great

interest in the research of innovative processes for transforming lactose, and expanding its applications in the food and pharmaceutical industries as value-added lactose derivatives. Some significant developments include the production of highly valued pharmaceutical products and functional food ingredients such as lactulose, lactitol, lactobionic acid, lactosucrose, and galacto-oligosaccharides [20].

Lactobionic acid (LBA) (4-O- β -D-galactopyranosyl-D-gluconic acid) is a high value-added product obtained from lactose oxidation, with excellent properties for food and pharmaceutical applications. The main commercial use of LBA is as ingredient of the solutions employed for stabilizing organs prior to transplantation [43]. LBA is also used in calcium supplementation, and represents a new ingredient in skin care products featuring potent antioxidant and humectant properties [8, 401]. In the food industry, LBA can be used as acidulant with a sweet taste; as filler in cheese production; as firming agent, and to fortify functional drinks with essential minerals such as Fe and Cu [8, 402].

LBA production by means of heterogeneous catalytic oxidation of lactose on Pd/C and Pd-Bi/C catalysts was first reported by Hendriks et al. [10]. Since then, some studies of lactose oxidation over platinum, palladium and bismuth-promoted palladium supported catalysts have been investigated [13, 16, 77, 80-85, 87, 89, 403]. Although these reactions are environmentally safer than chemical and biochemical oxidations, the main problem reported for these catalysts is their deactivation during reaction [404]. Platinum is less prone to deactivation by over-oxidation, but its selectivity towards aldonic acids formation is lower than that of palladium. It has been also demonstrated that the presence of bismuth or lead as promoters, and the strict control of the oxygen concentration, diminish the susceptibility of catalyst to poisoning, and it improves its selectivity towards aldonic acids [85, 87, 405]. In recent published works of our research group, bimetallic catalyst supported on mesoporous SBA-15 (1.02%Pd, 0.64%Bi; Bi/Pd molar ratio of 0.3) was used for lactose oxidation at 65°C under microaerobic and alkaline conditions (pH 9.0). This catalyst was highly active (96% lactose conversion) and 100% selective towards LBA, when the reaction was conducted during 3 h with consecutive addition of air and nitrogen periodically to avoid the catalyst poisoning by over-oxidation [85, 87]. However, even if bismuth-promoted palladium catalysts are promising for the oxidation of lactose to LBA, improved catalysts showing high activity and selectivity towards LBA are needed, in order to facilitate the reaction control, to avoid the presence of toxic substances derived from the possible leaching of Pd and Bi, and to make the catalytic process more competitive [4].

Supported gold catalysts have shown to outperform palladium catalysts for the oxidation of carbohydrates, because they are less prone to over-oxidation, and they exhibit high activity and selectivity towards aldonic acids [404]. However, the oxidation of lactose over gold catalyst has been scarcely investigated. Recent studies indicate that supporting gold nanoparticles on Al_2O_3 , TiO_2 , and CeO_2 allowed to achieve moderate to high conversions (>80%) and selectivities (up to 95%), using Au loadings in the range of 0.4–2.0% [13-16]. Even though these relatively high conversions and selectivities were reached, the oxidation of lactose to LBA still necessitates cumbersome and costly downstream separation steps.

Since the pioneering work of Haruta [406], intensive research efforts were initiated to use gold-based catalysts for liquid phase oxidation. The activity of heterogeneous gold catalysts strongly depends on the gold cluster size deposited on the catalyst surface. Then, a weak stability of these clusters against sintering during the synthesis of the catalyst is problematic and undesirable and could hamper the catalyst applications [407].

Owing to their high surface area, highly ordered structure, good thermal stability and excellent mechanical properties, mesoporous silicas are considered very attractive catalyst supports. Consequently, synthesis of metal nanoparticles supported on such materials has received much attention in recent years [231]. However, gold nanocrystallites dispersed on silica materials are mobile and sinter easily under severe synthesis conditions of temperature, especially during the calcination step. To avoid this problem, Hu et al. [280] reported a simple method to confine gold nanoparticles in the mesoporous silica walls in the presence of BTESPTS. This catalytic system exhibited fairly interesting activity for alcohol oxidation.

The aim of this work focuses on the synthesis and characterization of gold nanoclusters highly dispersed on mesostructured silica material using BTESPTS and application of this material as a catalyst for selective oxidation of lactose to LBA. Specifically, the catalyst characterization by means of nitrogen sorption, powder X-ray diffraction (XRD), X-ray photoelectron spectroscopy (XPS) and transmission electron microscopy (TEM) was investigated, as well as the influence of the reaction conditions, *i.e.*, temperature, pH value, gold loading and catalyst-to-lactose ratio (catalyst/lactose), on lactose conversion. To the best of our knowledge, mesostructured silica has not been used as support in the oxidation of lactose over gold catalysts.

3.3. Experimental

3.3.1. Materials

All reagents were of the highest purity and were used without further purification. Gold (III) chloride trihydrate ($\text{HAuCl}_4 \cdot 3\text{H}_2\text{O}$), tetraethyl orthosilicate (TEOS), *bis*-[3-(triethoxysilyl) propyl] tetrasulfide (BTESPTS), α -lactose monohydrate and LBA were purchased from Sigma Aldrich. Pluronic P123 ($\text{EO}_{20}\text{PO}_{70}\text{EO}_{20}$, $M_{av} = 5900$ g/mol) was graciously offered by BASF. For HPLC analysis, sodium hydroxide solution 50% and HPLC grade anhydrous sodium acetate from Fluka, were used for eluents preparation.

3.3.2. Catalyst preparation

Gold catalysts were synthesized as reported recently by Hu et al. [280]. In a typical synthesis, 10 g of P123 were dissolved in 375 mL of a 2 N HCl solution at room temperature. After complete dissolution of the template agent, the temperature was increased to 40°C. Then, a mixture of 20.8 g TEOS and 2.1 g *bis*-[3-(triethoxysilyl) propyl] tetrasulfide was added drop wise under continuous and vigorous agitation. Subsequently, solutions of HAuCl_4 in 2 N HCl were added drop wise, according to the different investigated catalyst gold loadings (0.4, 0.5, 0.7, 0.8 and 1.0%). The obtained mixture was stirred at 600 rpm for 24 h at 40°C, and then hydrothermally aged for 72 h at 100°C. After vacuum filtration, the solid was thoroughly washed with deionized water and ethanol at room temperature. Finally, the catalyst was vacuum-dried overnight at 100°C, and the resulting solids were calcined at 500°C for 5 h at a heating rate of 1°C/min, using a programmable oven.

3.3.3. Characterization

Nitrogen adsorption/desorption isotherms of calcined samples were obtained using a volumetric adsorption analyzer (Model Autosorb-1, Quantachrome Instruments, Boyton Beach, FL) at 77 K. Before the adsorption analysis, the samples were degassed for 3 h at 200°C. Total pore volume was estimated from the amount adsorbed at 0.99 relative pressures. Pore size distributions were calculated using the desorption branch of the N_2 adsorption/desorption isotherms and the Barrett–Joyner–Halenda (BJH) method [408].

Powder X-ray diffraction (XRD) patterns were obtained using an Ultima III Rigaku Monochromatic Diffractometer using Cu K α radiation ($\lambda = 1.5406$ Å). Small angle powder diffraction patterns were

acquired at a scanning rate of 1°/min in the 2θ range of 0.6–3°, while wide angle powder XRD were obtained at the same scanning rate in the 2θ range 25–80°.

The catalyst surface and the oxidation state of gold in the catalysts were studied by X-ray Photoelectron Spectroscopy (XPS) analysis using an Axis-Ultra spectrometer from Kratos (UK) equipped with an electrostatic analyzer of large ray, a source of double X-rays Al–Mg without monochromator and an Al source with monochromator. The pressure in the XPS room was maintained between 5×10^{-9} and 5×10^{-8} torr during the analysis. All the spectra were recorded with the Al monochromatic source with a power of 300 W. The flyover spectrum used to determine the elementary composition was recorded with pass energy in the analyzer of 160 eV and an energy step of 1 eV, using lenses in hybrid mode, which maximizes the sensitivity. The detailed spectra with high resolution were recorded with pass energy of 40 or 20 eV, and step energy of 50 or 100 meV. The spectra with high resolution are used for the chemical analysis [409]. The adjustment of the envelope calculated with the experimental spectrum was carried out using CasaWPS software from Kratos (UK). The binding energy (BE) scale was calibrated by measuring C1s peak (BE = 285.0 eV) from the surface contamination.

Transmission electron microscopy (TEM) images were taken on a JEM-3010 electron microscope (JEOL, Japan) with an acceleration voltage of 80–120 kV. The catalysts samples were suspended in methanol and ultrasonically treated during 10 min. Then, the suspension (5 μ L) were disposed uniformly and dried on a nickel grid.

3.3.4. Lactose oxidation experiments

Lactose oxidation experiments were carried out at atmospheric pressure in a thermostated and magnetically stirred 300 mL-glass reactor. In a typical oxidation reaction, 175 mL of 20 mM lactose solution were heated under continuous agitation (600 rpm) until the desired reaction temperature was reached, whereas 500 mL/min of nitrogen flow were simultaneously bubbled for stripping off the dissolved oxygen. Once the reaction temperature was reached, the stirring was increased to 900 rpm, the catalyst was added and the pH of the solution was adjusted at the desired value, by the addition of few drops of 1 M NaOH aqueous solution. Then, air was bubbled through the reaction mixture at a constant flow rate of 40 mL/min. During the reaction, the pH value was kept constant by adding 1 M aqueous NaOH solution, by means of a pH STAT Titrator (Metrohm® 842 Titrand®),

Switzerland), and the dissolved oxygen concentration was monitored using an oxygen probe (Ocean Optics, Inc., USA) connected to an optic fiber sensor system (TauTheta Instruments LLC, USA).

The time 'zero' of the reaction corresponded to the moment when air was bubbled through the reaction mixture. Reactions were carried out during 180 min. In order to optimize the reaction conditions, the effects of reaction temperature (50–70°C), pH (7.0–10.0), catalysts metal loading (0.4–1.0%), as well as catalyst/lactose ratio (0.1–0.3) were evaluated. Liquid samples were taken at regular intervals for the subsequent HPLC analyses.

3.3.5. Reaction sample analysis

Samples of reaction mixture were analyzed using a chromatographic system DX-ICS 2500 (Dionex, USA) equipped with a gradient pump GP50 and an electrochemical detector ED50 with a thin-layer type amperometric cell outfitted with gold electrodes and an Ag/AgCl reference electrode. The chromatographic separation of lactose and LBA was performed on a CarboPac PA1 analytical column (4 mm × 250 mm i.d., Dionex) and a CarboPac PA1 guard column (4 mm × 50 mm i.d., Dionex) at a flow-rate of 1 mL/min. Sodium hydroxide solution 50% and anhydrous sodium acetate (NaOAc) from Fluka diluted in deionized water were used as eluents. Chromeleon software (Dionex, USA) was used to perform all the calibration and integration of chromatographic data. All supplementary details can be found in Belkacemi et al. [85].

3.4. Results and discussion

3.4.1. Material characterization

3.4.1.1. Nitrogen physisorption

Textural properties of the mesoporous silica (SiO₂-meso) and Au/SiO₂-meso catalysts were obtained from low-temperature (77 K) nitrogen adsorption/desorption isotherm measurements, which allow calculation of the specific surface areas, specific pore volumes, and mesopore size distributions, as summarized in Table 3.1. These isotherms and the corresponding pore size distributions using the BJH theory are depicted in Figure 3.1 and Figure 3.2 for the initial mesoporous silica material and Au catalysts with Au loadings of 0.4, 0.7 and 1%. As shown in Figure 3.1, the shape of the obtained isotherms corresponds to type IV according to IUPAC classification and displayed a broad H1 type hysteresis loop characteristic of large pore mesoporous solids [410]. The initial increase in adsorption capacity at low relative pressure is due to monolayer adsorption on mesopores. The upward

deviation in the range of $P/P_0 = 0.4-0.8$ is associated with progressive mesopores filling. As the relative pressure increases, the adsorption isotherm for the mesoporous support displays a sharp increase characteristic of capillary condensation inside uniform mesopores. There were uncommon hysteresis loops at P/P_0 values between 0.4 and 0.7 for the Au/SiO₂-meso catalysts. These loops look more flat in comparison to that of initial mesoporous silica support indicating that some structural defects were formed in the mesoporous framework [411-412]. Similarly when they incorporated gold nanoparticles in mesoporous silica, Hu et al. [280] reported the formation of void defects in their catalysts and concluded that the formation of these structural defects that could be attributed to the incorporation of gold in the mesoporous silica walls.

The nitrogen physisorption of the support and Au catalysts reveals also that they have high BET surface areas. The support exhibited dual pores size distribution which reduces to one pore distribution of nearly 4 nm of average pore size after gold incorporation as depicted in Figure 3.2 and Table 3.1.

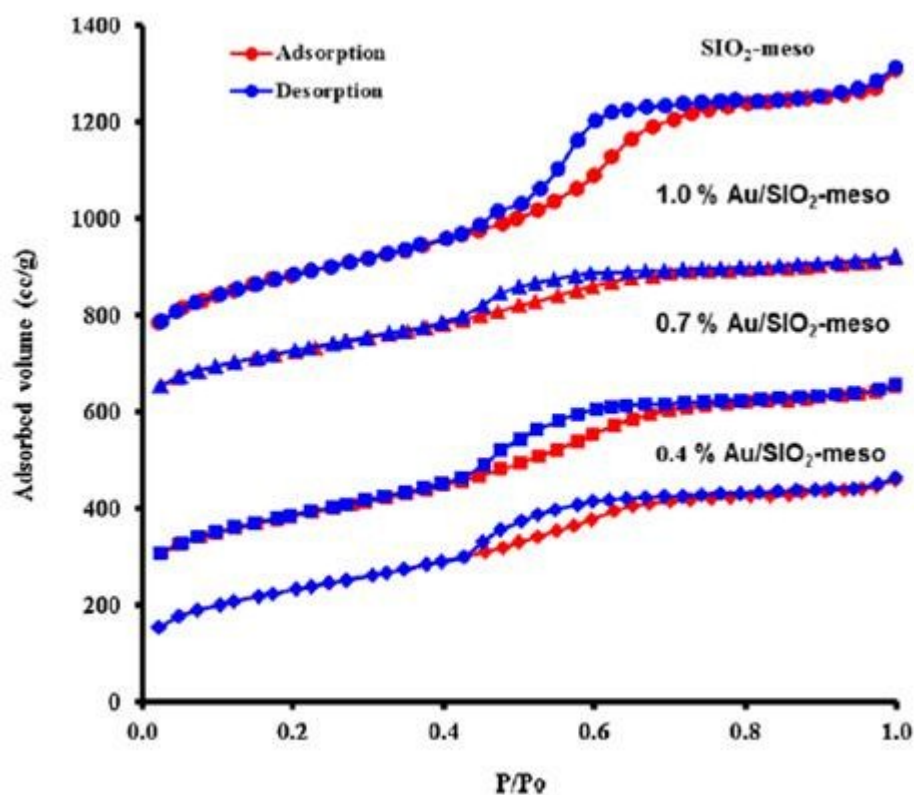


Figure 3.1. Nitrogen adsorption/desorption of mesoporous silica material and Au on mesoporous silica at different Au loadings.

Table 3.1. The textural parameters of the mesoporous silica support as well as Au catalyst samples prepared at different Au loadings.

Materials	BET surface area ($\text{m}^2\cdot\text{g}^{-1}$)	Pore diameter (nm)	Total pore volume ($\text{cm}^3\cdot\text{g}^{-1}$)
SiO_2 meso	995.7	3.70 and 4.73	1.087
0.4%Au/ SiO_2 -meso	813.9	3.50	0.716
0.7%Au/ SiO_2 -meso	827.3	3.70	0.779
1.0%Au/ SiO_2 -meso	790.1	3.70	0.651

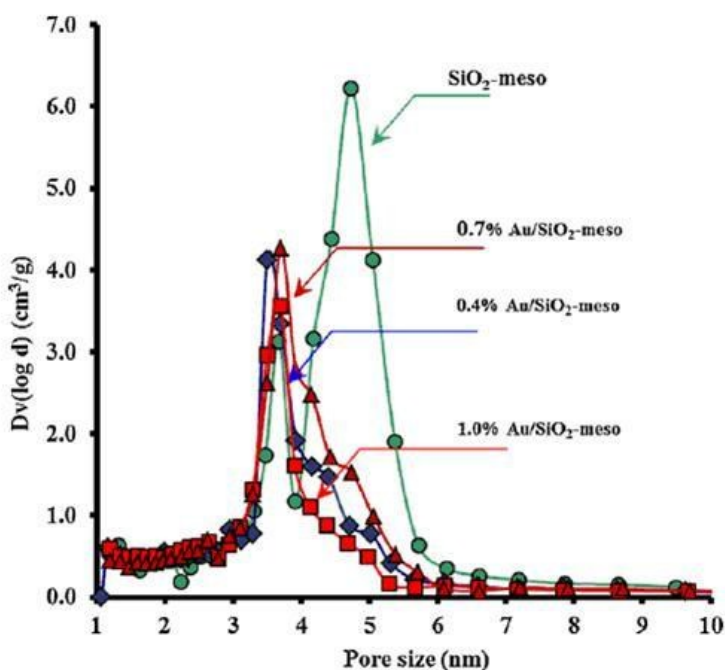


Figure 3.2. Pore size distributions of mesoporous silica material and Au/ SiO_2 -meso at different Au loadings.

It is noticed in Table 3.1, that the BET surface area of mesoporous silica support approaches $1000 \text{ m}^2 \text{ g}^{-1}$ with a total pore volume of $\approx 1.1 \text{ cm}^3 \text{ g}^{-1}$ and dual-pore size distributions centered at around 3.7 and 4.7 nm. By incorporation of gold crystallites, the BET surface area decreased notably to $\sim 820 \text{ m}^2 \text{ g}^{-1}$ for the catalysts with Au loadings of 0.4 and 0.7%. Further increment of Au loading to 1% decreases further the BET surface area. Similar tendency can be observed for the total pore volume where about 41% of the initial pore volume of the support is lost when 1% of Au is

impregnated by filling the support pore size of 4.7 nm. Therefore, incorporation of metallic gold has a consequential impact on the BET specific surface area, specific pore volume and pore size of the silica material. The pore and structural morphology of the synthesized mesoporous silica material and those of the Au catalysts can be further verified by transmission electron microscopy (TEM).

3.4.1.2. X-ray diffraction

The small angle XRD patterns of the mesoporous silica support and the synthesized catalysts with different gold loadings (0.4, 0.7 and 1.0%) are shown in Figure 3.3. It can be noticed that there is a peak at about $2\theta = 1.0$ degree, which is broader than the narrow peak normally reported for the well-ordered hexagonal mesoporous silica such as SBA-15 [145]. Then the structure obtained by co-condensing silica source and BTESPTS as a silane coupling agent to immobilize gold in the presence of P123 is not that of SBA-15 for all tested gold loadings. Similar low angle XRD patterns were previously reported by Besson et al. [413] using *bis*-[3-(triethoxysilyl) propyl] disulfide and TEOS in the presence of P123. These patterns signify the presence of a correlated distribution of framework pores but the lack of a regular cylindrical pore structure. This is in agreement with the TEM findings presented below.

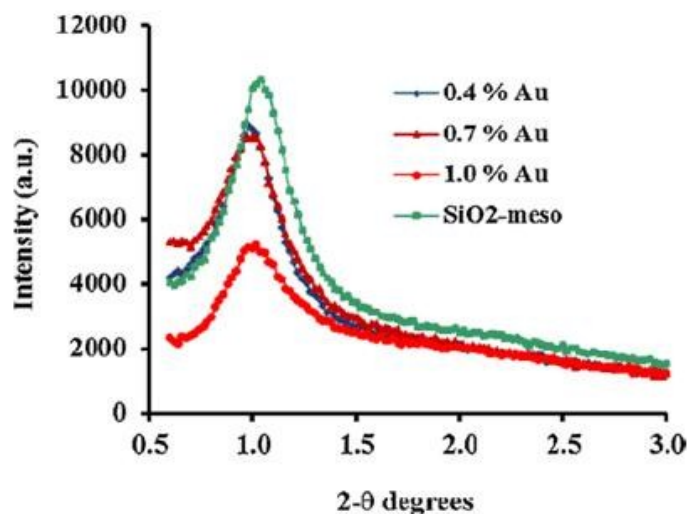


Figure 3.3. Low angle XRD profiles of mesoporous silica material and Au/SiO₂-meso at different Au loadings.

Figure 3.4 shows the wide angle XRD patterns of the catalysts loaded with gold at 0.4, 0.7 and 1.0%. The well resolved characteristic diffraction peaks at around 38°, 45° and 65°, assigned to the (1 1 1), (2 0 0), and (2 2 0) lattice planes of face-centered cubic structure of gold, indicate that gold is in

crystalline form after the catalysts synthesis, and reveal the presence of metallic gold species [224, 400]. It can be noticed that for a 0.4 and 0.7% gold loadings, the diffraction peaks are weak. This can be attributed to the low Au loading and the better Au crystallite dispersion on the mesoporous silica support.

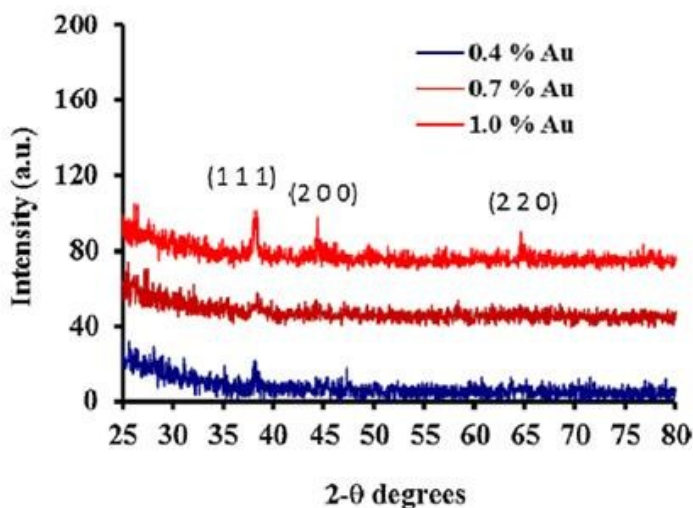


Figure 3.4. Wide angle XRD profiles of Au on mesoporous silica at different Au loadings.

3.4.1.3. Transmission electron microscopy

Figures 3.5a–f show the transmission electron microscopy (TEM) micrographs of the mesoporous silica material, and Au catalysts with Au loading of 0.4, 0.5, 0.7, 0.8 and 1.0%, respectively. The TEM image of the mesoporous silica material (Figure 3.5a) clearly shows the wormhole pore arrangement structure confirming the small angle XRD analysis stipulating the existence of wormhole structure. It can be understood from these results that unlike SBA-15 which have a hexagonal framework structure with cylindrical mesopores, the present mesoporous material presents a wormhole-like framework structure containing interconnected 3D-mesopores that can be ideal for the minimization of diffusion limitation phenomena often encountered in adsorption and catalytic reactions.

The TEM image of 0.4% Au/SiO₂-meso shows similar wormhole-like framework mesostructure (Figure 3.5b). The average pore size is generally up to 3–4 nm. Some of gold crystallites are distinguishable and their dimension can be located between 11 and 18 nm, with an average value of ~14 nm then excluded from the pores and indicating that they are on the external catalyst surface. The TEM image of 0.7 and 0.8% Au/SiO₂-meso shows identical pattern where Au crystallites seemed

to be better dispersed having dimensions between 3 and 14 nm, with an average values of ~7 and 9 nm, respectively (Figures 3.5d and e). Au crystallites in 0.5 and 1.0% Au/SiO₂-meso have larger size up to 21 nm with average values of circa 11 for both catalysts (Figures 3.5c and f).

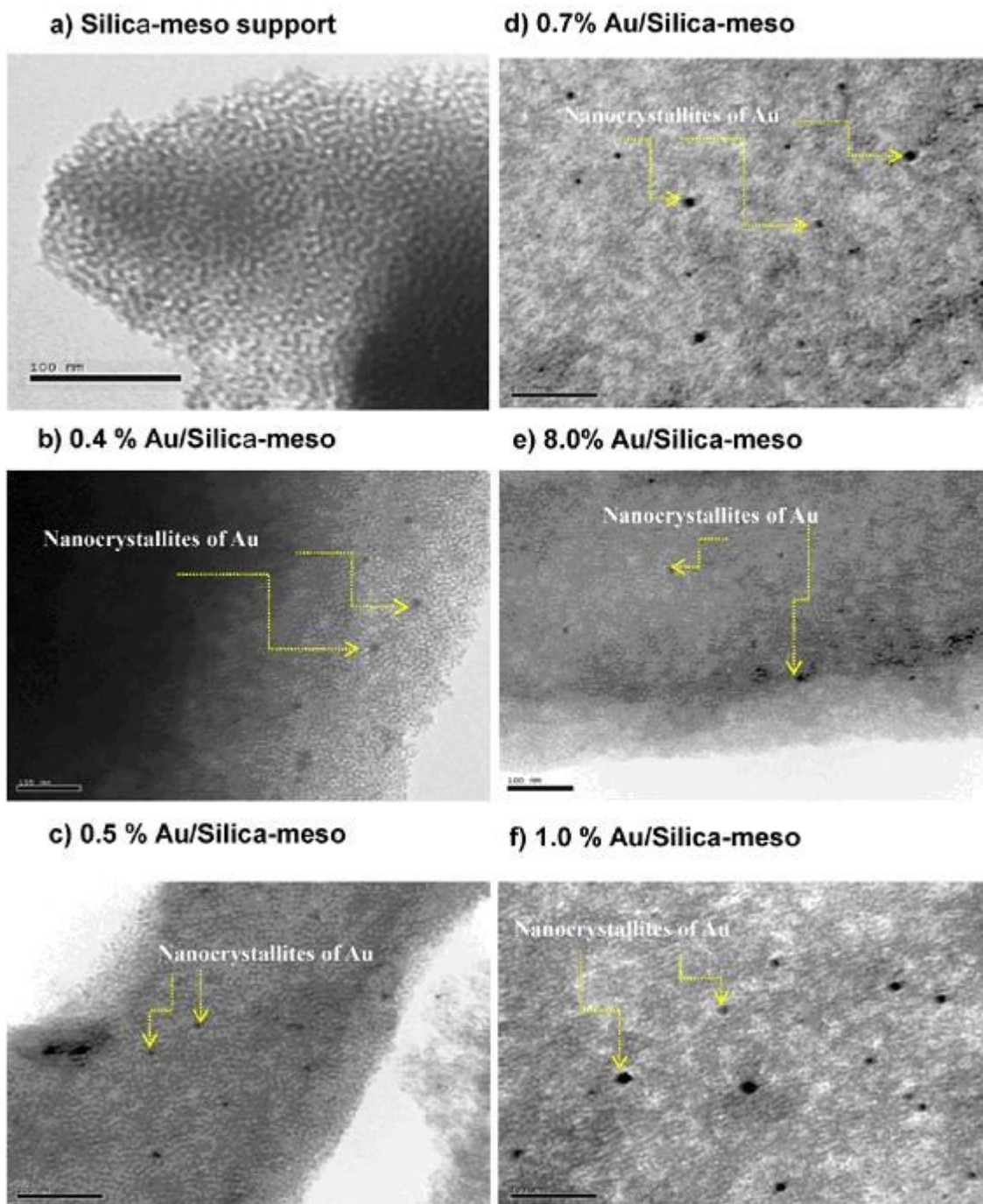


Figure 3.5. (a) TEM micrographs of mesoporous silica material; (b) 0.4% Au/SiO₂-meso; (c) 0.5% Au/SiO₂-meso; (d) 0.7% Au/SiO₂-meso; (e) 0.8% Au/SiO₂-meso; (f) 1.0% Au/SiO₂-meso.

Table 3.2 compares the average Au crystallite dimensions obtained by TEM and those computed using wide angle XRD analysis data and Scherrer's equation. The average Au crystallite sizes obtained with the two methods are somewhat different. As the estimated crystallite size using Sherrer's equation gives a rough estimate of the crystallite size and is known to lack precision, the more trustful crystallite size data could be those estimated using TEM analysis.

Table 3.2. Average crystallite size of Au catalyst samples obtained with TEM and XRD analysis of catalyst samples prepared at different Au loadings.

Catalyst	TEM average metal crystallite size (nm)	XRD average metal crystallite size (nm)
0.4%Au/SiO ₂ -meso	14 ± 1	20 ± 1
0.5%Au/SiO ₂ -meso	11 ± 1	-
0.7%Au/SiO ₂ -meso	7 ± 1	14-15 ± 1
0.8%Au/SiO ₂ -meso	9 ± 1	-
1.0%Au/SiO ₂ -meso	11 ± 1	24-25 ± 1

3.4.1.4. X-ray photoelectron spectroscopy (XPS) analysis

The oxidation state of the loaded gold on the catalysts was investigated by XPS. The presence of Au 4f, Si 2p, Si 2s, C1s and O photoelectron peaks in all catalysts was detected by XPS measurements. For the sake of clarity only Au 4f photoelectron peaks are presented and discussed for the Au/SiO₂-meso catalysts with Au loadings of 0.4, 0.7 and 1.0%. The spectra of the Au 4f peaks for the 3 catalysts are depicted in Figures 3.6a–c for Au loadings of 0.4, 0.7 and 1.0%, respectively. The experimental curves of Au 4f core levels spectra present well-defined 2 spin orbit split Au 4f_{5/2} and 2Au 4f_{7/2} components, after the peak deconvolution process using Kratos software. Table 3.3 summarizes the binding energies (BE) of these spin orbit split components for all Au loadings. The components Au 4f_{7/2} (1) and Au 4f_{7/2} (2) binding energies are important and can be used to determine the oxidation state of gold species [414-416]. The Au 4f_{7/2} (1) component with BE values between 84.1 and 84.4 eV can typically be assigned to pure metallic Au⁰ species for all Au loadings [409, 414, 416]. The 4f_{7/2} (2) component at 85.2–85.5 eV ascertains the presence of Au⁺ in catalyst loadings of 0.4 and 0.7%, while the 4f_{7/2} (2) component at ~86.5 eV confirmed the presence of Au³⁺ species in catalyst loading of 1.0% [416]. Owing to the peak surfaces of Au⁺¹ and Au⁺³ species which are

significantly smaller than that of Au⁰ species, most of the gold crystallites are present in the metallic state even though Au⁺ and Au³⁺ presence can be detectable.

Table 3.3. Binding energies of Au 4f_{7/2} and 4f_{5/2} deconvoluted peaks of catalyst samples prepared at different Au loadings.

Au loading (%)	4f _{7/2} (1) (eV)	4f _{5/2} (1) (eV)	4f _{7/2} (2) (eV)	4f _{5/2} (2) (eV)
0.4	84.20	87.85	85.45	89.05
0.7	84.10	87.60	85.20	88.80
1.0	84.37	88.07	86.47	90.17

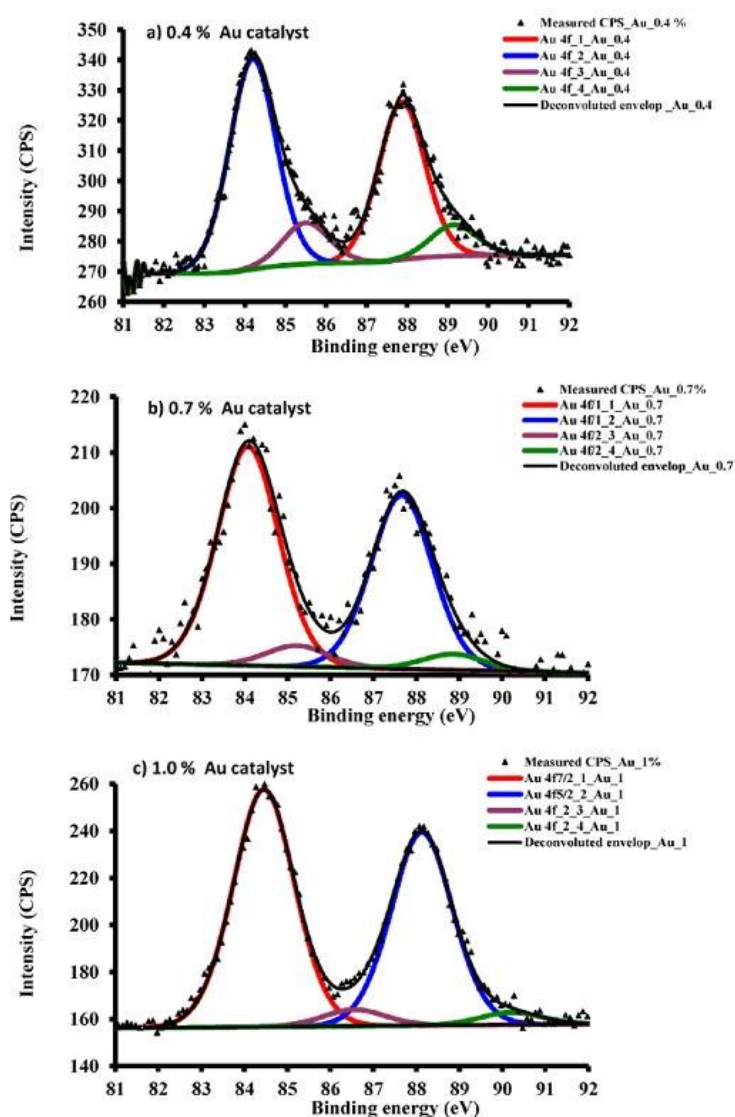


Figure 3.6. XPS-spectra of Au 4f photoelectron peak for: (a) 0.4% Au/SiO₂-meso; (b) 0.7% Au/SiO₂-meso; (c) 1.0% Au/SiO₂-meso.

3.4.2. Catalyst activity

As mentioned in the introduction section, gold nonclusters dispersed on ordered mesoporous silica has never been tested to evaluate their capability to partially oxidize lactose to LBA. The next sections will treat on the optimization of lactose conversion to LBA over Au/SiO₂-meso as an oxidation catalyst where main conditions such as the reaction temperature, pH, catalyst to lactose ratio and catalyst gold loading are investigated.

3.4.2.1. Effect of Au catalyst loading on lactose oxidation kinetics

Figure 3.7 shows the kinetic profiles of lactose oxidation to LBA over Au/SiO₂-meso at 0.7%. The Au/SiO₂-meso silica at 0.7% Au loading exhibited a pretty good activity to oxidize lactose to LBA. The lactose oxidation over this catalyst exhibited favorable and outstanding lactose conversion to LBA where the rates of lactose consumption as well as LBA formation were markedly high and the lactose conversion essentially completed (it reached about 100%) after 80 min of reaction. It is worth mentioning that lactose was almost depleted after only 80 min of reaction where LBA concentration reached a value of 7.8 g/L starting from exactly 7.5 g/L of lactose. This means that 7.5/342.29 ~0.022 moles of lactose were oxidized to give 7.8/358.3 ~0.022 moles of LBA consequently, 100% of selectivity towards LBA formation was reached using this catalyst.

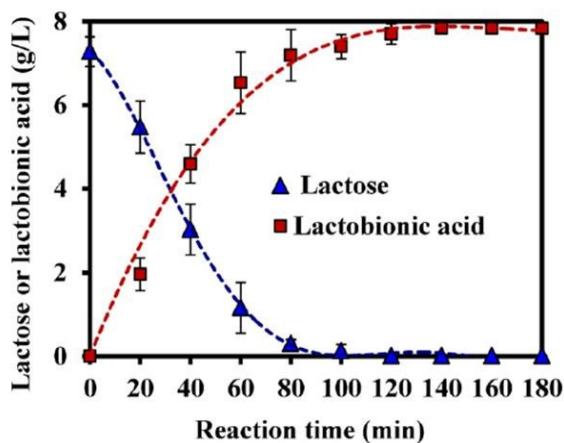


Figure 3.7. Kinetic profiles of lactose uptake and LBA production during lactose oxidation over 0.7% Au/SiO₂-meso catalyst. Conditions: T = 65°C; pH 9; Catalyst to lactose ratio R = 0.2. Bares stand for the standard deviation for two repetitions.

The oxidation of lactose over other investigated catalysts (0.4, 0.5, 0.8 and 1% Au/SiO₂-meso) showed clearly much lower kinetic patterns. Even if the conversion of lactose was not complete for these catalysts, the selectivity towards lactose was also 100%.

At Au loading of 0.4, 0.5 and 1%, the formation of larger metal crystallites (see Table 3.2) built up and lowered the metal availability at the reaction surface area. This diminution of the catalyst dispersion is one possible reason which could presumably affect the catalyst activity. However, the small metal cluster size is not the only sufficient condition to ensure a good catalyst activity. It is well known that the oxidation state of metals is a very important parameter in the catalytic activity. In the case of the carbohydrate oxidation over gold catalysts, the oxidation state of gold species could play an important role in the catalyst activity and this has been hardly investigated. As shown by XPS analysis, our results indicate that the presence of oxidized gold species may affect the activity of gold catalysts in carbohydrate oxidation.

Although some works found in the literature for the oxidation of alcohols over Au supported catalysts reported the presence of mainly the metal Au⁰ with the presence of Au⁺ and rarely Au³⁺ species [417-418], in the similar manner as reported in the present work, however, it cannot be stated clearly which species are responsible for the Au oxidation activity in the liquid phase and the role of the oxidation state of gold is still matter of discussion.

Exploiting the determination of the initial reaction rate of lactose conversion to LBA for each investigated Au loading, as evaluated by Eq. (1):

$$r_o = \left. \frac{d[LBA]_t}{dt} \right|_{t=0} \quad (1)$$

allowed to show that maximum catalyst activity was obtained at Au loading of 0.7% as depicted in Figure 3.8. As we can observe in this figure, the trend in the particle size with Au loading variation shows a minimum value of ~7 nm at Au loading of 0.7% where the catalyst activity is at its maximum value. It is possible to state that the Au catalyst, as prepared by the reported procedure, is very sensitive to the catalyst loading which may control the gold particle size. Furthermore, in the liquid phase reactions, which is the case for the present work, the activity of supported gold catalysts could depend on the gold cluster size and the reaction kinetics could be structure-sensitive depending on the support chemical nature [419], particularly if the support is a metal oxide which is the case in the present study. This could be ascribed to the significant interactions between the noble metal and the support [420]. Actually, the reason why this behavior occurs is not known for the moment and needs deep investigations.

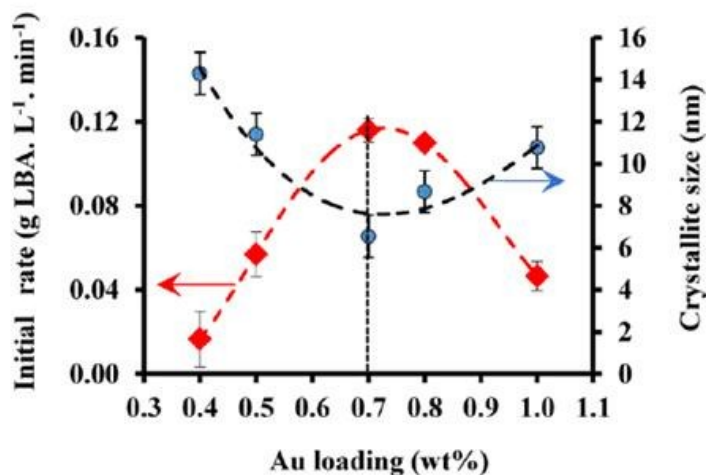


Figure 3.8. Trends of the initial rate and the Au crystallite size versus Au loading. Bares stand for the standard deviation for two repetitions for each catalyst synthesis.

The initial rate r_0 is plotted versus the gold crystallite size as depicted in Figure 3.9, shows a volcano-type tendency if the trivial point (0, 0), corresponding to the reaction activity of the pure support, *i.e.*, SiO₂-meso, which was verified to not exhibit any oxidation activity) is included in the data. From this figure, the crystallite size where maximum of activity is obtained is in the vicinity of 6 nm. This finding fairly corroborates those of other works reported in the literature for reactions catalyzed by gold [186, 188, 421].

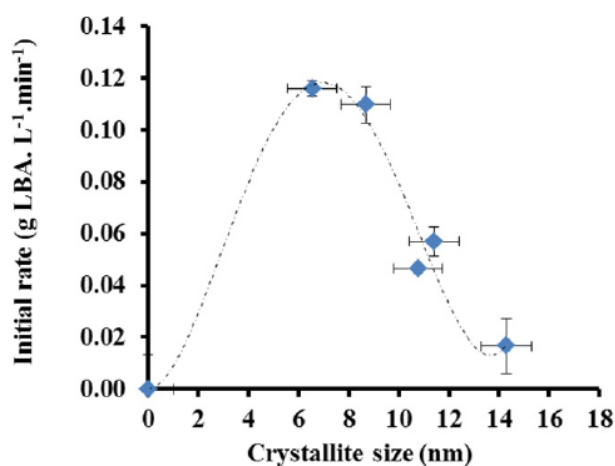


Figure 3.9. Trend of the initial rate versus the Au crystallite size. The vertical bares stand for the standard deviation in the initial rate while horizontal bares stand for the standard deviation in the crystallite size for two repetitions for each catalyst synthesis. Dashed line represents only a general tendency.

3.4.2.2. Effect of catalyst/lactose ratio on the oxidation kinetics using 0.7% Au/SiO₂-meso

In our recent work [85], using 0.21 g catalyst (1.02%Pd–0.64%Bi/SBA-15)/g lactose for the microaerobic oxidation of lactose, we found the maximal conversion of lactose to LBA at 65°C in alkaline conditions (pH 9.0). Based on these results, in this study we have evaluated the effect of different catalyst/lactose ratio on the oxidation of lactose over 0.7% Au/SiO₂-meso at 65°C and pH 9.0 under agitation of 900 rpm, using air (40 mL/min) as oxidizing agent. Figure 3.10 shows the effect of this ratio on the reaction kinetics. The evaluation effect of this ratio on the initial reaction rate r_0 as depicted in Figure 3.10, allows clearly to observe that the kinetic behavior is well favored at $R = 0.2$ and levels off. Irrefutably, the more concise observation of the reaction kinetics with r_0 determination at the beginning of the reaction asserted that the reaction kinetics can be considered identical at R ratios of 0.2 and 0.3. Decreasing this ratio to 0.1 led to a significant decrease in the reaction kinetics. From these results, it is decided to select the 0.2 catalyst/lactose ratio as the optimal value for the evaluation of the effects of temperature and pH on the lactose conversion. This ratio is comparable to that obtained in our recent work [85] for the catalytic oxidation of lactose over bimetallic 1.02%Pd–0.64%Bi/SBA-15 catalyst, with the advantage that in the case of gold catalysts, the bubbling of nitrogen, required to avoid the catalyst' over oxidation when using Bi–Pd catalysts, is not necessary, making easier the reaction control.

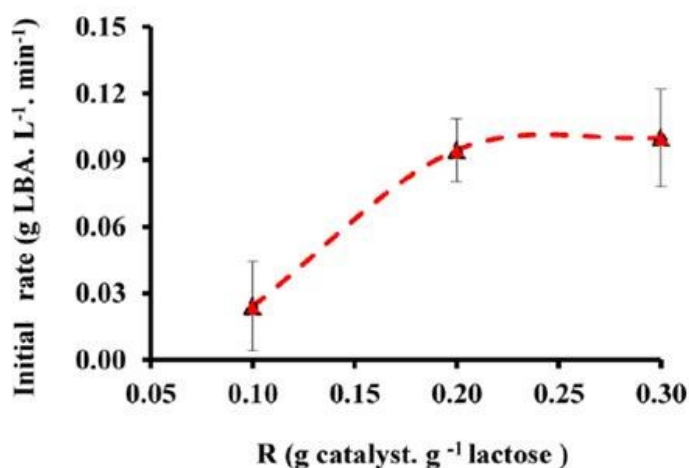


Figure 3.10. Effect of the catalyst/lactose ratio, R , on the initial reaction rate, r_0 during the partial oxidation of lactose to LBA over 0.7% Au/SiO₂-meso catalyst. Conditions: T=65°C; pH 9.0. Bars stand for the standard deviation for two repetitions of the catalyst synthesis.

3.4.2.3. Effect of pH on the oxidation kinetics using 0.7% Au/SiO₂-meso

The influence of pH, in the range of 7–10, on the lactose conversion was investigated using the 0.7%Au/SiO₂-meso at 0.2 catalyst/lactose ratio. During these experiments, temperature, agitation and airflow were kept constant at 65°C, 900 rpm and 40 mL/min, respectively. As shown in Figure 3.11, the oxidation of lactose over gold catalyst is pH-dependent as reported for the oxidation of other carbohydrates over metal catalysts [85-86, 404]. The initial reaction rate was clearly enhanced by increasing the pH value up to 9.0, where a maximum of activity was reached which led to nearly 100% lactose conversion with 100% selectivity towards LBA. Similar to our recent findings for lactose oxidation over bimetallic 1.02%Pd–0.64%Bi/SBA-15 catalyst [86], it has been recently reported that gold catalysts could be deactivated by the strong adsorption of the reaction products, which occupy the active sites of the catalyst surface, when pH is neutral (pH 7) [13]. However, the catalyst activity declined readily at pH 10. This strongly alkaline condition induced a partial decomposition of the catalyst due to the dissolution of silica material at very high alkaline conditions. Similar results were reported by Mirescu and Prüße [14], who found a pronounced decrease in the activity and selectivity in the oxidation of lactose with Au/TiO₂ and Au/Al₂O₃ catalysts, when the pH values were higher than 9.0. This behavior was also reported in our investigations on the partial oxidation of lactose to LBA over bimetallic Pd–Bi/SBA-15 catalyst [85-86]. Consequently, the pH of 9.0 was kept constant to the further experiments evaluating the effect of the reaction temperature on the catalytic activity of the 0.7%Au/SiO₂-meso.

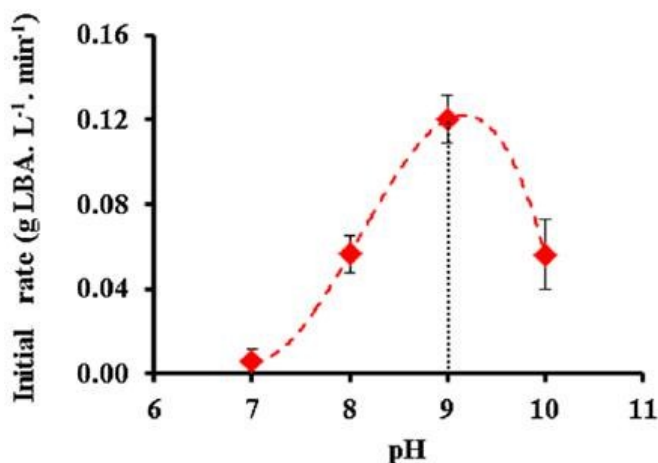


Figure 3.11. Effect of the pH on the initial reaction rate, r_0 during the partial oxidation of lactose to LBA over 0.7% Au/SiO₂-meso catalyst. Conditions: T = 65°C; R = 0.2. Bares stand for the standard deviation for two repetitions of the catalyst synthesis.

3.4.2.4. Effect of temperature on the oxidation kinetics using 0.7% Au/SiO₂-meso

The effect of temperature on lactose oxidation kinetics over fresh 0.7% Au/SiO₂-meso catalyst was investigated in the range (50–70°C).

The pH has been kept constant at 9.0 and the ratio catalyst/lactose used was 0.2 g catalyst/g lactose. The reaction kinetics in terms of production rate of LBA versus the temperature variation is depicted in Figure 3.12. At 50°C the reaction kinetics is slow. The main reason could be the poor activation state of the reaction at this temperature. The reaction kinetics carried out at 60°C exhibited clearly a more pronounced rate of LBA production. The greater activation of the reaction at this temperature could constitute the main reason of the kinetic improvement. Even if the obtained rate is relatively high, it is a room to further improvement at higher temperature. Indeed, the kinetics of lactose oxidation to LBA performed at 65°C showed during the first 100 min of reaction a very high rate of lactose depletion, reaching a conversion of almost 100%. After only 80 min, the lactose conversion was 96%. The selectivity of the catalyst during the reaction of lactose oxidation into LBA was found always 100% (see Figure 3.7). The rate of LBA production increased significantly and reached ~ 0.12 g LBA L⁻¹ min⁻¹, as exhibited in Figure 3.12. The kinetics of lactose oxidation performed at 70°C exhibited an acceptable but slower consumption rate of lactose, reaching a conversion 94% after 100 min and residual non consumed lactose representing about 6% of the initial concentration even after prolonged time of reaction (results not shown). This indicates that the reaction halted after 100 min due to a possible depletion of oxygen in the reaction medium. Indeed, at relatively higher temperature (80°C), the oxygen solubility decreased readily and its concentration is almost zero at atmospheric pressure as measured using the optic fiber oxygen sensors. Consequently, the available O₂ concentration was too low to sustain and maintain the oxidation activity, which could explain the decrease in the lactose conversion. This is clearly shown in terms of LBA production rate (Figure 3.12), where further increment in the temperature higher than 65°C affected markedly the kinetics due to the lack of oxygen at the surface of the catalyst. However, it is worth to mention that the temperature has not affected the catalyst selectivity towards LBA production, which remained 100% in all cases.

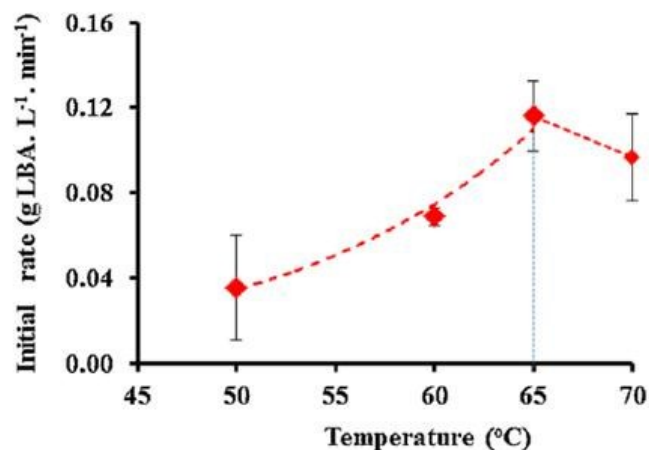


Figure 3.12. Effect of the reaction temperature on the initial reaction rate, r_0 during the partial oxidation of lactose to LBA over 0.7% Au/SiO₂-meso catalyst. Conditions: pH 9.0; R = 0.2. Bares stand for the standard deviation for two repetitions of the catalyst synthesis.

3.5. Conclusions

For the first time, gold catalysts supported on mesoporous silica material functionalized with silane coupling agent (BTESPTS) were successfully investigated for lactose oxidation using air as oxidizing agent.

XPS analysis suggested that gold nanoparticles were present in the catalysts as both metallic and oxidized species. Furthermore, these nanoparticles seemed to be within the mesoporous framework and on the surface of silica material, as indicated by TEM measurements.

After catalyst evaluation in a certain range of gold loadings, catalyst/lactose ratio, temperature and pH, the 0.7%Au/SiO₂-meso catalyst was found highly active (100% of conversion, after only 80–100 min of reaction) and 100% selective towards LBA when it was added at a ratio of 0.2 catalyst/lactose under the reaction conditions of 65°C, pH of 9, 40 mL/min, 900 rpm. Comparing with the palladium or bismuth-promoted palladium supported catalysts, the reaction control using 0.7%Au/SiO₂-meso catalyst is easier because the control of oxygen flow, required to avoid the over oxidation of Pd and Bi–Pd catalysts, is not necessary, and additionally, no side products are detected. Thus, due to the ease of synthesis, as well as because of its excellent catalytic performance, the 0.7%Au/SiO₂-meso catalyst can be regarded as major breakthrough on the way to an industrial process of catalytic oxidation of lactose.

Chapter 4. Characteristics and lactose oxidation activity of gold catalysts supported on mesoporous silica synthesized in the presence of thioether functional groups

This chapter presents the influence of different molar ratios of BTESPTS/TEOS in the synthesis mixture of Au/MSM on the characteristics and activity for the lactose oxidation.

4.1. Abstract

Gold catalysts supported on mesoporous silica materials (Au/MSM) were synthesized by co-condensation of a mixture of *bis* [3-(triethoxysilyl) propyl] tetrasulfide (BTESPTS), tetraethyl orthosilicate (TEOS) and the gold precursor (HAuCl₄) in acidic media, using the triblock co-polymer EO₂₀PO₇₀EO₂₀ (P123) as template. In order to investigate the effect of the thioether functionalities on the characteristics and lactose oxidation activity of the catalytic materials, different BTESPTS/TEOS molar ratios were added to the synthesis mixture. The characterization analyses (XRD, N₂-physisorption, and TEM) indicated that with increasing the BTESPTS/TEOS molar ratio, the structure of the catalysts changed from a highly ordered 2D hexagonal structure to a mixed hexagonal-vesicle and cellular foam structure. This mesostructure transformation affected the catalytic activity, mainly by the accessibility of reagent to the AuNPs. Although all the Au/MSM catalysts were 100% selective towards the desired lactobionic acid, the samples synthesized with BTESPTS molar concentrations of 6-10% showed the highest catalytic activity (100% lactose conversion, after about 120 min of reaction). The coexistence of metallic and oxidized Au species with relative abundances of Au⁰ (80-85%) >>>Au⁺¹ (10-15%) > Au⁺³ (4-6%) was revealed by XPS analysis.

4.2. Introduction

One of the most important contributions to the catalysis science has been the discovery of the catalytic activity of gold in the late 80s, by the Haruta's group [167]. Since then, gold at the nanoscale has been deeply studied as a catalyst in a variety of industrially relevant reactions, including oxidation and hydrogenation of organic compounds [11, 90, 168-170], C—C coupling reactions [422-426], water-gas shift reaction [171-173], acetylene hydrochlorination [175, 427], direct synthesis of hydrogen peroxide [176], reduction of NO to N₂ [177-178] and the addition of nucleophiles to acetylenes [179]. As a result of this wide investigation on gold catalysis, nowadays it is well known

that the catalytic activity of supported gold catalysts is strongly influenced by different factors, including the size and shape of gold nanoparticles (AuNPs), the synthesis procedure, the support's nature, the gold-support interface interactions, as well as the oxidation state of gold [146].

Owing to their unique physicochemical and mechanical properties (ordered and controllable porous structure, high surface area, pore volume, thermal stability, easy functionalization and good biocompatibility), mesoporous silica materials (MSM) are very suitable as catalyst supports, since they provide high dispersion of metal nanoparticles and facilitate the access of the substrates to the active sites [18]. However, the interaction of gold with most of the oxide material supports is weak, as demonstrated by experimental and theoretical calculations where the binding energy of Au to an oxide support was found to be weaker than the Au–Au bonds leading to agglomeration [428]. Due to the low isoelectric point of silica (~ 2), the deposition-precipitation method is not appropriate for the synthesis of gold catalysts supported on MSM (Au/MSM), because under the high pH conditions required to hydrolyze the HAuCl_4 , the weak interaction between the negatively charged silica surface and the $[\text{Au}(\text{OH})_n\text{Cl}_{4-n}]^-$ species hinders the gold adsorption and facilitates the mobility of AuNPs, which can sinter easily during the synthesis process, especially during the calcination step, yielding low gold loadings and inactive catalysts [19]. Consequently, various alternative methods have been proposed, which have been comprehensively reviewed recently [146]. Among them, the one-pot synthesis method in the presence of *bis*-[3-(triethoxysilyl) propyl] tetrasulfide (BTESPTS, $\text{C}_{18}\text{H}_{42}\text{O}_6\text{S}_4\text{Si}_2$) as thioether functionality proposed by the Richards's group [280], is one of the simplest procedures allowing the synthesis of highly active and robust Au/MSM. The catalysts synthesized following this approach have demonstrated excellent catalytic performance in various redox reactions [281, 429]. We prepared recently various Au/MSM with different nominal gold loadings (0.4-1.0%), in which the BTESPTS/TEOS molar ratio was about 0.04 (corresponding to a BTESPTS molar concentration in the synthesis mixture of about 7.2%). These catalysts were found highly active and 100% selective towards lactobionic acid (LBA) from lactose oxidation. However, unlike of the SBA-15 which has a 2D hexagonal framework structure with cylindrical mesopores, they exhibited wormhole-like framework structure with interconnected 3D-mesopores [11].

Taking into account that this synthesis method has been scarcely studied, with the aim of getting a better understanding of the effect of the thioether functionalization on the characteristics of Au/MSM catalysts, herein we synthesized various Au/MSM samples varying the BTESPTS/TEOS molar ratio

from 0 to 0.11, corresponding to molar concentrations of the thioether functionality in the synthesis mixture from 0 to 18%. These catalysts were characterized by means of BET surface, powder X-ray diffraction (XRD), X-ray photoelectron spectroscopy (XPS) and transmission electron microscopy (TEM). The catalytic activity of the synthesized Au/MSM materials was investigated on the partial oxidation of lactose, under the optimal conditions found in our recent works [11, 90].

4.3. Materials and methods

4.3.1. Materials

All reagents were of the highest purity and were used without further purification. Gold (III) chloride trihydrate ($\text{HAuCl}_4 \cdot 3\text{H}_2\text{O}$) ($\geq 99.9\%$), tetraethyl orthosilicate (TEOS) ($\geq 99.0\%$), *bis* [3-(triethoxysilyl) propyl] tetrasulfide (BTESPTS) ($\geq 90.0\%$), α -lactose monohydrate ($\geq 96\%$) and lactobionic acid ($\geq 97\%$) were purchased from Sigma Aldrich. The triblock co-polymer P123 ($\text{EO}_{20}\text{PO}_{70}\text{EO}_{20}$, $M_{av}=5900 \text{ g}\cdot\text{mol}^{-1}$) was graciously offered by BASF. Sodium hydroxide solution 50% and anhydrous sodium acetate, both HPLC grade from Fluka, were used for eluents preparation for HPLC analysis.

4.3.2. Catalysts preparation

Gold catalysts were synthesized following a similar procedure to that of mesoporous silica SBA-15 [145], as reported in our previous work [11]. The Au/MSM catalysts were synthesized by co-condensation of a mixture of TEOS, BTESPTS and HAuCl_4 in acidic media, using P123 as template. In a typical synthesis procedure, after the complete dissolution of P123 in 2N HCl solution, the temperature was increased to 40°C , and a mixture of TEOS and BTESPTS was added drop wise under continuous and vigorous agitation. Subsequently, the proper amount of HAuCl_4 in 2N HCl solution was added drop wise, in order to obtain a nominal gold loading of 0.7%. The obtained mixture was stirred at 600 rpm for 24 h at 40°C , and then it was hydrothermal aged under static conditions for 72h at 100°C . After vacuum filtration, the recovered solids were thoroughly washed with water and ethanol at room temperature. Finally, the catalysts were vacuum-dried overnight at 100°C and then calcined at 500°C for 5h at a heating rate of $1^\circ\text{C}/\text{min}$, using a programmable oven. When 4 g of P123 were used, the molar composition of each mixture was $x\text{TEOS}:(0.041 - x)\text{BTESPTS}:0.24\text{HCl}:6.67\text{H}_2\text{O}:8.75 \times 10^{-5}\text{HAuCl}_4$, where $x = 0.041, 0.0406, 0.0402, 0.0394, 0.0385, 0.0377, 0.0369, 0.0361, 0.0353, 0.0344$ and 0.0336 , corresponding to BTESPTS molar concentrations of 0, 1, 2, 4, 6, 8, 10, 12, 14, 16 and 18%, respectively. The calcined catalysts were designated F0, F1,

F2, F4, F6, F8, F10, F12, F14, F16 and F18, corresponding to the different BTESPTS molar concentrations, respectively.

4.3.3. Catalysts characterization

Powder X-ray diffraction (XRD) patterns were obtained with an Ultima III Rigaku monochromatic diffractometer using $\text{CuK}\alpha$ radiation ($\lambda=1.5406\text{\AA}$). Small angle powder diffraction patterns were acquired at a scanning rate of $1^\circ/\text{min}$ in the 2θ range of $0.6\text{-}3^\circ$, while wide angle powder XRD was obtained at the same scanning rate in the 2θ range $25\text{-}80^\circ$.

Transmission electron microscopy (TEM) images were taken on a JEM-3010 electron microscope (JEOL, Japan) with an acceleration voltage up to 200 kV. The catalysts samples were suspended in methanol and ultrasonically treated during 10 minutes. Then, the suspension ($5\ \mu\text{L}$) were disposed uniformly and dried on a nickel grid.

Nitrogen adsorption/desorption isotherms of the calcined samples were obtained using a volumetric adsorption analyzer (Model Autosorb-1, Quantachrome Instruments, Boyton Beach, FL) at -196°C . Before the adsorption analysis, the samples were degassed for 3h at 200°C . Total pore volume was estimated from the amount adsorbed at 0.99 relative pressures. Pore size distributions were calculated using the desorption branch of the N_2 adsorption/desorption isotherms and the Barrett-Joyner-Halenda (BJH) method [408].

The catalyst surface and the oxidation state of gold in some representative Au/MSM samples were studied by X-ray Photoelectron Spectroscopy (XPS) analysis using an Axis-Ultra system spectrometer from Kratos (UK), equipped with an electrostatic analyzer of large ray, a source of double X-rays Al-Mg without monochromator and an Al source with monochromator. The pressure in the XPS room was maintained between 5×10^{-9} and 5×10^{-8} torr during the analysis. All the spectra were recorded with the Al monochromatic source with a power of 300 Watts. The flyover spectrums used to determine the elementary composition was recorded with pass energy in the analyzer of 160 eV and an energy step of 1 eV, using lenses in hybrid mode, which maximizes the sensitivity. The detailed spectra with high resolution were recorded with pass energy of 20 or 40 eV, and step energy of 50 or 100 meV. The spectra with high resolution are used for the chemical analysis [409]. The adjustment of the envelope calculated with the experimental spectrum was carried out using

CasaWPS software from Kratos (UK). The binding energy (BE) scale was calibrated by measuring C1s peak (BE = 285.0 eV) from the surface contamination.

4.3.4. Lactose oxidation experiments

Lactose oxidation experiments were carried out at atmospheric pressure in a thermostated and magnetically stirred 300 mL-glass reactor, following the optimal conditions found in our previous works [11, 90]. In a typical oxidation reaction, 175 mL of 20 mM lactose solution were heated under continuous agitation (600 rpm) until the temperature reached 65°C, while nitrogen (500 mL·min⁻¹) was simultaneously bubbled for stripping off the dissolved oxygen. Subsequently, the stirring was increased to 900 rpm, the catalyst was added at a 0.2 catalyst/lactose ratio and the pH of the solution was adjusted to 9.0 by the addition of few drops 1M NaOH aqueous solution. Then, air was bubbled through the reaction mixture at a constant flow rate of 40 mL·min⁻¹. During the reaction, the pH value was kept constant by adding 1M NaOH aqueous solution, by means of a pH STAT Titrator (Metrohm® 842 Titrand®, Switzerland), and the dissolved oxygen concentration was monitored using an oxygen probe (Ocean Optics, Inc., USA) connected to a fiber optic sensor system (TauTheta Instruments LLC, USA).

The time 'zero' of the reaction corresponded to the moment when air was bubbled through the reaction mixture. Triplicate reactions were carried out during 180 min. Liquid samples were taken at regular intervals for the subsequent HPLC analyses.

4.3.5. Reaction sample analysis

Samples of the reaction mixture were analyzed using a chromatographic system DX- ICS 2500 (Dionex, USA) equipped with a gradient pump GP50 and an electrochemical detector ED50 with a thin-layer type amperometric cell outfitted with gold electrodes and an Ag/AgCl reference electrode. The chromatographic separation of lactose and LBA was performed on a CarboPac PA1 analytical column (4mm×250 mm i.d., Dionex, USA) in conjunction with a CarboPac PA1 guard column (4mm×50mm i.d., Dionex, USA). Sodium hydroxide solution 50% and anhydrous sodium acetate (NaOAc) were used to prepare the eluents (0.1M NaOH and 0.1M NaOH-0.5M NaOAc) in filtered and vacuum-degassed HPLC-Grade water. Chromeleon software (Dionex, USA) was used to perform all the calibration and integration of chromatographic data. The complete details of the analysis method can be found in our previous work [90].

4.4. Results and discussion

4.4.1. Catalysts characterization

4.4.1.1. X-ray diffraction

The low-angle XRD patterns of the mesoporous silica SBA-15 and Au/MSM catalysts synthesized with different BTESPTS/TEOS molar ratios are presented in Figure 4.1. Three well-resolved diffraction peaks: one high-intensity peak at about $2\theta=0.9^\circ$, and two low-intensity peaks at circa $2\theta=1.6^\circ$ and 1.8° , corresponding to the (100), (110), and (200) reflections, respectively, can be seen in F1 and F2 samples, indicating that catalysts synthesized with low molar concentrations of BTESPTS retained the bi-dimensional $p6mm$ hexagonal symmetry typical of the mesoporous SBA-15 materials [145]. However, the patterns of F1 and F2 samples shifted to a higher value and showed a slight decrease in the diffraction-peaks' intensity, indicating that the incorporation of both the thioether functionalities and gold caused some loss of symmetry, as well as an effect on the interplanar distance and angle of the mesoporous SBA-15 [90].

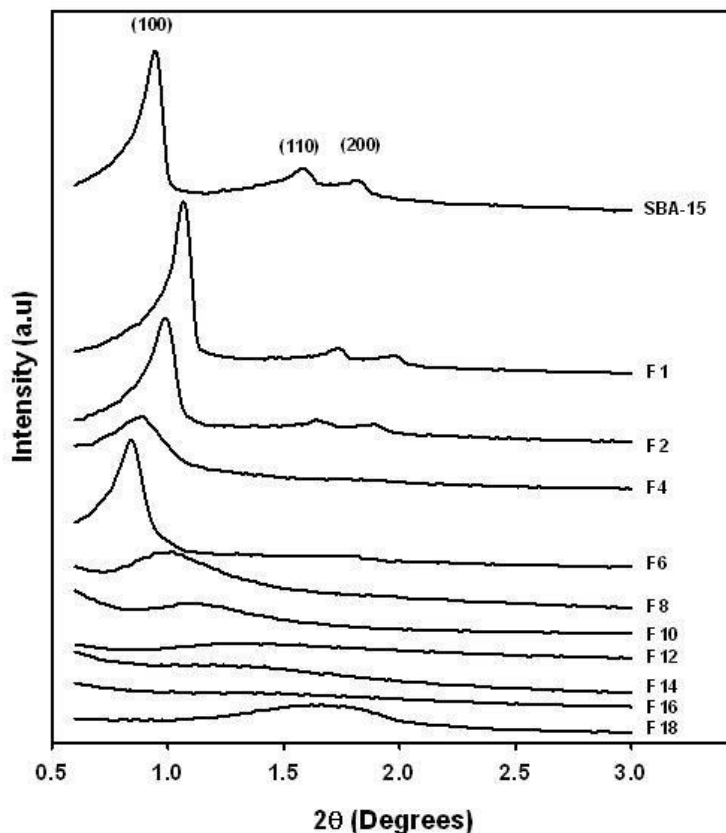


Figure 4.1. Low-angle XRD patterns of mesoporous silica SBA-15 and Au/MSM catalysts synthesized with different BTESPTS/TEOS molar ratios.

On the other hand, it can be observed that with increasing the molar concentration of TESPTS in the synthesis mixture, the (110) and (200) diffraction peaks became less intense and ultimately disappeared, revealing that the incorporation of the thioether functionalities destroyed partly the ordered structure of the mesoporous SBA-15 [430]. In samples with molar concentration of BTESPTS higher than 10%, the main (100) peak almost disappeared, indicating that from this concentration level, the BTESPTS might hinder the condensation of the silica source (TEOS) to form an ordered mesoporous framework. This trend might be due to the formation of a micro-emulsion between the BTESPTS and the triblock co-polymer P123 during the synthesis process, which could destroy or alter the ordered mesoporous structure of silica, as demonstrated by Liu et al. [431] during the preparation of thioether-bridged mesoporous organosilicas by co-condensation of a mixture of BTESPTS and tetramethoxysilane in the presence of P123.

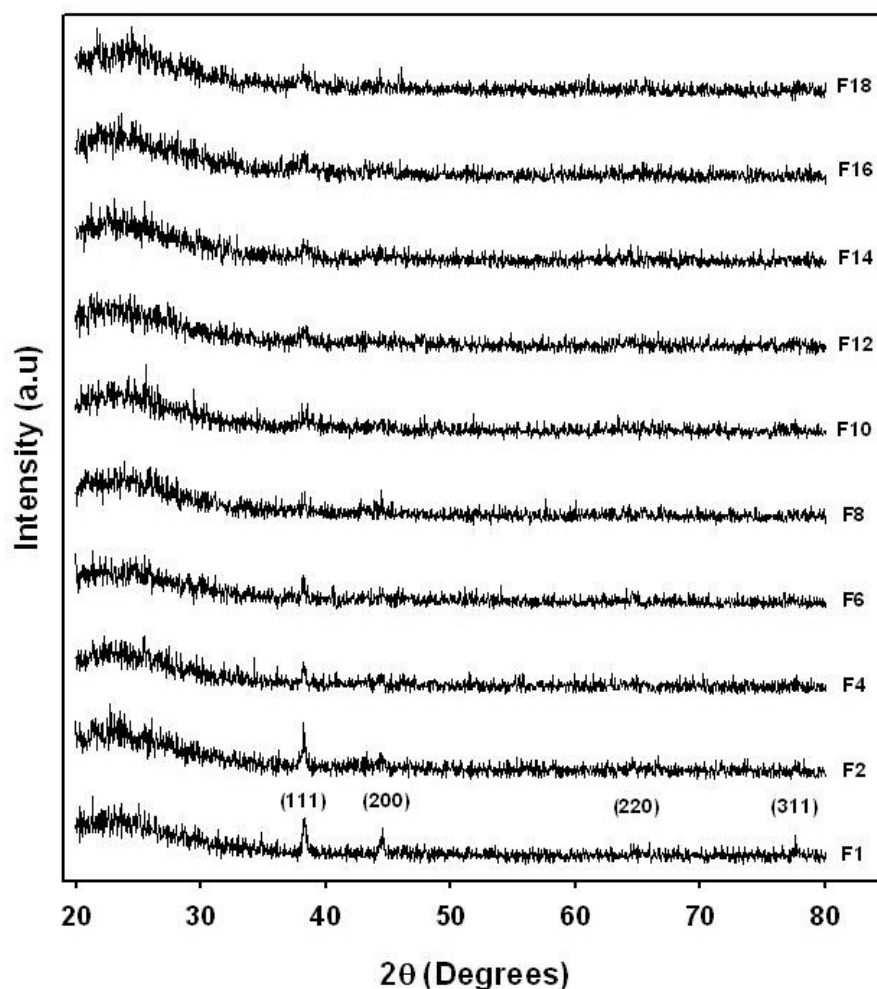


Figure 4.2. Wide-angle XRD patterns of Au/MSM catalysts synthesized with different BTESPTS/TEOS molar ratios.

The wide-angle XRD patterns of the Au/MSM samples are presented in Figure 4.2. For the catalysts prepared with low amounts of BTESPTS (F1 to F6), it can be observed the well resolved characteristic diffraction peaks at around 38°, 45°, 65° and 78°, assigned to the (111), (200), (220) and (311) lattice planes of face-centered cubic structure of gold (JCPDS Card No. 4-784), indicating the crystalline state of gold after the removal of the template and the thioether functionalities, and revealing the presence of metallic gold species [400]. However, with the increase of the BTESPTS loading, the (111) diffraction peak became less intense, while the (200), (220) and (311) diffraction peaks are difficult to observe accurately, suggesting a better dispersion of small AuNPs. According to the Scherrer's equation the size of AuNPs decreased from about 50 to 5 nm, with the increase of the molar concentration of BTESPTS in the synthesis mixture. This behavior could be due to the fact that higher amounts of BTESPTS facilitate the formation of the AuCl_4^- -thioether complexes, which during the hydrothermal aging form Au clusters stabilized by thioether groups, and are subsequently decomposed to produce well dispersed small AuNPs after the calcination at high temperature [279]. However, taking into account that is difficult to estimate the true particle size and to understand the structural changes only from the XRD analysis, TEM was used to further elucidate the XRD data.

4.4.1.2. Transmission electron microscopy

The TEM images of the mesoporous silica SBA-15 and of some representative Au/MSM catalysts are shown in Figure 4.3. As it can be observed, the mesoporous SBA-15 sample shows the well-ordered 2D hexagonal pore arrangement and the long-range mesopore architecture described by Zhao et al. [145]. This structure was retained when low amounts of BTESPTS were added to the catalysts synthesis mixture, as observed in the F2 sample. However, when the amount of BTESPTS increased in the synthesis mixture (*i.e.* F4-F12 samples), the 2D hexagonal structure was no longer the dominant phase, and instead an irregular wormhole-like framework structure was observed, consistent with the loss of symmetry suggested by the XRD analysis. In the case of the F6 sample, a mixed hexagonal symmetric structure with a vesicle-like structure is clearly observed, while as far as F8 and F10 are concerned, a wormhole-like structure is predominant. As the molar concentration of BTESPTS increased in the synthesis mixture, the mesophase transformation continued, forming a mixed phase of hexagonal-vesicle and mesostructured cellular foam material, as it can be seen in F14 and F18 catalysts. The same behavior was reported by Liu et al. [431] for mesoporous organosilicas synthesized with different molar ratios of BTESPTS/TMOS.

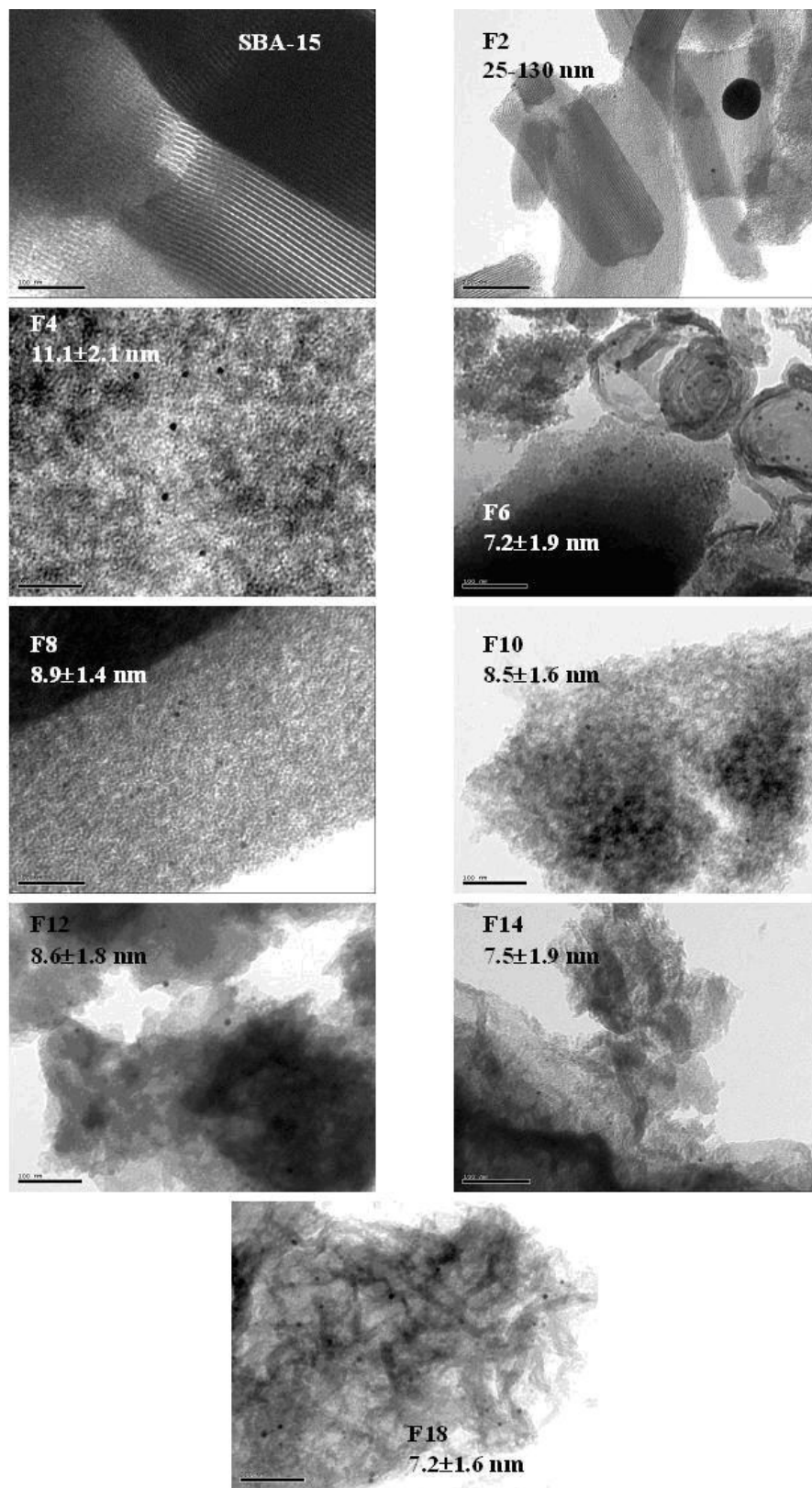


Figure 4.3. TEM micrographs of mesoporous silica SBA-15 and Au/MSM catalysts synthesized with different BTESPTS/TEOS molar ratios.

As far as the particle size is concerned, the TEM images revealed that the amount of BTESPTS added to the synthesis mixture has also an influence on both the size and the dispersion of the AuNPs. For low values of BTESPTS (*i.e.* F2 sample), large spherical gold aggregates with sizes varying from 25 to 130 nm predominated on the surface of the mesoporous silica support, which is in good agreement with the high intensity of the XRD diffraction peaks obtained for this sample. The formation of these large gold aggregates could be explained taking into account that with low concentrations of BTESPTS in the synthesis mixture, only few AuCl_4^- –thioether might be produced, and since the interaction between the silica surface and the hydrolyzed gold species is weak, the adsorbed gold particles coalesced easily during calcination at high temperature, forming large gold aggregates. When the molar concentration of BTESPTS was 4% (F4 sample), unevenly distributed AuNPs with sizes varying from 7 to 15 nm were observed. However, consistent with the wide-angle XRD results, a further increase of the molar concentration of BTESPTS in the synthesis mixture led to the formation of well dispersed AuNPs with sizes in the range of about 5 to 11 nm, as depicted in the TEM images of F6 to F18 samples. This trend is probably due to the presence of higher amounts of the BTESPTS which facilitate the complexation of AuCl_4^- with the thioether groups and the stabilization and dispersion of the AuNPs on the mesoporous silica support, after the template removal.

4.4.1.3. Nitrogen physisorption

The textural properties of the mesoporous silica SBA-15 and the calcined Au/MSM catalysts obtained from the low temperature nitrogen sorption analysis are summarized in Table 4.1, while the nitrogen adsorption/desorption isotherms are shown in Figure 4.4. As it can be noticed, the isotherms of all samples exhibited the characteristic type IV according to IUPAC classification [165], with a hysteresis loop due to the capillary condensation of nitrogen inside the mesopores. However, it can be noticed that the hysteresis loops of the Au/MSM catalysts synthesized in the presence of BTESPTS concentrations in the range of 4 and 12% looks flatter in comparison to that of the catalysts prepared with lower amounts of BTESPTS, confirming that above certain BTESPTS concentration, structural defects are formed in the mesoporous framework [412]. According to Wu et al. [279], these defects are formed after the removal of the thioether functionalities during the calcination at high temperature, and they are considered favorable sites for the formation of AuNPs. A further increase in the BTESPTS concentration (14% or more) led to a deviation of the hysteresis loop from the H1 type to a hysteresis loop that could be regarded as H2. The observation of hysteresis loops type H2 suggests

the presence of nonuniform size pores and/or pores with narrow necks and wide bodies (usually referred as “ink-bottle” pores) [165]. These results are consistent with the TEM images, as well as with previous reports [280-281, 429]. Thus, the structure of the catalysts synthesized in the presence of high concentrations of BTESPTS may be a wormhole-like or a foam-like structure with irregular porosity.

Table 4.1. Textural parameters of the mesoporous SBA-15 and Au/MSM synthesized in the presence of different amounts of BTESPTS.

Sample	BET surface area (m ² /g) ^a	Pore diameter (nm) ^b	Total pore volume (cm ³ /g) ^c
SBA-15	931.2	6.80	1.260
F0	718.2	3.72	0.868
F1	771.9	2.92	0.923
F2	754.1	3.71	0.800
F4	779.2	3.71	0.885
F6	806.8	3.72	0.752
F8	812.8	3.73	0.707
F10	790.2	1.85	0.637
F12	841.1	1.84	0.749
F14	729.5	1.97	0.677
F18	738.5	1.97	0.691

^a Calculated according to Brunauer–Emmett–Teller (BET) equation for data collected in the relative equilibrium pressure interval of $0.03 < P/P_0 < 0.3$. ^b BJH pore diameter calculated from the desorption branch. ^c Estimated from the amount of nitrogen adsorbed at a relative pressure P/P_0 of 0.99.

From data presented in Table 4.1, it is noticed that the BET surface area, pore diameter and total pore volume of all the Au/MSM catalysts is lower than that of SBA-15, as a consequence of the incorporation of gold species, and according to the different amounts of BTESPTS in the synthesis mixture. Moreover, the catalysts synthesized with BTESPTS concentration between 6 and 12% showed values of BET surface area higher than those of the samples synthesized in the presence of low and high amounts of BTESPTS (1-4 and 14-18%, respectively). This trend can be explained taking into account that after the removal of the thioether functionalities by calcination, void defects in the pore walls of the F6 to F12 samples can be formed which might lead to an increase in the total surface area [277]. However, because of the interactions between the surfactant molecules and the

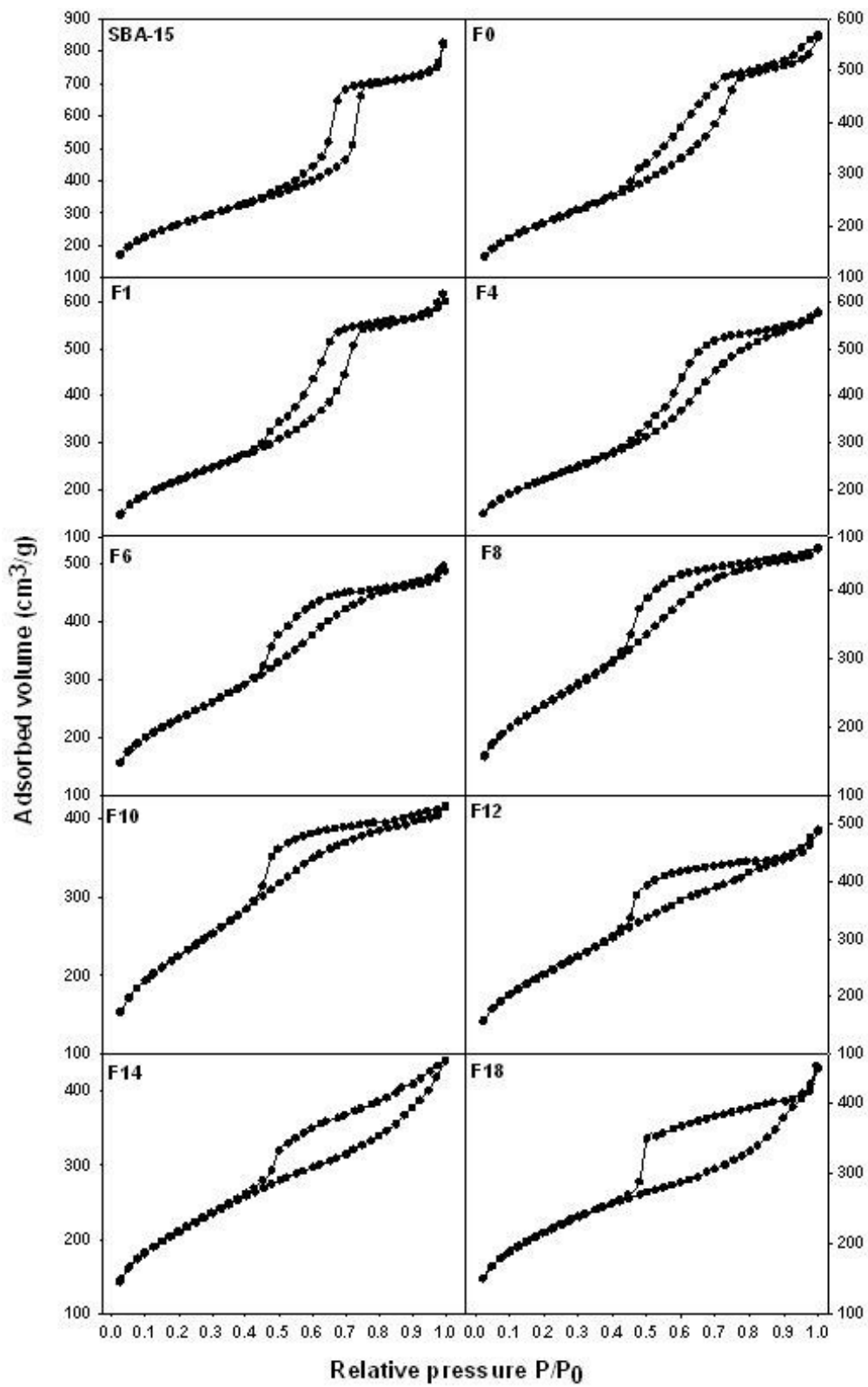


Figure 4.4. Nitrogen adsorption/desorption isotherms of mesoporous silica SBA-15 and Au/MSM catalysts synthesized with different BTESPTS/TEOS molar ratios.

silicate and organosilicate precursors during the hydrothermal aging step, higher amounts of BTESPTS in the synthesis mixture can generate the contraction of the micelle size and even destruction of the self assembly behavior, deteriorating the mesostructure and reducing the surface area. As reported by Liu et al. [431], a strong interaction between the hydrophobic bridging groups in BTESPTS (*i.e.*, $-\text{CH}_2\text{CH}_2\text{CH}_2-\text{S}-\text{S}-\text{S}-\text{S}-\text{CH}_2\text{CH}_2\text{CH}_2-$) with the more hydrophobic polypropyleneoxide blocks of the surfactant, can induce the penetration of silicate species into the micelle core, leading to a reduction of the pore diameter and the total pore volume, as observed in Table 4.1.

4.4.1.4. X-ray photoelectron spectroscopy (XPS) analysis

In order to investigate if the BTESPTS concentration could affect the oxidation state of gold in the calcined catalysts, XPS analysis were carried out on three representative Au/MSM samples (F2, F8 and F14). Although the presence of C 1s, O 1s, Si 2p, Si 2s and Au 4f photoelectron peaks was detected in the XPS measurements, only the spectra of the Au 4f core levels of the Au/MSM catalysts are shown in Figure 4.5, since typical spectra of these elements can be found in our previous work [90]. As seen, the experimental curves of the Au 4f core-level spectra of the three catalysts presented two spin-orbit split peaks centered at binding energies (BE) of ~ 84.0 and 87.8 eV, which are typical BE values of the spin doublet of the metallic state Au $4f_{7/2}$ and Au $4f_{5/2}$, respectively [409]. Both peaks were deconvoluted into three well-defined components using the Kratos software. These components, designed as Au $4f_{7/2-1}$, Au $4f_{7/2-2}$ and Au $4f_{7/2-3}$ for the Au $4f_{7/2}$ peak, and Au $4f_{5/2-1}$, Au $4f_{5/2-2}$ and Au $4f_{5/2-3}$ for the Au $4f_{5/2}$ peak, were assigned to Au⁰, Au⁺¹ and Au⁺³ [409], respectively, indicating the coexistence of metallic and oxidized species on the catalysts after the calcination at high temperature. However, the relative surface concentrations of the three gold species followed the order Au⁰ \gg Au⁺ > Au³⁺, as shown in Table 4.2. Moreover, the concentration value of metallic gold Au⁰ in the catalysts followed the order F8 (85.85%) > F2 (80.3%) > F14 (79%), while the concentration of Au³⁺ was similar in the three samples ($\sim 5\%$). Although we have obtained similar Au species distributions in gold catalysts supported on mesoporous silica and mesoporous silica decorated by ceria [11, 90], the differences found between the relative surfaces concentrations of gold species, suggest that the concentration of the BTESPTS in the synthesis mixture could affect the oxidation state of gold in the Au/MSM catalyst, in agreement with the color of the samples (Figure 4.6). During calcination at high temperature, the color of the samples changed from the pale beige, characteristic of the presence of thioether-stabilized Au clusters (sample Au/MSM-as), to the pink-

ruby, characteristic of the presence of metallic AuNPs. This color change indicates that most of the Au species are reduced to metallic Au⁰ during the calcination step [287] However, it is worth noting, that the color intensity of the catalysts increased as the molar concentration of BTESPTS increased in the synthesis mixture. The pale pink color of the catalysts synthesized in the presence of low concentrations of BTESPTS (1-4%), became light pink and pink-violet, when the BTESPTS concentrations increased from 6 to 10% and from 12 to 18%, respectively. Moreover, it can be observed in the F18 sample, the presence of some violet agglomerates, characteristic of oxidized Au species.

Table 4.2. Binding energies (BE) of Au 4f_{7/2} and 4f_{5/2} deconvoluted peaks and its relative surface distribution in Au/MSM catalysts.

Catalyst sample	Peak	BE (eV)	Gold species	Concentration (%) ^a
F2	Au 4f _{7/2-1}	84.07	Au ⁰	45.88
	Au 4f _{7/2-2}	84.85	Au ⁺	8.72
	Au 4f _{7/2-3}	86.59	Au ³⁺	2.52
	Au 4f _{5/2-1}	87.77	Au ⁰	34.45
	Au 4f _{5/2-2}	88.52	Au ⁺	6.55
	Au 4f _{5/2-3}	90.26	Au ³⁺	1.89
F8	Au 4f _{7/2-1}	84.19	Au ⁰	49.09
	Au 4f _{7/2-2}	85.43	Au ⁺	5.65
	Au 4f _{7/2-3}	87.24	Au ³⁺	2.45
	Au 4f _{5/2-1}	87.89	Au ⁰	36.74
	Au 4f _{5/2-2}	89.10	Au ⁺	4.23
	Au 4f _{5/2-3}	90.91	Au ³⁺	1.84
F14	Au 4f _{7/2-1}	83.93	Au ⁰	45.11
	Au 4f _{7/2-2}	84.97	Au ⁺	8.56
	Au 4f _{7/2-3}	86.89	Au ³⁺	3.45
	Au 4f _{5/2-1}	87.63	Au ⁰	33.88
	Au 4f _{5/2-2}	88.64	Au ⁺	6.42
	Au 4f _{5/2-3}	90.56	Au ³⁺	2.59

^a Expressed as a percentage of the total area of the Au 4f peak (taken as 100%).

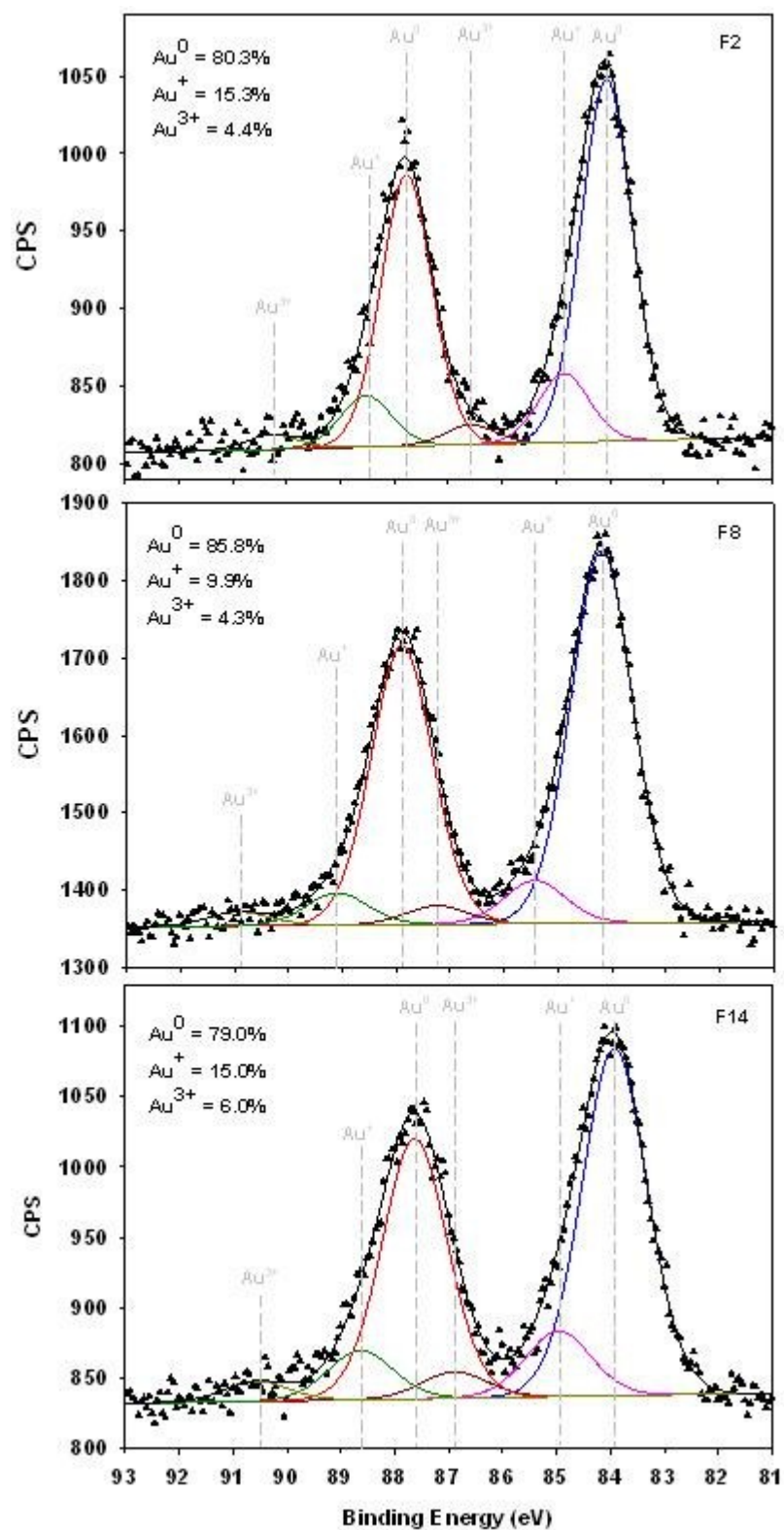


Figure 4.5. XPS-spectra of the Au 4f core-level of Au/MSM catalysts synthesized with different BTESPTS/TEOS molar ratios.

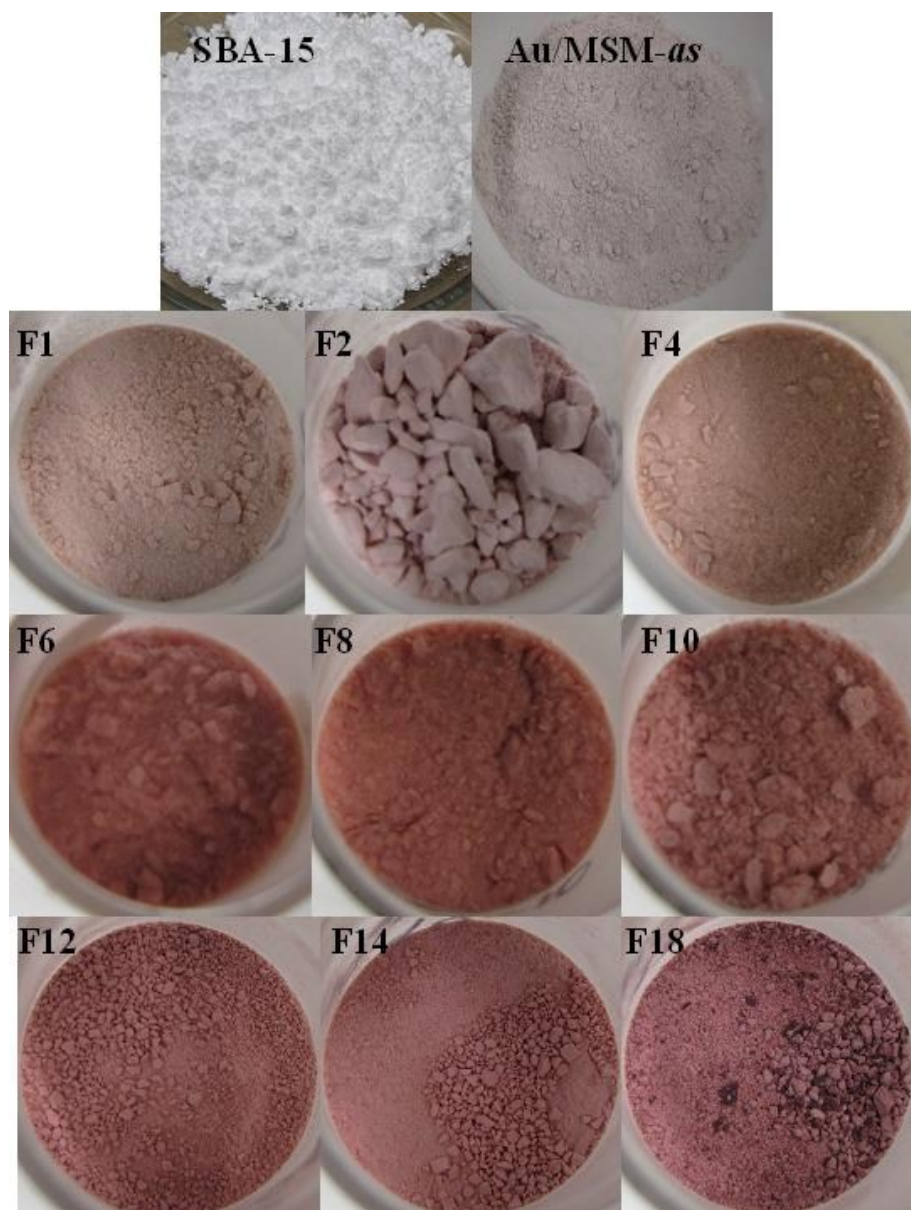


Figure 4.6. Images of mesoporous silica SBA-15 and Au/MSM catalysts synthesized with different BTESPTS/TEOS molar ratios.

4.4.2. Catalytic activity

The catalytic performance of the Au/MSM catalysts was investigated on the selective production of LBA by aerobic oxidation of lactose, since this relatively new product is a high value-added lactose derivative with excellent properties for food and pharmaceutical applications [6].

Figure 4.7 shows the kinetic profiles of lactose oxidation to LBA over the Au/MSM catalysts prepared with different concentrations of BTESPTS in the catalysts synthesis mixture. F1 and F2 samples did

not show any catalytic activity, because of the high size of the loaded gold particles (see Figure 4.3). The kinetic of lactose oxidation over F4 catalysts was characterized by a slow reaction rate, reaching a lactose conversion of about 95% after 3h of reaction. With increasing the molar concentration of BTESPTS in the synthesis mixture to 6-10%, the obtained F6-F10 catalysts showed similar pretty good activity to oxidize lactose to LBA, allowing conversions close to 100% after 80-100 min of reaction. A further increase in the amounts of BTESPTS, led to a catalytic materials (F12-F18) showing lower lactose conversion patterns, as clearly depicted in Figure 4.7. It is worth mentioning that all the Au/MSM catalysts were 100% selective towards LBA, since no side products were detected by HPLC analysis.

The activity of gold catalysts has been mainly attributed to the Au particle size. Nevertheless, the small metal cluster size is not the only sufficient condition to ensure a good catalyst activity [11]. Herein, with the exception of the F4 sample, we have Au/MSM catalysts with similar nominal gold loadings and particle sizes, but with significant differences in their catalytic activity. It is possible that the different speciation of gold on the catalysts could have affected their catalytic activity, and that catalysts containing more metallic Au⁰ are more active, as suggested by the XPS analysis. However, in our recent study, the 0.7%Au/SBA-15 catalysts with similar Au speciation than the F14 sample were highly active for lactose oxidation under the same reaction conditions [90]. Thus, if the chemical state of the loaded gold can not explain the trend in the kinetic behavior of the Au/MSM, a better AuNPs dispersion and reagent' accessibility is other possible reason which could presumably affect the catalyst activity. As depicted in Figure 4.3, F6-F10 materials presented a wormhole-like structure containing interconnected 3D-mesopores that can be ideal for the minimization of diffusion limitation phenomena often encountered in adsorption and catalytic reactions. On the contrary, in the F12-F18 catalysts a mixed hexagonal-vesicle and cellular foam mesostructure is predominant, in which not all the AuNPs can be attained by the reagent, thus decreasing the effective area of the catalysts and consequently their catalytic activity.

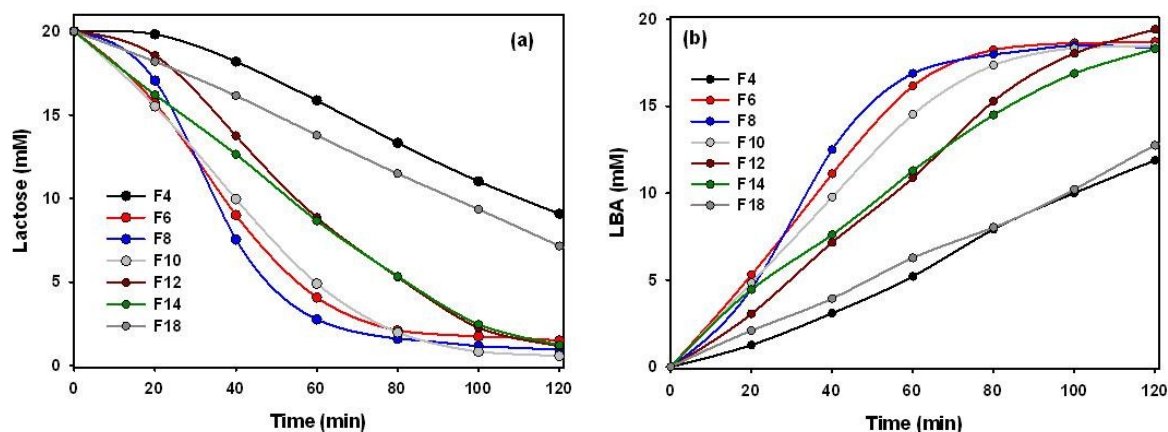


Figure 4.7. Kinetics profiles of lactose oxidation to LBA over Au/MSM catalysts synthesized with different BTESPTS/TEOS molar ratios.

4.5. Conclusion

The characteristics of Au/MSM synthesized in the presence of different BTESPTS/TEOS molar ratios were investigated by means of XRD, N₂-physisorption, TEM and XPS analysis. It was found that with increasing the molar concentration of BTESPTS the structure of the synthesized materials changes from a highly ordered 2D hexagonal structure to a mixed hexagonal-vesicle and cellular foam structure. This mesostructure transformation affected the lactose oxidation activity of the synthesized materials. The highest lactose conversions were obtained after 80-100 min reaction using the catalysts synthesized from mixtures containing 6-10% molar concentration of BTESPTS, which were characterized by the predominance of a wormhole-like structure, favorable for the reagent accessibility to the AuNPs of about 8 nm intercalated in the silica wall. Lower concentrations of BTESPTS led to materials with unevenly catalytically inactive large AuNPs (25-130 nm), while higher amounts of BTESPTS produce materials whose mesostructure do not allow the easy access of reagents to the AuNPs, thus with lower catalytic activity. These results indicate that the amount of thioether functionalities can be systematically modified to synthesize gold catalysts with different structures.

Chapter 5. Effective gold catalyst supported on mesoporous silica decorated by ceria for the synthesis of high value lactobionic acid

This chapter relates the synthesis and characterization of Au/SBA-15 and various Au/SBA-15-CeO₂ catalysts synthesized by cation adsorption of the gold complex Au(en)₂Cl₃. The effects of various Ce/Si molar ratios on the activity for selectively oxidize lactose into lactobionic acid is discussed.

Published in *Applied Catalysis A: General* 2012, 425-426, 213-223 by **Luis-Felipe Gutiérrez, Safia Hamoudi, Khaled Belkacemi**.

5.1. Abstract

Gold supported on mesoporous SBA-15 and SBA-15-CeO₂ with Ce/Si molar ratios of 0.1, 0.2, 0.4 and 0.6 were synthesized via wet chemical process using a gold cationic complex precursor [Au(en)₂]³⁺ (en = ethylenediamine), and investigated as catalysts for the partial oxidation of lactose to selectively synthesize lactobionic acid (LBA) for therapeutic, pharmaceutical and food grade applications.

These catalysts were characterized by N₂ physisorption, XRD, FTIR, TEM and XPS. N₂ physisorption and XRD analysis revealed that SBA-15-CeO₂ with the investigated Ce/Si molar ratios support possess ordered hexagonal mesoporous structure, characterized with a high surface area and large pore volume, similar to SBA-15, whereas BET surface area and pore volume of catalyst were significantly decreased upon impregnation. XPS analysis revealed the coexistence of metallic and oxidized gold species (Au⁰, Au⁺ and Au³⁺) in all prepared catalysts and the presence of both Ce³⁺ and Ce⁴⁺ oxidation states for gold supported on mesoporous SBA-15-CeO₂ catalysts.

The influence of the pH value on lactose conversion was also investigated. After 60 min of reaction, the 0.7%Au/SBA-15-CeO₂ (Ce/Si = 0.1 and 0.2) catalysts showed high catalytic activity (100% lactose conversion) and a 100% selectivity towards LBA, when they were used at a catalyst/lactose ratio of 0.2, under alkaline (pH 9.0) and mild reaction temperature (65°C). At the optimized conditions, 0.7% Au/SBA-15-CeO₂ catalysts with Ce/Si of 0.1, 0.2 and 0.4 were more active than 0.7% Au/SBA-15 catalyst. A maximum of activity is reached at Ce/Si of 0.2. The experimental catalytic tests and

characterizations show clearly the role of Ce in the enhancement in the catalyst activity where the coordination and agglomeration states of Ce atoms could have an important effect.

5.2. Introduction

Since the pioneering work of Haruta et al. [167], it is now well known that the catalytic performance of heterogeneous gold catalysts strongly depends on the synthesis method, the nature of support, the gold cluster size deposited on the catalyst surface, and the thermal history of the catalyst [432]. However, the conventional wet-impregnation methods are not appropriate to obtain the required highly dispersed gold nanoparticles (AuNPs), since they usually yield inactive large spherical particles which weakly bind to the support [303]. To avoid these problems, other methods (*i.e.* coprecipitation, deposition–precipitation and chemical vapor deposition) have been developed for the synthesis of gold catalysts [194, 198, 207]. Among them, the deposition–precipitation (DP) of HAuCl_4 aqueous solution in alkaline media (pH 6–10) has been proposed as one of the simplest techniques to obtain high dispersion of Au-NPs and highly active supported gold catalysts [303]. Nevertheless, the DP method is not appropriate for the incorporation of AuNPs into silica materials, because under the high pH conditions required to hydrolyze the HAuCl_4 , the weak interaction between the negatively charged silica surface and the $[\text{Au}(\text{OH})_n\text{Cl}_{4-n}]^-$ species facilitates the mobility of gold particles, which can easily sinter during the synthesis process, especially during the calcination step, yielding inactive catalysts [207]. To overcome this drawback, various alternative methods have been proposed, given that mesoporous silicas are considered very attractive catalyst supports, because of their high surface area, thermal stability, ordered structure and excellent mechanical properties. Some well documented techniques include the chemical vapor deposition using expensive organometallic gold precursors [207]; the modification of SiO_2 with organic functional groups before gold loading [203]; the one-pot synthesis by the incorporation of both gold and the coupling agent containing functional groups into the synthesis of mesoporous SiO_2 [205]; the use of cationic gold complexes such as $[\text{Au}(\text{en})_2]\text{Cl}_3$ (en = ethylenediamine) and $\text{Au}(\text{PPh}_3)_3\text{Cl}$ [297, 433]; the synthesis of SiO_2 in the presence of gold colloids or the dispersion of gold colloids protected by ligands or polymers onto SiO_2 [208, 311]; and the modification of SiO_2 supports by other metal oxides, such as TiO_2 , Al_2O_3 and CeO_2 to form SiO_2 -based gold catalysts [210-211].

Particularly, ceria is known for its high oxygen storage capacity and for its favorable oxidation activity, and it has been reported that the addition of CeO_2 improves the activity of gold catalysts supported

on SiO₂ for gas-phase reactions [434]. Moreover, the most frequently adopted catalytic reaction to evaluate the performance of gold catalysts has been the CO oxidation. However, the catalysts synthesized by the above mentioned techniques have been hardly investigated for liquid phase oxidations, which include interesting industrial applications for the synthesis of a wide variety of fine chemicals.

On the other hand, lactose is an important by-product of the cheese and casein manufacture that can be used as raw material for the production of high value lactobionic acid (LBA) (4-O-β-D-galactopyranosyl-D-gluconic acid) via heterogeneous catalytic oxidation. LBA has showed excellent properties for food and pharmaceutical applications. The main commercial use of LBA is as ingredient of the solutions employed for stabilizing organs prior to transplantation [43], and it represents a new ingredient in skin care products featuring potent antioxidant and humectant properties [401]. LBA can be also used in calcium supplementation, as acidulant with a sweet taste; as filler in cheese production; as firming agent, and to fortify functional drinks with essential minerals such as Fe and Cu [8, 402].

The oxidation of lactose over platinum, palladium and bismuth-promoted palladium supported catalysts has been largely investigated [10, 13, 16, 80, 82-85, 87, 89, 403], and it is well documented that the main problem of these catalysts is their poisoning and deactivation by over-oxidation during reaction [85, 87, 404]. Supported gold catalysts have been suggested to outperform palladium catalysts for the oxidation of carbohydrates, because they are less prone to over-oxidation, and they exhibit high activity and selectivity towards aldonic acids [404]. However, the oxidation of lactose over gold catalyst has been scarcely investigated. Recent studies indicate that gold catalysts supported on Al₂O₃, TiO₂, and CeO₂ allowed to achieve moderate to high conversions (>80%) and selectivities (up to 95%), using Au loadings in the range of 0.4–2.0% [13-16].

Very recently, our research group successfully synthesized highly active gold crystallites dispersed on mesoporous silica (SiO₂-meso) using *bis*-[3-(triethoxysilyl) propyl] tetrasulfide (BTESPTS), as a silane coupling agent to immobilize gold. This catalytic material was found 100% selective towards LBA production from lactose partial aerial oxidation [11].

Although these relatively high conversions and selectivities were reached, the oxidation of lactose to LBA over gold catalysts still necessitates the development of new catalysts with high activity, stability and selectivity towards LBA.

The main objectives of this work were to synthesize and characterize a new gold catalyst supported on mesostructured silica decorated by ceria for the oxidation of lactose to LBA. Specifically, the catalyst characterization by means of BET surface, powder X-ray diffraction (XRD), X-ray photoelectron spectroscopy (XPS), Fourier transform infrared spectroscopy (FTIR) and transmission electron microscopy (TEM) has been investigated, as well as the influence of the pH value on lactose conversion. To the best of our knowledge, it is the first time that the oxidation of lactose to LBA over gold catalyst supported on mesoporous silica decorated by ceria is reported.

5.3. Experimental

5.3.1. Materials

All reagents were of the highest purity and were used without further purification. Gold (III) chloride trihydrate ($\text{HAuCl}_4 \cdot 3\text{H}_2\text{O}$), tetraethyl orthosilicate (TEOS), cerium (III) nitrate hexahydrate ($\text{Ce}(\text{NO}_3)_3 \cdot 6\text{H}_2\text{O}$), α -lactose monohydrate and LBA were purchased from Sigma Aldrich. Pluronic P123 ($\text{EO}_{20}\text{PO}_{70}\text{EO}_{20}$, $M_{av} = 5900 \text{ g/mol}$) was graciously offered by BASF. For HPLC analysis, sodium hydroxide solution 50% and HPLC grade anhydrous sodium acetate from Fluka, were used for eluents preparation.

5.3.2. Synthesis of mesoporous SBA-15 and SBA-15-CeO₂

The synthesis of SBA-15 was carried out in acidic media using Pluronic P123 as a templating agent, as described by Zhao et al. [145]. Hexagonally ordered SBA-15-CeO₂ was synthesized using triblock copolymer (P123) as a templating agent, and tetraethyl orthosilicate (TEOS) and cerium nitrate as silicon and cerium precursors, respectively. In a typical synthesis, 4 g of P123 were dissolved in 140 mL of HCl solution (pH 2.0) at room temperature. After complete dissolution of the template agent, appropriate amounts of cerium nitrate and TEOS were added in order to reach a molar ratio Ce/Si of 0.1. The obtained mixture was stirred at 600 rpm for 2 h at room temperature and subsequently kept under static conditions for 24 h at 40°C, transferred into a 1000 mL Pyrex bottle and then hydrothermally aged for 48 h at 100°C. After vacuum filtration, the solid phase was thoroughly washed with deionized water and ethanol at room temperature. Finally, the solid was vacuum-dried

overnight at 100°C, and then calcined at 550°C for 6 h at a heating rate of 1°C/min, using a programmable oven.

5.3.3. Synthesis of Au(en)₂Cl₃

The cationic gold complexes Au(en)₂Cl₃ were synthesized as described by Zhu et al. [206]. Typically, 0.5 g of HAuCl₄·3H₂O were dissolved in 5 mL of deionized water, and then ethylenediamine (en) was dropwise added until the formation of a transparent brown solution. The solution was stirred for 30 min, and subsequently ethanol (~35 mL) was added. After vacuum filtration, the solid was washed with ethanol and then vacuum-dried overnight at 100°C.

5.3.4. Catalyst preparation

Gold-supported SBA-15 and SBA-15-CeO₂ catalysts were synthesized via wet chemical process, following the procedure reported by Zhu et al. [206]. In our previous work [11] we found that gold catalysts supported on mesoporous silica containing 0.7% Au exhibited a high catalytic activity (~100% lactose conversion) and a 100% selectivity towards LBA, when it was used at a catalyst/lactose ratio of 0.2 under alkaline (pH 9.0) and mild reaction temperature (65°C). Thus, in order to obtain a nominal gold loading of 0.7%, 30 mg of [Au(en)₂]Cl₃ were dissolved in ~40 mL of deionized water, and the pH was adjusted to 10 by the addition of 1-M NaOH aqueous solution. Then, 2 g of support were added and the mixture was stirred for 3 h, maintaining the pH at a value of 10 by the addition of 1-M NaOH aqueous solution. After vacuum filtration, the solid was washed with deionized water. Finally, the catalyst was vacuum dried overnight at 100°C, and the resulting solids were calcined at 500°C for 5 h at a heating rate of 1°C/min, using a programmable oven.

5.3.5. Catalyst characterization

Nitrogen adsorption/desorption isotherms of calcined samples were obtained using a volumetric adsorption analyzer (Model Autosorb-1, Quantachrome Instruments, Boyton Beach, FL) at -196°C (77 K). Before the adsorption analysis, the samples were degassed for 3 h at 200°C. Total pore volume was estimated from the amount adsorbed at 0.99 relative pressures. Pore size distributions were calculated using the desorption branch of the N₂ adsorption/desorption isotherms and the Barrett–Joyner–Halenda (BJH) method [408].

Powder X-ray diffraction (XRD) patterns were obtained with an Ultima III Rigaku Monochromatic Diffractometer using CuK α radiation ($\lambda = 1.5406 \text{ \AA}$). Small angle powder diffraction patterns were

acquired at a scanning rate of $1^\circ/\text{min}$ in the 2θ range of $0.6\text{--}3^\circ$, while wide angle powder XRD was obtained at the same scanning rate in the 2θ range $20\text{--}80^\circ$.

Transmission electron microscopy (TEM) images were taken on a JEM-3010 electron microscope (JEOL, Japan) with an acceleration voltage up to 200 kV. The catalysts samples were suspended in methanol and ultrasonically treated during 10 min. Then, the suspension ($5\ \mu\text{L}$) were disposed uniformly and dried on a nickel grid.

Transform Infrared (FTIR) spectra were recorded in absorption mode on a Varian 1000 FTIR spectrometer in the range of $400\text{--}4000\ \text{cm}^{-1}$ by the co-addition of 20 scans at a $8\ \text{cm}^{-1}$ resolution. FT-IR analysis were carried out at room temperature using potassium bromide (KBr) pellets containing about 0.5% of the solid samples, which were compacted in a uniaxial press under a nominal pressure of 6.89 kPa. The spectrum of dry KBr was taken for background subtraction, before recording the samples.

The catalyst surface and the oxidation state of gold in the catalysts were studied by X-ray Photoelectron Spectroscopy (XPS) analysis using an Axis-Ultra system spectrometer from Kratos (UK) equipped with an electrostatic analyzer of large ray, a source of double X-rays Al–Mg without monochromator and an Al source with monochromator. The pressure in the XPS room was maintained between 5×10^{-9} and 5×10^{-8} Torr during the analysis. All the spectra were recorded with the Al monochromatic source with a power of 300 W. The flyover spectrum used to determine the elementary composition was recorded with pass energy in the analyzer of 160 eV and an energy step of 1 eV, using lenses in hybrid mode, which maximizes the sensitivity. The detailed spectra with high resolution were recorded with pass energy of 40 or 20 eV, and step energy of 50 or 100 meV. The spectra with high resolution are used for the chemical analysis [409]. The adjustment of the envelope calculated with the experimental spectrum was carried out using CasaWPS software from Kratos (UK). The binding energy (BE) scale was calibrated by measuring C 1s peak (BE = 285.0 eV) from the surface contamination.

5.3.6. Lactose oxidation experiments

Lactose oxidation experiments were carried out at atmospheric pressure in a thermostated and magnetically stirred 300 mL-glass reactor, following the optimal conditions found in our previous work [11], as described above in the catalyst preparation section. In a typical oxidation reaction, 175 mL of

20 mM lactose solution were heated under continuous agitation (600 rpm) until the temperature reached $65 \pm 0.5^\circ\text{C}$, whereas 500 mL/min of nitrogen flow were simultaneously bubbled for stripping off the dissolved oxygen. Subsequently, the stirring was increased to 900 rpm, the catalyst was added and the pH of the solution was adjusted at the desired value, by the addition of few drops 1-M NaOH aqueous solution. Then, air was bubbled through the reaction mixture at a constant flow rate of 40 mL/min. During the reaction, the pH value was kept constant by adding 1-M NaOH aqueous solution, by means of a pH STAT Titrator (Metrohm® 842 Titrando®, Switzerland), and the dissolved oxygen concentration was monitored using an oxygen probe (Ocean Optics, Inc., USA) connected to a fiber optic sensor system (TauTheta Instruments LLC, USA).

The time 'zero' of the reaction corresponded to the moment when the air was bubbled through the reaction mixture. Reactions were carried out using a catalyst/lactose ratio of 0.2. Liquid samples were taken at regular intervals for the subsequent HPLC analyses.

5.3.7. Reaction sample analysis

Samples of reaction mixture were analyzed using a chromatographic system DX-ICS 2500 (Dionex, USA) equipped with a gradient pump GP50 and an electrochemical detector ED50 with a thin-layer type amperometric cell outfitted with gold electrodes and an Ag/AgCl reference electrode. In order to improve sensitivity, minimize the baseline drift and clean the gold working electrode, a triple potential waveform of E_1 : 0.1, E_2 : 0.6 and E_3 : -0.8 V was applied for duration times of t_1 : 0.5, t_2 : 0.09 and t_3 : 0.07 s. The chromatographic separation of lactose and LBA was performed on a CarboPac PA1 analytical column (4mm \times 250 mm i.d., Dionex) in conjunction with a CarboPac PA1 guard column (4mm \times 50 mm i.d., Dionex). Sodium hydroxide solution 50% and anhydrous sodium acetate (NaOAc) from Fluka were used to prepare the eluents A (0.1 M NaOH) and B (0.1 M NaOH–0.5 M NaOAc) in filtered and vacuum degassed HPLC-Grade water. All eluents were stored in closed and pressurized bottles with helium. The flow rate was set at 1 mL/min. For the analysis the flow gradient was programmed as follows: From 100% eluent A (isocratic for 10 min) to an eluent composition of 60% A- and 40% B-solutions in 10 min using a linear gradient. Then, isocratic period of this eluent composition for 10 min, and subsequently the eluent was returned to 100% A-solution in 5 min, using a linear gradient. Chromeleon software (Dionex, USA) was used to perform all the calibration and integration of chromatographic data.

5.4. Results and discussion

5.4.1. Catalyst characterization

5.4.1.1. Nitrogen physisorption

Textural properties of the mesoporous SBA-15 and SBA-15-CeO₂ materials as well as 0.7%Au/SBA-15 and 0.7%Au/SBA-15-CeO₂ catalysts were obtained from the low-temperature (77 K) nitrogen adsorption/desorption isotherm measurements, from which the specific surface areas, specific pore volumes and mesopore size distributions were calculated and summarized in Table 5.1. It is noticed that the direct synthesis of SBA-15-CeO₂ allows conserving high values of BET surface area (802.4 m²/g) and total pore volume (1.05 cm³/g). Compared with pure mesoporous SBA-15, the total pore volume of SBA-15-CeO₂ reduces slightly. Similar results have been reported by Mu et al. [435] for the incorporation of ceria into SBA-15 at different Ce/Si molar ratios (0.02–0.2). However, the BET surface area and the total pore volume decreased notably after gold loading, because of the partial pore blockage of the support. When comparing with the SBA-15-CeO₂ support, the BET surface area and the total pore volume were reduced in about 60 and 40%, respectively. Moreover, as depicted in Figure 5.1b, the SBA-15-CeO₂ support and the gold catalyst showed a binodal pore size distribution with very similar values (3.9 and 6.6 nm and 3.7 and 6.2 nm, respectively). The pore and structural morphology of the synthesized SBA-15-CeO₂ support and of the supported gold catalyst can be further verified by transmission electron microscopy (TEM).

Table 5.1. Textural parameters of the mesoporous SBA-15-CeO₂ support and 0.7%Au/SBA-15-CeO₂ catalyst (Ce/Si molar ratio 0.1).

Material	BET surface area (m ² /g) ^a	Pore diameter (nm) ^b	Total pore volume (cm ³ /g) ^c
SBA-15	931.2	6.8	1.260
SBA-15-CeO ₂	802.4	3.9 and 6.6	1.052
0.7%Au/SBA-15	479.1	6.2	0.849
0.7%Au/SBA-15-CeO ₂	310	3.7 and 6.2	0.627

^a Calculated according to Brunauer-Emmett-Teller (BET) equation for data collected in the relative equilibrium pressure interval of $0.03 < P/P_0 < 0.3$. ^b BJH pore diameter calculated from the desorption branch. ^c Estimated from the amount of nitrogen adsorbed at a relative pressure P/P_0 of 0.99.

Overall, it can be observed that both catalysts are quite similar. Owing to the incorporation of ceria in SBA-15 framework, 0.7% Au/SBA-15 presents relatively better textural characteristics than 0.7% Au/SBA-15-CeO₂ catalyst.

The N₂ adsorption–desorption isotherms and the corresponding BJH pore size distributions calculated from the desorption-branch for SBA-15, SBA-15-CeO₂ and 0.7% Au/SBA-15-CeO₂ materials are shown in Figure 5.1. The isotherms for 0.7% Au/SBA-15 catalyst are not shown in this figure. However, they displayed a similar pattern like those of SBA-15.

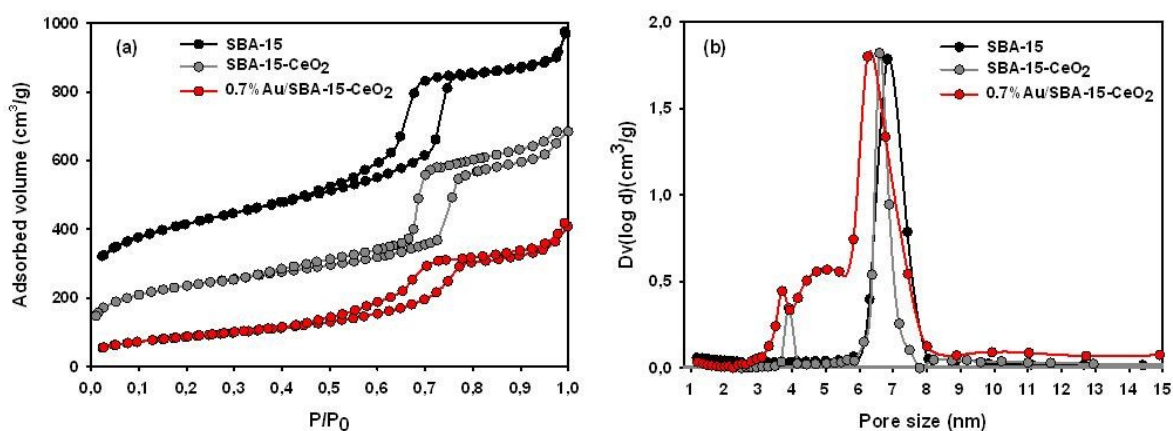


Figure 5.1. Nitrogen adsorption/desorption isotherms (a) and pore size distributions (b) of SBA-15, SBA-15-CeO₂ and 0.7% Au/SBA-15-CeO₂ materials (Ce/Si molar ratio 0.1) (for clarity, the isotherms of SBA-15 were up-shifted 150 cm³/g).

As it can be observed in this figure, the shape of the nitrogen adsorption/desorption isotherms of all samples exhibits the characteristic type IV according to IUPAC classification [165], and displayed a broad H1 type hysteresis loop characteristic of large pore mesoporous solids [410], indicating that the mesoporous structure has been maintained after incorporation of ceria and gold. The initial increase in adsorption capacity at low relative pressure is due to monolayer adsorption on mesopores, whereas the upward deviation in the range of P/P_0 between 0.4 and 0.8 is associated with progressive mesopores filling. As the relative pressure increases, the adsorption isotherms display a sharp increase characteristic of the capillary condensation inside uniform mesopores. However, it can be noticed in Figure 5.1a that the incorporation of ceria and gold into the mesoporous SBA-15 led to a slight reduction in the N₂ adsorption capacity. Moreover, similar to the results obtained by Mu et al. [435], the desorption branch of the isotherms of SBA-15-CeO₂ and 0.7% Au/SBA-15-CeO₂ indicates that these materials have both a regular cylindrical mesopore system, as well as an ink bottle type

mesopores [158]. This is in accordance with the binodal pore size distributions exhibited for these materials, as illustrated in Figure 5.1b. Furthermore, the hysteresis loop at P/P_0 values between 0.4 and 0.8 for the 0.7%Au/SBA-15-CeO₂ catalyst looks more flat in comparison to that of SBA-15-CeO₂ support, indicating that some structural defects were formed in the mesoporous framework [412], which is in agreement with the small angle XRD diffraction peaks for this material, as showed in Figure 5.2.

5.4.1.2. X-ray diffraction

The small angle XRD patterns of the mesoporous SBA-15, SBA-15-CeO₂ and 0.7%Au/SBA-15-CeO₂ materials are illustrated in Figure 5.2. For SBA-15 and SBA-15-CeO₂ materials, it can be noticed the presence of three well-resolved diffraction peaks, associated with the bi-dimensional $p6mm$ hexagonal symmetry typical of the mesoporous SBA-15 materials [145]: one high-intensity peak at about $2\theta = 0.9^\circ$, and two low-intensity peaks at circa $2\theta = 1.6^\circ$ and 1.8° , corresponding to (1 0 0), (1 1 0), and (2 0 0) reflections, respectively. Similar low-angle XRD patterns have been reported by Mu et al. [435] for the direct synthesis of lanthanide-containing SBA-15 under weak acidic conditions (pH 1.5–3.0), indicating that the addition of ceria at a molar Ce/Si ratio of 0.1 does not destroy the characteristic structure of SBA-15. However, the decrease in the intensity of the diffraction peaks observed for the SBA-15-CeO₂ sample indicates a slight loss of the long-range order typical of the SBA-15 silica material. On the other hand, it can be seen in Figure 5.2 that after impregnation, the intensity of the diffraction peaks of the catalyst was reduced, and the peaks shifted to a higher value, indicating that the incorporation of gold species causes some loss of symmetry as well as an effect on the interplanar distance and angle of the mesoporous SBA-15-CeO₂ support. For sake of clarity in this figure, the XRD pattern of 0.7%Au/SBA-15 catalyst is not shown. Meanwhile, it was similar to SBA-15 XRD pattern.

The inset in Figure 5.2 depicts the wide angle XRD patterns of the 0.7%Au/SBA-15-CeO₂ catalyst. The XRD pattern presented three characteristic diffraction peaks at around 38° , 45° and 65° , assigned to the (1 1 1), (2 0 0), and (2 2 0) lattice planes of face-centered cubic structure of gold, indicating that gold is in crystalline form after the catalysts synthesis, and revealing the presence of metallic gold species [400]. However, owing to the peak-broadening effect of the small crystallite size and low loading, XRD Au peaks are difficult to observe accurately. On the other hand, the wide-angle XRD diffractograms of the gold supported catalyst show no characteristic diffraction peaks belonging

to CeO₂, which can be due to cerium crystallites being too small and well dispersed in the framework of SBA-15 to be detectable by XRD. Similar results have been published by Dai et al. [161] for the direct synthesis of cerium(III)-incorporated SBA-15 mesoporous molecular sieves with a molar ratio of Si/Ce = 10.

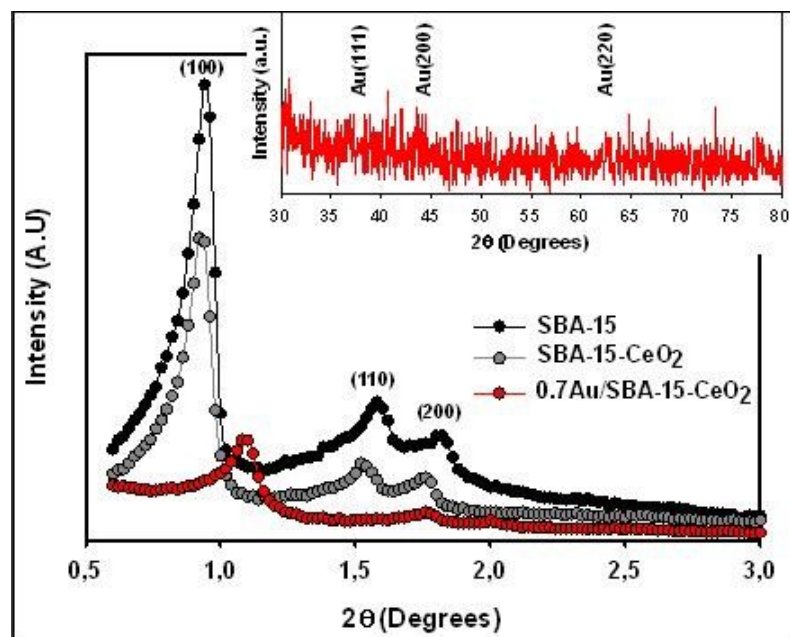


Figure 5.2. Low angle XRD patterns of SBA-15, SBA-15-CeO₂ and Au/SBA-15-CeO₂ materials. Inset: Wide angle XRD pattern of 0.7%Au/SBA-15-CeO₂ catalyst (Ce/Si molar ratio 0.1).

5.4.1.3. Transmission electron microscopy

Figures 5.3a–d show the transmission electron microscopy (TEM) micrographs of the mesoporous SBA-15, SBA-15-CeO₂, 0.7%Au/SBA-15 and 0.7%Au/SBA-15-CeO₂ catalyst, respectively. The TEM image of SBA-15 silica material (Figure 5.3a) clearly shows the well-ordered 2D hexagonal pore arrangement and the long-range mesopore architecture as described by Zhao et al. [145]. Figure 5.3b shows the TEM image of the SBA-15-CeO₂ material, in which it can be noticed the well-preserved structure of SBA-15, confirming that the introduction of ceria at a Ce/Si molar ratio of 0.1 does not alter its regular order array of mesopores, as indicated by the XRD analysis. Similar results have been recently published by Li et al. [436] for the direct synthesis of CeO₂/SiO₂ via sol-gel process, with Ce/Si molar ratio ranging from 0.03 to 0.3. The TEM micrographs of calcined 0.7%Au/SBA-15 and 0.7%Au/SBA-15-CeO₂ catalysts presented in Figures 5.3c and d, respectively, show a regular array of mesopores, as well as well dispersed and not aggregated spherical gold nanoparticles, having dimensions of about 5–6 nm. However, in agreement with the low-angle XRD

analysis, it can be observed that the hexagonal order of the 0.7%Au/SBA-15-CeO₂ sample was weakened after gold loading, in comparison with the mesoporous SBA-15-CeO₂ support.

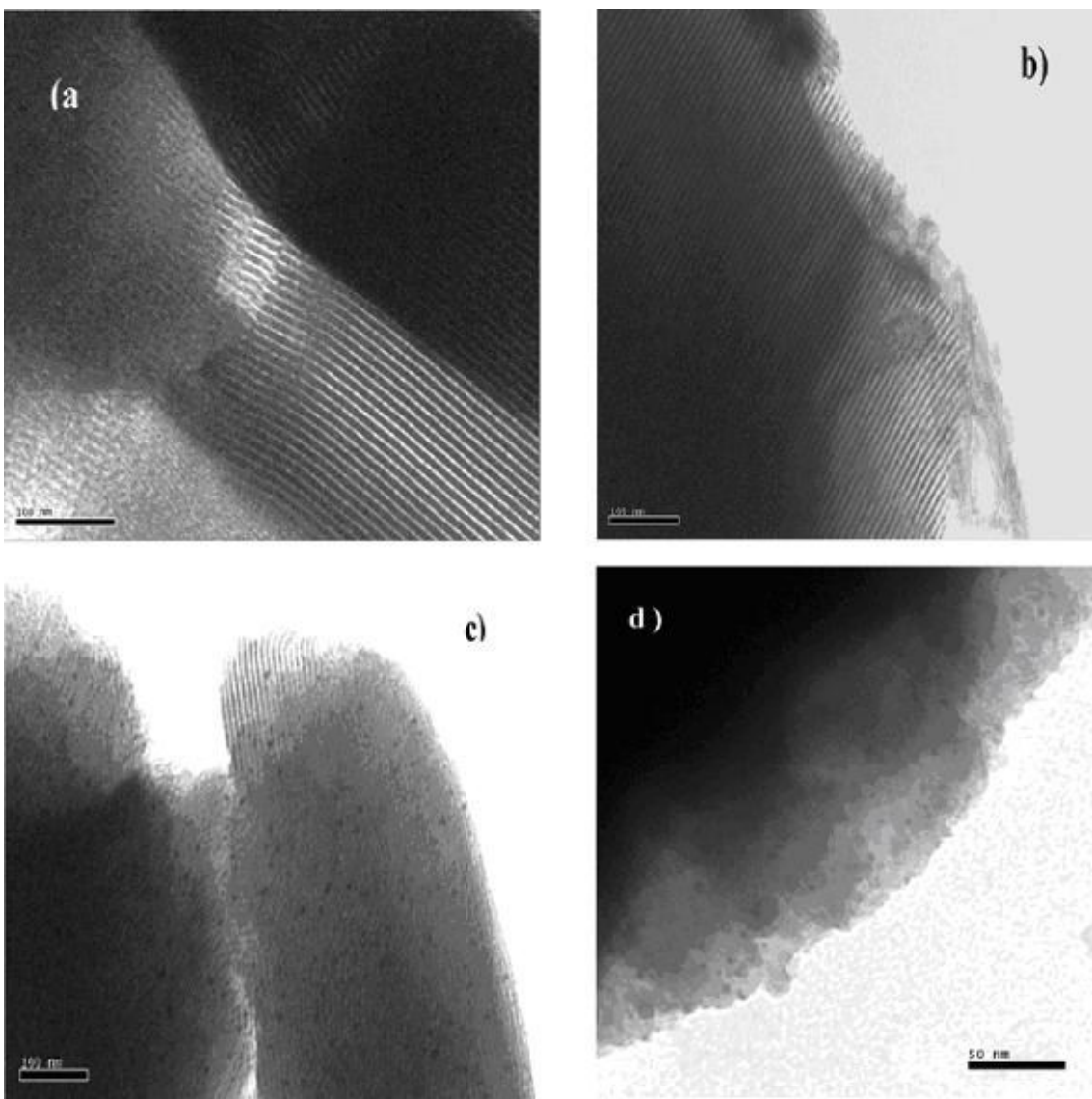


Figure 5.3. TEM micrographs of (a) mesoporous SBA-15; (b) SBA-15-CeO₂ (Ce/Si molar ratio 0.1); (c) 0.7%Au/SBA and (d) 0.7%Au/SBA-15-CeO₂.

5.4.1.4. Fourier transform infrared spectroscopy (FTIR) analysis

The FTIR spectra of the mesoporous SBA-15, SBA-15-CeO₂ and 0.7%Au/SBA-15-CeO₂ catalyst in the range of 400–4000 cm⁻¹ are shown in Figure 5.4. As it can be seen in this figure, the IR patterns of the mesoporous SBA-15-CeO₂ and gold supported mesoporous SBA-15-CeO₂ catalyst were almost the same than those of the SBA-15 silica material. It is also the case for that of 0.7%Au/SBA-

15 catalyst (results not shown). In the hydroxyl region (3000–4000 cm^{-1}) all samples presented a characteristic broad low-frequency absorption band between 3000 and 3700 cm^{-1} , centered circa 3430 cm^{-1} , which is assigned to the stretching vibrations of the hydrogen-bonded surface silanol ($\equiv\text{Si}-\text{OH}$) groups, and to the adsorbed water situated inside the channels of the mesoporous materials [437]. The slight shift to a higher value observed in this absorption band for SBA-15- CeO_2 (3435 cm^{-1}) and 0.7% Au/SBA-15-CeO_2 (3433 cm^{-1}) materials, compared with pure SBA-15 (3430 cm^{-1}), is probably due to the presence of some defect sites created for the incorporated materials [161]. Moreover, it can be observed in Figure 5.4 that gold loading significantly diminished the peak intensity of this absorption band, which could be associated to the partial blockage or destruction of the support pore structure, in agreement with the obtained results of the N_2 adsorption–desorption and XRD analysis.

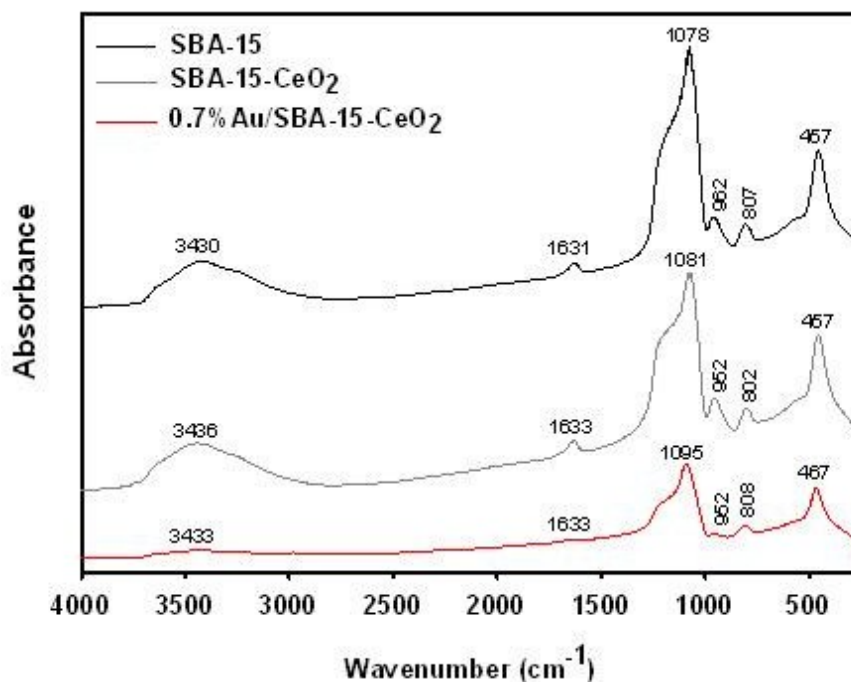


Figure 5.4. FTIR spectra of mesoporous SBA-15, SBA-15- CeO_2 (molar ratio $\text{Ce/Si} = 0.1$) and 0.7% Au/SBA-15-CeO_2 (molar ratio $\text{Ce/Si} = 0.1$).

The absorption band presented at about 1630 cm^{-1} is attributed to the remaining water physisorbed on the materials surface at room temperature [438]. Moreover, all materials presented the typical absorption band centered at circa 1080 cm^{-1} and its shoulder part between the IR bands of 1100–1300 cm^{-1} , ascribed to the asymmetric stretching vibration of $\text{Si}-\text{O}-\text{Si}$, which are a result of partial ordering of the silicate framework at the pore surface [439]. The absorption band observed in the

mesoporous SBA-15 centered at 962 cm^{-1} can be attributed to the stretching vibrations of Si—O in the Si—O—R⁺ groups, as R⁺=H⁺ in the calcined sample, that is the Si—OH groups [161]. For the SBA-15-CeO₂ and 0.7%Au/SBA-15-CeO₂ materials, this band shifted towards a lower wavenumber values after the incorporation of ceria and gold species (962 vs. 952), which could be attributed to the asymmetric vibration of the Si—O—Ce after the incorporation of ceria in the framework of these materials. However, since multiple species are believed to absorb in this frequency region, the assignment of this peak is the source of controversy, and because of the large number of silanol groups present in the calcined silica materials shows an absorption peak at this frequency, this band cannot be taken as a definitely proof of ceria incorporation [439]. It is worth noting that gold addition weakened both the peak intensities of bands centered at 960 and 1080 cm^{-1} , probably as a consequence of the partial blocking or partial damage of the support pores, in agreement with the XRD and N₂ adsorption–desorption analysis. On the other hand, the characteristic IR absorption bands of SiO in SBA-15, centered at circa 805 and 460 cm^{-1} , were assigned to the symmetric stretching and bending vibrations of the intertetrahedral oxygen atoms of SiO₂, respectively [161].

5.4.1.5. X-ray photoelectron spectroscopy (XPS) analysis

X-ray photoelectron spectroscopy was used to determine the chemical state of the elements in the 0.7%Au/SBA-15-CeO₂ catalyst. The presence of C 1s, O 1s, Si 2p, Si 2s, Au 4f, and Ce 3d photoelectron peaks was detected in the XPS measurements. The spectra of the O 1s, Si 2p, Au 4f and Ce 3d core levels have been collected and shown in Figures 5.5a–d, respectively. The O 1s XPS spectrum depicted in Figure 5.5a shows the presence of two oxygen components at binding energies (BE) of 530.3 and 532.9 eV, which can be assigned to CeO₂ and SiO₂, respectively [440]. Figure 5.5b presents the symmetrical Si 2p photoelectron peak centered at 103.9 eV, which agree well with the values reported in the literature for SiO₂–CeO₂ [441].

The oxidation states of the loaded gold and their surface proportions on the 0.7%Au/SBA-15-CeO₂ and 0.7%Au/SBA-15 catalysts were investigated by XPS. The experimental curves of Au 4f core levels spectra of the 0.7%Au/SBA-15-CeO₂ (Ce/Si = 0.1 M), showed in Figure 5.5c, present the doublet of two spin orbit components Au 4f_{7/2} and Au 4f_{5/2} separated by 3.7 eV, which were characterized by the presence of three well-defined spin orbit split Au 4f_{7/2} and three Au 4f_{5/2} components, after the peak deconvolution process using the Kratos software. The BE and the proportion of these spin orbit split components are summarized in Table 5.2, whereas Table 5.3

summarizes the chemical species of gold present in the fresh and spent Au/SBA-15-CeO₂ and Au/SBA-15 catalysts after reaction at pH 9. As it can be noticed in Figure 5.5c, the Au 4f curve fitting showed the presence of three Au 4f_{7/2} components (Au 4f_{7/2-1}, Au 4f_{7/2-2} and Au 4f_{7/2-3}) with photoelectron peaks located at BE 83.4, 84.9 and 86.3 eV, which can be assigned to Au⁰, Au⁺¹ and Au⁺³, respectively [409], indicating the coexistence of metallic and oxidized species on the catalyst, with relative surface concentrations of Au⁰ (78.17%) > Au⁺ (13.08%) > Au³⁺ (8.76%). Similar Au 4f spectra were found for the 0.7%Au/SBA-15 and 0.7%Au/SBA-15-CeO₂ catalysts at other Ce/Si molar ratios. These results are in agreement with the findings of Carretin et al. [442], who demonstrated that the cationic species of gold (Au⁺ and Au³⁺) can be stabilized on the ceria surface by creating Ce³⁺ and oxygen-deficient sites in the ceria. For gold catalysts supported on mesoporous silica at 0.7% gold loading, we found that gold crystallites were mainly present in the metallic state (91.44%) even though oxidized Au⁺ was also present (8.56%) [409].

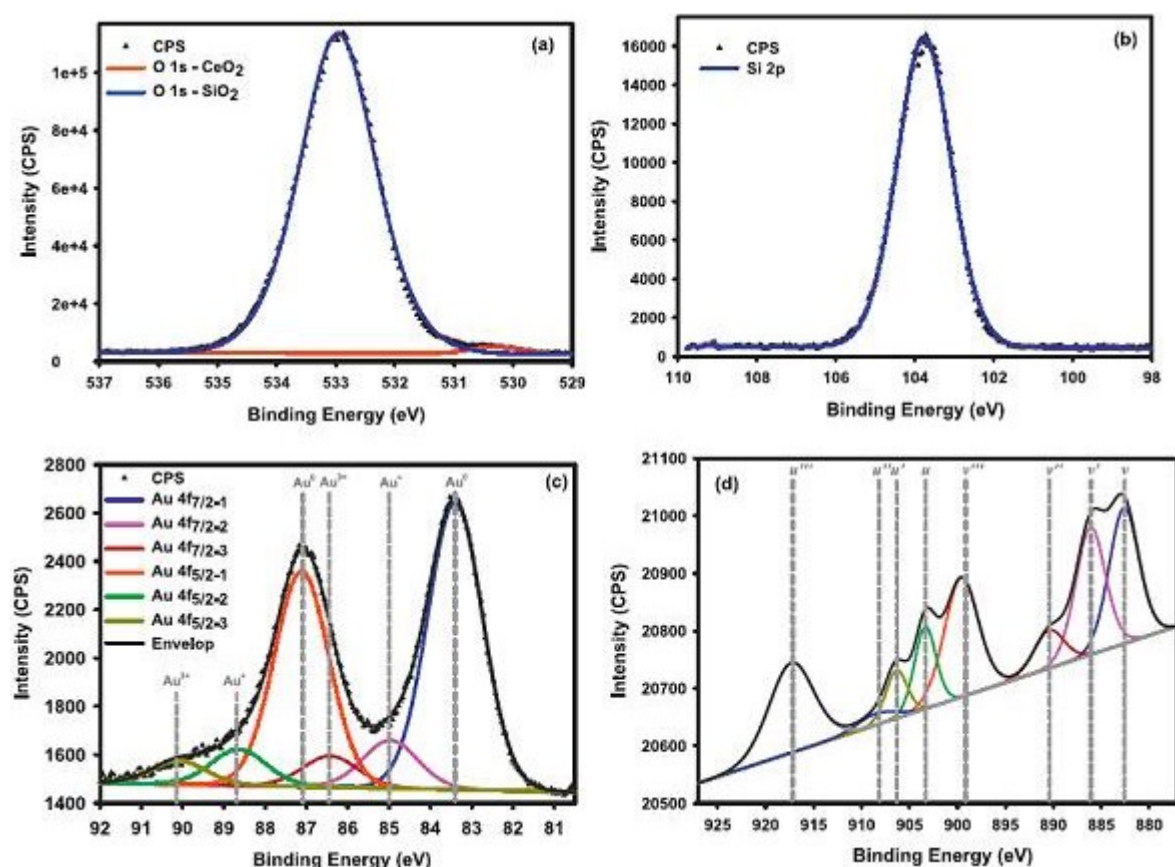


Figure 5.5. XPS-spectra of (a) O 1s, (b) Si 2p, (c) Au 4f and (d) Ce 3d core-level photoelectron spectra of the 0.7%Au/SBA-15-CeO₂ catalyst (molar ratio Ce/Si = 0.1).

Table 5.2. Binding energies of Au 4f_{7/2} and 4f_{5/2} deconvoluted peaks and its relative surface distribution in 0.7%Au/SBA-15-CeO₂ (Ce/Si = 0.1 M).

Peak	Binding energy (eV)	Gold species	Concentration (%) ^a
Au 4f _{7/2-1}	83.4	Au ⁰	44.71 (40.10)
Au 4f _{7/2-2}	84.9	Au ⁺	7.48 (12.92)
Au 4f _{7/2-3}	86.3	Au ³⁺	5.67 (4.17)
Au 4f _{5/2-1}	87.1	Au ⁰	33.46 (30.01)
Au 4f _{5/2-2}	88.6	Au ⁺	5.60 (9.67)
Au 4f _{5/2-3}	90.01	Au ³⁺	3.09 (3.12)

^a Expressed as a percentage of the total area of the Au 4f peak (taken as 100%). Values in parenthesis correspond to concentration of catalyst after reaction at pH=9.0.

Figure 5.5d shows the XPS spectra of the Ce 3d core level of the 0.7%Au/SBA-15-CeO₂ (Ce/Si 0.1 M) catalyst, which was fitted into eight components in accordance with Burroughs et al. [443]. In general, it appears that the cerium binding energies in the 0.7%Au/SBA-15-CeO₂ catalyst are slightly higher than in pure ceria, which could be ascribed to the coordinative unsaturation of surface cerium ions as a consequence of the very small ceria particle size, as reported previously for silica-supported ceria [441]. Nevertheless, it can be seen in Figure 5.5d that Ce 3d XPS spectra are composed of two sets of spin-orbital multiplets labeled as *v* and *u* as proposed by Burroughs et al. [443]. The bands labeled *v* together represent the 3d_{5/2} ionization states, whereas the group of *u* bands corresponds to the 3d_{3/2} ionization states [443]. It is well known that peaks *u*, *u'*, *u''*, *v*, *v'* and *v''* are characteristic of Ce⁴⁺ 3d final states, whereas *u'* and *v'* are typical of Ce³⁺ 3d final states [444]. The doublets *u*, *v* and *u'*, *v'* are attributed to the Ce⁴⁺ 3d⁹4f² O 2p⁴ and Ce⁴⁺ 3d⁹4f¹ O 2p⁵, respectively [443]. The photoelectron peaks *v''* and *u''* are assigned to the Ce⁴⁺ 3d⁹4f⁰ O 2p⁶ state, and this last one peak, associated to the Ce 3d_{3/2} and located at BE of around 917 eV, has been established as the best characteristic peak to differentiate Ce⁴⁺ from Ce³⁺ [444]. Moreover, the presence of *v'* is characteristic of the Ce⁴⁺ oxidation state in CeO₂ [444]. Consequently, from Ce 3d XPS spectra showed in Figure 5.5d, it is clear that cerium displays the presence of both Ce³⁺ and Ce⁴⁺ oxidation states in the 0.7%Au/SBA-15-CeO₂ catalyst. Following the method proposed by Wang

et al. [444], from the peak area obtained by the deconvolution procedure, the $\text{Ce}^{4+}/\text{Ce}^{3+}$ atomic ratio and $\text{Ce}^{3+}/(\text{Ce}^{3+} + \text{Ce}^{4+})$ ratio were 3.21 and 0.24, respectively.

5.4.2. Catalytic activity

5.4.2.1. Optimization of the pH

The optimization of the catalytic activity of the 0.7%Au/SBA-15-CeO₂ (Ce/Si = 0.1) and 0.7%Au/SBA-15 catalysts was investigated on the partial oxidation of lactose for the selective synthesis of lactobionic acid (LBA) at different pH values (see Figures 5.6a–e). The temperature, catalyst/lactose ratio, agitation and airflow were kept constants at 65°C, 0.2, 900 rpm and 40 mL/min, respectively, during these experiments, since they were found the optimal values in our previous work using gold supported on mesoporous silica material, allowing 100% lactose conversion and 100% selectivity towards LBA, after 100 min of reaction under alkaline (pH 9.0) conditions [11]. As shown in Figures 5.6a–e the oxidation of lactose over both gold-based catalysts is pH-dependent as reported for the oxidation of other carbohydrates on metal catalysts [85-86, 404]. Similar to our recent findings for lactose oxidation over 0.7%Au/mesoSiO₂ [11] and bimetallic 1.02%Pd-0.64%Bi/SBA-15 catalysts [86], at low pH of 7 (Figure 5.6a) the kinetics of lactose oxidation is characterized by a slow reaction rate, and after 100 min of reaction the conversion reached was about 80%. No side products were detected by HPLC analysis indicating 100% selectivity towards LBA. As in the case of Pd catalysts, it has been recently reported that gold catalysts could be deactivated by the strong adsorption of the reaction products, which occupy the active sites of the catalyst surface [13]. As depicted in Figures 5.6b and c, when increasing the pH value up to 9.0, the reaction exhibited favorable and outstanding lactose conversion to LBA, and the rates of lactose consumption as well as LBA formation were markedly high. A similar behaviour was found when using the 0.7%Au/SBA-15 catalyst, as presented in Figures 5.6d and e. It is worth mentioning that lactose was almost depleted after only 60 min of reaction where LBA concentration reached a value of 7.37 g/L starting from 7.28 g/L of lactose. This means that $7.28/342.29 \sim 0.021$ moles of lactose were oxidized to give $7.37/358.3 \sim 0.021$ moles of LBA consequently, 100% of selectivity towards LBA formation was reached. Higher pH values (>9.0) were not tested, because in our previous work we found that at these very high alkaline conditions (pH >9.0), the gold catalysts supported on mesoporous SiO₂ were partially decomposed, due to the dissolution of silica material [11, 85]. Similar results have been reported by Mirescu and Prusse [14], who found a pronounced decrease in the activity and selectivity

in the oxidation of lactose with Au/TiO₂ and Au/Al₂O₃ catalysts, when the pH values were higher than 9.0. This behavior was also reported in our investigations on the partial oxidation of lactose to LBA over bimetallic Pd-Bi/SBA-15 catalyst [85-86].

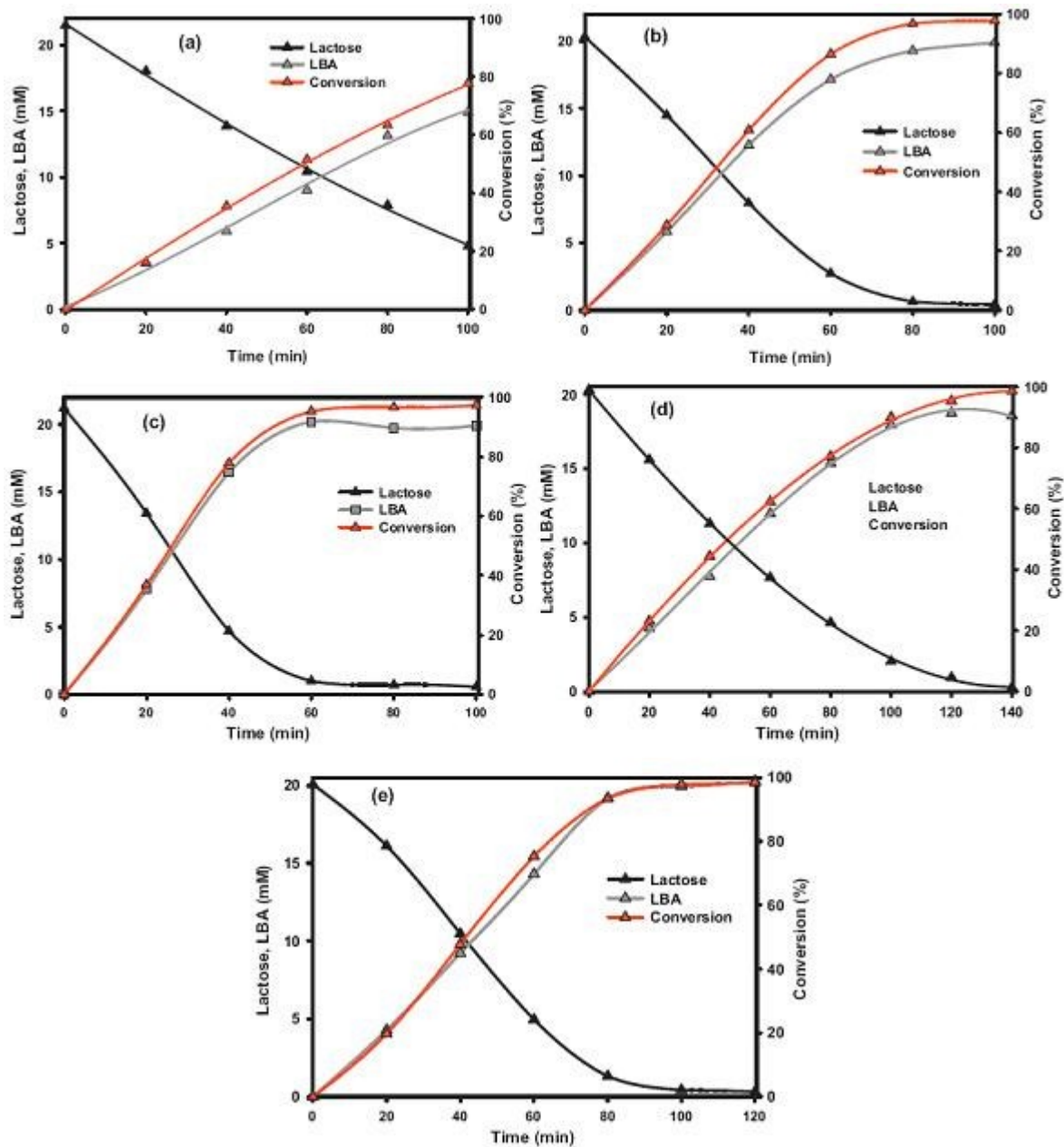


Figure 5.6. Effect of the pH on the kinetics of lactose oxidation to LBA acid over 0.7%Au/SBA-15-CeO₂ catalyst (Ce/Si=0.1 M). (a) pH 7; (b) pH 8; (c) pH 9 and 0.7%Au/SBA-15 catalysts (d) pH 8; (e) pH 9. Conditions: T=65°C; catalyst/lactose ratio 0.2, air flow=40 mL/min, agitation = 900 rpm.

The activity of gold catalysts has been mainly attributed to the size of gold particles. However, the small metal cluster size is not the only sufficient prerequisite to ensure a good catalyst activity, because it is well known that the oxidation state of metals is a very important parameter in the catalytic activity [14]. Despite the extensive work on the gold catalysts, different controversial proposals are found in the literature about the nature of the active species responsible for the oxidation reactions. Moreover, since most of the studies deal with the CO oxidation because it is the most frequently adopted catalytic reaction to evaluate the performance of gold catalysts, in the case of the carbohydrate oxidation over gold catalysts, the role of metallic and oxidized gold species in the reaction mechanisms has been hardly investigated and is still under debate. In order to have a better understanding of the activity of gold species in the lactose oxidation over 0.7%Au/SBA-15-CeO₂ catalysts, XPS analysis were made after the reaction carried out at pH value of 9.0. The relative surface concentrations are of Au species and their binding energies as determined by deconvoluted peaks of Au 4f_{7/2} and Au 4f_{5/2} are shown in Table 5.2 for 0.7% Au/SBA-15-CeO₂ with Ce/Si molar ratio of 0.1. These Au species surface concentrations are also comparatively depicted in Table 5.3 for Au/SBA-15-CeO₂ (Ce/Si = 0.1), Au/SBA-15 and Au/meso-SiO₂ previously published [11] with Au loading of 0.7%.

Table 5.3. Comparative preponderance of Au species in Au/SBA-15, Au/SBA-15-CeO₂, and Au/SiO₂-meso [11].

Catalyst		Au/SBA-15-CeO ₂	Au/SBA-15	Au/ SiO ₂ -meso
• Fresh	Au ⁰	78.17	79.00	91.44
	Au ⁺	13.08	14.10	4.89
	Au ³⁺	8.76	6.90	3.66
• Spent	Au ⁰	70.11	77.00	ND*
	Au ⁺	22.59	14.10	ND
	Au ³⁺	7.29	8.90	ND

In general, it can be noticed that after reaction the concentration of Au⁰ and Au³⁺ diminished, whereas the concentration of Au⁺ increased. It is well known that the oxidation state of metals is a very important parameter in the catalytic activity. In the case of the carbohydrate oxidation over gold

catalysts, the oxidation state of gold species could play a role in the catalyst activity and this has been hardly investigated. We wanted tentatively find out if really the oxidation state is involved to determine the catalyst activity. As shown by XPS analysis investigated for the Au 4f core level as summarized in Table 5.3, our results indicate that the presence of oxidized gold species (such as Au⁺ and/or Au³⁺) may affect the activity of gold catalysts in carbohydrate oxidation. From Table 5.3, it is worth mentioning that fresh Au/SBA-15-CeO₂ and Au/SBA-15 have somewhat similar composition in their oxidized species. However ceria-doped catalyst exhibited more pronounced activity than Au/SBA-15. Furthermore, Even if Au/meso-SiO₂ (see our previous publication [11]) is characterized by higher level in Au⁰, its activity was lower than that of Au/SBA-15-CeO₂. To be consistent, the Au oxidation state is not solely the parameter which controls the catalyst activity for this reaction. Other not known parameters could effectively have an effect on this activity.

Although some works found in the literature for the oxidation of alcohols over Au supported catalysts [445-446] reported the presence of mainly the metal Au⁰ with the presence of Au⁺ and rarely Au³⁺ species, in the similar manner as reported in the present work. However, it cannot state clearly which species are responsible for the Au oxidation activity in the liquid phase and the role of the oxidation state of gold is still matter of discussion.

5.4.2.2. Catalyst support effect on the activity

It is well known that the nature of support is also important for the catalytic performance of supported gold catalysts. For that purpose a comparative activity study was carried out using 0.7%Au/SBA-15 and 0.7%Au/SBA-15-CeO₂ (Ce/Si = 0.1) catalysts at pH 8 and 9. Figure 5.7 comparatively summarizes these activities in terms of initial reaction rate r_0 (LBA formed/min), for Au/SBA-15, Au/SBA-15-CeO₂ at Ce/Si = 0.1 as well as Au/meso-SiO₂ (from our previous published work), under identical reaction conditions.

As depicted in this figure, Au/SBA-15-CeO₂ catalyst exhibited enhanced activity towards lactose conversion towards LBA for both pH conditions. From these results, it is to expect that possibly Ce played a certain role in this enhanced activity.

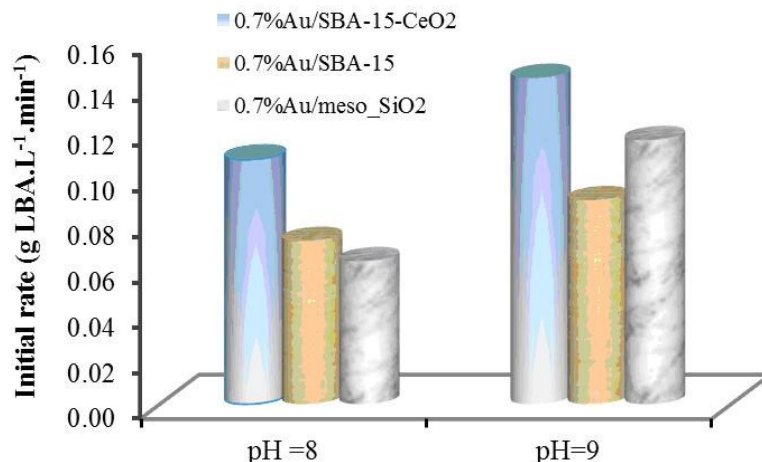


Figure 5.7. Activity comparison of the catalysts at pH 8 and pH 9. Conditions: T = 65°C; catalyst/lactose ratio 0.2, air flow = 40 mL/min, agitation = 900 rpm.

5.4.2.3. Ce/Si molar ratio effect on the activity

Because of its high oxygen storage capacity and well-known catalytic and redox properties, the presence of ceria in the catalyst not only might contribute to the stabilization and the dispersion of gold particles, but also might contribute to the reaction mechanism.

To investigate the effect of Ce/Si molar ratio selective promotion of Au/SBA-15 catalyst by progressive addition of CeO₂ was carried out to see whether the activity changes because of Ce dependence. We prepared 4 new catalysts Au/SBA-15-CeO₂ with Ce/Si molar ratios of 0.1, 0.2, 0.4 and 0.6 and carried out the activity tests at pH 9 under identical other reaction conditions. Figure 5.8 depicts the initial reaction rate of LBA formation for all Au/SBA-15-CeO₂ catalysts at Ce/Si = 0.1, 0.2, 0.4, and 0.6 as well as for Au/SBA-15 catalyst.

As depicted in Figure 5.8, the Au/SBA-15-CeO₂ catalyst activity depends greatly on the Ce/Si molar ratio. A maximum of activity is reached at Ce/Si of 0.2. Furthermore, catalysts prepared with Ce/Si molar ratio of 0.1, 0.2, 0.4 exhibited enhanced activity in comparison to that of Au/SBA-15 catalyst. The catalyst with Ce/Si of 0.6 seems to exhibit similar activity of the Ce-non promoted Au/SBA-15 catalyst.

To verify if the Au crystallite size has an effect on the enhancement of this activity we carried out the TEM characterization of the different Au/SBA-15-CeO₂ catalysts and proceeded to the determination of the average Au crystallite size. As shown in Figure 5.9, the Au crystallite size was mostly invariant

with Ce/Si molar ratio and remains in the vicinity of 4 ± 0.5 nm in the same magnitude of the Au crystallite size obtained for Au/SBA-15.

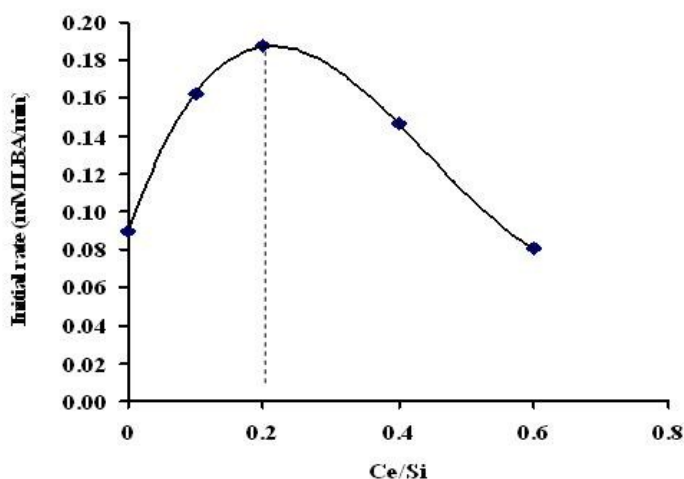


Figure 5.8. Initial rate of LBA formation vs. Ce/Si molar ratio for 0.7% Au/SBA-15-CeO₂ catalysts.

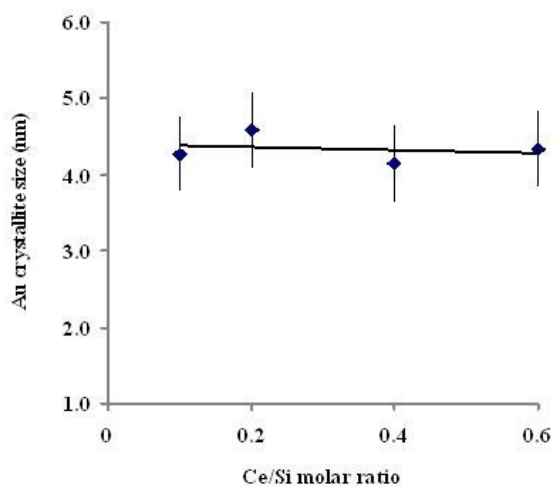


Figure 5.9. Au crystallite size vs. Ce/Si molar ratio for 0.7% Au/SBA-15-CeO₂ catalysts.

Also to verify if the Ce/Si molar ratio has an effect on the Au speciation changes in fresh and spent Au/SBA-15-CeO₂ as well as Au/SBA-15 catalysts which possibly can be responsible in the enhancement of catalyst activity and the selectivity, we have carried out XPS characterization of the different Au/SBA-15-CeO₂ catalysts before and after the reaction and proceeded to the determination of the gold species prevalence or preponderance. As shown in Table 5.4, the prevalence of Au⁰ and Au³⁺ species was mostly invariant with Ce/Si molar ratio for fresh and spent catalysts. Only very slight

variations can be observed for the Au⁺ specie for both fresh and spent catalysts. The standard deviation from the average content of Au⁺ remains to <8% which can be considered within the standard error of the procedure to quantify these contents. The Au speciation changes without the presence of Ce occur also where for Au/SBA-15 catalyst Au⁰ undergoes oxidation by forming Au³⁺ in the presence of lactose while the prevalence of Au⁺ species remains constant at pH 9.

Table 5.4. Au speciation changes as determined by XPS characterization for fresh and spent Au/SBA15 and Au/SBA-15-CeO₂ catalysts at different pH and Ce/Si molar ratios.

Catalyst	Concentration of gold species (%) ^a		
	Au ⁰	Au ⁺	Au ³⁺
0.7Au/SBA-15-CeO ₂ Ce/Si 0.1M	62.75	32.28	4.97
0.7Au/SBA-15-CeO ₂ Ce/Si :0.1M after RxN at pH 9	52.5	38.57	8.93
0.7Au/SBA-15-CeO ₂ Ce/Si 0.1M after contact H ₂ O at pH 9	69.13	24.97	5.89
0.7Au/ SBA-15-CeO ₂ Ce/Si 0.2M	61.66	32.54	5.79
0.7Au/SBA-15-CeO ₂ Ce/Si :0.2M after RxN at pH 9	48.94	42.2	8.86
0.7Au/SBA-15-CeO ₂ Ce/Si:0.2M after contact H ₂ O at pH 9	67.36	24.58	8.06
0.7Au/SBA-15-CeO ₂ Ce/Si = 0.6M	64.56	29.88	5.56
0.7Au/SBA-15-CeO ₂ Ce/Si = 0.6M after RxN at pH 9	44.95	47.43	7.62
0.7Au/SBA-15-CeO ₂ Ce/Si = 0.1M ^b	78.17	13.08	8.76
0.7Au/SBA-15-CeO ₂ Ce/Si = 0.1M after RxN at pH 7 ^b	75.11	17.74	7.15
0.7Au/SBA-15-CeO ₂ Ce/Si = 0.1M after RxN at pH 9 ^b	70.11	22.59	7.29
0.7Au/SBA-15-CeO ₂ Ce/Si : 0.4M	60.02	31.26	8.72
0.7Au/SBA-15	79.0	14.10	6.90
0.7Au/SBA-15 after RxN at pH 9	77.0	14.10	8.90

^a Expressed as a percentage of the total area of the Au 4f peak (taken as 100%). ^b This sample was taken from the first batch of Au/SBA-15 CeO₂ catalyst, for which the composition in gold species was a little different. It had more metallic gold.

These experiments and characterizations results state clearly that Au crystallites properties such as their size and the prevalence of their oxidation state remained mostly invariant with Ce/Si molar ratio despite the enhancement of the catalyst's activity. Then possibly other catalyst properties such as the

catalyst coordination environment could be affected with the presence of CeO₂ within the catalysts making that Au/SBA-15-CeO₂ catalyst activity is greatly dependent from the Ce/Si molar ratio. Similar findings were reported by Timofeeva et al. [447] when they investigated the Ce-SiO₂ mesoporous SBA-15 materials for oxidative catalysis of cyclohexene and cyclohexanol with increasing Ce content. They investigated deeply the behavior of these materials in terms of IR, DR-UV-vis and DRIFT spectroscopy characterizations where they found that the coordination and the agglomeration states of cerium atoms as well as the density and the content of silanol groups on the surface of the Ce-SBA-15 are the key factors determining the catalytic activity of Ce-modified SBA-15 supports. Also identical explanations were also given by Chen et al. [448] when they studied the dual promotions of catalytic activity of Ce dopant and Ce loading based on Pt/SBA-15 catalysts used for CO oxidation. They concluded that the obvious activity promotion of Pt/Ce-SBA-15 catalysts was highly depend on the strong metal-support interactions induced by the Ce loading where new coordination environments and Ce aggregation appeared after Ce species introduction depending on Ce/Si ratio.

For example for 0.7%Au/SBA-15-CeO₂ catalyst with Ce/Si = 0.1, the Ce⁴⁺/Ce³⁺ ratio was diminished to 1.54 after reaction as determined by XPS analysis. Thus, it is possible that CeO₂ assists in the oxidation of lactose to LBA under reducing conditions through the reduction of Ce⁴⁺ to Ce³⁺.

5.5. Conclusions

For the first time gold catalyst (0.7% Au nominal loading) supported on mesoporous SBA-15-CeO₂, synthesized via wet chemical process using a gold cationic complex precursor [Au(en)₂]³⁺ (en = ethylenediamine), was successfully investigated for lactose oxidation using air as oxidizing agent.

Through XRD, TEM, and N₂ adsorption analysis, we found that the support possess ordered hexagonal mesoporous structure, high surface area and large pore volume, similar to SBA-15. Introduction of gold species causes some of defects in hexagonal ordering structure and decreases the BET surface area and the total pore volume. Gold nanoparticles were well dispersed and not aggregated, and seem to be within the mesoporous framework channels.

XPS analysis indicated the coexistence of metallic and oxidized species on the catalyst, with relative abundances of Au⁰ > Au⁺ > Au³⁺, whereas the XPS spectra of the Ce 3d core level suggested the presence of both Ce³⁺ and Ce⁴⁺ oxidation states in the 0.7%Au/SBA-15-CeO₂ catalyst.

The catalytic activity investigated at different pH values, indicated that when increasing the pH value up to 9.0, the reaction exhibited 100% of conversion, after only 60–80 min, and 100% selective towards LBA, when the catalyst was added at a ratio of 0.2 catalyst/lactose under the reaction conditions of 65°C, 40 mL/min, 900 rpm. The high activity and selectivity of the 0.7%Au/SBA-15-CeO₂ catalyst could be due to a synergy of the following factors: (i) the low size (~5 nm) of well dispersed gold nanoparticles; (ii) the presence to CeO₂ which can stabilize the dispersion of gold particles and enhance the mobility of surface oxygen species; and (iii) the redox properties of Ce that might contribute to the reaction mechanism.

This study demonstrated clearly that 0.7%Au/SBA-15-CeO₂ catalyst outperforms 0.7%Au/SBA-15 catalyst in terms of activity. This activity depends greatly on the Ce/Si molar ratio were the coordination and agglomeration states of cerium atoms could probably have an important effect.

Comparing with the palladium or bismuth-promoted palladium supported catalysts normally used in carbohydrates oxidation, the reaction control using 0.7%Au/SBA-15-CeO₂ catalyst is easier because the control of oxygen flow, required to avoid the over oxidation of Pd and Bi-Pd catalysts, is not necessary, and additionally, no side products are detected. Thus, owing to the ease of synthesis, as well as because of its excellent catalytic performance, the 0.7%Au/SBA-15-CeO₂ catalyst is very efficient for the catalytic oxidation of lactose to high value lactobionic acid.

Chapter 6. Synthesis of high value lactobionic acid by aerobic oxidation of lactose on Au/SiO₂ catalysts

Submitted to *Catalysis Science & Technology* by **Luis-Felipe Gutiérrez, Safia Hamoudi, Khaled Belkacemi**

6.1. Abstract

Gold supported on mesoporous SBA-15 and amorphous fumed silica (Cab-O-Sil) were synthesized via wet chemical process using a gold cationic complex precursor Au(en)₂Cl₃ (en = ethylenediamine) and evaluated as catalysts for the synthesis of high value lactobionic acid (LBA) by aerobic oxidation of lactose. The catalysts were characterized by N₂ physisorption, XRD, FTIR, TEM and XPS. N₂ physisorption and XRD analyses revealed that Au/SBA-15 possesses ordered hexagonal mesoporous structure, high surface area and large pore volume, similar to the pristine SBA-15 support. However, the BET surface area and pore volume of SBA-15 support were significantly decreased upon gold loading. Conversely, Au/Cab-O-Sil exhibited N₂ adsorption-desorption isotherm typical of macroporous amorphous materials, and its BET surface area was very similar to that of Cab-O-Sil support, indicating that gold species were mainly located on the support surface. XPS analysis indicated the coexistence of metallic and oxidized species (Au⁰, Au⁺ and Au³⁺) in both Au/SBA-15 and Au/Cab-O-Sil catalysts. Both catalysts exhibited high activity and 100% selectivity towards LBA. Lactose was almost depleted after 100 min (Au/SBA-15) and 140 min (Au/Cab-O-Sil) of reaction under alkaline (pH 9.0) and mild reaction temperature (65°C), when they were used at a catalyst/lactose ratio of 0.2, respectively, indicating the better performance of gold catalyst supported on SBA-15.

6.2. Introduction

Carbohydrates have long time been used in the manufacture of bulk and fine chemicals, and they are currently viewed as renewable raw material for the “green chemistry” of the future. Because of its worldwide surplus and low cost, the transformation of lactose into high value derivatives has drawn the attention of researchers and industry in the last years. As a result, products such as epilactose, galacto-oligosaccharides, lactitol, lactobionic acid, lactosucrose, lactulose, sialyllactose and tagatose,

have found important applications in the food and pharmaceutical industries, as value-added lactose derivatives [21, 25].

Owing to its antioxidant, chelating and humectant properties, lactobionic acid (LBA) (4-O- β -D-galactopyranosyl-D-gluconic acid; C₁₂H₂₂O₁₂) is a high value-added oxidation product of lactose, with high potential applications in the food, pharmaceutical and chemical industries. The main commercial use of LBA is as ingredient of the solutions employed for stabilizing organs prior to transplantation [43], and it represents a new ingredient in skin care products featuring potent antioxidant, wound healing, humectant anti-aging and keratinizing properties [115, 401]. It is also commercially applied as ion sequestrant in detergent solutions [95]. LBA is an excellent carrier for calcium supplementation, and it has recently been employed in the design of functional nanoparticles for carrying drugs [96, 98]. LBA can be also used as acidulant with a sweet taste; as filler in cheese production; as firming agent, and to fortify functional drinks with essential minerals such as Fe and Cu [8, 402].

The selective conversion of lactose to LBA relates to the oxidation of the free aldehyde group of the glucose-moiety in the lactose molecule. Although this reaction can be accomplished by chemical, biochemical, electrochemical and heterogeneous catalytic processes, the latter can be considered as the “greenest” approach.

Lactose oxidation on Pt, Pd and Bi-promoted Pd supported catalysts has been largely investigated [10, 13, 16, 80, 82-85, 87, 89, 403], and it is well documented that problems connected to their deactivation by over-oxidation and Bi leaching during the reaction limit their utilization [404]. Moreover, since bismuth is prone to leaching, applications of catalysts containing this metal are not appropriate for food and pharmaceutical applications [9]. Conversely, gold catalysts have shown high activity, selectivity, reusability and resistance to poisons for the selective oxidation of carbohydrates. Therefore, they can be recommended for the green production of fine chemicals, pharmaceuticals and food ingredients, owing to its bio-compatibility [12, 404]. Except for few reported works [13-16, 449], LBA production by means of heterogeneous catalytic oxidation over gold catalysts has been hardly investigated. These studies indicated that gold nanoparticles supported on Al₂O₃, TiO₂, and CeO₂ allowed to attain moderate to high conversions (>80%) and selectivities (up to 95%).

Mesoporous silica materials with ordered and controllable porous structure, excellent mechanical properties, high surface area, pore volume and thermal stability are very suitable catalyst supports, because they provide high dispersion of metal nanoparticles and facilitate the access of the substrates to the active sites [146]. Nevertheless, the conventional deposition precipitation method is not appropriate for the incorporation of gold nanoparticles (AuNPs) into silica materials, because under the high pH conditions required to hydrolyze the most commonly used gold precursor (HAuCl_4), the weak interaction between the negatively charged silica surface and the $[\text{Au}(\text{OH})_n\text{Cl}_{4-n}]^-$ species facilitates the mobility of gold particles, which can easily sinter during the synthesis process, especially during the calcination step, yielding inactive catalysts [207]. Consequently, alternative synthesis methods have been proposed, which have been recently thoroughly reviewed [146].

We have recently reported highly active gold crystallites dispersed on mesoporous silica using *bis*-[3-(triethoxysilyl) propyl] tetrasulfide (BTESPTS), as a silane coupling agent to immobilize gold onto the SiO_2 support. This catalyst with irregular shapes and pores presenting a wormhole-like framework structure containing interconnected 3D-mesopores was found 100% selective towards LBA production from partial aerial oxidation of lactose. However, the use of BTESPTS to immobilize gold species is costly procedure. Moreover, relatively moderate to high BTESPTS/Si molar ratios are required to have active and selective Au/mesoporous SiO_2 catalysts. For these ratios, the well ordered structure of hexagonal silica materials is destroyed. On the other hand, the effect of the siliceous structure of the support on the lactose oxidation using supported AuNPs on silica materials has been very scarcely studied.

In order to contribute to the fascinating topic of catalysis by gold, the main objectives of this work are: (i) to prepare and characterize a gold catalyst supported on mesoporous SBA-15, using a cationic gold complex $\text{Au}(\text{en})_2\text{Cl}_3$ (*en* = ethylenediamine) as relatively cheaper precursor, where the morphology and porous highly ordered structure of the support can be conserved; (ii) to evaluate the activity of this catalyst in the selective LBA synthesis from lactose oxidation, and (iii) to investigate the influence of the support structure by comparing this catalyst with a gold catalyst supported on amorphous fumed SiO_2 (Cab-O-Sil) similarly synthesized, and with a gold catalyst supported on a wormhole-like SiO_2 obtained in our recent work [11]. The catalysts characterization by means of BET surface, powder X-ray diffraction (XRD), X-ray photoelectron spectroscopy (XPS), Fourier transform infrared spectroscopy (FTIR) and transmission electron microscopy (TEM) was investigated, as well

as the influence of the pH value on lactose conversion. To the best of our knowledge, it is the first time that the oxidation of lactose to LBA over gold catalysts supported on silica materials having different structures, is comparatively investigated.

6.3. Experimental details

6.3.1. Materials

All reagents were of the highest purity and were used without further purification. Gold (III) chloride trihydrate ($\text{HAuCl}_4 \cdot 3\text{H}_2\text{O}$), tetraethyl orthosilicate (TEOS), α -Lactose monohydrate and lactobionic acid were purchased from Sigma Aldrich. Amorphous fumed silica Cab-O-Sil® M5 was obtained from CABOT. Pluronic P123 ($\text{EO}_{20}\text{PO}_{70}\text{EO}_{20}$, $M_{av} = 5900$ g/mol) was graciously offered by BASF. Sodium hydroxide solution 50% and anhydrous sodium acetate, both HPLC grade from Fluka, were used for eluents preparation for HPLC analysis.

6.3.2. Synthesis of mesoporous SBA-15

Mesoporous SBA-15 was synthesized in acidic media using Pluronic P123 as templating agent, as described previously by Zhao et al [145].

6.3.3. Synthesis of $\text{Au}(\text{en})_2\text{Cl}_3$

The cationic gold complexes $\text{Au}(\text{en})_2\text{Cl}_3$ were synthesized as described by Zhu et al [206]. Typically, 0.5 g of $\text{HAuCl}_4 \cdot 3\text{H}_2\text{O}$ were dissolved in 5 mL of deionized water, and then ethylenediamine was added dropwise until the formation of a transparent brown solution. This solution was stirred for 30 minutes, and subsequently ethanol (~35 mL) was added. After centrifugation, the solid was washed with ethanol and then vacuum-dried overnight at 100°C. The yellowish gold precursor was kept protected from light to prevent its decomposition [146].

6.3.4. Catalyst preparation

The cationic gold complexes $\text{Au}(\text{en})_2\text{Cl}_3$ may act as acid by losing a proton from the coordinated amine group, under basic conditions. Based on this principle, Au/SBA-15 and Au/Cab-O-Sil catalysts were synthesized by deposition-precipitation of $\text{Au}(\text{en})_2\text{Cl}_3$ at pH 10 as reported by Zhu et al. [206], given that in alkaline media the negative-charged surface of SiO_2 can readily adsorb the $[\text{Au}(\text{en})_2]^{3+}$ cations, by deprotonation reaction of ethylenediamine ligands [146]. In a typical synthesis, in order to obtain a nominal gold loading of about 0.7%, 30 mg of $\text{Au}(\text{en})_2\text{Cl}_3$ were dissolved in 40 mL of

deionized water, and the pH was adjusted to 10 by the addition of 1-M NaOH aqueous solution. Then, 2 g of siliceous support were added and the mixture was stirred for 3 h, maintaining the pH at a value of 10 by adequate addition of few drops of 1-M NaOH aqueous solution. After vacuum filtration, the yellowish solids were washed with deionized water. Subsequent to vacuum-drying overnight at 100°C, the obtained catalysts were calcined at 500°C for 5 h at a heating rate of 1°C/min, using a programmable oven. Calcined samples showed a light pink color, as showed in Figure 6.1, which is characteristic of the presence of AuNPs.

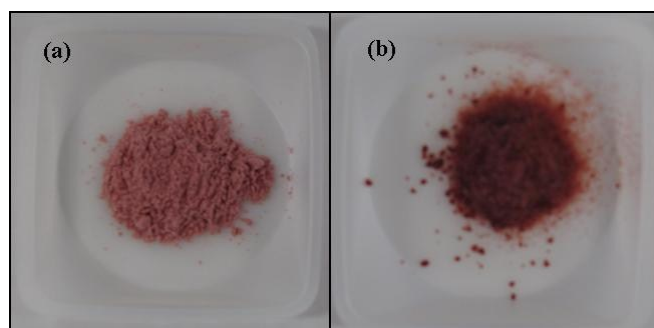


Figure 6.1. (a) Au/SBA-15 (b) Au/Cab-O-Sil

6.3.5. Catalysts characterization

Nitrogen adsorption/desorption isotherms of SiO₂ supports and calcined Au/SiO₂ catalysts were obtained using a volumetric adsorption analyzer (Model Autosorb-1, Quantachrome Instruments, Boyton Beach, FL) at -196°C. Before the adsorption analysis, the samples were degassed for 3h at 200°C. Total pore volume was estimated from the amount adsorbed at 0.99 relative pressures. Pore size distributions were calculated using the desorption branch of the N₂ adsorption/desorption isotherms and the Barrett-Joyner-Halenda (BJH) method [408].

Powder X-ray diffraction (XRD) patterns were obtained with an Ultima III Rigaku Monochromatic Diffractometer using CuK α radiation ($\lambda=1.5406\text{\AA}$). Small angle powder diffraction patterns were acquired at a scanning rate of 1°/min in the 2 θ range of 0.6-3°, while wide angle powder XRD was obtained at the same scanning rate in the 2 θ range 20-80°.

Transmission electron microscopy (TEM) images were taken on a JEM-3010 electron microscope (JEOL, Japan) with an acceleration voltage up to 200 kV. The catalysts samples were suspended in methanol and ultrasonically treated during 10 minutes. Then, the suspension (5 μL) were disposed uniformly and dried on a nickel grid.

Transform infrared (FTIR) spectra were recorded in absorption mode on a Varian 1000 FTIR spectrometer in the range of 400-4000 cm^{-1} . FTIR analysis was carried out at room temperature using potassium bromide (KBr) pellets containing about 0.5% of the solid samples, which were compacted in a uniaxial press under a nominal pressure of 6.89 kPa. The spectrum of dry KBr was taken for background subtraction, before recording the samples.

The catalyst surface and the oxidation state of gold in the catalysts were studied by X-ray Photoelectron Spectroscopy (XPS) analysis using an Axis-Ultra system spectrometer from Kratos (U.K.) equipped with an electrostatic analyzer of large ray, a source of double X-rays Al-Mg without monochromator and an Al source with monochromator. The pressure in the XPS room was maintained between 5×10^{-9} and 5×10^{-8} torr during the analysis. All the spectra were recorded with the Al monochromatic source with a power of 300 watts. The flyover spectrum used to determine the elementary composition was recorded with pass energy in the analyzer of 160 eV and an energy step of 1 eV, using lenses in hybrid mode, which maximizes the sensitivity. The detailed spectra with high resolution were recorded with pass energy of 40 or 20 eV, and step energy of 50 or 100 meV. The spectra with high resolution are used for the chemical analysis [409]. The adjustment of the envelope calculated with the experimental spectrum was carried out using CasaWPS software from Kratos (U.K.). The binding energy (BE) scale was calibrated by measuring C1s peak (BE=285.0 eV) from the surface contamination.

6.3.6. Lactose oxidation experiments

Lactose oxidation experiments were carried out at atmospheric pressure in a thermostated and magnetically stirred 300 mL-glass reactor, following the optimal conditions found in our previous work [11]. In a typical reaction, 175 mL of 20 mM lactose solution were heated under continuous agitation (600 rpm) until the temperature reached $65 \pm 0.5^\circ\text{C}$, while nitrogen (500 mL/min) was simultaneously bubbled for stripping off the dissolved oxygen. Subsequently, the stirring was increased to 900 rpm, the catalyst was added and the pH of the solution was adjusted at the desired value, by the addition of few drops 1-M NaOH aqueous solution. Then, air was bubbled through the reaction mixture at a constant flow rate of 40 mL/min. During the reaction, the pH value was kept constant by adding 1-M NaOH aqueous solution, by means of a pH STAT Titrator (Metrohm® 842 Titrando®, Switzerland), and the dissolved oxygen concentration was monitored using an oxygen probe (Ocean Optics, Inc., USA) connected to a fiber optic sensor system (TauTheta Instruments LLC, USA).

The time 'zero' of the reaction corresponded to the moment when the air was bubbled through the reaction mixture. The reactions were carried out during 180 minutes using a catalyst/lactose ratio of 0.2 as optimized in our previous work [11]. Liquid samples were taken at regular intervals for the subsequent HPLC analyses.

6.3.7. Reaction sample analysis

Samples of reaction mixture were analyzed using a chromatographic system DX- ICS 2500 (Dionex, USA) equipped with a gradient pump GP50 and an electrochemical detector ED50 with a thin-layer type amperometric cell outfitted with gold electrodes and an Ag/AgCl reference electrode. In order to improve sensitivity, minimize the baseline drift and clean the gold working electrode, a triple potential waveform of E_1 : 0.1, E_2 : 0.6 and E_3 : -0.8V was applied for duration times of t_1 : 0.5, t_2 : 0.09 and t_3 : 0.07 s. The chromatographic separation of lactose and LBA was performed on a CarboPac PA1 analytical column (4mm×250 mm i.d., Dionex, USA) in conjunction with a CarboPac PA1 guard column (4mm×50mm i.d., Dionex, USA). Sodium hydroxide solution 50% and anhydrous sodium acetate (NaOAc) were used to prepare the eluents A (0.1M NaOH) and B (0.1M NaOH-0.5M NaOAc) in filtered and vacuum-degassed HPLC-Grade water. All eluents were stored in closed and pressurized bottles with helium. The flow-rate was set at 1 mL/min. For the analysis, the flow gradient was programmed as follows: From 100% eluent A (isocratic for 10 min) to an eluent composition of 60%A and 40%B in 10 min using a linear gradient. Then, isocratic period of this eluent composition for 10 min, and subsequently the eluent was returned to 100%A in 5 min, using a linear gradient. Chromeleon software (Dionex, USA) was used to perform all the calibration and integration of chromatographic data.

6.4. Results and discussion

6.4.1. Catalyst characterization

6.4.1.1. Nitrogen physisorption

Textural properties of the SiO₂ supports (mesoporous SBA-15, Cab-O-Sil and SiO₂-meso) and Au/SiO₂ catalysts (0.7%Au/SBA-15, 0.7%Au/Cab-O-Sil and 0.7%Au/SiO₂-meso) were obtained from the low-temperature (-196°C) nitrogen adsorption/desorption isotherm measurements, from which the specific surface areas, specific pore volumes and mesopore size distributions were calculated and summarized in Table 6.1. It is noticed that the BET surface area and the total pore volume of the

SBA-15 decreased notably after incorporation of gold, because of the partial blockage of the support pores. When comparing with the pristine mesoporous SBA-15 support, the BET surface area and the total pore volume were reduced by ≈ 50 and 30%, respectively. On the other hand, the BET surface area of Cab-O-Sil and 0.7%Au/ Cab-O-Sil were very similar (~ 190 m²/g), indicating that gold species were mainly located on the support surface. Now, when comparing these catalysts with the 0.7%Au/SiO₂-meso obtained in our recent work [11] using BTESPTS as organic functional ligand, the BET surface area of the latter catalyst (827.3 m²/g) was about twice than that of 0.7%Au/SBA-15 and more than four times than that of 0.7%Au/Cab-O-Sil. This can be explained by the fact that after the removal of the functional ligands by calcination, void defects on the pore walls are formed, which leads to higher values of surface area higher than pure SBA-15. However, the pore diameter and the total pore volume of this catalyst (3.7 nm and 0.779 cm³/g, respectively) were lower than those of the Au/SBA-15 catalysts synthesized using the Au(en)₂Cl₃ complex.

Table 6.1. Textural parameters of silica supports and gold on silica catalysts

Material	BET surface area (m ² /g) ^a	Pore diameter (nm) ^b	Total pore volume (cm ³ /g) ^c
SBA-15	931.2	6.8	1.260
0.7%Au/SBA-15	479.1	6.2	0.849
Cab-O-Sil	188.1	-	0.889
0.7%Au/Cab-O-Sil	190.4	-	0.713
SiO ₂ -meso ^d	995.7	3.70 and 4.73	1.087
0.7%Au/SiO ₂ -meso ^d	827.3	3.70	0.779

^a Calculated according to standard Brunauer–Emmett–Teller (BET) equation for data collected in the relative equilibrium pressure interval of $0.03 < P/P_0 < 0.3$. ^b BJH pore diameter calculated from the desorption branch. ^c Estimated from the amount of nitrogen adsorbed at a relative pressure P/P_0 of 0.99. ^d Data from reference [11]

The N₂ adsorption–desorption isotherms of the synthesized materials are shown in Figure 6.2a. As it can be observed, the shape of the N₂ adsorption-desorption isotherms of SBA-15 and 0.7%Au/SBA-15 exhibited the characteristic type IV according to IUPAC classification [165], and displayed a broad H1 type hysteresis loop characteristic of large pore mesoporous solids [410], indicating that the mesoporous structure was maintained after gold loading. However, the incorporation of gold into the mesoporous SBA-15 led to a slight reduction in the N₂ adsorption capacity. The initial increase in adsorption capacity at low relative pressure is due to monolayer-multilayer adsorption on mesopores,

whereas the upward deviation in the range of P/P_0 between 0.5 and 0.8 is associated with progressive mesopores filling. As the relative pressure increases, the adsorption isotherms displayed a sharp increase characteristic of the capillary condensation inside uniform mesopores. Furthermore, the hysteresis loop at P/P_0 values between 0.5 and 0.8 for the 0.7%Au/SBA-15 catalyst looks slightly different in comparison to that of SBA-15 support, indicating that some structural defects were formed in the mesoporous framework [412], which is in agreement with the small angle XRD diffraction peaks for this material, as shown in Figure 6.3. On the other hand, the shape of the N_2 adsorption-desorption isotherms of Cab-O-Sil and 0.7%Au/ Cab-O-Sil exhibited the characteristic type II according to IUPAC classification [165], and displayed a narrow H3 type hysteresis loop at P/P_0 values higher than 0.8, characteristic of aggregates or agglomerates of particles forming slit shaped pores with non-uniform size and/or shape [450].

The BJH pore size distributions calculated from the desorption branch of the synthesized SBA-15, SiO_2 -meso, 0.7%Au/SBA-15 and 0.7%Au/ SiO_2 -meso materials are shown in Figure 6.2b. It is observed that SBA-15 support exhibited a narrow pore distribution centered at about 6.8 nm of average pore size, which was reduced to 6.2 nm after incorporation of gold nanoparticles into the channel system. On the other hand, the SiO_2 -meso support presented dual-pore size distribution centered at around 3.7 and 4.7 nm, which reduces to one pore distribution of ~ 4 nm average pore size after gold loading. The structural morphology of the synthesized Au/ SiO_2 catalysts can be further verified by transmission electron microscopy (TEM).

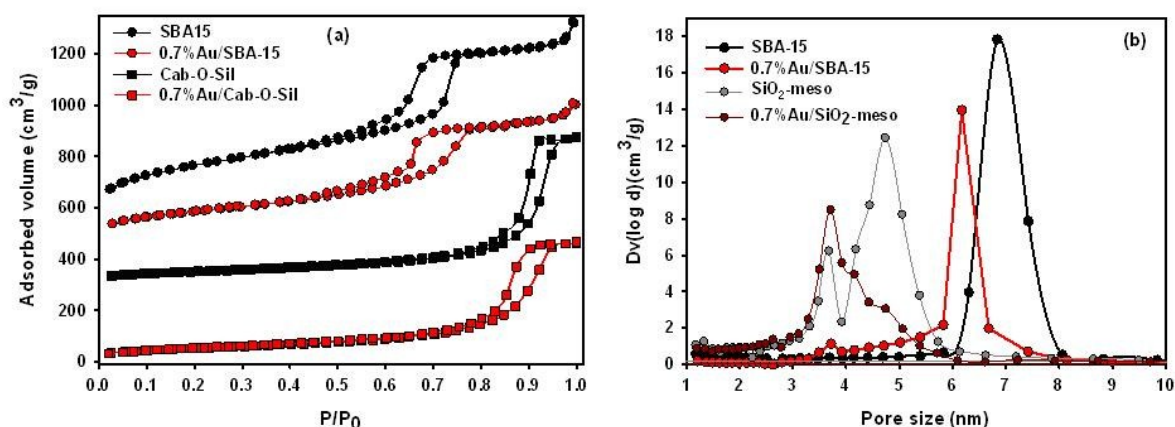


Figure 6.2. Nitrogen adsorption-desorption isotherms (a) and pore size distributions (b) of SBA-15, 0.7%Au/SBA-15, Cab-O-Sil and 0.7%Au/Cab-O-Sil materials (for clarity, the isotherms of SBA-15, 0.7%Au/SBA-15 and Cab-O-Sil were up-shifted by 500, 450 and 300 $cm^3 \cdot g^{-1}$, respectively).

6.4.1.2. X-ray diffraction

The small angle XRD patterns of the SBA-15 support and Au/SBA-15 catalyst are illustrated in Figure 6.3a. Both materials showed the presence of three well-resolved diffraction peaks, associated with the bi-dimensional $p6mm$ hexagonal symmetry typical of the mesoporous SBA-15 materials [145]: one high intensity peak at about $2\theta = 0.9^\circ$, and two low-intensity peaks at *circa* $2\theta = 1.6^\circ$ and 1.8° , corresponding to (100), (110), and (200) reflections, respectively. However, it can be seen in Figure 6.3a that after gold loading the intensity of the diffraction peaks of the catalyst was reduced, and the peaks shifted to a higher value, indicating that the incorporation of gold caused some loss of symmetry and long-range order, as well as a decrease in the interplanar distance of the mesoporous SBA-15, which is in agreement with the N_2 adsorption results discussed above. In contrast, the small angle XRD patterns of the Cab-O-Sil support and Au/Cab-O-Sil catalyst presented in Figure 6.3b confirmed that these samples were amorphous, because of the absence of reflection peaks. In our previous work we found for both silica support and Au/SiO₂-meso catalyst a single peak at about $2\theta = 1.0^\circ$ (Figure 6.3c), which was broader than the narrow peak normally reported for the well-ordered hexagonal mesoporous SBA-15, indicating the presence of a correlated distribution of framework pores but a lack of regular cylindrical pore structure [11]. Thus, from these results we can state that the use of the Au(en)₂Cl₃ complex allows preserving the structure of the SiO₂ support, while the modification of the silica support with the functional ligand BTESPTS leads to the formation of some structural defects in the mesoporous silica framework.

The wide angle XRD patterns of the 0.7%Au/SBA-15, 0.7%Au/Cab-O-Sil and 0.7%Au/SiO₂-meso catalysts presented in Figure 6.3d, showed three characteristic diffraction peaks at around 38° , 45° and 65° , assigned to the (111), (200), and (220) lattice planes of face-centered cubic structure of gold, indicating that gold was in crystalline form after the catalysts synthesis, and revealing the presence of metallic gold species [400]. However, owing to the peak-broadening effect of the small crystallite size and low loading, the estimation of gold particle size from the XRD Au peaks is quite difficult to determine accurately. Thus, we used transmission electron microscopy (TEM) analysis in order to know the gold particle size ranges in the Au/SiO₂ catalysts, as presented below.

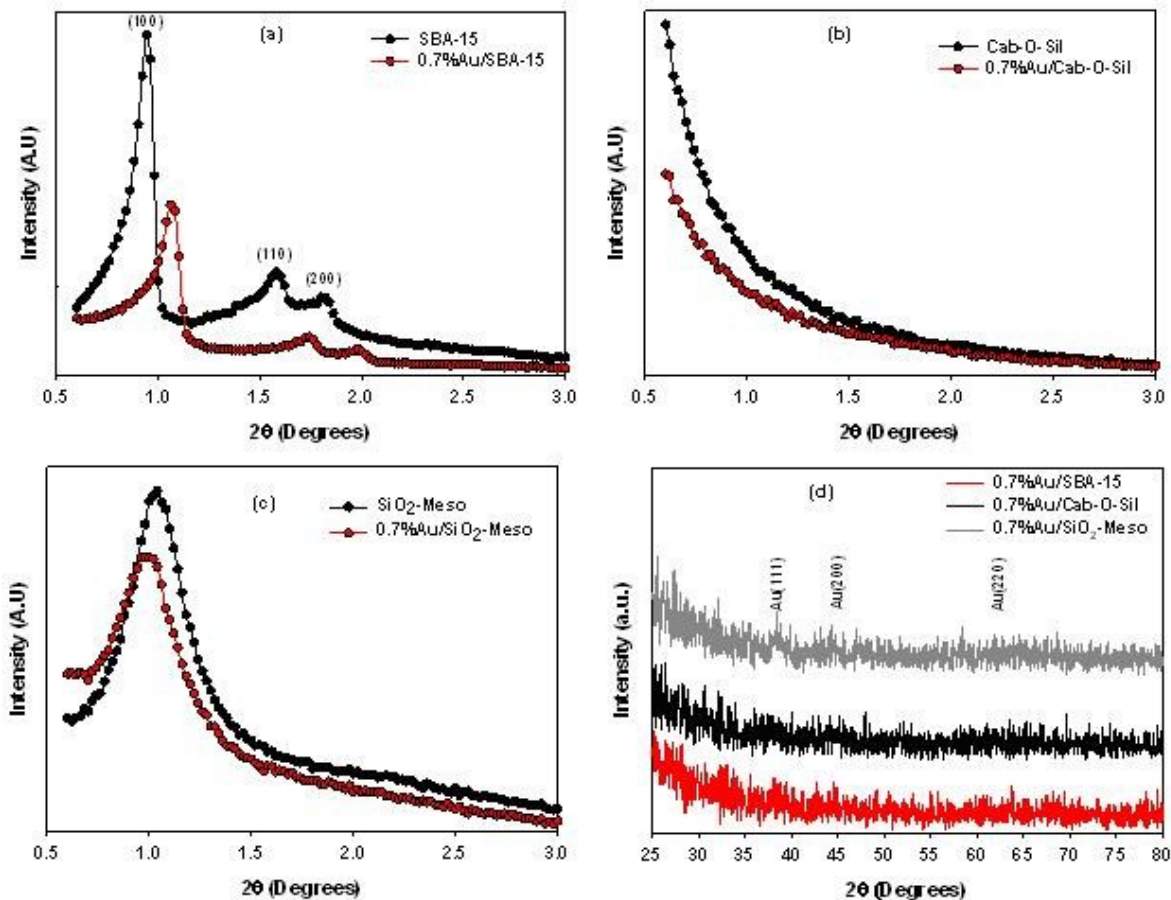


Figure 6.3. (a) Low angle XRD patterns of SBA-15 and 0.7%Au/SBA-15 materials. (b) Low angle XRD patterns of Cab-O-Sil and 0.7%Au/Cab-O-Sil materials. (c) Low angle XRD patterns of SiO₂-meso and 0.7%Au/SiO₂-meso materials. (d) Wide angle XRD patterns of 0.7%Au/SBA-15, 0.7%Au/Cab-O-Sil and 0.7%Au/SiO₂-meso catalysts.

6.4.1.3. Transmission electron microscopy

Representative transmission electron micrographs of the Au/SiO₂ catalysts and their corresponding gold particle size distributions are presented in Figures 6.4a-c.

The TEM image of 0.7%Au/SBA-15 catalyst (Figure 6.4a) clearly shows the well-ordered 2D hexagonal pore arrangement and the long-range mesopore architecture typical of SBA-15 material [145], confirming that the introduction of gold using the Au(en)₂Cl₃ complex as precursor does not alter the regular order array of mesopores, as indicated above by the XRD and N₂ physisorption analyses. Moreover, the TEM images of the 0.7%Au/SBA-15 sample revealed that AuNPs with sizes of about 6.1±1.0 nm were well dispersed and not aggregated, and most of them were located within the mesoporous framework channels of the SBA-15 support. On the contrary, the TEM image of

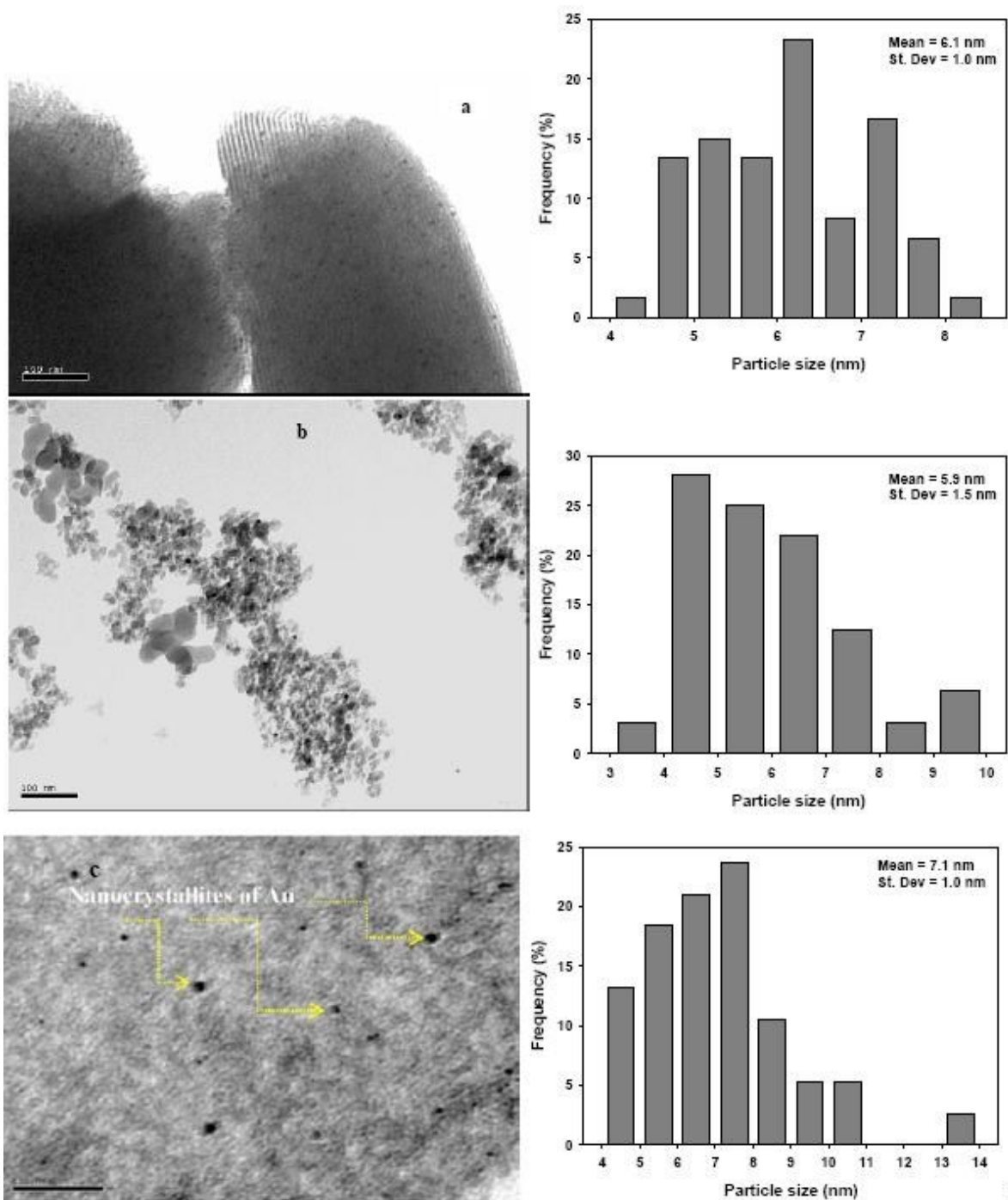


Figure 6.4. Representative transmission electron micrographs and gold particle size distributions of (a) 0.7% Au/SBA-15, (b) 0.7% Au/Cab-O-Sil and (c) 0.7% Au/SiO₂-meso (Reproduced by permission of Elsevier from Reference [11])

0.7% Au/Cab-O-Sil (Figure 6.4b) shows an amorphous bulk material with large grains. The AuNPs were also well dispersed and not aggregated on the surface of the SiO₂ support, since their

penetration into the Cab-O-Sil support needs to overcome significant barriers [290]. The mean gold particle size in this catalyst was determined as 5.9 ± 1.5 nm. Figure 6.4c shows the TEM image of the 0.7%Au/SiO₂-meso, in which a wormhole-like framework structure containing interconnected 3D-mesopores can be observed, confirming the results of the small angle XRD analysis. This catalyst presented well dispersed and not aggregated Au crystallites having dimensions between 3 and 14 nm, with an average values of about 7.0 ± 1.0 nm. Thus, taking into account that the silica support did not have significant influence on the gold particle size, the use of the Au(en)₂Cl₃ complex also results in well dispersed AuNPs without important modifications of the support architecture, because the positively charged [Au(en)₂]³⁺ ions undergo ion-exchange with the surface protons of supports with a low isoelectrical point, such as silica [298]. Moreover, it is worth to mention that even if we used two silica supports considered as vulnerable to the aggregation of AuNPs (amorphous Cab-O-Sil and wormhole 3D mesoporous silica) [451], no significant growth of the AuNPs was observed after calcination at 500°C with both synthesis methods. This could be due to the low gold loading employed in the catalysts synthesis.

6.4.1.4. Fourier transform infrared spectroscopy (FTIR) analysis

The infrared spectra at the Si–O vibration region of the SBA-15 and Cab-O-Sil supports and both 0.7%Au/SBA-15 and 0.7%Au/Cab-O-Sil catalysts are shown in Figure 6.5. For sake of clarity, the FTIR spectra of the SiO₂-meso support and the 0.7%Au/SiO₂-meso catalyst are not presented in this figure, because they showed identical patterns to the illustrated samples.

As it can be noticed in this figure, the IR patterns of all samples were very similar, indicating the easy loading of gold on SiO₂ using the Au(en)₂Cl₃ complex, since no other special absorption bands different than those corresponding to SiO₂ were detected in the FTIR analysis. In the hydroxyl region (3000-4000 cm⁻¹) all samples presented a very weak band at ~ 3746 cm⁻¹ corresponding to the terminal silanol groups [300], and a characteristic broad low frequency absorption band centered at about 3430 cm⁻¹, which is assigned to the stretching vibrations of the hydrogen-bonded surface silanol (\equiv Si–OH) groups, and to the adsorbed water situated inside the channels of the mesoporous materials [437]. The gold loading diminished the peak intensity of this absorption band in Au/SBA-15 catalyst, which could be associated to the partial pore blockage and loss of symmetry of the pristine SBA-15 support structure, in agreement with the obtained results of the N₂ adsorption–desorption and XRD analyses.

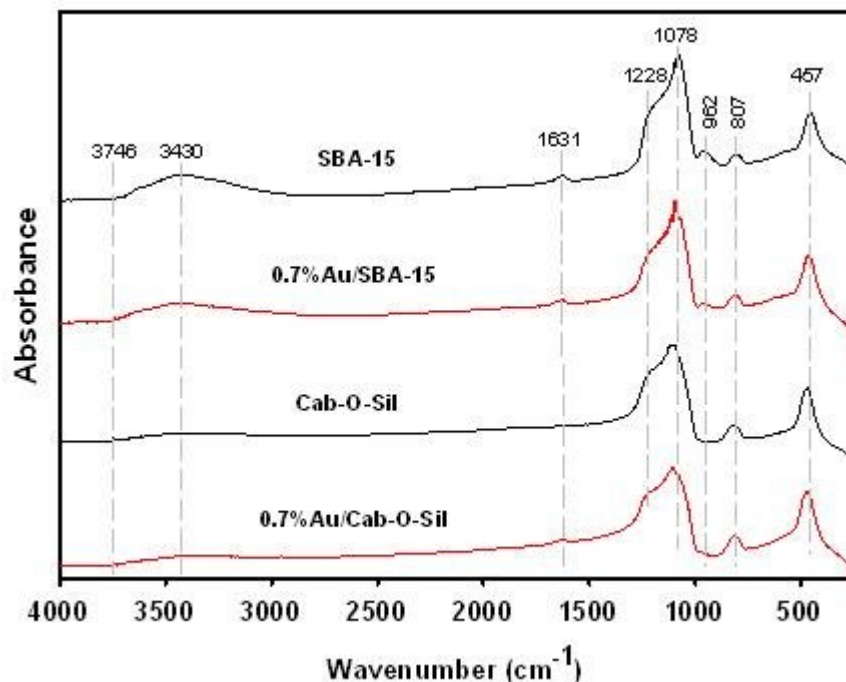


Figure 6.5 FTIR spectra at the Si–O vibration region of SBA-15, 0.7%Au/SBA-15, Cab-O-Sil and 0.7%Au/Cab-O-Sil samples.

The absorption band presented at about 1631 cm^{-1} can be attributed to the remaining water physisorbed on the materials surface at room temperature [438], to the implication of the strong absorption band assigned to the different SiO_4 units vibrating modes, or to a possible H—O—H deformation which interacts through hydrogen bonds with silanol groups [300].

The typical absorption band centered at $\sim 1078\text{ cm}^{-1}$ and its shoulder part at $\sim 1228\text{ cm}^{-1}$ could be ascribed to the asymmetric stretching vibration of Si—O—Si bridging the SiO_4 structural units, which are a result of partial ordering of the silicate framework at the pore surface [439]. The absorption band observed at nearly 962 cm^{-1} can be attributed to the stretching vibrations of Si—O in the Si—OH groups [161]. It is worth noting that gold addition weakened both the peak intensities of bands centered at 960 and 1080 cm^{-1} , probably as a consequence of the partial blocking or partial damage of the support pores of the Au/SBA-15 catalyst. On the other hand, the characteristic IR absorption bands of SiO centered at ~ 807 and $\sim 457\text{ cm}^{-1}$, correspond to the symmetric stretching and bending vibrations of the intertetrahedral oxygen atoms of SiO_2 , respectively [161].

6.4.1.5. X-ray photoelectron spectroscopy analysis

The oxidation state of the loaded gold in the Au/SiO₂ catalysts was determined by means of X-ray photoelectron spectroscopy (XPS) analysis. Although the presence of C 1s, O 1s, Si 2p, Si 2s, and Au 4f photoelectron peaks was detected in the XPS measurements, only the spectra of the Au 4f core levels of 0.7%Au/SBA-15 and 0.7%Au/Cab-O-Sil catalysts are shown in Figures 6.6a and 6.6b, respectively.

As it can be noticed in Figure 6.6, the experimental curves of Au 4f core level spectra of both catalysts presented a doublet of two spin orbit components Au 4f_{7/2} and Au 4f_{5/2} separated by 3.7 eV, which were characterized by the presence of three well-defined spin orbit split Au 4f_{7/2} and three Au 4f_{5/2} components (Au 4f_{5/2-1}, Au 4f_{5/2-2} and Au 4f_{5/2-3}), after the peak deconvolution process using Kratos software. The BE and the proportion of these spin orbit split components are summarized in Table 6.2. The Au 4f curves fitting showed the presence of three Au 4f_{7/2} components (Au 4f_{7/2-1}, Au 4f_{7/2-2} and Au 4f_{7/2-3}) with photoelectron peaks located at about 84.0, 85.0 and 86.6 eV, which were assigned to Au⁰, Au⁺¹ and Au⁺³, respectively [409], indicating the coexistence of both metallic and oxidized species on the catalysts. However, it can be noticed that most of the AuNPs were present in the metallic state, since the relative surface concentrations found in the 0.7%Au/SBA-15 and 0.7%Au/Cab-O-Sil catalysts followed the order Au⁰ (79.0 and 81.6%) > Au⁺ (14.1 and 12.7%) > Au⁺³ (6.9 and 5.7%), respectively. Similar distribution of gold species were found in the 0.7%Au/SiO₂-meso catalyst using BTESPTS as a functional ligand to immobilize gold on silica support [11]. The slight variation in peak positions could be due to the surface charging effects.

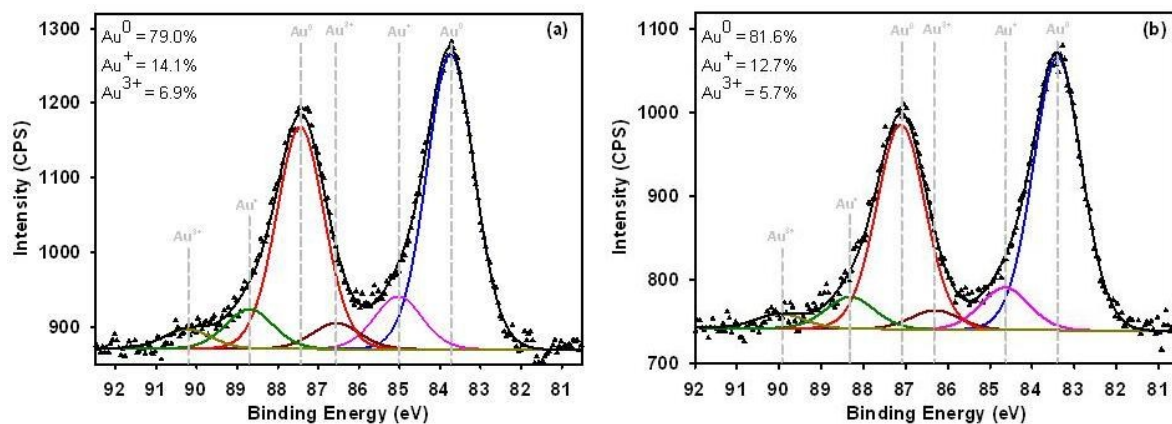


Figure 6.6. XPS-spectra of Au 4f core-level of (a) 0.7%Au/SBA-15 and (b) 0.7%Au/Cab-O-Sil catalysts.

Table 6.2. Binding energies (BE) of Au 4f_{7/2} and 4f_{5/2} deconvoluted peaks and its relative surface distribution in 0.7%Au/SiO₂ catalysts.

Catalyst sample	Peak	BE (eV)	Gold species	Concentration (%) ^a
0.7%Au/SBA-15	Au 4f _{7/2-1}	83.74	Au ⁰	45.12 (44.02)
	Au 4f _{7/2-2}	85.03	Au ⁺	8.05 (8.08)
	Au 4f _{7/2-3}	86.56	Au ³⁺	3.95 (5.10)
	Au 4f _{5/2-1}	87.45	Au ⁰	33.88 (32.94)
	Au 4f _{5/2-2}	88.70	Au ⁺	6.04 (6.05)
	Au 4f _{5/2-3}	90.23	Au ³⁺	2.96 (3.82)
0.7%Au/Cab-O-Sil	Au 4f _{7/2-1}	83.40	Au ⁰	46.60 (47.12)
	Au 4f _{7/2-2}	84.64	Au ⁺	7.25 (5.79)
	Au 4f _{7/2-3}	86.30	Au ³⁺	3.26 (4.20)
	Au 4f _{5/2-1}	87.11	Au ⁰	35.00 (35.39)
	Au 4f _{5/2-2}	88.31	Au ⁺	5.44 (4.35)
	Au 4f _{5/2-3}	89.97	Au ³⁺	2.45 (3.16)
0.7%Au/SiO ₂ -meso	Au 4f _{7/2-1}	84.03	Au ⁰	45.71 (ND) ^b
	Au 4f _{7/2-2}	85.07	Au ⁺	8.27 (ND)
	Au 4f _{7/2-3}	86.76	Au ³⁺	3.22 (ND)
	Au 4f _{5/2-1}	87.73	Au ⁰	34.20 (ND)
	Au 4f _{5/2-2}	88.74	Au ⁺	6.19 (ND)
	Au 4f _{5/2-3}	90.43	Au ³⁺	2.41 (ND)

^a Expressed as a percentage of the total area of the Au 4f peak (taken as 100%). Values in parenthesis correspond to concentration of gold species on the spent catalysts after reaction at pH=9.0. ^b ND: Not determined

6.4.1.6. Catalytic activity

After the pioneering work of Haruta's group [167], nowadays it is well known that the catalytic performance of gold catalysts is highly influenced by the size and shape of gold particles, the catalyst synthesis methods, the nature of the support, the gold support interface interactions and the oxidation states of gold in the synthesized catalysts. Herein, the catalytic activity of the 0.7%Au/SiO₂ catalysts was investigated on the partial aerobic oxidation of lactose for the selective synthesis of lactobionic

acid (LBA) at pH values of 8.0 and 9.0 as depicted in Figures 6.7a-d. The temperature, agitation, airflow and catalyst/lactose ratio were kept constants at 65°C, 900 rpm, 40 mL/min and 0.2, respectively, since they were found optimal values in our recent work using the 0.7%Au/SiO₂-meso catalyst, allowing 100% lactose conversion and 100% selectivity towards LBA, after about 100 min of reaction under alkaline conditions [11]. pH values higher than 9.0 were not tested, because we found in our previous works a pronounced decrease in the catalytic activity at very high alkaline conditions, since the Au/SiO₂-meso and the bimetallic Pd-Bi/SBA-15 catalysts partially decomposed, due to the dissolution of silica support [11, 85-86]. Similar results have been published by Mirescu and Prüße [14] for the oxidation of lactose over Au/TiO₂ and Au/Al₂O₃ catalysts.

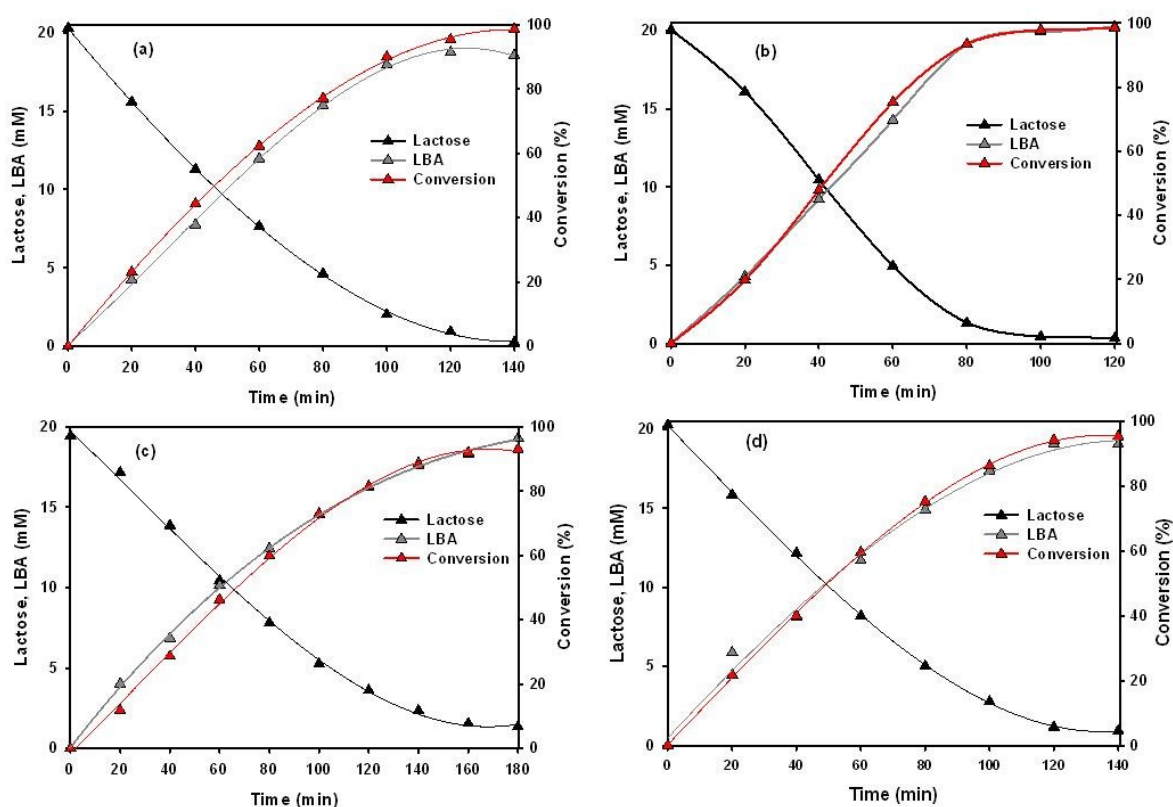


Figure 6.7 Effect of the pH on the kinetics of lactose oxidation to LBA acid over Au/SiO₂ catalysts. **(a)** 0.7%Au/SBA-15 at pH=8.0; **(b)** 0.7%Au/SBA-15 at pH=9.0; **(c)** 0.7%Au/Cab-O-Sil at pH=8.0; and **(d)** 0.7%Au/Cab-O-Sil at pH=9.0. Reaction conditions: T=65°C; Catalyst/Lactose ratio 0.2, air flow = 40 mL/min, agitation=900 rpm.

As it can be observed in Figures 6.7a-d, the oxidation of lactose over Au/SiO₂ catalysts is pH-dependent as reported for the oxidation of carbohydrates and alcohols on metal catalysts [404, 452], and both catalysts were 100% selective towards LBA, since no side products were detected by HPLC

analysis. Moreover, it can be noticed in Figure 6.7 that the Au/SBA-15 catalyst showed a better performance than the Au/Cab-O-Sil material. When increasing the pH value up to 9.0, the reaction exhibited favorable and outstanding lactose conversion to LBA. Indeed, the rates of lactose consumption as well as LBA formation were markedly high and the lactose conversion essentially completed (nearly 100% conversion) after 100 and 140 min of reaction, respectively.

Although the activity of gold catalysts has been mainly attributed to the size and oxidation state of gold particles, these parameters are not the only sufficient prerequisite to define the catalyst activity, because it is well known that the nature of support is also important for the catalytic performance of supported gold catalysts. Thus, taking into account that the loading, particle size and oxidation state of gold in the investigated Au/SiO₂ samples were almost similar, in order to evaluate the effect of support on the catalytic activity, we determined the initial reaction rate of lactose conversion to LBA for the three Au/SiO₂ catalysts (Au/SBA-15, Au/Cab-O-Sil and Au/SiO₂-meso) by means of equation (1). The results are presented in Figure 6.8.

$$r_o = \left. \frac{d[LBA]_t}{dt} \right|_{t=0} \quad (1)$$

It is noticed in Figure 6.8 that the initial reaction rate at pH 8.0 is quite similar for all Au/SiO₂ catalysts with values close to 0.07 g LBA·L⁻¹·min⁻¹. However, when increasing the pH value up to 9.0, the initial reaction rate was significantly improved and the nature of support played a certain role in the catalytic activity, following the same order of the specific surface area of catalysts (Au/SiO₂-meso > Au/SBA-15 > Au/Cab-O-Sil). In addition, the different architectures of the silica supports allow us to explain these results. The Au/SiO₂-meso catalyst showed a wormhole-like framework structure containing interconnected 3D-mesopores, which may fairly favor transport phenomena inside the pores than the hexagonal framework structure with cylindrical mesopores of the Au/SBA-15, can do. The amorphous architecture and lower surface area of Cab-O-Sil, give rise to a limited number of active sites, thus lowering the reaction rate. Consequently, the connectivity of cubic and 3D mesoporous architectures could make easier the diffusivity of reactants and products, enhancing the mass transfer and reaction rate, while the AuNPs were kept inside the pores.

In order to have a better understanding of the gold species activity during the lactose oxidation over the 0.7%Au/SBA-15 and 0.7%Au/Cab-O-Sil, XPS analysis were carried out on spent catalysts

obtained after reaction at pH value of 9.0. However, the slight variation in the relative surface concentrations after reaction, presented in parenthesis in Table 6.2, does not allow determining accurately the nature of the active species responsible for the lactose oxidation.

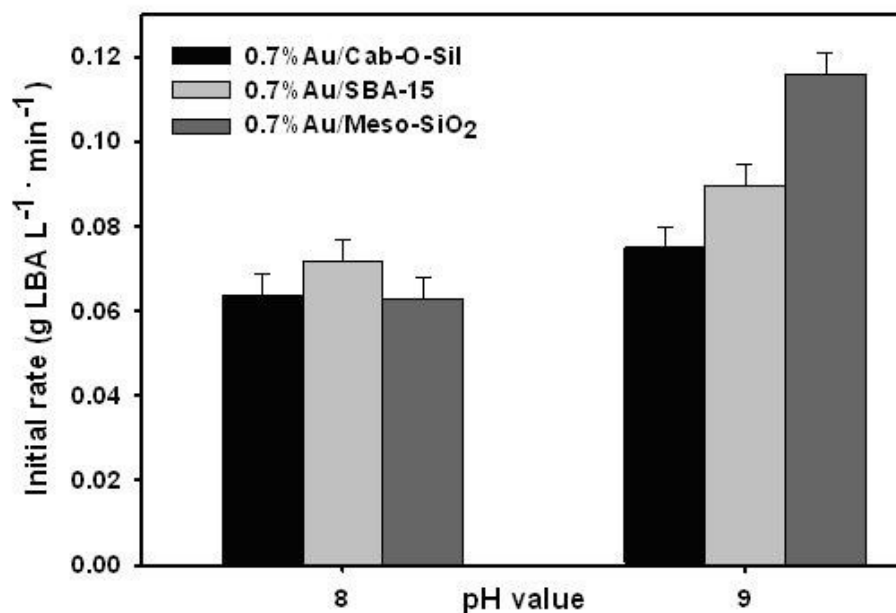


Figure 6.8 Initial rate of LBA synthesis by aerobic oxidation of lactose on Au/SiO₂ catalysts. Reaction conditions: T=65°C; Catalyst/Lactose ratio 0.2, air flow = 40 mL/min, agitation=900 rpm.

6.5. Conclusions

Different Au/SBA-15 and Au/Cab-O-Sil catalysts (0.7% Au nominal load) were synthesized *via* wet chemical process using a gold complex precursor Au(en)₂Cl₃ (en = ethylenediamine), and successfully investigated for the aerobic oxidation of lactose. Through XRD, TEM, and N₂ adsorption analyses, we found that the use of this precursor allows the preservation of the silica support SBA-15 structure, where AuNPs of ~ 6.0 nm were well dispersed and not aggregated. Moreover, XPS analysis indicated the coexistence of metallic and oxidized species on the catalyst, with relative abundances of Au⁰ > Au⁺ > Au³⁺.

Although the Au/SiO₂ catalysts showed high activity and 100% selectivity towards LBA, the Au/SBA-15 catalyst was more active than the Au/Cab-O-Sil sample, converting nearly 100% lactose after 100 and 140 min of reaction, respectively, under identical reaction parameters.

The effect of the catalyst support was investigated by comparing three Au/SiO₂ catalysts with the same loading, particle size and oxidation state of gold, but having different specific surface area and structure (3D-mesoporous Au/SiO₂-meso, 2D-mesoporous Au/SBA-15 and amorphous Au/Cab-O-Sil). The catalytic activity varied with the same order as the surface area for the investigated catalysts. Moreover, the 3D-mesoporous architecture allowed ensuring a better catalytic performance, because of higher surface area and pore connectivity, which could lead to a higher number of active sites, thus enhancing the mass transfer and reaction rate.

Considering that the success of the introduction of AuNPs into mesoporous silica requires the fulfillment of three criteria [205]: (i) retaining the order structure of the silica support; (ii) achieving very small uniform and well dispersed AuNPs; and (iii) attaining high and controlled gold loading; the use of the gold complex Au(en)₂Cl₃ can be regarded as a promising precursor for the synthesis of gold supported on mesoporous silicas for the oxidation of organic compounds in liquid phase.

Chapter 7. Catalysts recycle and deactivation

Supported gold catalysts have shown very high activity and selectivity in carbohydrates oxidation reactions. However, the catalyst stability is equally important, since if they maintain their activity and selectivity after recycling and regeneration, the process costs could be reduced. This chapter presents a preliminary study on the catalysts performance after consecutive lactose oxidation reactions, in order to have a better understanding of the deactivation causes and to propose an efficient catalyst regeneration procedure.

7.1. Experimental methodology

7.1.1. Catalysts synthesis

For these experiments, two new catalysts (Au/SBA-15 and Au/SBA-15-CeO₂ (molar ratio Ce/Si of 0.2)) with nominal gold loadings of 1.9 and 0.9%, respectively, were synthesized by the cation adsorption procedure using the complex Au(en)₂Cl₃, following the method described in Chapter 5. The samples were stored away from light in plastic bottles under N₂ atmosphere at ambient temperature, in order to prevent any alteration [453].

7.1.2. Lactose oxidation reactions

Reactions were carried out in a similar manner to that described in previous chapters, with some modifications. Typically, lactose solutions (~20 mM) were oxidized during 60 min at pH 8.0 under continuous agitation (1000 rpm), using a catalyst/lactose ratio of 0.2. The temperature was maintained at 65±1°C, while air was continuously bubbled at about 200 mL/min. HPLC was used to analyze the reaction products, according to the method described previously (Chapters 3-6).

7.1.3. Catalyst deactivation study

Considering that the main causes of gold catalysts deactivation are the sintering of gold nanoparticles, the changes in the oxidation states of gold, the leaching of the active phase and the strong adsorption of the reaction products on the catalyst surface [14, 454], the following procedure was used for understanding the catalysts deactivation phenomena:

Three consecutive reactions cycles were carried out using the synthesized catalysts. However, given that after every reaction there is an inevitable catalyst loss after its recovery by filtration, in order to use always the same catalyst/lactose ratio, the first cycle consisted in three oxidation reactions. The

catalysts recovered from these three reactions were used in the second cycle (two reactions), and the third cycle (one reaction) was performed using the catalysts recovered from the second cycle.

Fresh and spent catalysts were analyzed by means XPS and TEM. Histograms of the gold particle size distribution were obtained by counting at least 100 particles on the TEM images for each sample. The leaching of gold was investigated by means of ICP-AES analysis of the solutions after reaction.

7.1.4. Catalyst regeneration procedures

Two catalyst regeneration procedures were investigated: *(i)* For the Au/SBA-15 samples, the catalysts were recovered by filtration after each reaction, then thoroughly washed with enough deionized water at room temperature and subsequently dried overnight under vacuum at 40°C. *(ii)* In the case of Au/SBA-15-CeO₂ samples the procedure *(i)* was used to regenerate the catalysts after the first reaction cycle. However, after the second cycle, the catalysts were recovered by filtration, thoroughly washed with enough deionized water at room temperature, dried overnight under vacuum at 40°C, and calcined in air at 400°C for 4h at a heating rate of 2°C/min, using a programmable oven. The samples were stored under the same conditions described above (See 7.1.1.).

7.2. Results and discussion

7.2.1. Catalysts activity and selectivity after consecutive reactions

Table 7.1 presents the conversions and selectivities towards lactobionic acid obtained after three consecutive lactose oxidation reactions using Au/SBA-15 and Au/SBA-15-CeO₂ catalysts. As it can be observed, the lactose conversion over fresh and regenerated Au/SBA-15 catalysts decreased continuously after the first cycle. The fresh catalyst was highly active, but its activity diminished about 40% and 65% after being regenerated by washing with water, and recycled one and two times, respectively. However, in spite of this activity decrease, the selectivity towards lactobionic acid was always 100%, since no other products were found by means of HPLC analysis.

On the other hand, it can be noticed that the activity of the Au/SBA-15-CeO₂ catalysts decreased about 73% after the first cycle. However, after regeneration by calcination the catalytic activity and selectivity were similar to those of the fresh catalysts, suggesting that organic components from the substrate and the reaction product are strongly adsorbed on the catalyst surface. Similar to Au/SBA-

15 samples, this catalyst showed 100% selectivity towards lactobionic acid after consecutive reaction cycles.

Table 7.1. Effect of catalyst reuse on the lactose conversion (X) and selectivity (S) towards lactobionic acid ^a.

Catalyst	Cycle 1		Cycle 2		Cycle 3	
	X (%)	S (%)	X (%)	S (%)	X (%)	S (%)
Au/SBA-15	100	100	63	100	25	100
Au/SBA-15-CeO ₂	100	100	27	100	100 ^b	100 ^b

^a Values after 60 min of reaction. ^b Values after 40 min of reaction using the catalysts regenerated by calcination.

7.2.2. Catalysts deactivation

7.2.2.1. Gold particle size of fresh and spent catalysts

Since it is well known that the activity of supported gold catalysts is strongly influenced by the gold particle size, samples of Au/SBA-15 and Au/SBA-15-CeO₂ before and after oxidation reactions were analyzed by means of TEM. A slight increase in the gold particle size after every reaction was observed in the case of Au/SBA-15 catalysts, as presented in Figure 7.1. The fresh catalysts showed well distributed spherical gold nanoparticles of about 7.1±1.7 nm. After two and three reactions the gold nanoparticles were still well dispersed on the mesoporous silica support, but their average particle size increased up to 8.6±1.3 and 9.7±1.9 nm, respectively. Although this increase in the particle size could have affected the catalyst activity, any conclusion cannot be drawn only with these data, taking into account that gold nanocrystallites of 9.0±1.0 nm supported on mesoporous silica were also highly active in the same reaction [11]. On the other hand, the TEM images of the fresh and spent Au/SBA-15 catalysts show the well-ordered 2D hexagonal pore arrangement and the long-range mesopore architecture typical of mesoporous silica materials [145], indicating that the catalyst structure was conserved after three consecutive reactions.

Similar to Au/SBA-15 samples, some slight increase in the gold particle size of Au/SBA-15-CeO₂ catalysts was observed after consecutive lactose oxidation reactions (Figure 7.2). The fresh catalyst presented well dispersed gold nanoparticles of about 6.6±1.4 nm, which increased up to 7.1±1.7 and 8.2±1.7 nm after two and three reactions, respectively. However, given that after the second reaction the lactose conversion was significantly reduced (See Table 7.1), while there was only a minor

increase in the gold particle size (6.6 ± 1.4 vs. 7.1 ± 1.7), the catalyst deactivation cannot be attributed to the sintering of gold nanoparticles, and other causes could be responsible of this phenomena.

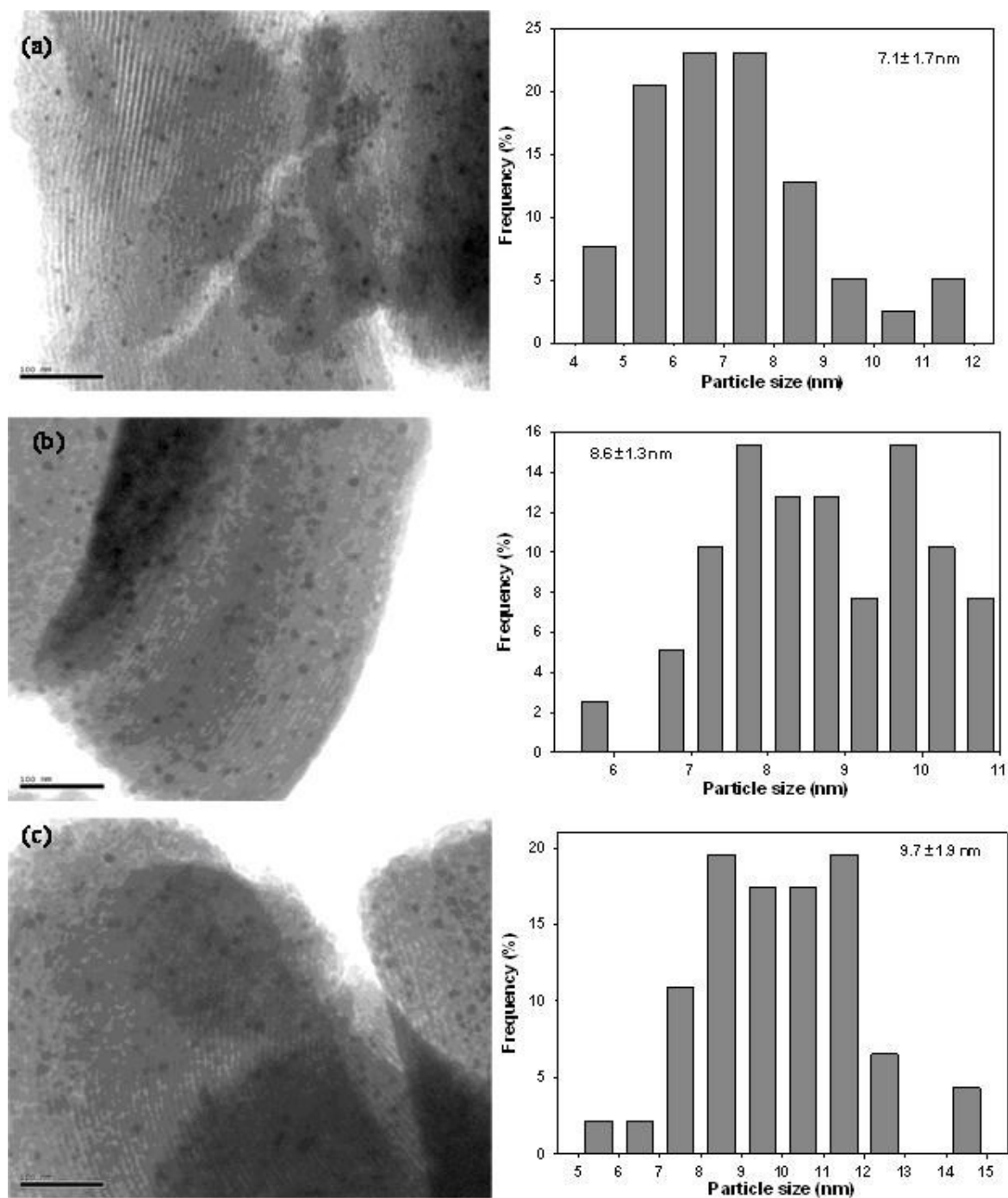


Figure 7.1. TEM images and particle size distribution Au/SBA-15 catalysts. **(a)** Before the reaction. **(b)** After two reactions. **(c)** After three reactions.

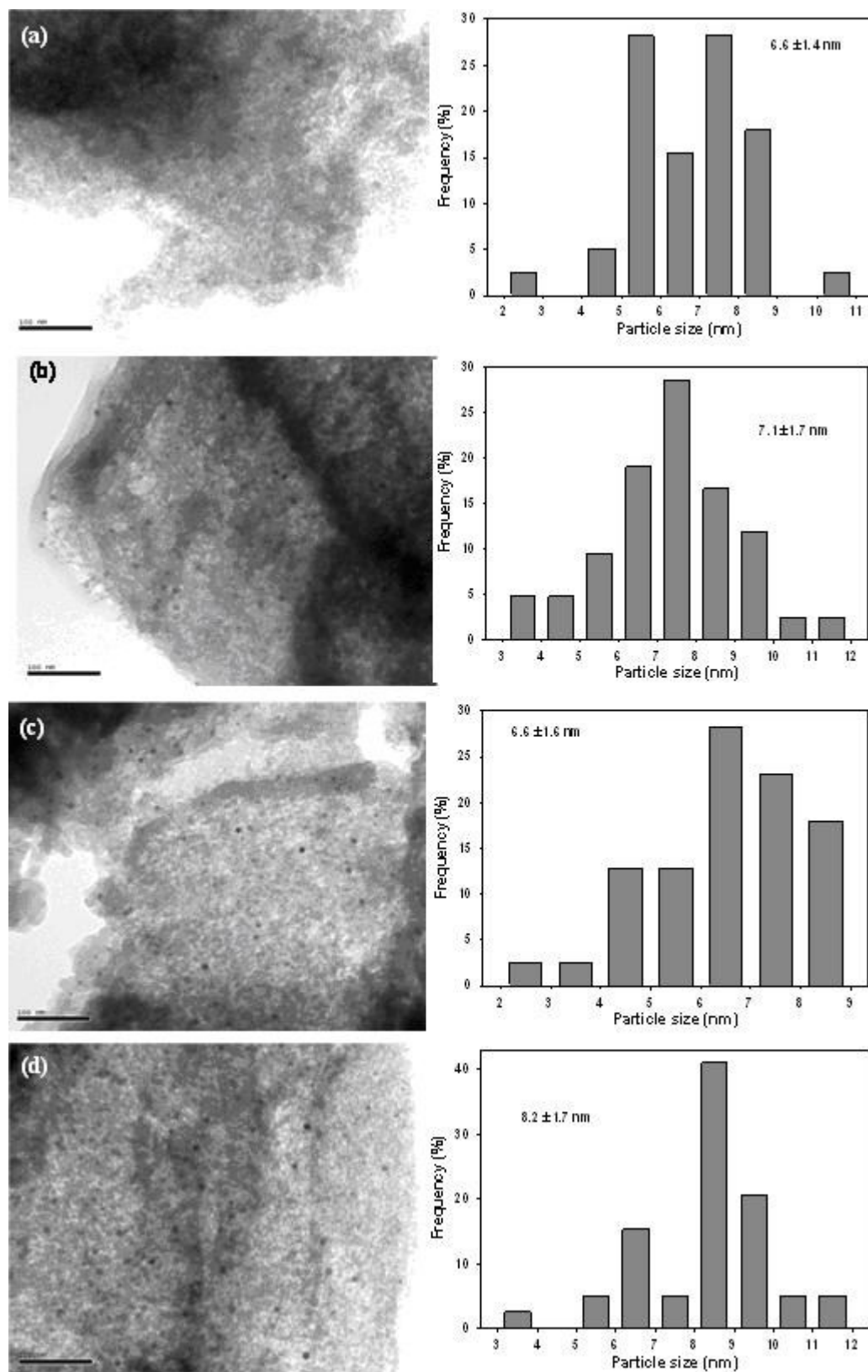


Figure 7.2. TEM images and particle size distribution Au/SBA-15-CeO₂ catalysts. **(a)** Before the reaction. **(b)** After two reactions. **(c)** After two reactions and calcination at 400°C during 4h. **(d)** After three reactions.

It is worth noting that after the catalyst regeneration by calcination at 400°C for 4h, the gold particle size did not show any significant increase in comparison to the fresh and spent catalysts after two reactions cycles. Nevertheless, after the third reaction cycle the size of gold particles on this regenerated catalyst increased more than those on the fresh catalyst after two reactions, which could be due to some structural damages after the regeneration process by calcination.

7.2.2.2. Oxidation states of gold in fresh and spent catalysts

With the aim to investigate if the oxidation state of the loaded gold on the Au/SBA-15 and Au/SBA-15-CeO₂ catalysts could be involved in the catalytic activity decline, fresh and spent catalysts samples were analyzed by means of X-ray photoelectron spectroscopy.

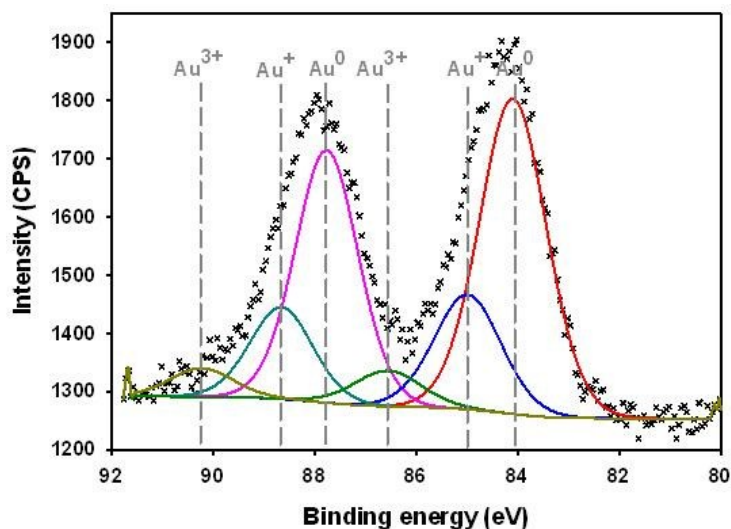


Figure 7.3. Typical XPS-spectra of Au 4f core-level photoelectron spectra of fresh and spent Au/SBA-15 and Au/SBA-15-CeO₂ catalysts.

Similar to the XPS spectra presented in Chapters 5 and 6, the experimental curves of Au 4f core levels spectra of the fresh and spent catalysts, showed in Figure 7.3, presented the doublet of two spin orbit components Au 4f_{7/2} and Au 4f_{5/2} separated by 3.67 eV, which were characterized by the presence of three well-defined spin orbit split Au 4f_{7/2} and three Au 4f_{5/2} components (Au 4f_{5/2-1}, Au 4f_{5/2-2} and Au 4f_{5/2-3}), after the peak deconvolution process using the Kratos software. The BE and the proportion of these spin orbit split components are presented in Table 7.2, while the comparative preponderance of Au species in the fresh and spent samples is showed in Table 7.3. The Au 4f curves fitting showed the presence of three Au 4f_{7/2} components (Au 4f_{7/2-1}, Au 4f_{7/2-2} and Au 4f_{7/2-3}) with photoelectron peaks located at around 84.0, 85.1 and 86.7 eV, which were assigned to Au⁰, Au⁺

and Au³⁺, respectively [409], indicating the coexistence of metallic and oxidized species on the catalysts. The slight variation in the peak positions could be due to the surface charging effects, as well as to the different size of gold nanoparticles [455].

Table 7.2. Binding energies (BE) of Au 4f_{7/2} and 4f_{5/2} deconvoluted peaks and its relative surface distribution in fresh and spent Au/SBA-15 and Au/SBA-15-CeO₂ catalysts.

Catalyst	Peak	BE (eV)	Gold species	Concentration (%) ^a
Au/SBA-15	Au 4f _{7/2-1}	84.10	Au ⁰	38.74
	Au 4f _{7/2-2}	84.99	Au ⁺	14.08
	Au 4f _{7/2-3}	86.56	Au ³⁺	4.38
	Au 4f _{5/2-1}	87.77	Au ⁰	28.99
	Au 4f _{5/2-2}	88.66	Au ⁺	10.54
	Au 4f _{5/2-3}	90.23	Au ³⁺	3.28
Au/SBA-15 after three reactions	Au 4f _{7/2-1}	84.00	Au ⁰	43.75
	Au 4f _{7/2-2}	84.82	Au ⁺	10.19
	Au 4f _{7/2-3}	86.35	Au ³⁺	3.25
	Au 4f _{5/2-1}	87.67	Au ⁰	32.74
	Au 4f _{5/2-2}	88.49	Au ⁺	7.63
	Au 4f _{5/2-3}	90.02	Au ³⁺	2.44
Au/SBA-15-CeO ₂	Au 4f _{7/2-1}	83.94	Au ⁰	40.54
	Au 4f _{7/2-2}	85.53	Au ⁺	13.29
	Au 4f _{7/2-3}	87.45	Au ³⁺	3.36
	Au 4f _{5/2-1}	87.61	Au ⁰	30.34
	Au 4f _{5/2-2}	89.20	Au ⁺	9.95
	Au 4f _{5/2-3}	91.12	Au ³⁺	2.52
Au/SBA-15-CeO ₂ after two reactions	Au 4f _{7/2-1}	83.83	Au ⁰	41.37
	Au 4f _{7/2-2}	85.25	Au ⁺	11.05
	Au 4f _{7/2-3}	86.52	Au ³⁺	2.87
	Au 4f _{5/2-1}	87.50	Au ⁰	34.29
	Au 4f _{5/2-2}	88.92	Au ⁺	8.27
	Au 4f _{5/2-3}	90.10	Au ³⁺	2.15
Au/SBA-15-CeO ₂ regenerated by calcination at 400°C for 4h after two reactions	Au 4f _{7/2-1}	84.20	Au ⁰	49.6
	Au 4f _{7/2-2}	86.06	Au ⁺	4.26
	Au 4f _{7/2-3}	89.00	Au ³⁺	3.53
	Au 4f _{5/2-1}	87.87	Au ⁰	37.12
	Au 4f _{5/2-2}	89.73	Au ⁺	2.85
	Au 4f _{5/2-3}	92.67	Au ³⁺	2.64

^a Expressed as a percentage of the total area of the Au 4f peak (taken as 100%).

From the results presented in Tables 7.2 and 7.3, it can be noticed that the relative surface concentrations found in both fresh and spent catalysts samples followed the order $\text{Au}^0 > \text{Au}^+ > \text{Au}^{3+}$, respectively, and that after oxidation reactions the concentration of metallic gold increased while those of the oxidized species decreased. Moreover, it can be observed that the fresh and spent Au/SBA-15 and Au/SBA-15-CeO₂ catalysts have somewhat similar gold species composition. However, in agreement with the results presented in Chapter 5, ceria-doped catalyst exhibited more pronounced activity than Au/SBA-15, taking into account that the kinetic behavior of both catalysts was comparable, but the gold content in the Au/SBA-15 catalyst was almost twice than the loaded on the Au/SBA-15-CeO₂ samples. The redox properties of ceria probably have contributed to increase their activity.

Table 7.3. Comparative preponderance of gold species in fresh and spent Au/SBA-15 and Au/SBA-15-CeO₂ catalysts.

Catalyst	Gold species (%)		
	Au ⁰	Au ⁺	Au ³⁺
Au/SBA-15	67.73	24.62	7.66
Au/SBA-15 after three reactions	76.49	17.82	5.69
Au/SBA-15-CeO ₂	70.88	23.24	5.88
Au/SBA-15-CeO ₂ after two reactions	75.66	19.32	5.02
Au/SBA-15-CeO ₂ regenerated by calcination at 400°C for 4h after two reactions	86.72	7.11	6.17

Noteworthy is the fact that the catalysts regenerated by calcination showed the highest concentration of metallic gold, and that they were most active than the fresh catalysts, given that in the third reaction cycle lactose was almost depleted after only 40 min. However, it can be noticed that for this catalyst the BE shifted to higher values, and this makes complicated the interpretation of the gold species present in this sample. Nevertheless, if the XPS spectra of this sample is deconvoluted to four subspectra, as presented in Figure 7.4, the Au 4f curves fitting showed the presence of two Au 4f_{7/2} components with photoelectron peaks located at around 84.2 and 86.2 eV, which are related to Au⁰ and Au³⁺, respectively [409]. The relative abundances of Au⁰ and Au³⁺ are 92.8 and 7.2%, respectively.

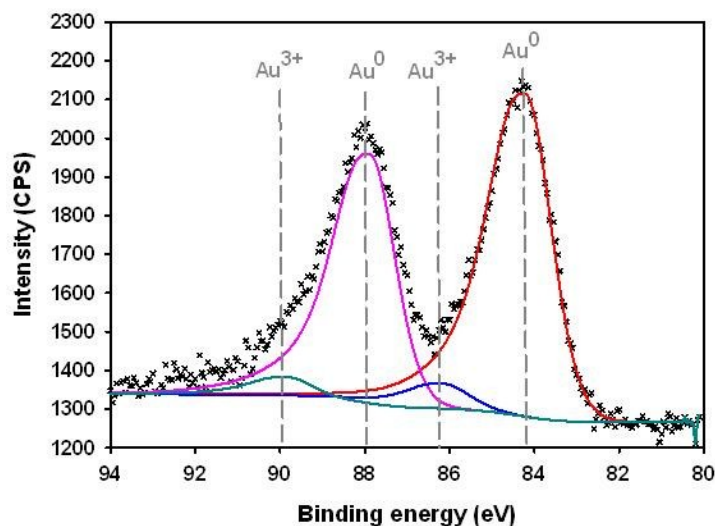


Figure 7.4. XPS-spectra of Au 4f core-level photoelectron spectra of spent Au/SBA-15-CeO₂ catalyst regenerated by calcination at 400°C for 4h.

An extensive work has been made on various reactions catalyzed by gold, however as far as oxidation reactions in liquid phase are concerned, different controversial proposals are found in the literature about the nature of the active species, and the role of metallic and oxidized gold species in the reaction mechanism is still under debate. We have tentatively tried to find out if the oxidation state was involved in the catalyst activity decline, but unfortunately the obtained results do not allow drawing any conclusion. Although the data presented in Table 7.3 suggest that high concentrations of metallic gold could enhance the catalytic activity, the presence of oxidized gold species may also affect the activity of gold catalysts in carbohydrates oxidations. Further studies are needed to confirm which species are responsible of the catalytic activity in these reactions. Moreover, it is interesting to remind that Au³⁺ is very unstable even at room temperature, and it can be easily reduced to Au⁺ and Au⁰ during exposition to electron or photon beam in TEM and XPS analyses [453].

7.2.2.3. Leaching of the active phase

To study the leaching of the active phase, liquid samples were taken after oxidation reactions cycles and analyzed by means of ICP. As it can be noticed in Table 7.4, gold starts to leach into the reaction solution from the second oxidation cycle, and the leaching increased after the third cycle. At the beginning, the concentrations of gold were about 27.1 and 12.9 ppm for the catalytic systems (lactose solution + catalyst) of Au/SBA-15 and Au/SBA-15-CeO₂, respectively. After the first reaction cycle, about 1.5% of the active phase present in the Au/SBA-15 catalyst, leachs into the solution.

This amount increased until 4.1% after the second reaction cycle. In the case of the Au/SBA-15-CeO₂ the percentage of gold leached into the reaction solution after the first and second reaction cycles were 2.9% and 6.7%. These important values suggest that leaching of the active phase is an important cause of deactivation of these catalytic samples.

Table 7.4. Gold content in the reaction solutions after consecutive oxidation cycles.

Catalyst	Gold content (ppm)		
	Cycle 1	Cycle 2	Cycle 3
Au/SBA-15	< DL	0.395	1.121
Au/SBA-15-CeO ₂	< DL	0.378	0.863

7.3. Conclusions

The nature of the deactivation of gold catalysts supported on mesoporous SBA-15 and SBA-15-CeO₂ after consecutive lactose oxidation reactions has been investigated by means of TEM, XPS and ICP-EOS analysis. Regeneration of the catalysts was carried out by washing with water and by calcination at 400°C for 4h. The catalysts regenerated by washing with water showed lower activity than the fresh ones, whereas the catalyst calcination after washing with water can be regarded as an efficient regeneration procedure, since the regenerated catalysts displayed similar activity than the fresh ones.

Although a combination of numerous factors may be the reason of the catalysts deactivation, the obtained results indicate that the main cause of deactivation is the strong adsorption of organic species on the catalyst surface, although leaching of gold during the reaction and sintering of gold nanoparticles could have contributed to the overall decline of catalyst activity. More analysis such as TPO and DSC-TGA are necessary to verify the nature and amount of these adsorbed species.

Chapter 8. Production of lactobionic acid by means of a process comprising the catalytic oxidation of lactose and bipolar membrane electrodialysis

In this chapter, the feasibility for recovering lactobionic acid from its sodium salt obtained at the reactor outlet after lactose oxidation over gold catalysts supported on mesoporous silica materials.

Published in *Separation and Purification Technology* 2013, 109, 23-32 by **Luis-Felipe Gutiérrez, Laurent Bazinet, Safia Hamoudi and Khaled Belkacemi.**

8.1. Abstract

Lactobionic acid (LBA) is a high value-added oxidation product of lactose with numerous potential applications in the food, pharmaceutical and chemical industries. This study aimed to investigate the viability of producing LBA from a sodium lactobionate (LBNa) solution obtained by the aerobic oxidation of lactose over gold nanoparticles supported on mesoporous silica, using a three-compartment bipolar membrane electrodialysis (BMED) stack with an effective area of 0.01 m². The results indicated that LBNa was continuously split in LB⁻ (lactobionate anion) and Na⁺ ions during BMED, which formed LBA and NaOH in the acid and base compartments, respectively. A demineralization rate of about 50% was achieved after applying a voltage difference of 5.0 V during 100 min followed by 5.5V during 80 min, while the LBA concentration increased about 2.5 times in the acid compartment. The specific energy consumption was 0.57 kW·h·kg⁻¹ over the whole stack. Although sodium was found in small amounts (17.5 ppm) in the acid compartment, these results show for the first time the viability of producing LBA by means of an integral process comprising the catalytic oxidation of lactose and BMED, with the advantage that the NaOH could be efficiently recovered for its reutilization in further oxidation reactions.

8.2. Introduction

LBA (4-O-β-D-galactopyranosyl-D-gluconic acid; C₁₂H₂₂O₁₂; FW 358.30 Da; pKa 3.8) is an aldonic acid obtained from the oxidation of lactose. The chemical structure of LBA comprises a galactose moiety linked to one gluconic acid molecule *via* an ether-like linkage. LBA and its mineral salts (mainly Ca-, K- and Na-lactobionate) are commercially produced in small quantities for industrial and medical applications, as well as for research use. According to Affertsholt-Allen [7], the LBA market is

between 15000 and 17000 tons per year, with an expected annual growth rate of 5%. LBA has numerous potential applications as ingredient in foods, pharmaceutical and chemical products, due to its antioxidant, chelating and humectant properties. The main commercial application of LBA is as ingredient of the solutions employed for stabilizing organs prior to transplantation [43], and it represents a new ingredient in skin care products featuring potent antioxidant, wound healing, humectant anti-aging and keratinizing properties [115, 401]. LBA is an excellent carrier for calcium supplementation, and it has recently been employed in the design of functional nanomaterials for carrying drugs [96, 98]. LBA has also been proposed as acidulant with a sweet taste; filler in cheese production; firming agent, and to fortify functional drinks with essential minerals such as Fe and Cu [8, 402]. Additional commercial and proposed applications of LBA can be found in the complete review recently published by our research group [6].

The selective conversion of lactose to LBA can be accomplished by chemical, electrochemical, biocatalytic or heterogeneous catalytic oxidation processes. However, since the pH must be kept in alkaline conditions during reaction by adequate addition of a Na-, Ca- or K- base, the obtained product is mainly a salt solution of lactobionate, which must be demineralized if the desired final product is LBA.

The use of ion-exchange resins is normally the first choice for acidifying organic salts due to its simplicity and low cost. Nevertheless, BMED could be preferable because it can be considered as a “green” process to achieve the conversion of the acid salts into their acidic forms [17], given that this technology does not generate large volumes of chemical effluents, thus avoiding a cumbersome regeneration step required in the ion-exchange technologies.

The production of organic acids by means of BMED has been largely studied. The general process is based on the ability of bipolar membranes (BM) to split water into H^+ and OH^- at the membrane bilayer interface [456-457]. Thereby, the acid salts dissociating in the same way than in conventional electrodialysis, can form acids and bases with the H^+ and OH^- ions generated by the BM [458]. The stack unit may use BM in combination with conventional cation- and/or anionexchange membranes (CEM and AEM, respectively) [459]. Under this approach, numerous acids of low and/or medium molecular size (under 203 Da), such as acetic [460-461], ascorbic [462], citric [463-467], formic [456, 468-470], galacturonic [471], gluconic [17, 463], itaconic [472], lactic [461], malic [473], *p*-toluenesulfonic [474], propionic [461], salicylic [475], sebacic [476] and tartaric [477-478] has been

recovered from their organic salts. However, the recovery of large size organic acids such as LBA (358.3 Da) using electro dialysis processes is a challenging task, because of the difficulties for their migration across the anion-exchange membranes, which normally show high resistances to the transport of larger compounds. To the best of our knowledge, the only study for separating LBA by means of electro dialysis was carried out by Peretti et al. [479]. They reported a LBA recovery of only 16.2%wt after applying a conventional electro dialysis treatment during 250 min at 15V to a lactose bioconversion solution containing LBA, lactose, fructose and sorbitol. This low yield was attributed to the system mass transfer limitations, particularly to the small permeability of the ion-exchange membranes.

In this study we aimed to investigate the viability of producing LBA by means of an integral process comprising the catalytic oxidation of lactose followed by a BMED treatment, making special emphasis on the electro dialysis step. Thus, the LBNa solution obtained in our recent work by the oxidation of lactose over gold nanoparticles supported on mesoporous silica [11], was passed through a three-compartment BMED system, with the purpose of recovering both the LBA and the NaOH solutions, the latter being able to be utilized in further oxidation reactions to control the pH. To the best of our knowledge, the viability of such process is hardly investigated.

8.3. Experimental details

8.3.1. Materials

8.3.1.1. Chemicals

All reagents were of the highest purity and were used without further purification. α -lactose monohydrate ($\geq 96\%$), lactobionic acid ($\geq 97\%$) and NaCl ($\geq 98\%$) were purchased from Sigma Aldrich. Sodium hydroxide solution 50% and anhydrous sodium acetate, both HPLC grade from Fluka, were used for eluents preparation for HPLC analysis.

8.3.1.2. LBNa production

LBNa was synthesized by aerobic oxidation of lactose over gold nanoparticles supported on mesoporous silica, according to our recent work [11], with some modifications. In a typical oxidation reaction, 175-200 mL of 20 mM lactose solution were heated under continuous agitation (600 rpm) until $65 \pm 1^\circ\text{C}$, while $500 \text{ mL} \cdot \text{min}^{-1}$ of nitrogen flow were simultaneously bubbled for stripping off the dissolved oxygen. Once the temperature was reached, the stirring rate was increased to about 1000

rpm and the catalyst (0.7%Au) was added at a catalyst/lactose ratio of 0.2. Subsequently, air flow was continuously bubbled at 400 mL·min⁻¹, while the pH of the reaction media was adjusted to 8.0±0.5 by addition of 0.5 M NaOH aqueous solution. Under these conditions, lactose was completely depleted after 60 min, as indicated by HPLC analysis of the reaction medium. Under these operating conditions, the oxidation reactions were 100% selective towards LBA, since no side products were detected by HPLC analysis. After reaction, the catalyst was separated from the slurry by filtration, and the filtrate was further used in the BMED experiments. Supplementary details, including the synthesis, properties and characteristics of the catalyst, as well as the optimization of the oxidation reaction, can be found in Gutiérrez et al. [11].

8.3.1.3. Membranes

The membranes used in the electrodialysis experiments were a cation-exchange membrane Neosepta CMX-SB (Tokuyama Soda Ltd., Tokyo, Japan), an anion-exchange membrane ASM (Tokuyama Soda Ltd., Tokyo, Japan), and two bipolar membranes BP-1 (Tokuyama Soda Ltd., Tokyo, Japan). The ASM membrane was selected for this study, since it has one of the loosest structures among all the anionic-exchange membranes commercially available, according to the manufacturer. The main properties of these three membranes are presented in Table 8.1.

Table 8.1. Main properties of the cationic, anionic and bipolar membranes used in the stack.

Membrane	Thickness (μm)		Electric resistance ($\Omega \text{ cm}^2$) ^a		Electrical conductivity (mS/cm)	
	Clean	After 3 runs	Clean	After 3 runs	Clean	After 3 runs
CMX-SB	168 ± 3	173 ± 3	1.81 ± 0.29	1.78 ± 0.03	9.64 ± 1.98	9.78 ± 0.19
ASM	161 ± 4	175 ± 3	1.19 ± 0.14	1.41 ± 0.07	13.79 ± 1.79	12.57 ± 0.71
BP-1 ^b	225 ± 2	228 ± 2	9.49 ± 0.57	6.39 ± 0.19	2.38 ± 0.18	3.56 ± 0.11
BP-1 ^c	225 ± 2	229 ± 2	9.49 ± 0.57	7.28 ± 0.14	2.38 ± 0.18	3.14 ± 0.08

^a Equilibrated with 0.1 N NaCl solution at 25°C. ^b Membrane close to cathode. ^c Membrane close to anode.

8.3.2. BMED cell and protocol

Figure 8.1 illustrates the configuration of the BMED stack employed in this study, which was operated in recirculation mode. The module was an MP type cell (ElectroCell AB, Täby, Sweden). Specifically,

the stack comprised a 316 stainless-steel electrode as cathode, and a dimensionally stable electrode (DSA) as anode, both giving 0.01 m² of effective electrode area.

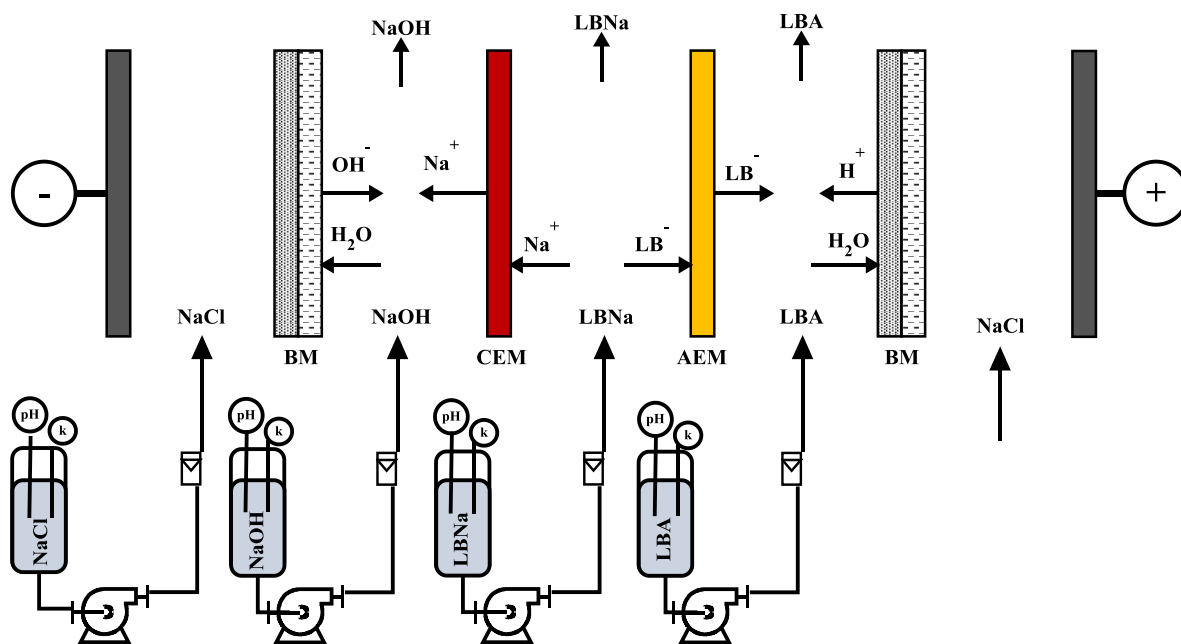


Figure 8.1. Configuration of the BMED cell. AEM: anion-exchange membrane; BM: bipolar membrane, CEM: cation-exchange membrane.

The membranes, separated by flow distribution gaskets, were arranged to give one cell unit of three compartments for passing the following three solutions: LBNa ($\sim 5 \text{ g}\cdot\text{L}^{-1}$, $\text{pH}\sim 8$, $k \sim 1150 \mu\text{S}\cdot\text{cm}^{-1}$, 350 mL, $300 \text{ mL}\cdot\text{min}^{-1}$), LBA ($\sim 2 \text{ g}\cdot\text{L}^{-1}$, $\text{pH}\sim 2.7$, $k \sim 150 \mu\text{S}\cdot\text{cm}^{-1}$, 300 mL, $300 \text{ mL}\cdot\text{min}^{-1}$) and NaOH ($\sim 0.013 \text{ g}\cdot\text{L}^{-1}$, $\text{pH}\sim 10.5$, $k \sim 300 \mu\text{S}\cdot\text{cm}^{-1}$, 500 mL, $300 \text{ mL}\cdot\text{min}^{-1}$) solutions. The electrolyte solution (NaCl, $20 \text{ g}\cdot\text{L}^{-1}$) was pumped into a closed loop at a flow rate of $800 \text{ mL}\cdot\text{min}^{-1}$. Each compartment was connected to an external reservoir to allow a continuous recirculation. The solutions were circulated using centrifugal pumps, and their flow rates were controlled by means of flow-meters. In order to eliminate all the gas bubbles, the solutions were circulated in the system for 5-10 min before the current was switched on.

During the BMED process the total increase of the current intensity was 17 mA (from 28 mA to 45 mA, at the end of the experience). The voltage was maintained constant at 5V during the first 100 min and increased further to a value of 5.5 V for the last 80 min. The first step, where the voltage was constant, allowed avoiding water splitting at membrane interfaces, and consequently a decrease in

the LBA potential migration. The subsequent increase of the voltage to a value of 5.5V, and keeping it constant during 80 min using a programmable 0-60V DC power supply (Xantrex HPD 300 W, model 60-5, Xantrex Technology Inc., Burnaby, Canada), will allow to accelerate the LBA migration, always without water splitting. The effective membrane area of the system was 0.01 m². All the experiments were started at about 25°C, but since the BMED system was not equipped to maintain constant temperature, the temperature slightly increased by 6°C after 180 min of operation.

8.3.3. Analysis methods and calculations

8.3.3.1. pH

The pH of solutions in each compartment was continuously measured using a pH-meter model SP20 (epoxy gel combination pH electrode, VWR Symphony), produced by Thermo Orion (West Chester, PA).

8.3.3.2. Conductivity

The conductivity of solutions in each compartment was continuously measured with an YSI conductivity meter (model 3100–115V, YSI Inc. Yellow Springs, Ohio, USA) with an automatic temperature compensation (ATC) immersion probe (model 3252, $k = 1 \text{ cm}^{-1}$, YSI Inc.). The collected data were employed to calculate the demineralization rate (DR), as reported by Bazinet [480]:

$$DR = \frac{k_i - k_f}{k_i} \times 100 \quad (1)$$

where k_i and k_f are the initial and final conductivities of the diluate solution, respectively.

8.3.3.3. LBA determination

The concentration of LBA in the diluate and concentrate solutions was determined by HPLC, as reported in our recent works [11, 90]. Liquid samples (750 μL) were taken from each compartment at regular intervals and analyzed using a liquid chromatographic system DX- ICS 2500 (Dionex, USA) equipped with a gradient pump GP50 and an electrochemical detector ED50 with a thin-layer type amperometric cell outfitted with gold electrodes and an Ag/AgCl reference electrode. In order to improve sensitivity, minimize the baseline drift and clean the gold working electrode, a triple potential waveform of E_1 : 0.1, E_2 : 0.6 and E_3 : -0.8V was applied for duration times of t_1 : 0.5, t_2 : 0.09 and t_3 : 0.07 s. The chromatographic peak separation was performed on a CarboPac PA1 analytical column

(4mm×250 mm i.d., Dionex, USA) in conjunction with a CarboPac PA1 guard column (4mm×50mm i.d., Dionex, USA). Sodium hydroxide solution 50% and anhydrous sodium acetate (NaOAc) were used to prepare the eluents A (0.1M NaOH) and B (0.1M NaOH-0.5M NaOAc) in filtered and vacuum-degassed HPLC-Grade water. Both eluents were stored in closed and helium-pressurized bottles. The flow-rate was set at 1 mL·min⁻¹. For the analysis, the flow gradient was programmed as follows: From 100% eluent A (isocratic for 10 min) to an eluent composition of 60%A and 40%B in 10 min using a linear gradient. Then, isocratic period of this eluent composition for 10 min, and subsequently the eluent was returned to 100%A in 5 min, using a linear gradient. Calibration and integration of chromatographic data was carried out with Chromeleon software (Dionex, USA).

8.3.3.4. Sodium determination

Sodium was measured with a flame atomic absorption spectrometer (Analyst 200, PerkinElmer, Inc, USA), using an air-acetylene flame. Before measuring the samples at 589 nm, the spectrometer was calibrated with three standard solutions. Blanks and standards were periodically analyzed between samples on a randomized basis, to confirm the validity of the calibration curve.

8.3.3.5. Zeta potential

Zeta potential of the LBNa solution was measured using a Zetasizer Nano ZS (Malvern Instruments Ltd, UK). This instrument calculates the zeta potential by determining the electrophoretic mobility (the rate of migration per unit electric field strength of a charged particle), following the Smoluchowski approximation. Indeed, by directly measuring the electrophoretic mobility of a particle, the zeta potential may then be determined using the well-known Henry Equation:

$$U_E = \frac{2\varepsilon Z f(K_a)}{3\eta_f} \quad (2)$$

where U_E is the electrophoretic mobility, ε is the dielectric constant, Z is the zeta potential, $f(K_a)$ is Henry's function, and η_f is the viscosity. Henry's function generally has value of either 1.5 or 1.0. For measuring zeta potential in aqueous solutions of moderate electrolyte concentration, a value of 1.5 is used and this is referred to as the Smoluchowski approximation.

The electrophoretic mobility is obtained by performing an electrophoresis experiment on the sample and measuring the velocity of the particles using laser doppler velocimetry. Samples (~750 μ L) were

poured into zeta potential cells (Disposable capillary cell DTS 1060, Malvern Instruments Ltd, UK) and analyzed at 25°C. Before each measurement, the cells were rinsed with ethanol and HPLC grade water, and then dried with an air blast [481].

8.3.3.6. Current efficiency, energy consumption and system resistance

The current efficiency (η), defined by the ratio between the produced LBA and the electric charge passed through the stack, was calculated according to the Eq. (3), proposed by Wang et al. [482]:

$$\eta(\%) = \frac{(C_t - C_0)zVF}{NIt} \times 100 \quad (3)$$

where C_t and C_0 (mol·L⁻¹) are the concentrations of LBA in the acid compartment at time t and 0 , respectively; z is the ion's absolute valence; V (L) is the circulated volume of solution; F is the Faraday constant (96500 C mol⁻¹); I (A) is the current, N is the number of repeating units in the stack, and t (s) is the operation time. Since the volume change in the acid compartment was negligible during the process, V was equal to 0.3 L throughout.

The specific energy consumption E (kW·h·kg⁻¹) was calculated by means of Eq. (4) [483], which allows extrapolating the results for the production of 1 kg of LBA:

$$E = \int \frac{UI}{C_t VM} dt \quad (4)$$

where U (V) is the voltage across the BMED stack, I (A) is the current, C_t (mol·L⁻¹) is the concentration of produced LBA at time t , V is the solution volume (0.3 L), and M is the molar mass of LBA (358.30 g mol⁻¹).

The system resistance was determined using Ohm's Law, from the voltage read directly from the indicators of the power supply and the current intensity from a digital multimeter (model MX 52, ITT Instruments, Bagneux, France).

8.3.3.7. Membrane thickness

The membrane thickness was measured using a Mitutoyo Corp. IDC type Digimatic indicator with automatic encoder (Model ID-C112 EB, Kanagawa-Ken, Japan) especially devised for plastic film thickness measurements, with a resolution of 1 μm and a range of 12.7-0.001 mm, as indicated by

Bazinet and Araya-Farias [484]. The Digimatic indicator was equipped with a 10-mm-diameter flat contact point. The membrane thickness values were averaged from at least six measurements at different locations on the effective surface of each membrane.

8.3.3.8. Membrane electrical conductivity

The membrane electrical conductance (G) was measured with a specially designed cell (Laboratoire des Matériaux Echangeurs d'Ions, Créteil, France) coupled to a YSI conductivity meter (Model 35; Yellow Springs Instrument Co., Yellow Springs, OH, USA) as described by Bazinet and Araya-Farias [484]. A 0.1N NaCl reference solution at about 25°C was used. The membrane electrical resistance was calculated as indicated by Cifuentes-Araya et al. [485]:

$$R_m = \frac{1}{G_m} = \frac{1}{G_{m+s}} - \frac{1}{G_s} = R_{m+s} - R_s \quad (5)$$

where R_m is the transverse electric resistance of the membrane (Ω), R_{m+s} is the resistance of the membrane and of the reference solution measured together (Ω), R_s is the resistance of the reference solution (Ω), G_m is the conductance of the membrane (S), G_{m+s} is the conductance of the membrane and of the reference solution measured together (S), and G_s is the conductance of the reference solution (in S). The membrane electrical conductivity κ_m ($\text{mS}\cdot\text{cm}^{-1}$) was calculated as proposed by Lteif et al. [486]:

$$\kappa_m = \frac{L}{R_m A} \quad (6)$$

where L is the membrane thickness (cm) and A the electrode area (1 cm^2).

8.3.3.9. Scanning electron microscopy

Scanning electron microscopy (SEM) images of membranes were taken using a scanning electron microscope (JEOL, model JSM-840A, Peabody, Massachusetts, USA) equipped with an energy dispersive X-ray spectrometer (EDS) (NORAN Instruments, Inc., USA). The EDS conditions were 15 kV accelerating voltage with a working distance of 12-13 mm. The samples were coated with a thin layer of gold/palladium in order to make them electrically conductive, and to increase the image quality [485].

All assays were carried out in triplicate. Data are reported as mean \pm standard deviation.

8.4. Results and discussion

8.4.1. Process parameters

8.4.1.1. pH

The pH variation of the three compartments during the BMED process is presented in Figure 8.2. As it can be noticed, the pH of the LBNa solution decreased from a mean value of 7.7 to about 6.2, due to its demineralization. Under the influence of an electric field, sodium ions migrate towards the cathode and leave the diluate compartment by crossing the CEM, while the lactobionate ions (LB^-) diffuse in the direction of the anode, leaving the diluate compartment and moving through the AEM into the acid compartment. As confirmed by the zeta potential and electrophoretic mobility values of the LBNa solution, which were -30.45 ± 1.77 mV and $-2.39 \pm 0.14 \times 10^{-8}$ $m^2V^{-1}s^{-1}$ at the beginning, and -21.90 ± 1.84 mV and $-1.71 \pm 0.14 \times 10^{-8}$ $m^2V^{-1}s^{-1}$ at the end of the process, respectively, the migration of LB^- was towards the anode. Owing to these dissociation and migration, the pH of the feed solution drops progressively, without observations of reaching a plateau after 180 min of operation.

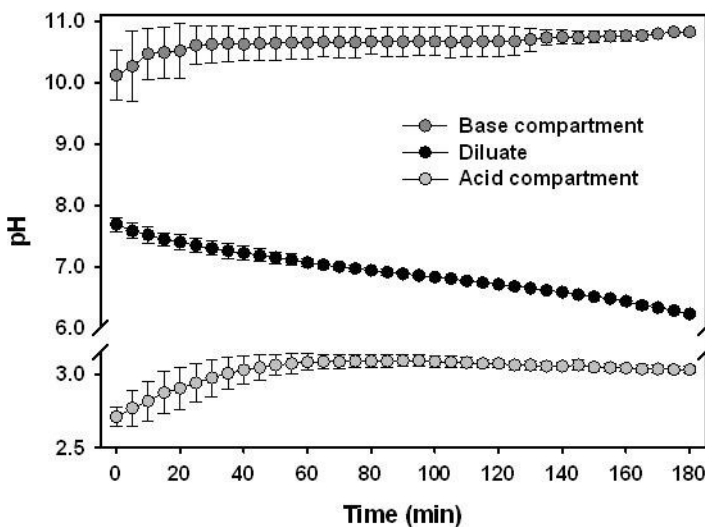


Figure 8.2. Variation of the pH values in the diluate, base and acid compartments during the recovery of LBA from LBNa by means of BMED.

By combination with the hydroxide ions (OH^-) produced by water splitting at the anionic side of the BM, the Na^+ ions coming from the diluate solution formed NaOH, as indicated by the slight increase of the pH value observed in the base compartment (from about 10.1 until a constant value close to

10.7, Figure 8.2). On the other hand, LBA was continuously produced in the acid compartment by the reaction between the LB^- ions coming from the diluate and the H^+ generated by the BM. The pH value of the acid compartment, showed a slight increase from a mean value of 2.7 until *circa* 3.0 in the first hour of treatment, and this latter value remained constant until the end of the process. This minor pH raise could be due to the leakage of Na^+ ions through the BM, as confirmed by the sodium analysis and discussed below; and/or to a possible leakage of OH^- ions coming from the BM through the CEM. A similar behavior was reported by Jaime-Ferrer et al. [456] in the splitting of sodium formate into formic acid and sodium hydroxide, using a two-compartment BMED system. Moreover, since the pH of the LBNa solution is still basic during the first hour of the electro dialysis process, some hydroxide ions could have passed through the AEM, contributing to the slight pH increase in the acid compartment.

8.4.1.2. Conductivity

Figure 8.3 shows the conductivity variation of each one of the solutions during the BMED treatment. As depicted in this figure, the conductivity of the LBNa solution continuously decreased from about 860 to around $\mu\text{S}\cdot\text{cm}^{-1}$, due to the migration of Na^+ and LB^- ions through the CEM and AEM membranes into the base and acid compartments, respectively. This drop in the electrical conductivity represented an average demineralization rate of $46.0\pm 3.1\%$, as calculated by means of Eq. 1.

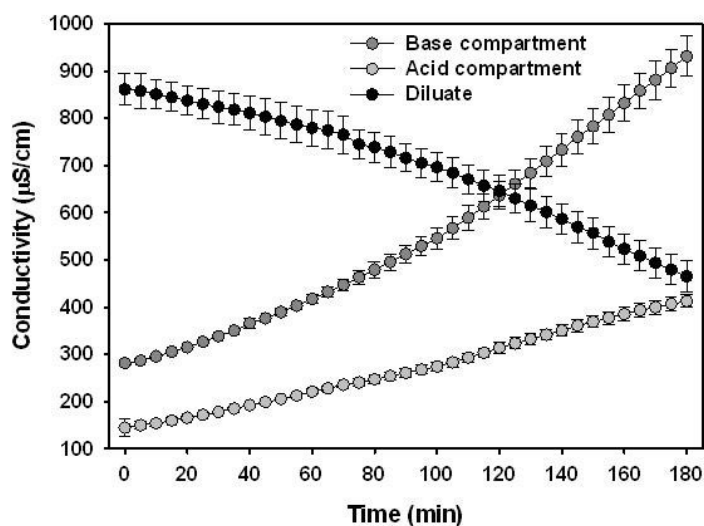


Figure 8.3. Variation of the electrical conductivity in the diluate, base and acid compartments during the recovery of LBA from LBNa by means of BMED.

As far as the acid and base solutions are concerned, the conductivities of these solutions in the acid and base compartments constantly increased from about 150 and 280 to *circa* 410 and 930 $\mu\text{S}\cdot\text{cm}^{-1}$, respectively, as a result of the constant formation of LBA and NaOH, by the reaction between the LB^- and Na^+ ions coming from the diluate compartment, with the H^+ and OH^- generated by water splitting in the BP, respectively. Furthermore, taking into account that the conductivity of the base solution was higher than that of the LBA solution, and that protons are transported more rapidly from the membrane interphase than the lactobionate ions, the increase in the electrical conductivity of the solution in the base compartment was faster than in the acid compartment.

It can also be noticed in Figure 8.3 that when increasing the voltage difference from 5 to 5.5V after the first 100 min of treatment, the slope of the conductivity curves became more pronounced, indicating a higher demineralization rate at higher voltage values. This effect can be better observed in Figure 8.4, in which we have plotted the number of transported charges ($q=I \times t$) during the operation time, as proposed by Casademont et al. [487]. From this figure, it can be observed that during the first 100 min at a constant voltage of 5V, there were less transported charges than those transported in 80 min at 5.5V ($\sim 12 \times 10^3$ vs. 13.3×10^3 C, respectively). This rapid increase in the transported charges, as well as the pronounced increase in the slope observed in Figure 8.4, indicates that a higher voltage could be employed in order to promote the mass transfer and the process yield, without water splitting at AEM and CEM.

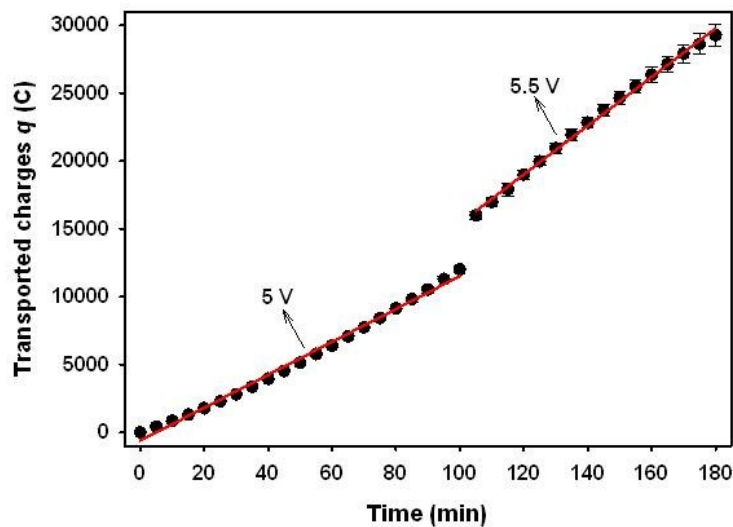


Figure 8.4. Effect of voltage on the number of charges transported during the recovery of LBA from LBNa by means of BMED.

8.4.1.3. LBA and Na⁺ concentrations

Figure 8.5a presents the variation of the LBA concentration in the diluate and acid compartments during the BMED treatment. As it can be observed in this figure, the LBA concentration in the diluate compartment diminished from 13.6 ± 0.97 to 7.6 ± 0.86 mM, indicating that approximately 45% of the LBNa present in the feed solution was recovered as LBA in the acid compartment. These values were in agreement with the formation of LBA in the acid compartment, where the LBA concentration increased from a mean value of 4.4 ± 0.15 to about 11.4 ± 0.17 mM, according to the HPLC analysis. Thus, the LBA recovery obtained in this preliminary study is more than twice than that reported by Peretti et al. [479] for the LBA separation from the lactose bioconversion medium by means of *Zymomonas mobilis*.

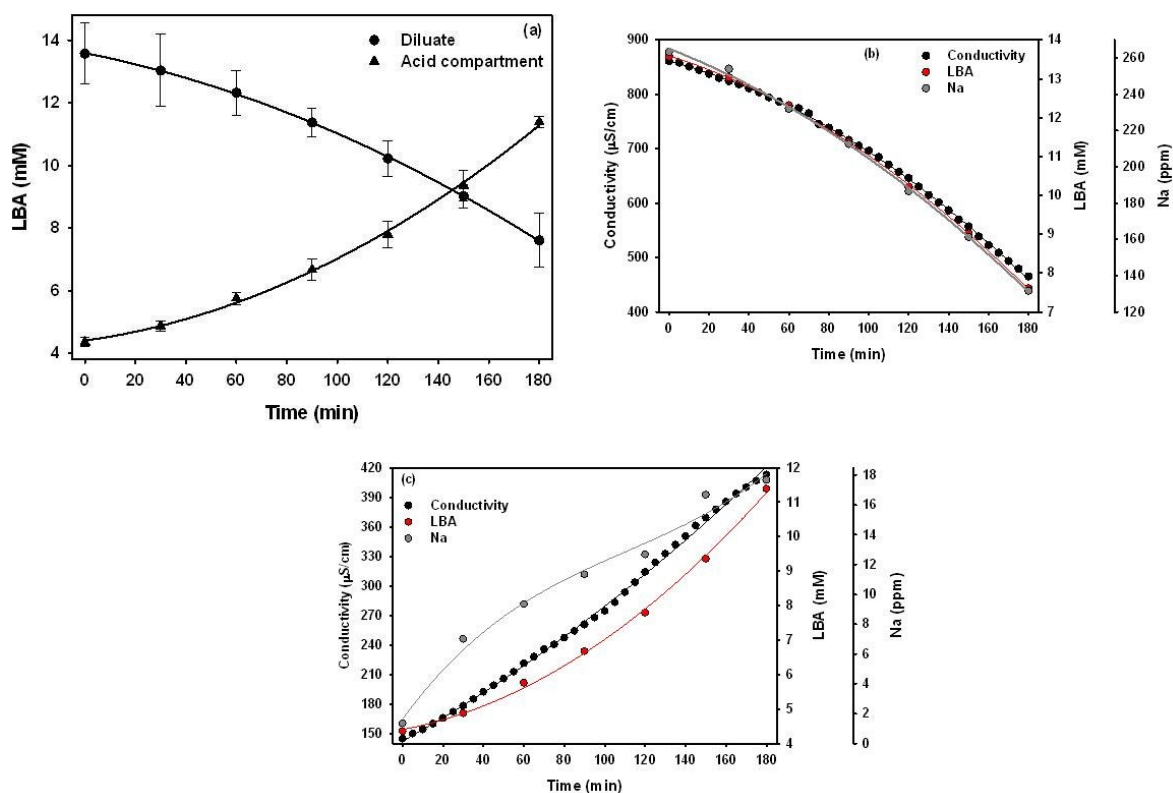


Figure 8.5. (a) LBA concentration in the diluate and acid compartments, and sodium concentration in the diluate (b) and acid (c) compartments during the recovery of LBA from LBNa by means of BMED.

On the other hand, Figure 8.5b shows that Na⁺ concentration in the diluate solution diminished from a mean value of 260 ± 12 to 130 ± 9 ppm, which means that about 50% of the Na⁺ ions passed through the CEM into the base compartment to produce NaOH by combination with the OH⁻ ions generated by the BM. This value is quite similar to the average demineralization rate calculated from the

conductivity data ($46.0 \pm 3.1\%$) by means of Eq. (1). Moreover, it is worth noting that the decreasing rates of the electrical conductivity, LBA and Na^+ concentrations in the diluate solution followed similar trends, as depicted in Figure 8.5b, while the increasing rate of the LBA followed almost the same tendency than the electrical conductivity, as showed in Figure 8.5c.

Unexpectedly, the concentration of sodium ions increased in the acid compartment from 1.0 to about 17.5 ppm. The presence of Na^+ ions in this compartment could be due to their leakage through the BM, because under the applied current the dissociated Na^+ ions from the electrolyte solution may migrate into the acid compartment due to both the concentration gradient between the electrolyte solution and the LBA solution, and to the voltage difference, which act as driving forces. Effectively, it has been demonstrated that salt ions can diffuse across commercial BM, resulting in a salt contamination of the produced acids, when using high electrolyte concentrations in the solution next to the BM [488]. For example, Jaime-Ferrer et al. [456, 468] recently reported a Na^+ flux rate of leakage through the bipolar membrane of $2 \times 10^{-5} \text{ dm}^3 \text{ Ah}^{-1}$, which caused 0.1% of current efficiency loss, when using a three compartments cell for regenerating formic acid and sodium hydroxide from a sodium formate solution. The passage of sodium ions from the diluate compartment containing the LBNa solution through the AEM is quite difficult, because the migration of the dissociated Na^+ and LB^- ions were towards the cathode and anode, respectively, as demonstrated previously with the Na^+ and LB^- concentrations and the conductivity data, as well as with the zeta potential and electrophoretic mobility values.

8.4.1.4. Current efficiency, energy consumption and system resistance

The performance of the BMED process was estimated by means of the current efficiency and the specific energy consumption, since they are important parameters for assessing the suitability of any electro-membrane process for practical applications. The current efficiency, representing the ratio of the produced LBA and the number of Faradays passed through the system, was calculated for the two steps of constant voltage difference (5.0 and 5.5V). The results indicated that during the period at 5.0V, the current efficiency rapidly increased until reaching a plateau at about 40% after the first 60 min of operation. However, when the voltage difference was increased to 5.5V, the current efficiency of the system constantly increased, with no signs of reaching a plateau. Thus, the current efficiency of the global process after 180 min was about 42%. Although low, this value of current efficiency was similar to that obtained by Saxena et al. [489] for the production of lactic acid from lactate salts, and

to that reported by Molnár et al. [471] for the recovery of galacturonic acid by means of bipolar electro dialysis.

The low current efficiency obtained in this preliminary study was thought to be owing to the following factors: (i) the low conductivity of the solutions in the acid and diluate compartments, which make difficult the ion's mobility in the electro dialysis stack, and (ii) the low applied voltage, which leads to a low current density. Due to the low conductivities of the feed and acid solutions, it is possible that part of the applied electricity could have been consumed for water splitting rather than in the migration of ions [490]. Higher concentrations of the LBNa solution in the feed stream, as well as an increase in the voltage difference could enhance the migration rate of LB^- ions into the acid compartment, increasing the current efficiency of the system. However, taking into account that the LBNa solution employed in these experiments was the solution obtained at the outlet of the oxidation reactor (see 8.3.1.2.), an increase in the concentration of the initial lactose solution should be done, in order to reach higher concentrations of LBNa.

On the other hand, the specific energy consumption calculated from Eq. (4) was $0.57 \text{ kW}\cdot\text{h}\cdot\text{kg}^{-1}$ over the whole stack. This value was similar to that obtained by Madzingaidzo et al. for the recovery of lactic acid from sodium lactate [490], but lower than that reported for the recovery of other acids, such as galacturonic [471] acid, for example.

As far as the system global resistance is concerned, at the beginning of the process, the electrical conductivities of the solutions in the base and acid compartments were too low, which conduct to a high system global resistance ($\sim 215 \Omega$). However, once the LB^- and Na^+ ions began to migrate from the diluate solution, the electrical conductivities of the solutions in the base and acid compartments increased. This phenomenon favored the decrease in the system global resistance as a function of time. Nevertheless, after increasing the voltage difference at 5.5V, the decrease rate of the system resistance was lower than in the first 100 min, and a plateau was reached at about 150 min. Then, the system resistance showed a tendency to increase, since the conductivity of the feed solution become lower, generating a higher resistance to the current pass.

8.4.2. Membrane parameters

Thickness, electrical resistance, electrical conductivity and scanning electron micrographs were used to characterize the membranes, as well as to determine the presence of fouling after three

consecutive runs. The results of these analyses are presented in Table 8.1 and in Figures 8.6a, 8.6b and 8.6c.

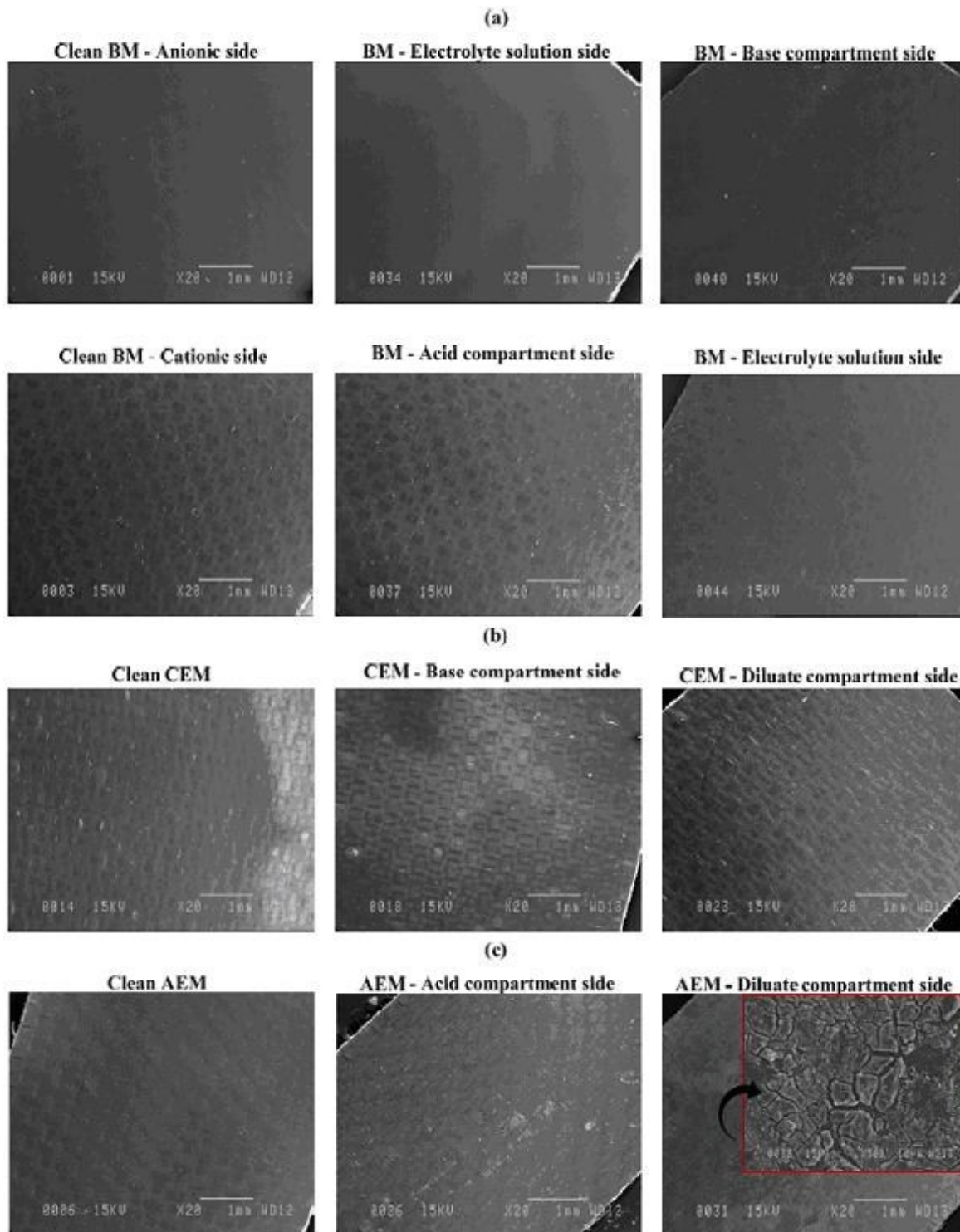


Figure 8.6. Scanning electron micrographs of the surface of **(a)** BM, **(b)** CEM and **(c)** AEM before and after the BMED process.

As it can be noticed in Table 8.1, the thickness values of the CEM (168 ± 3 vs. $173 \pm 3 \mu\text{m}$) and BM (225 ± 2 vs. $228 \pm 2 \mu\text{m}$) did not show significant changes after the BMED process. This indicated that no fouling was formed on these membranes, as confirmed by the SEM images of both sides of the membrane surfaces presented in Figures 8.6a and 8.6b. On the contrary, the AEM showed a significant increase in its thickness value after the three consecutive runs (161 ± 4 vs. $175 \pm 3 \mu\text{m}$), compared with the clean membrane. In Figure 8.6c it can be observed a fouling layer deposited on the diluate compartment side of the AEM. In order to identify the nature of this fouling layer, we used X-ray elemental analysis (Figures 8.7a and 8.7b). It can be noticed in Figure 8.7a that chloride and carbon were the predominant elements of the clean AEM surface. However, after the three run experiments, it was observed that the chloride peak is no more present, while two peaks corresponding to Si and O appeared (Figure 8.7b). Taking into account that we used gold crystallites supported on mesoporous silica as catalyst for producing the LBNa solution from lactose, the fouling layer on the surface of the AEM was attributed to minor amounts of the insoluble silica support (SiO_2) of the catalyst that could have passed through the filter paper after the oxidation reaction. The presence of this membrane fouling could also have contributed to decrease the current efficiency of the global process.

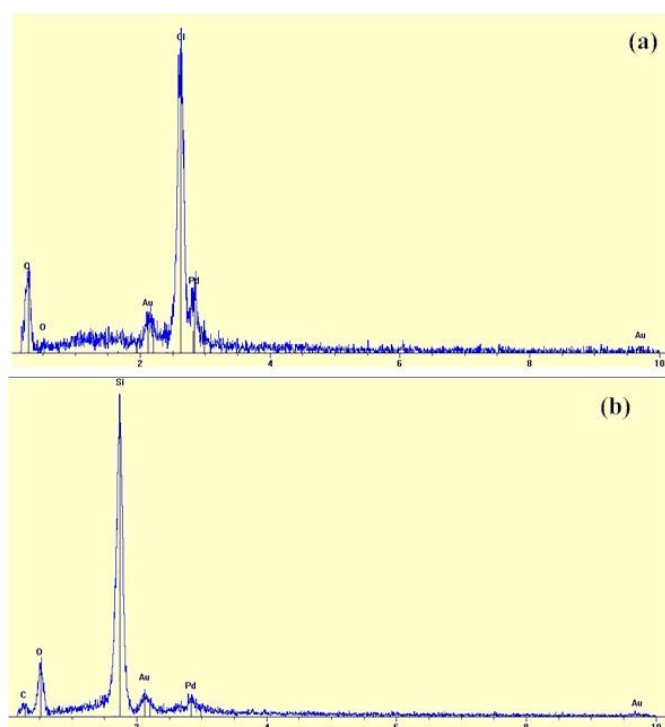


Figure 8.7. X-ray elemental analyses of the AEM surface before (a) and after (b) the BMED process.

The above results of the membrane parameters are in agreement with the obtained values of electric resistance and electrical conductivity of the membranes, which are known to increase and decrease, respectively, in the presence of membrane fouling [484]. For this reason, the electric resistance of the AEM increased (1.19 ± 0.14 vs. $1.41 \pm 0.07 \Omega$), while its electrical conductivity slightly decreased (13.79 ± 1.79 vs. $12.57 \pm 0.71 \text{ mS}\cdot\text{cm}^{-1}$) after the BMED process.

8.5. Conclusions

The production of LBA by means of an integrated process comprising the catalytic oxidation of lactose and BMED, with special emphasis on the electro dialysis step, was demonstrated for the first time. By circulating a LBNa solution obtained from the oxidation of lactose over gold catalysts through a three-compartment BMED system, LBA was obtained. Indeed, under the low voltage difference applied during BMED (5.0-5.5 V), the current efficiency after 180 min was about 42%, and the conversion of LBNa into LBA was *circa* 50%. This LBA recovery was more than twice than that reported previously by Peretti et al. [479]. However, there is still space to improve the process performance for industrial applications, since low yield and current efficiency were obtained in this study compared to the data given in the literature for the recovery of other acids by means of BMED. Further improvement of the process in terms of yield and current efficiency may be possible by: (i) adding more cell units into the electro dialysis system, which would increase the effective area; (ii) increasing the concentration of the solutions circulating through the stack; and (iii) using a higher voltage difference during the operation of the system, but lower to the limiting current densities for AEM and CEM for avoiding water splitting. Owing to the high value and potential applications of this practically new lactose derivative, work is underway to optimize this electro dialysis process LBA recovery from its sodium salt.

Chapter 9. Production of lactobionic acid from sodium lactobionate solution by ion exchange on a commercial strong acid resin: Kinetic data and modeling

Submitted to *Solvent Extraction and Ion Exchange* by Luis-Felipe Gutiérrez, Safia Hamoudi and Khaled Belkacemi.

9.1. Abstract

Lactobionic acid (LBA) is a high value added product obtained by the oxidation of lactose. Since this reaction should be conducted in alkaline media by adequate addition of a Na-, Ca- or K-base, the final product is usually a lactobionate salt solution instead the acid form. In this study, we have investigated the behavior of a strong cation exchange resin (Amberlite™ FPC23 H) for the production of a LBA solution from its sodium lactobionate salt (LBNa). The sodium exchange efficiency was evaluated at three different temperatures (5, 25 and 35°C). The strong cation exchange resin exhibited a good performance in the removal of sodium from the LBNa solution. In all cases, sodium concentration in LBA solution was reduced below 5 ppm. A complete sodium removal was achieved after about 30 min at 5°C, and after circa 10 min at 25 and 35°C. Various kinetic models were used for the evaluation of experimental ion-exchange kinetic data. The rate constants, equilibrium capacities and related correlation coefficients for each kinetic model were calculated and discussed. Results showed that both the pseudo-second order and the reversible reaction models adequately describe the experimental kinetic data. The activation energies computed using the rate constants obtained with these models were 50.87 and 36.12 kJ/mol, respectively. SEM images indicate that resin showed some physical attrition after ion-exchange process.

9.2. Introduction

Carbohydrates have long been used in the production of fine chemicals, and they are currently viewed as renewable raw materials for the “green chemistry” [6]. Lactose, the important cheese and casein manufacturing by-product, has been extensively employed for producing high value derivatives, owing to its worldwide surplus and low cost. Some significant developments include the production of a variety of functional food ingredients and pharmaceutical products, such as epilactose, galacto-oligosaccharides, lactitol, lactobionic acid (LBA), lactosucrose, lactulose,

sialyllactose and tagatose, which can be obtained by enzymatic, microbial or chemical modification of lactose [6, 21, 25].

Owing to its antioxidant, chelating, humectant and emulsifying properties, LBA (4-O- β -D-galactopyranosyl-D-gluconic acid; $C_{12}H_{22}O_{12}$; FW 358.30 Da; pKa 3.8) is a high value-added oxidation product of lactose, with high potential applications in the food, pharmaceutical and chemical industries [6, 90]. The main commercial application of LBA is as ingredient of the solutions employed for stabilizing organs prior to transplantation [43], and it represents a new ingredient in skin care products, featuring potent antioxidant, wound healing, humectant anti-aging and keratinizing properties [115, 401]. LBA is an excellent carrier for calcium supplementation, and it has also been proposed as acidulant with a sweet taste; filler in cheese production; firming agent, and to fortify functional drinks with essential minerals such as Fe and Cu [8, 402]. Additional commercial and proposed applications of LBA have been recently reviewed [6].

The selective production of LBA from lactose relates to the oxidation of the free aldehyde group of the glucose-moiety in the lactose molecule. Although this reaction can be accomplished by chemical, biochemical, electrochemical and heterogeneous catalytic processes, the heterogeneous catalytic oxidation is a promising process, since it can easily be integrated into other lactose transformation technologies, besides being considered as a “green” approach [6, 9]. However, the main product of this reaction is a lactobionate salt solution rather than the protonated acid form, given that the pH must be kept in alkaline conditions during reaction by adequate addition of a Na-, Ca- or K-base. This is mandatory in order to enhance the reaction rate and to avoid the adsorption of the reaction products on the catalyst surface. We have recently reported the selective production of sodium lactobionate (LBNa) by the aerial oxidation of lactose over gold nanocrystallites supported on mesoporous silica materials [11, 90]. Although various applications have been proposed for lactobionate salts [95], if the desired product is LBA, the demineralization of the sodium salt solution produced at the reactor outlet, is a prerequisite.

There are three techniques available for industrial acidification of organic salts: adding inorganic acids, ion-exchange processing, and demineralization using bipolar membrane electrodialysis (BMED) [17]. Very recently we obtained a demineralization rate of about 50% after applying a voltage difference of 5-5.5V during 180 min to a BMED stack with three-compartment configuration [491]. Although this preliminary study indicated that BMED could be a promising technology for recovering

LBA from LBNa, with the advantage that the NaOH solution could be efficiently recovered for being re-used in further oxidation reactions, this process still needs additional improvement for achieving the goal of eventual industrial applications.

Ion-exchange processing has been widely used for organic acid production. Various studies related to the recovery of lactic acid from fermentation broths by means of ion-exchange technology have been published [492-493]. However, studies on the recovery of LBA by means of ion-exchange are lacking in the open literature.

Herein, we investigated the efficiency of producing LBA from LBNa as a function on the temperature, using a strongly acidic commercial cation exchange resin (Amberlite™ FPC23 H). A kinetic investigation on the sodium exchange was carried out employing various simplified kinetic models to describe the experimental data. The activation energy was calculated from the Arrhenius plots of the rate constants. To the best of our knowledge, it is the first time that acidifying of LBNa into LBA by means of ion exchange technology is reported.

9.2. Experimental details

9.2.1. Materials

9.2.1.1. Chemicals

All the chemicals employed were of the highest purity and were used without further purification. α -lactose monohydrate ($\geq 96\%$) and lactobionic acid ($\geq 97\%$) were purchased from Sigma Aldrich (Oakville, ON, Canada). Hydrochloric acid (35-38%) was acquired from Fisher Scientific (Ottawa, ON, Canada). Sodium hydroxide solution 50% and anhydrous sodium acetate, both HPLC grade were procured from Fluka (Oakville, ON, Canada).

9.2.1.2. Resin

The macroreticular strongly acidic cation exchange resin in its hydrogen ion form, Amberlite™ FPC23 H (Rohm and Haas Company, Philadelphia, PA), was chosen because it is in compliance with FDA for being used in food industry. Its physical and chemical properties, as well as the specifications as reported by the manufacturers are given in Table 9.1.

Before performing the ion exchange experiments, the resin was pre-treated as advised by the manufacturer, in order to remove the residual sulfonated polystyrene that may leach in the liquid phase during the process. This

preconditioning step was carried out by rinsing the resin beads with enough demineralized water (about 20 bed volumes), and then with sufficient 5% hydrochloric acid solution (4 bed volumes), for converting the resin in the desired H⁺ ionic form.

Table 9.1. Physical and chemical properties of the Amberlite FPC23 H^a

Properties	Value
Matrix	Macroreticular crosslinked polystyrene
Functional groups	Sulfonates
Physical form	Spherical beads
Ionic form as shipped	H ⁺
Uniformity coefficient	1.34
Harmonic mean size (mm)	0.580-0.800
Mean beads size (mm) ^b	0.569 ± 0.103
Fines content (<425 mm)	5.0% max
Total exchange capacity (eq/L)	≥2.21
Moisture holding capacity (%)	44-53
Moisture content as shipped (%) ^c	77.28 ± 0.36
Bulk apparent density (g/L)	830
pH (aqueous slurry)	3.0-5.0
Maximum operating temperature	135°C
Relative density	1.25

^a Data collected from the product brochure provided by the manufacturer. ^b Determined by measuring beads from SEM images. ^c Determined by vacuum drying at 80°C during 48h.

9.2.2. LBNa production

LBNa was produced by the aerobic oxidation of lactose over gold crystallites supported on mesoporous silica, according to our recent work [11], with some modifications. Typically, 175-200 mL of ~20 mM lactose solution were heated under continuous agitation (600 rpm), while 500 mL/min of nitrogen were simultaneously bubbled for stripping off the dissolved oxygen. Once the temperature reached 65±1°C, the stirring rate was increased to ~1000 rpm and the catalyst was added at a catalyst/lactose ratio of 0.2. Subsequently, air was continuously bubbled at 200 mL/min, while the pH of the reaction media was adjusted at 8.0±0.5 by addition of 0.5 M NaOH aqueous solution. Once the reaction was completed, the the liquid phase obtained by filtration was poured in plastic bottles and stored at -15°C until the subsequent ion-exchange experiments.

9.2.3. Ion-exchange experiments

The cation exchange experiments were carried out in a batch system consisting in a well magnetically stirred (~700 rpm) beaker flask immersed in a controlled thermostatic bath to maintain the temperature constant at the desired value. Preliminary equilibrium experiments were first conducted at room temperature for systems containing different resin/solution (w/v) ratios (R), in order to obtain the optimal R value to guarantee a complete sodium removal from the LBNa solution. Once the R value was determined, the effect of three temperatures (5, 25 and $35\pm 1^\circ\text{C}$) on the ion-exchange kinetics was investigated. During these experiments, the temperature and pH of the slurry were continuously measured by means of a thermocouple connected to a sensor system (TauTheta Instruments LLC, USA), and using a pH STAT Titrator (Metrohm® 842 Titrand®[®], Switzerland), respectively. Kinetics data were obtained by taking liquid samples at regular intervals, which were subsequently analyzed for their sodium content. Each experiment was carried out at least in duplicate under identical conditions.

9.2.4. Analysis methods and calculations

9.2.4.1. LBA determination

LBA was determined by HPLC, as reported previously in our recent works [11, 90]. Samples were analyzed using a liquid chromatographic system DX-ICS 2500 (Dionex, USA) equipped with a gradient pump GP50 and an electrochemical detector ED50 with a thin-layer type amperometric cell outfitted with gold electrodes and an Ag/AgCl reference electrode. In order to improve sensitivity, minimize the baseline drift and clean the gold working electrode, a triple potential waveform of E_1 : 0.1, E_2 : 0.6 and E_3 : -0.8V was applied for duration times of t_1 : 0.5, t_2 : 0.09 and t_3 : 0.07 s. The chromatographic peak separation was performed on a CarboPac PA1 analytical column (4mm×250 mm i.d., Dionex, USA) in conjunction with a CarboPac PA1 guard column (4mm×50mm i.d., Dionex, USA). Sodium hydroxide solution 50% and anhydrous sodium acetate (NaOAc) were used to prepare the eluents A (0.1M NaOH) and B (0.1M NaOH-0.5M NaOAc) in filtered and vacuum-degassed HPLC-Grade water. Both eluents were stored in closed and helium-pressurized bottles. The flow-rate was set at 1.0 mL/min. The flow gradient was programmed as follows: From 100% eluent A (isocratic for 10 min) to an eluent composition of 60%A and 40%B in 10 min using a linear gradient. Then, isocratic period of this eluent composition for 10 min, and subsequently the eluent was returned to

100% eluent A in 5 min, using a linear gradient. Calibration and integration of chromatographic data was carried out using Chromeleon software (Dionex, USA).

9.2.4.2. Sodium determination

The sodium remaining in liquid samples during the cation exchange experiments was measured with a flame atomic absorption spectrometer (AAAnalyst 200, PerkinElmer, Inc, USA) at 589 nm wavelength, using an air-acetylene flame. Before analysis, the spectrometer was calibrated with standard solutions. Blanks and standards were periodically analyzed between samples on a randomized basis, to confirm the validity of the calibration curve.

9.2.4.3. Scanning electron microscopy

In order to determine if there were any structural changes and/or any adsorbed materials on the resin beads surface, scanning electron microscopy (SEM) images were taken before and after cation exchange experiments, using a scanning electron microscope (JEOL, model JSM-840A, Peabody, Massachusetts, USA) equipped with an energy dispersive X-ray spectrometer (EDS) (NORAN Instruments, Inc., USA). The EDS conditions were 15 kV accelerating voltage with a working distance of 12-13 mm. The resin samples were coated with a thin layer of gold/palladium before analysis, to make them electrically conductive and to increase the image quality.

9.2.4.4. Sodium exchange and ion exchange efficiency

The amount of sodium exchanged per unit amount of resin at any time, t , (Q_t in mg/g) and the ion exchange efficiency η (%) were calculated using the following equations [494]:

$$Q_t = \frac{(C_0 - C_t)V}{w} \quad (1)$$

$$\eta = \frac{C_0 - C_t}{C_0} \times 100 \quad (2)$$

where C_0 and C_t are the concentrations of sodium in the solution at the initial and any time t , respectively (mg/L), V the volume of LBNa solution (L); and w is the mass of the resin employed (g).

9.3. Results and discussion

9.3.1 LBNA production

Typical kinetic profiles of the lactose oxidation reaction over gold catalysts supported on mesoporous silica are presented in Figure 9.1. As seen, lactose was completely depleted after about 60 min, as indicated by the constant values of dissolved oxygen and pH obtained after this time, and subsequently confirmed by HPLC analysis. The reaction was 100% selective towards LBA, since no side products were detected by HPLC. This was also confirmed by molar mass balance where always molar equality was obtained between lactose consumption and LBA formation. More details on the catalytic production of LBNA production over gold catalysts, including the catalysts properties as well as the oxidation reaction optimization, can be found in our recent works [6, 11, 90].

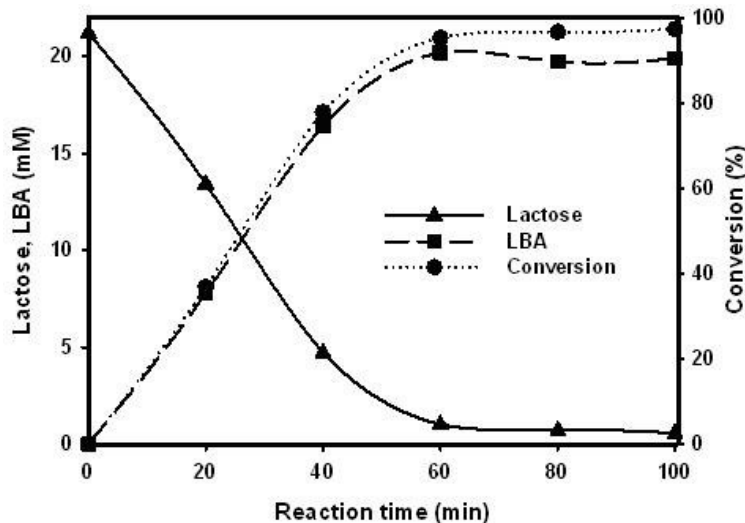
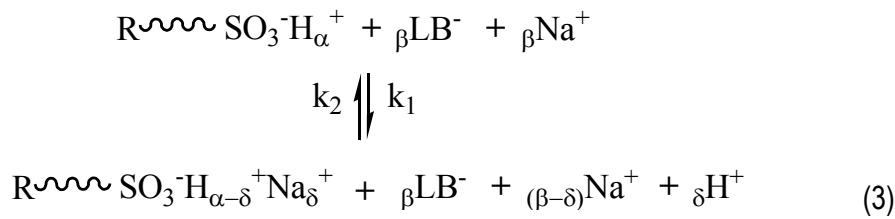


Figure 9.1. Experimental kinetic profiles of lactose oxidation over gold catalysts supported on mesoporous silica. Lines stand for experimental tendency.

9.3.2 LBA production by adsorption exchange

The production of LBA from its sodium salt using cation exchange resins involves the ion-exchange equilibrium at the resin-solution interface, in which the H^+ initially present in the resin are partially replaced by the dissociated Na^+ ions coming from the LBNA solution. The H^+ ions released by the resin form LBA with the lactobionate ions (LB^-) present in the solution. The general reaction of this process may be schematized as:



where $R \text{---} \text{SO}_3^- \text{H}_{\alpha}^{+}$ represents the cationic resin in its initial hydrogen ion form containing α active sites; LB^{-} and Na^{+} indicate the dissociated form of the LBNa solution; and $R \text{---} \text{SO}_3^- \text{H}_{\alpha-\delta}^{+} \text{Na}_{\delta}^{+}$ corresponds to the cationic resin after the ion exchange process, with δ active sites occupied by the Na^{+} ions.

9.3.2.1. Effect of the resin/solution ratio on exchange kinetics

A first series of experiments were carried out in order to investigate the effect of the resin/solution ratio (R) on the sodium exchange kinetics. Figure 9.2 shows the kinetics profiles of Na^{+} exchange obtained at room temperature, using three different R values (14.3, 20.0 and 30.0 mg resin/mL LBNa solution).

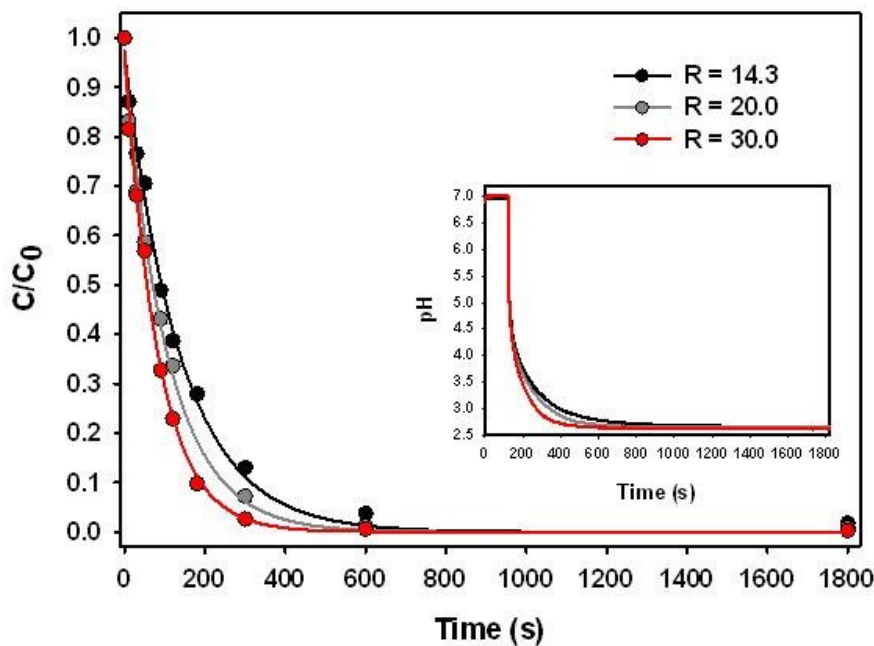


Figure 9.2. Sodium concentration kinetic profiles in LBNa solution during the exchange adsorption process of sodium on Amberlite™ FPC23 H at different resin/solution (mg/mL) ratios.

As it can be observed, the sodium exchange kinetics was enhanced with the increase of R. For the three R values investigated, the concentration of Na^{+} in the LBNa solution decreased rapidly in the

early stage of the process (3-5 min). The equilibrium was attained at about 10 min, where the amount of Na^+ in the LBNa solution did not change significantly. In all cases, sodium concentration was reduced below 5 ppm, as indicated by sodium analyses. Moreover, it should be noted that after 10 min, the pH values of the slurry (insert in Figure 9.2) are very close to those of the pure resin in aqueous solution (See Table 9.1), which allowed us to confirm that the Na^+ exchange was complete. However, the ion exchange efficiency, calculated by means of Eq. (2), increased from 96.2 to 99.4% when R was augmented from 14.3 to 30.0. For this reason, the R value of 30.0 was selected for evaluating the influence of temperature on the sodium exchange kinetics from the LBNa solution.

9.3.2.2. Effect of the temperature on exchange kinetics

Figure 9.3 presents the kinetics profiles of sodium adsorption exchange obtained at three different temperatures, using a constant R value of 30 mg resin/mL LBNa solution.

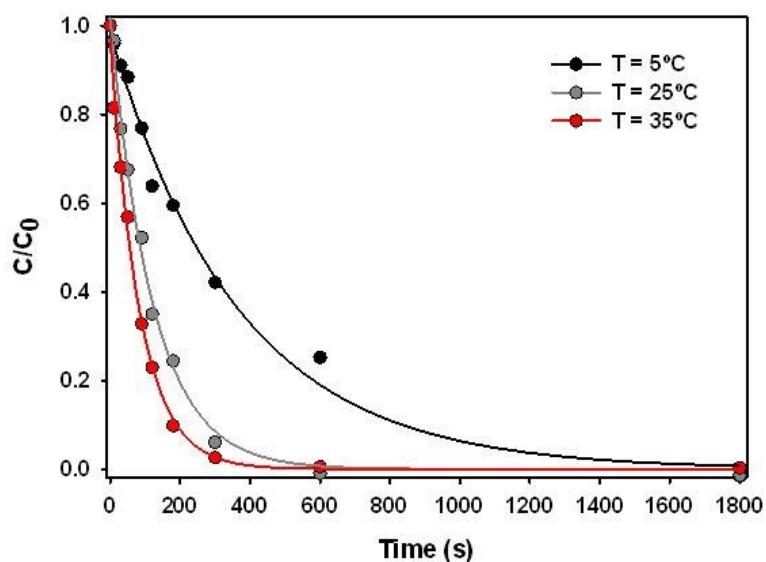


Figure 9.3. Kinetic profiles of sodium adsorption exchange on Amberlite™ FPC23 H at different temperatures.

As it can be seen, the kinetic curves indicate that higher amounts of sodium were exchanged by increasing the temperature. A complete Na^+ exchange was achieved after about 30 min at low temperature (5°C), while less than 10 minutes were necessary to exchange almost all the sodium present in the LBNa solution when the temperature was increased up to 25 and 35°C. However, neither the cation exchange efficiency nor the exchange capacity of the resin showed significant differences when the ion exchange experiments were carried out at temperatures of 25 and 35°C, as it can be noticed in the data listed in Table 9.2. Moreover, as observed in the kinetics curves, the

initial rate of exchange was very fast and thereafter it slowed down when the temperatures were 25 and 35°C, while for the experiments carried out at 5°C, the rate of exchange was slow and almost constant during the whole process. After 5 min of operation, the exchange conversion values of the resin ($1 < Q_t/Q_e < 0$) were 0.93 and 0.98 for the experiments at 25 and 35°C, respectively, while at low temperature of 5°C this value was only 0.57.

9.3.2.3. Kinetic modeling

The kinetics of ion-exchange processes is governed either by diffusion through a thin liquid film, by diffusion in and through the resin particles, or by the velocity of the chemical exchange occurring at the adsorbed sites inside the resin particles [495]. However, the rate equations describing the ion exchange reactions based on diffusion phenomena are quite complex and difficult to be solved. For example, the Nerst-Plank equation has been successfully applied to explain this kind of processes, but its mathematical complexity makes difficult its practical applications. Consequently, taking into account that the understanding of the kinetics might reveal the mechanism of the rate controlling process, and that for simplification commodities a lumped analysis of the kinetic data is sufficient for practical operations, simplified but reasonably adequate kinetic models are frequently employed [496-500]. In this study we used four different simplified kinetic models to describe the experimental kinetic data obtained at different temperatures, in an attempt to identify the controlling step of the adsorption exchange process.

Table 9.2. Exchange capacity and ion exchange efficiency as a function of temperature during the adsorption exchange of sodium from LBNa on Amberlite FPC23 H

Temperature (°C)	Q_e (mg/g) ^a	η (%) ^a
5	8.63 ± 0.51	74.8 ± 4.4
25	11.46 ± 0.31	99.3 ± 2.1
35	11.47 ± 0.84	99.4 ± 1.4

^a Data collected after 600 s of contact between the resin and the LBNa solution using a resin/solution (w/v) ratio of 30 mg/mL.

On the other hand, taking into account that correlation coefficients (R^2) indicate the fit between the experimental data and the linearized forms of the model, in order to have a better estimation of the model accuracy in comparison to experimental data, the average percentage error was also calculated, by means of Eq. (4):

$$APE(\%) = \frac{\left(\sum_{i=1}^N |(x_{i-\text{exp}} - x_{i-\text{pre}}) / x_{i-\text{exp}}| \right)}{N} \times 100 \quad (4)$$

where N is the number of experimental data, and $x_{i-\text{exp}}$ and $x_{i-\text{pre}}$ stand for experimental and predicted values, respectively.

9.3.2.3.1. Pseudo-first order kinetic model

The pseudo-first order model proposed by Lagergren [501] is one of the most widely used approaches to describe the kinetics of the adsorption and ion-exchange processes. This model can be expressed in its differential form as:

$$\frac{dQ_t}{dt} = k_1(Q_e - Q_t) \quad (5)$$

where Q_e and Q_t are the amounts of Na^+ exchanged per unit amount of resin at equilibrium and any time, t , respectively (mg/g), and k_1 is the pseudo-first-order rate constant (s^{-1}).

Assuming that k_1 and Q_e are constant, the integration of Eq. (5) employing the boundary conditions that at $t = 0$, $Q_t = 0$; and that at $t = t$, $Q_t = Q_t$, gives:

$$\ln(Q_e - Q_t) = \ln(Q_e) - k_1 t \quad (6)$$

The model parameters (k_1 and Q_e), computed from the slope and intercept of the plots of Eq. (6), respectively, as well as the R^2 and APE values, are presented in Table 9.3. The pseudo-first-order rate constants (k_1), varying in the range of 0.14–0.60 min^{-1} , increased with the ion-exchange process temperature. Moreover, it can be noticed that the predicted values of Q_e are lower than those obtained experimentally, with the exception of that determined at 25°C. On the other hand, although the R^2 values suggest good fit between the model and the experimental data, especially at 25°C, the APE values indicate that the experimental data deviated considerably from the predicted ones at all the temperatures investigated. As it can be observed in Figure 9.4a, there was a poor agreement between the model-predicted values (solid lines) and the experimental data at the three temperatures studied. The model seems to predict well the first stages of the process, where the diffusion of Na^+

through the solution would be rate controlling, but it failed to predict the subsequent process steps, as well as the value at equilibrium (Q_e).

Table 9.3. Kinetic model parameters of sodium exchange on Amberlite™ FPC23 H at different temperatures.

Kinetic model	Temperature (°C)		
	5	25	35
Q_e (experimental, mg/g)	11.47	11.50	11.50
<i>Pseudo-first order</i>			
k_1 (min ⁻¹)	0.144	0.564	0.600
Q_e (predicted, mg/g)	10.85	12.46	9.30
R^2	0.9763	0.9972	0.9785
APE (%)	18.19	31.40	26.03
<i>Pseudo-second order</i>			
k_2 (g/mg·min)	0.013	0.040	0.118
Q_e (predicted, mg/g)	13.70	12.52	11.85
R^2	0.9907	0.9801	0.9989
APE (%)	7.92	22.07	9.08
<i>Intra-particle diffusion</i>			
k_i (mg/g·min ^{0.5})	0.300	0.464	0.605
Q_e (predicted, mg/g)	12.93	15.12	14.98
R^2	0.947	0.716	0.618
APE (%)	34.29	1490.57	104.95
<i>Reversible reaction</i>			
k_1 (min ⁻¹)	0.149	0.550	0.636
k_2 (kg/m ³ ·min)	0.0120	0.0473	0.0520
R^2	0.9763	0.9972	0.9785
APE (%)	12.66	20.59	8.91

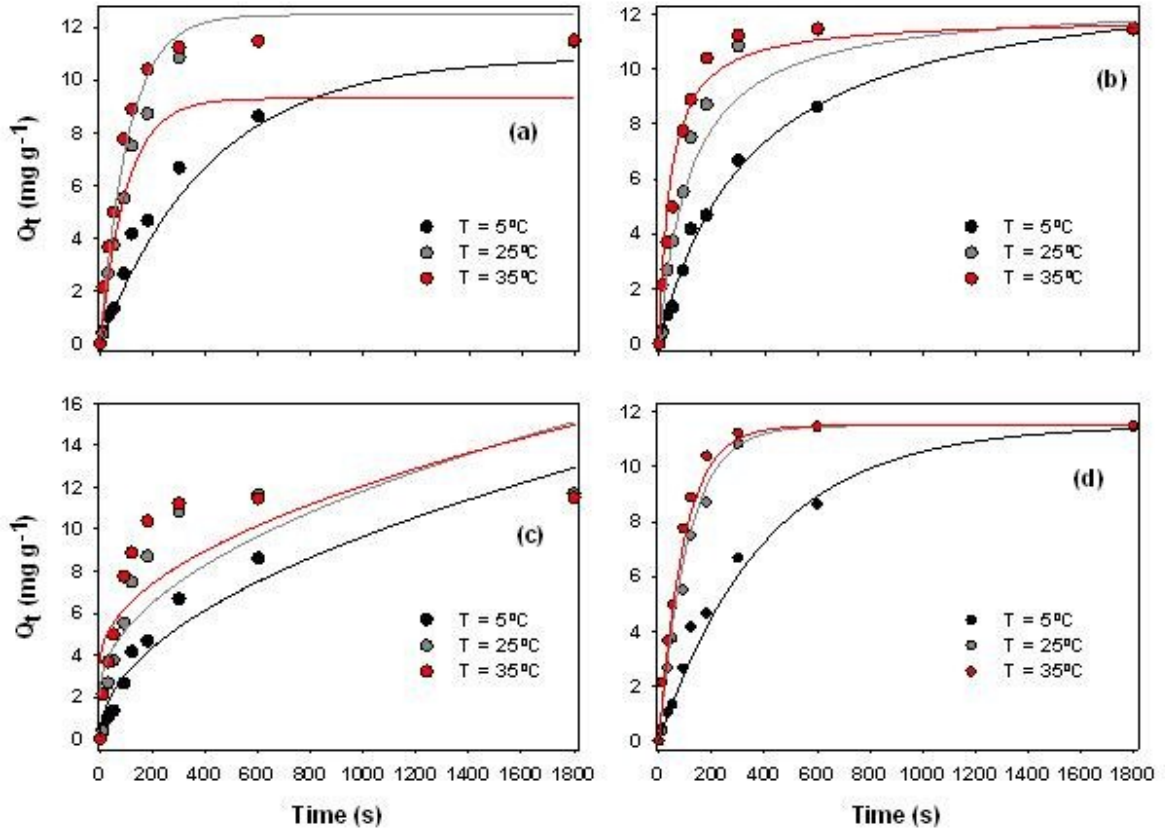


Figure 9.4. Modeling of sodium ion-exchange curves calculated by different kinetic model approaches: (a) Pseudo-first order model, (b) Pseudo-second-order model, (c) Intra-particle diffusion model, and (d) Reversible reaction model.

9.3.2.3.2. Pseudo-second order kinetic model

The pseudo-second order kinetic model proposed by Ho and McKay [502] considers as the rate-limiting step the formation of chemisorptive bonds involving sharing or exchange of electrons between adsorbate and the adsorbent [503]. It predicts the behavior over the whole range of the process, and is frequently used to provide the ion exchange capacity, rate constant and the initial rate of ion exchange systems [504]. Mathematically, this model is commonly expressed in its differential form as:

$$\frac{dQ_t}{dt} = k_2(Q_e - Q_t)^2 \quad (7)$$

After integrating the Eq. (7) employing the same boundary conditions used above for the pseudo-first order model, and re-arranging, the following equation in a linear form is obtained:

$$\frac{t}{Q_t} = \frac{t}{Q_e} + \frac{1}{k_2 Q_e^2} \quad (8)$$

where k_2 is the pseudo-second-order rate constant (g/mg·s).

The model parameters (k_2 and Q_e), calculated from the intercept and slope of the t/Q_t against t plot, respectively, as well as the R^2 and APE values, are listed in Table 9.3. Similar to the results found when applying the pseudo-first-order model, the k_2 values increased as the temperature increased, varying in the range of 0.011-0.118 g/mg·min. Although the predicted values of Q_e are somewhat higher than the experimental ones, as depicted in Figure 9.4b, the application of the pseudo-second order kinetic model indicated a good agreement between the experimental and the predicted data, especially for the experiments carried out at 5°C. For this low temperature, the model predicts well the behavior of the experimental values over the whole range of the process. However, for the experiments carried out at 25 and 35°C, the model failed to predict the second step of the adsorption exchange process, in which the diffusion of Na^+ ions within the resin matrix would be the rate controlling. Nevertheless, it is worth mentioning that the ion exchange rate data should not be expected to obey any equation very closely in a such region such where the diffusion and mass action velocities are comparable, because of the equilibrium closeness [495].

9.3.2.3.3. Intra-particle diffusion model

As mentioned previously, the rates of adsorption exchange process can be limited by boundary layer diffusion (external mass transfer), intra-particle diffusion (mass transfer through the pores) or by the exchange reaction, or by a combination of all these phenomena [505]. Thus, having in mind that neither the pseudo-first nor the pseudo-second kinetic order models can identify the diffusion mechanisms, the experimental data were treated with the intra-particle diffusion model proposed by Weber and Morris [506]:

$$Q_t = k_i \sqrt{t} \quad (9)$$

where k_i is the intra-particle diffusion rate constant (mg/g·min^{0.5}).

It has been proposed that if intra-particle diffusion is the rate-limiting step, the values of ion exchanged per unit amount of resin (Q_t) vary linearly with the time square root. Moreover, if the intra-

particle diffusion is the sole rate-limiting step, the Q_t vs. $t^{0.5}$ describes a linear plot where the ordinate to origin is zero [506]. However, this was not the case in this study, since the plots of the experimental data fitted to the intra-particle diffusion model are not linear over the whole time range. Consequently, as it can be observed in Figure 9.4c, this model failed to describe the experimental kinetic data. Thus, intra-particle diffusion could not be the only rate-controlling step of the process. However, as seen in Figure 9.5, the curves of Q_t vs. $t^{0.5}$ can be separated into three and two linear regions (for 25 and 35°C and 5°C, respectively), indicating that three or two steps take place [507]: The first, corresponding to the diffusion of Na^+ ions through the LBNA solution to the external surface of the resin beads, took place at high rate (0.6-0.8 $\text{mg/g}\cdot\text{min}^{0.5}$), especially at 25 at 35°C. The second linear portion may be attributed to the diffusion of Na^+ ions within the resin matrix, where intra-particle diffusion is the rate-limiting. The third is the final equilibrium stage where ion diffusion is very slow due to their extremely low Na^+ concentration in the solution. As observed, this last step was not observed in the experiments carried out at 5°C, because the equilibrium at this temperature was reached after about 30 min of operation.

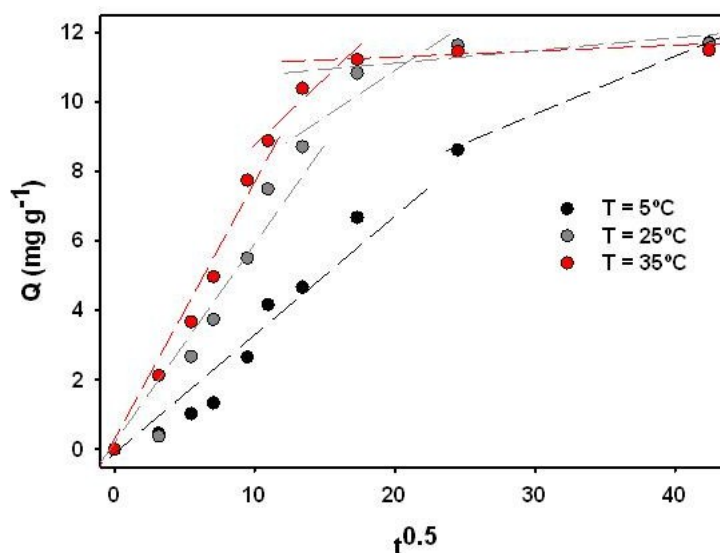


Figure 9.5. Intra-particle diffusion plots of sodium adsorption exchange on Amberlite™ FPC23 H at different temperatures.

9.3.2.3.4. Reversible reaction model

Various studies have been proposed a reversible reaction model, based on the mass action law and the reaction equilibrium relationship, to describe the kinetics of ion exchange processes, assuming that they can be considered as a reversible chemical reaction, in which an exchange of ions between

two phases (liquid and solid) takes place [495-496, 508-509]. Applying this approach to the reaction presented in Eq. (3), the rate of Na⁺ exchanged in the process can be written as:

$$\frac{d[Na^+]}{dt} = k_1[Na^+] - k_2[R \cdots Na] \quad (10)$$

where k_1 (min⁻¹) and k_2 (kg/m³·min) are the forward and reverse reaction rate constants, respectively.

If the concentration terms refer to the liquid phase, Eq. (10) can be rewritten as:

$$-\frac{dC_t}{dt} = k_1 C_t - k_2 \frac{(C_o - C_t)}{m} \quad (11)$$

where m is the amount of resin employed per unit volume of solution (kg/m³), and C_o and C_t are the concentrations of sodium in the solution at the initial and any time t , respectively (mg/L).

Taking into account that at the equilibrium the variation of the sodium concentration in the solution approaches to zero, Eq. (11) becomes:

$$K_d = \frac{k_1}{k_2} = \frac{(C_o - C_e)}{m C_e} \quad (12)$$

Combining Eqs. (11) and (12) yields:

$$-\frac{dC_t}{dt} = -\left(k_1 + \frac{k_2}{m}\right)(C_e - C_t) \quad (13)$$

The integration of Eq. (13) using the same boundary conditions described previously, gives the following linear equation:

$$\ln(1 - F_t) = -\left(k_1 + \frac{k_2}{m}\right)t \quad (14)$$

where $F_t = \frac{C_o - C_t}{C_o - C_e}$ is the dimensionless fractional variable describing the equilibrium state at time t .

The experimental plots of $\ln (1-F_t)$ versus t allow the determination of the values of the reaction constants k_1 and k_2 , values by combination with the equilibrium described by Eq. (12). These values, along with those of R^2 and APE are presented in Table 9.3. A good relationship between the experimental data and the predicted values was found for the three temperatures investigated, as it can be observed in Figure 9.4d. However, it is worth noting that the APE values are similar to those obtained when applying the pseudo-second order model, especially for the experiments carried out at 25 and 35°C. Moreover, it was also found that k_1 is temperature dependent, varying between 0.149 and 0.636 min^{-1} within the temperature interval of 5-35°C. Although k_2 also increased with temperature, their low values indicated that the reverse reaction is not favored under the experimental conditions employed in this study.

9.3.2.4. Evaluation of activation energy

Arrhenius plots of the obtained forward reaction rate constants using the pseudo-second order and the reversible reaction models at the three temperatures investigated were used to determine the apparent activation energy of the process. Using the pseudo-second order kinetic model, the activation energy was 50.87 kJ/mol. This value suggests that the ion-exchange process may be regarded as a chemical reaction one diffusion-controlled process, since high activation energies (40-800 kJ/mol) are suggested for chemisorption processes [510].

On the other hand, when using the rate constants obtained with the reversible reaction model the activation energy was 36.16 kJ/mol, suggesting that the process is close to the limit between physical adsorption and chemisorption [510].

9.3.2.5. Scanning electron microscopy

Representative scanning electron micrographs and X-ray elemental analyses of the Amberlite FCP23 H before and after the ion exchange process are presented in Figure 9.6. The SEM images presented in Figures 9.6a and 9.6b revealed that the mean diameter of the spherical resin, calculated by counting at least 100 beads, was 0.57 ± 0.10 mm, which is within the range of the harmonic mean size specified by the manufacturer (0.58-0.80 mm). Moreover, although there was no noteworthy deposition of ions on the resin beads surface, there appears to be some sort of damages, as judged by the fissures and physical attrition presented for some broken beads after the ion exchange process.

From the X-ray elemental analyses, it can be observed that sulfur is the predominant element of the resin, in agreement with its functional groups (sulfonates). After the ion exchange experiments a sodium peak was identified in Figure 9.6b, indicating that some Na^+ were present as adsorbed ions on the resin surface. However, the low intensity of this peak, suggest that Na^+ diffused within the resin matrix during the process.

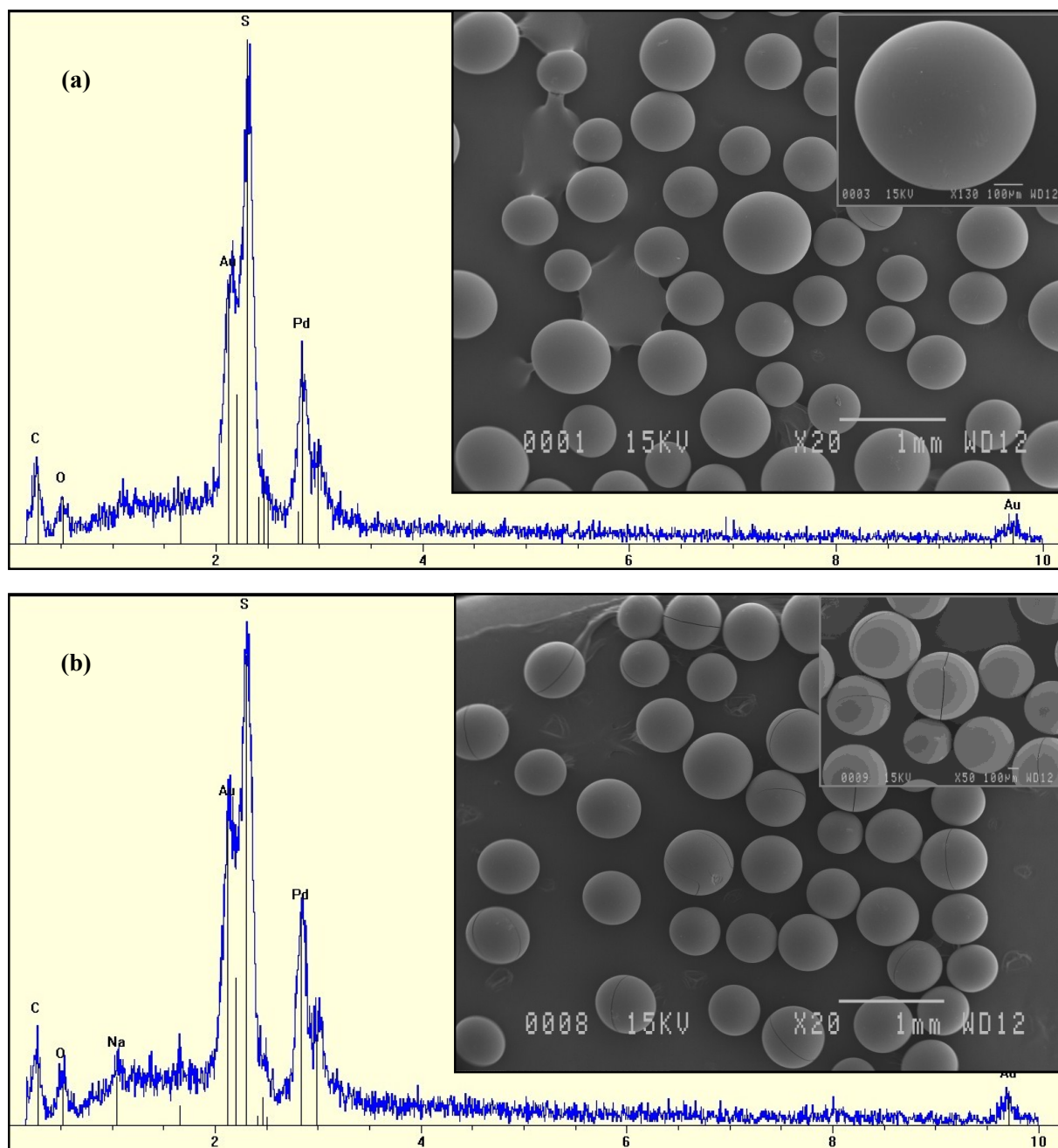


Figure 9.6. SEM micrographs and X-ray elemental analyses of the Amberlite™ FPC23 H before (a) and after (b) the adsorption exchange of Na^+ from LBNa.

9.4. Conclusion

The strongly acidic cation exchange resin Amberlite™ FPC23 H has been used for the production of LBA from a LBNa solution obtained by means of oxidation of lactose over gold catalysts supported on mesoporous silica materials. The adsorption exchange process was shown to be very fast. The equilibrium was reached after about 30 min at low temperature (5°C), and within 10 min at 25 and 35°C. Four simplified kinetic models were used for describing the experimental data. The pseudo-second order and the reversible reaction models were observed to predict reasonably well the kinetics of the process at all the temperatures investigated. These results suggest that the adsorption exchange can be seen as a kind of chemical reaction, for which the kinetic order is two with respect to the number of adsorption sites available for exchange, and in which the chemical adsorption exchange step is the rate controlling.

General conclusions

The studies described in this doctoral dissertation allowing drawing three general groups of conclusions concerning the synthesis and characterization of Au/MSM catalysts, their catalytic activity in the micro-aerial oxidation of lactose and the demineralization process, which can be summarized as follows:

- Synthesis and characterization of catalysts

In this thesis two approaches were employed to synthesize the Au/MSM materials: (*i*) co-condensation with thioether functionalities (BTESPTS) as stabilizing ligand following a similar procedure to that for mesoporous silica SBA-15, and (*ii*) the wet adsorption of the gold complex $[\text{Au}(\text{en})_2]^{3+}$ in alkaline media. Although these two approaches allowed the preparation of highly active and selective Au/MSM catalysts with nominal loading of 0.7% for the lactose oxidation, the main differences between the synthesized materials were related to their mesoporous structure.

As far as the co-condensation method is concerned, the studies on the increasing the concentration of BTESPTS in the synthesis reaction mixture, revealed that the structure of the catalytic materials was transformed from highly 2D-hexagonal to a mixed hexagonal-vesicle and cellular foam structure. Low concentrations of BTESPTS (0-4% molar) led to materials with ordered 2D-hexagonal structure typical of SBA-15, but with large inactive AuNPs. Catalysts synthesized from solutions containing 6-10% of BTESPTS showed a wormhole-like structure favorable for the access to reagent to the well dispersed AuNPs anchored on the silica walls. Higher concentrations of BTESPTS (12-18%) contributed to the structure transformation, and materials with a mixed hexagonal-vesicle and cellular foam structure, were obtained. The average particle size of the AuNPs loaded on the MSM following this method was about 8 nm.

On the other hand, the wet adsorption of the gold complex $[\text{Au}(\text{en})_2]^{3+}$ in alkaline media, can be regarded as a simple method to synthesize Au/SiO₂ catalysts, including amorphous, MSM and ceria modified MSM. The Au/SBA-15 and Au/SBA-15-CeO₂ catalysts prepared following this approach presented well dispersed AuNPs of about 5-6 nm, and they retained the structure of their original support.

From the characterization analysis, it is worth to mention that the XPS study on the oxidation states of gold on all the Au/MSM surfaces revealed the coexistence of metallic and oxidized Au species, with relative abundance following the order $Au^0 \gg Au^{+1} > Au^{+3}$, indicating that gold was not completely reduced after the calcination step at high temperature. In the case of Au/SBA-15-CeO₂ catalysts, cerium was found in both oxidized Ce³⁺ and Ce⁴⁺ states.

- Catalytic activity

The operating conditions of the lactose oxidation were optimized using Au/MSM catalysts synthesized from a mixture containing a molar concentration of BTESPTS of about 7%. The influence of temperature, pH value, metal loading and catalyst/lactose ratio on lactose conversion was investigated. After 100 min of reaction at pH 9.0 and T=65°C, the catalyst containing 0.7% Au showed the highest catalytic activity (100% lactose conversion) and a 100% selectivity towards LBA, when it was used at a catalyst/lactose ratio of 0.2.

The mesostructure transformation observed when increasing the molar concentration of BTESPTS in the synthesis mixture, affected the lactose oxidation activity of the synthesized materials. Under optimal operating conditions, the catalysts synthesized from mixtures with low concentrations of BTESPTS were inactive, probably since the amount of ligand was not enough to stabilize the loaded gold, allowing the formation of unevenly gold aggregates ranging between 25 to 130 nm. On the contrary, the catalysts synthesized from mixtures containing molar concentration of BTESPTS of 6-10%, showed the highest catalytic activity (100% lactose conversion after 80-100 min reaction with 100% selectivity towards LBA). Since the Au particle size of these materials was similar (~8 nm), this behavior was attributed to the predominance of a wormhole-like structure, favorable for the reagent accessibility to the AuNPs intercalated in the silica walls. Higher amounts of BTESPTS (12-18%) led to materials whose mesostructure do not allow the easy access of reagents to the AuNPs, thus with lower catalytic activity.

The Au/SBA-15 and Au/SBA-15-CeO₂ catalysts exhibit high activity for lactose oxidation and 100% selectivity towards LBA. The catalytic activity of the Au/SBA-15 was comparable to that of the Au/MSM synthesized by the co-condensation method. By varying the molar ratio of Ce/Si in the Au/SBA-15-CeO₂ catalysts, it was found that the maximum of activity was reached at Ce/Si of 0.2. Furthermore, catalysts prepared with Ce/Si molar ratio of 0.1, 0.2, 0.4 exhibited enhanced activity in

comparison to that of Au/SBA-15 catalyst, while the catalyst with Ce/Si of 0.6 exhibited similar activity to that showed by Au/SBA-15 catalyst. The high oxygen storage capacity and catalytic and redox properties of ceria, might have contributed to the stabilization and dispersion of gold particles, but also to the reaction mechanism. However, the coordination and agglomeration states of Ce atoms could also have an important effect on the catalytic activity.

The brief study on the catalysts performance after consecutive lactose oxidation reactions indicated the main causes of deactivation of Au/MSM catalysts are the leaching of the active phase and the strong adsorption of organic species on the catalyst surface. To overcome the loss of activity after consecutive reactions, the calcination was found to be an efficient regeneration procedure, since the catalytic activity of the calcined spent samples was similar to that of the fresh ones. However, this treatment generates structure defaults favouring the leaching of gold into the reaction solution.

In summary, highly active and selective Au/MSM for lactose oxidation can be synthesized by the co-condensation method using concentrations of the thioether functionalities in the range of 6-10%, or by the wet adsorption of the gold complex $[Au(en)_2]^{3+}$ in alkaline media, which can be efficiently reutilized after regeneration by calcination. In comparison to the Pd and Pd-Bi supported catalysts, the main advantage of the synthesized Au/MSM are their complete selectivity towards the desired LBA, and the easy control of the reaction.

- Demineralization process

The demineralization of the sodium lactobionate solution obtained at the reactor outlet was investigated by means of bipolar membrane electrodialysis and ion exchange technology. Both processes might be used for producing LBA from its sodium salt. A complete sodium removal was achieved after about 10 min at room temperature, when using a commercial strong cation exchange resin (Amberlite™ FPC23 H). On the other hand, in this study we used for the first time BMED for recovering LBA from its sodium lactobionate. A demineralization rate of 50% was achieved after applying a voltage difference of 5.0-5.5 V during 100-180 min to a three-compartment electrodialysis stack. This demineralization rate can be considered low, and consequently further improvement is needed for industrial applications.

Recommendations for future work

The following are some recommendations for those interested in further investigations on this research field:

1. Although most of the studies conducted for the aerobic oxidation of carbohydrates indicate that the reaction occurs via an oxidative dehydrogenation mechanism, it has been demonstrated that oxygen atoms originating from hydroxide ions, instead of molecular oxygen, have been incorporated into the substrate during the oxidation reactions which are promoted by alkaline conditions at high pH values. A deep study on the mechanism of lactose oxidation over Au/MSM would contribute to the incredible growing of catalysis by gold.
2. We tried tentatively to find the active Au species on the synthesized materials. However, we always found metallic and oxidized Au species in the fresh and spent catalysts, and the slight variation observed was not enough to draw any conclusion. More detailed experiments could help to find out if Au metallic species are the responsible of the catalytic activity of Au/MSM, and if the presence of oxidized Au species affects the catalytic activity of these materials.
3. The optimization of the bipolar membrane electro dialysis process for demineralizing the sodium lactobionate solution could be of great interest, taking into account that this technology might be easily coupled to the oxidation reaction, and it has the additional advantage that NaOH could be efficiently recovered for its reutilization in further oxidation reactions.

References

1. Corma, A., S. Iborra, and A. Velty, *Chemical routes for the transformation of biomass into chemicals*. Chemical Reviews, 2007. 107(6): p. 2411-2502.
2. Jelen, P., *WHEY PROCESSING | Utilization and Products*, in *Encyclopedia of Dairy Sciences (Second Edition)*, W.F. Editor-in-Chief: John, Editor. 2011, Academic Press: San Diego. p. 731-737.
3. Najafpour, G.D., et al., *Biological treatment of dairy wastewater in an upflow anaerobic sludge-fixed film bioreactor*. American-Eurasian Journal of Agriculture & Environmental Science, 2008. 4(2): p. 251-257.
4. Kowalczyk, J., et al., *Method for selective carbohydrate oxidation using supported gold catalysts*. 2007.
5. Global Industry Analysts, I. *Lactose - A global strategic business report*. 2011 [cited 2012 Access date: 27-02-2012]; Available from: http://www.strategyr.com/Lactose_Market_Report.asp.
6. Gutiérrez, L.-F., S. Hamoudi, and K. Belkacemi, *Lactobionic acid: A high value-added lactose derivative for food and pharmaceutical applications*. International Dairy Journal, 2012. 26(2): p. 103-111.
7. Affertsholt-Allen, T. *Market developments and industry challenges for lactose and lactose derivatives*. in *IDF Symposium "Lactose and its Derivatives"*. 2007. Moscow (Russia).
8. Playne, M.J. and R.G. Crittenden, *Galacto-oligosaccharides and Other Products Derived from Lactose*, in *Advanced Dairy Chemistry Volume 3: Lactose, Water, Salts and Minor Constituents*, P.L.H. McSweeney and P.F. Fox, Editors. 2009, Springer: New York. p. 121-201.
9. Climent, M.J., A. Corma, and S. Iborra, *Converting carbohydrates to bulk chemicals and fine chemicals over heterogeneous catalysts*. Green Chemistry, 2011. 13(3): p. 520-540.
10. Hendriks, H.E.J., B.F.M. Kuster, and G.B. Marin, *The Effect of Bismuth on the Selective Oxidation of Lactose on Supported Palladium Catalysts*. Carbohydrate Research, 1990. 204: p. 121-129.
11. Gutiérrez, L.-F., S. Hamoudi, and K. Belkacemi, *Selective Production of Lactobionic Acid by Aerobic Oxidation of Lactose over Gold Crystallites Supported on Mesoporous Silica*. Applied Catalysis A-General, 2011. 402(1-2): p. 94-103.
12. Della Pina, C., E. Falletta, and M. Rossi, *Update on selective oxidation using gold*. Chemical Society Reviews, 2012. 41(1): p. 350-369.
13. Kuusisto, J., et al., *From renewable raw materials to high value-added fine chemicals - Catalytic hydrogenation and oxidation of D-lactose*. Catalysis Today, 2007. 121(1-2): p. 92-99.
14. Mirescu, A. and U. Prusse, *A new environmental friendly method for the preparation of sugar acids via catalytic oxidation on gold catalysts*. Applied Catalysis B-Environmental, 2007. 70(1-4): p. 644-652.
15. Murzina, E.V., et al., *D-lactose oxidation over gold catalysts*. Catalysis Today, 2008. 131(1-4): p. 385-392.
16. Tokarev, A.V., et al., *Application of in situ catalyst potential measurements for estimation of reaction performance: Lactose oxidation over Au and Pd catalysts*. Chemical Engineering Journal, 2007. 134(1-3): p. 153-161.
17. Wang, Y.M., C.H. Huang, and T.W. Xu, *Which is more competitive for production of organic acids, ion-exchange or electrodialysis with bipolar membranes?* Journal of Membrane Science, 2011. 374(1-2): p. 150-156.
18. Liu, S.B., et al., *Gold nanoparticles supported on periodic mesoporous organosilicas for epoxidation of olefins: Effects of pore architecture and surface modification method of the supports*. Microporous and Mesoporous Materials, 2011. 143(2-3): p. 426-434.
19. Okumura, M., et al., *Chemical vapor deposition of gold on Al₂O₃, SiO₂, and TiO₂ for the oxidation of CO and of H₂*. Catalysis Letters, 1998. 51(1-2): p. 53-58.
20. Gänzle, M.G., G. Haase, and P. Jelen, *Lactose: Crystallization, hydrolysis and value-added derivatives*. International Dairy Journal, 2008. 18(7): p. 685-694.
21. Gänzle, M.G., *Lactose and Oligosaccharides | Lactose: Derivatives*, in *Encyclopedia of Dairy Sciences (Second Edition)*, W.F. Editor-in-Chief: John, Editor. 2011, Academic Press: San Diego. p. 202-208.
22. Gänzle, M.G., *Enzymatic synthesis of galacto-oligosaccharides and other lactose derivatives (hetero-oligosaccharides) from lactose*. International Dairy Journal, 2012. 22(2): p. 116-122.
23. Panesar, P.S. and S. Kumari, *Lactulose: Production, purification and potential applications*. Biotechnology Advances, 2011. 29(6): p. 940-948.
24. Schuster-Wolff-Buhring, R., L. Fischer, and J. Hinrichs, *Production and physiological action of the disaccharide lactulose*. International Dairy Journal, 2010. 20(11): p. 731-741.
25. Seki, N. and H. Saito, *Lactose as a source for lactulose and other functional lactose derivatives*. International Dairy Journal, 2012. 22(2): p. 110-115.

26. Torres, D.P.M., et al., *Galacto-Oligosaccharides: Production, Properties, Applications, and Significance as Prebiotics*. Comprehensive Reviews in Food Science and Food Safety, 2010. 9(5): p. 438-454.
27. Fischer, E. and J. Meyer, *Oxydation des Milchzuckers*. Ber Deut Chem Ges., 1889. 22(1): p. 361-364.
28. Nakano, H., et al., *Biocatalytic Production of Lactobionic Acid*, in *Biocatalysis and Biomolecular Engineering*. 2010, John Wiley & Sons, Inc. p. 391-404.
29. Stodola, F.H. and L.B. Lockwood, *The oxidation of lactose and maltose to bionic acids by Pseudomonas*. Journal of Biological Chemistry, 1947. 171(1): p. 213-221.
30. Alonso, S., M. Rendueles, and M. Diaz, *Efficient lactobionic acid production from whey by Pseudomonas taetrolens under pH-shift conditions*. Bioresource technology, 2011. 102(20): p. 9730-6.
31. Alonso, S., M. Rendueles, and M. Diaz, *Role of dissolved oxygen availability on lactobionic acid production from whey by Pseudomonas taetrolens*. Bioresource technology, 2012. 109(0): p. 140-147.
32. Pedruzzi, I., E.A. Borges da Silva, and A.E. Rodrigues, *Production of lactobionic acid and sorbitol from lactose/fructose substrate using GFOR/GL enzymes from Zymomonas mobilis cells: A kinetic study*. Enzyme and Microbial Technology, 2011. 49(2): p. 183-191.
33. da Silva, E.A.B., I. Pedruzzi, and A.E. Rodrigues, *Simulated moving bed technology to improve the yield of the biotechnological production of lactobionic acid and sorbitol*. Adsorption-Journal of the International Adsorption Society, 2011. 17(1): p. 145-158.
34. Severo Junior, J.B., et al., *Analysis of experimental errors in bioprocesses. 1. Production of lactobionic acid and sorbitol using the GFOR (glucose-fructose oxidoreductase) enzyme from permeabilized cells of Zymomonas mobilis*. Journal of Industrial Microbiology & Biotechnology, 2011. 38(9): p. 1575-1585.
35. Satory, M., et al., *Continuous enzymatic production of lactobionic acid using glucose-fructose oxidoreductase in an ultrafiltration membrane reactor*. Biotechnology Letters, 1997. 19(12): p. 1205-1208.
36. Van Hecke, W., et al., *A biocatalytic cascade reaction sensitive to the gas-liquid interface: Modeling and upscaling in a dynamic membrane aeration reactor*. Journal of Molecular Catalysis B-Enzymatic, 2011. 68(2): p. 154-161.
37. Van Hecke, W., et al., *Kinetic Modeling of a Bi-Enzymatic System for Efficient Conversion of Lactose to Lactobionic Acid*. Biotechnology and Bioengineering, 2009. 102(5): p. 1475-1482.
38. Maischberger, T., et al., *Production of lactose-free galacto-oligosaccharide mixtures: comparison of two cellobiose dehydrogenases for the selective oxidation of lactose to lactobionic acid*. Carbohydrate Research, 2008. 343(12): p. 2140-2147.
39. Splechtna, B., et al., *Production of a lactose-free galacto-oligosaccharide mixture by using selective enzymatic oxidation of lactose into lactobionic acid*. Enzyme and Microbial Technology, 2001. 29(6-7): p. 434-440.
40. Van Hecke, W., et al., *Bubble-Free Oxygenation of a Bi-Enzymatic System: Effect on Biocatalyst Stability*. Biotechnology and Bioengineering, 2009. 102(1): p. 122-131.
41. Ludwig, R., et al., *Continuous enzymatic regeneration of electron acceptors used by flavoenzymes: Cellobiose dehydrogenase-catalyzed production of lactobionic acid as an example*. Biocatalysis and Biotransformation, 2004. 22(2): p. 97-104.
42. Baminger, U., et al., *Continuous enzymatic regeneration of redox mediators used in biotransformation reactions employing flavoproteins*. Journal of Molecular Catalysis B-Enzymatic, 2001. 11(4-6): p. 541-550.
43. Nordkvist, M., P.M. Nielsen, and J. Villadsen, *Oxidation of lactose to lactobionic acid by a Microdochium nivale carbohydrate oxidase: Kinetics and operational stability*. Biotechnology and Bioengineering, 2007. 97(4): p. 694-707.
44. Budtz, P., et al., *Enzymatic process for obtaining increased yield of lactobionic acid*. WO/2005/104859. 2005.
45. Saha, T., et al., *Cellobiose dehydrogenase production by the mycelial culture of the mushroom Termitomyces clypeatus*. Process Biochemistry, 2008. 43(6): p. 634-641.
46. Canevascini, G., K. Etienne, and H. Meier, *A direct enzymatic lactose assay using cellobiose-(lactose-)dehydrogenase from Sporotrichum-thermophile*. Zeitschrift Fur Lebensmittel-Untersuchung Und-Forschung, 1982. 175(2): p. 125-129.
47. Dhariwal, A., V. Mavrov, and I. Schroeder, *Production of lactobionic acid with process integrated electrochemical enzyme regeneration and optimisation of process variables using response surface methods (RSM)*. Journal of Molecular Catalysis B-Enzymatic, 2006. 42(1-2): p. 64-69.
48. Hua, L., et al., *Scale-up of enzymatic production of lactobionic acid using the rotary jet head system*. Biotechnology and Bioengineering, 2007. 97(4): p. 842-849.
49. Kiryu, T., et al., *Purification and characterization of a carbohydrate: Acceptor oxidoreductase from Paraconiothyrium sp that produces lactobionic acid efficiently*. Bioscience Biotechnology and Biochemistry, 2008. 72(3): p. 833-841.

50. Lee, M.H., et al., *Purification and characterization of a novel cellooligosaccharide oxidase from rice pathogen Sarocladium oryzae*. *Enzyme and Microbial Technology*, 2006. 39(1): p. 85-91.
51. Volc, J., et al., *Conversion of lactose to beta-D-galactopyranosyl-(1 -> 4)-D-arabino-hexos-2-ulose-(2-dehydrolactose) and lactobiono-1,5-lactone by fungal pyranose dehydrogenase*. *Journal of Molecular Catalysis B-Enzymatic*, 2004. 30(3-4): p. 177-184.
52. Savary, B.J., K.B. Hicks, and J.V. O'Connor, *Hexose oxidase from Chondrus crispus: improved purification using perfusion chromatography*. *Enzyme and Microbial Technology*, 2001. 29(1): p. 42-51.
53. Lin, S.F., et al., *Production of Novel Oligosaccharide Oxidase by Wheat Bran Solid-State Fermentation*. *Biotechnology Advances*, 1993. 11(3): p. 417-427.
54. Murakami, H., et al., *Production of Calcium Lactobionate by a Lactose-oxidizing Enzyme from Paraconiothyrium sp. KD-3*. *Journal of Applied Glycoscience*, 2008. 55(2): p. 127-132.
55. Nishizuka, Y. and O. Hayaishi, *Enzymic Formation of Lactobionic Acid from Lactose*. *Journal of Biological Chemistry*, 1962. 237(9): p. 2721-&.
56. Wright, D.G. and A.G. Rand, *Direct Enzymatic Conversion of Lactose to Acid - Lactose Dehydrogenase*. *Journal of Food Science*, 1973. 38(7): p. 1132-1135.
57. Miyamoto, Y., T. Ooi, and S. Kinoshita, *Production of lactobionic acid from whey by Pseudomonas sp LS13-1*. *Biotechnology Letters*, 2000. 22(5): p. 427-430.
58. Kluyver, A.J., J. de Ley, and A. Rijken, *The formation and consumption of lactobionic and maltobionic acids by Pseudomonas species*. *Antonie van Leeuwenhoek*, 1951. 17(1): p. 1-14.
59. Murakami, H., et al., *Microbial Conversion of Lactose to Lactobionic Acid by Resting Cells of Burkholderia cepacia No. 24*. *Journal of Applied Glycoscience*, 2006. 53(1): p. 7-11.
60. Murakami, H., et al., *Fermentative production of lactobionic acid by Burkholderia cepacia*. *Journal of Applied Glycoscience*, 2003. 50: p. 117-120.
61. Murakami, H., et al., *Screening of Lactobionic Acid Producing Microorganisms*. *Journal of Applied Glycoscience*, 2002. 49(4): p. 469-477.
62. Kiryu, T., et al., *Involvement of Acetobacter orientalis in the production of lactobionic acid in Caucasian yogurt ("Caspian Sea yogurt") in Japan*. *Journal of Dairy Science*, 2009. 92(1): p. 25-34.
63. Kiryu, T., et al., *Optimization of Lactobionic Acid Production by Acetobacter orientalis Isolated from Caucasian Fermented Milk, "Caspian Sea Yogurt"*. *Bioscience Biotechnology and Biochemistry*, 2012. 76(2): p. 361-363.
64. Nakano, H., et al., *Lactobionic Acid and Its Biocatalytic Production*. *Foods & Food Ingredients Journal of Japan*, 2006. 211(10).
65. Tomlinson, G.A., M.P. Strohm, and L.I. Hochstein, *The metabolism of carbohydrates by extremely halophilic bacteria: The identification of lactobionic acid as a product of lactose metabolism by Halobacterium saccharovorum*. *Canadian Journal of Microbiology*, 1978. 24: p. 898-903.
66. Eddy, B.P., *Bacterial Oxidation of Lactose and Melibiose*. *Nature*, 1958. 181(4613): p. 904-905.
67. Cort, W.M., et al., *Evidence for the Formation and Utilization of Lactobionic Acid by Penicillium-Chrysogenum*. *Archives of Biochemistry and Biophysics*, 1956. 63(2): p. 477-478.
68. Isbell, H.S., *Process for the preparation of calcium lactobionate*. *US Patent 1.980.996*. 1934.
69. Magariello, E.R. and N.Y. Islip, *Production of lactobionic acid and its δ -lactone*. *US Patent 2.746.916*. 1956.
70. Aoun, S.B., et al., *Electrocatalytic oxidation of sugars on silver-UPD single crystal gold electrodes in alkaline solutions*. *Electrochemistry Communications*, 2003. 5(4): p. 317-320.
71. Dutta, S.K. and S.K. Basu, *Erythromycin Aldobionates*. *US Patent 4.137.397*. 1979.
72. Karim-Nezhad, G., et al., *Kinetic Study of Electrocatalytic Oxidation of Carbohydrates on Cobalt Hydroxide Modified Glassy Carbon Electrode*. *Journal of the Brazilian Chemical Society*, 2009. 20(1): p. 141-151.
73. Kokoh, K.B. and N. Alonso-Vante, *Electrocatalytic oxidation of lactose on gold nanoparticle modified carbon in carbonate buffer*. *Journal of Applied Electrochemistry*, 2006. 36(2): p. 147-151.
74. Druliolle, H., K.B. Kokoh, and B. Beden, *Electrooxidation of Lactose on Platinum and on Modified Platinum-Electrodes in Alkaline-Medium*. *Electrochimica Acta*, 1994. 39(17): p. 2577-2584.
75. Druliolle, H., K.B. Kokoh, and B. Beden, *Selective Oxidation of Lactose to Lactobionic Acid on Lead-Adatoms Modified Platinum-Electrodes in Na2co3+Nahco3 Buffered Medium*. *Journal of Electroanalytical Chemistry*, 1995. 385(1): p. 77-83.
76. Druliolle, H., et al., *On some mechanistic aspects of the electrochemical oxidation of lactose at platinum and gold electrodes in alkaline medium*. *Journal of Electroanalytical Chemistry*, 1997. 426(1-2): p. 103-115.
77. Hendriks, H.E.J., *Selective Catalytic Oxidation of Lactose and Related Carbohydrates*. 1991, Technische Universiteit Eindhoven: The Netherlands. p. 145.

78. Maki-Arvela, P., et al., *The effect of palladium dispersion and promoters on lactose oxidation kinetics*. Research on Chemical Intermediates, 2010. 36(4): p. 423-442.
79. Tokarev, A.V., et al., *Kinetic behaviour of electrochemical potential in three-phase heterogeneous catalytic oxidation reactions*. Journal of Molecular Catalysis a-Chemical, 2006. 255(1-2): p. 199-208.
80. Tokarev, A.V., et al., *Lactose oxidation over palladium catalysts supported on active carbons and on carbon nanofibres*. Research on Chemical Intermediates, 2009. 35(2): p. 155-174.
81. Karski, S., *Activity and selectivity of Pd-Bi/SiO₂ catalysts in the light of mutual interaction between Pd and Bi*. Journal of Molecular Catalysis a-Chemical, 2006. 253(1-2): p. 147-154.
82. Karski, S., I. Witonska, and J. Goluchowska, *Catalytic properties of Pd-Ti/SiO₂ systems in the reaction of liquid phase oxidation of aldoses*. Journal of Molecular Catalysis a-Chemical, 2006. 245(1-2): p. 225-230.
83. Tokarev, A.V., et al., *Influence of surface acidity in lactose oxidation over supported Pd catalysts*. Microporous and Mesoporous Materials, 2008. 113(1-3): p. 122-131.
84. Chia, Y.N., M.P. Latusek, and J.H. Holles, *Catalytic wet oxidation of lactose*. Industrial & Engineering Chemistry Research, 2008. 47(12): p. 4049-4055.
85. Belkacemi, K., et al., *Value-added processing of lactose: Preparation of bioactive lactobionic acid using a novel catalytic method*. International Journal of Chemical Reactor Engineering, 2007. 5.
86. Belkacemi, K. and S. Hamoudi, *Chemocatalytic Oxidation of Lactose to Lactobionic Acid over Pd-Bi/SBA-15: Reaction Kinetics and Modeling*. Industrial & Engineering Chemistry Research, 2010. 49(15): p. 6878-6889.
87. Bouasker, H., *Étude expérimentale et optimisation des conditions opératoires de l'oxydation catalytique du lactose en acide lactobionique*, in *Chemical Engineering*. 2009, Université Laval: Quebec. p. 99.
88. Maki-Arvela, P., et al., *Kinetics of lactose and rhamnose oxidation over supported metal catalysts*. Physical Chemistry Chemical Physics, 2011. 13(20): p. 9268-9280.
89. Abbadi, A., et al., *Selective chemo-catalytic oxidation of lactose and/of lactobionic acid towards 1-carboxylactulose (2-keto-lactobionic acid)*. Applied Catalysis a-General, 1997. 156(1): p. 105-115.
90. Gutierrez, L.-F., S. Hamoudi, and K. Belkacemi, *Effective gold catalyst supported on mesoporous silica decorated by ceria for the synthesis of high value lactobionic acid*. Applied Catalysis a-General, 2012. 425: p. 213-223.
91. Besson, M. and P. Gallezot, *Deactivation of metal catalysts in liquid phase organic reactions*. Catalysis Today, 2003. 81(4): p. 547-559.
92. Charloux, C., et al., *Inhibition of Hydroxyl Radical Production by Lactobionate, Adenine, and Tempol*. Free Radical Biology and Medicine, 1995. 19(5): p. 699-704.
93. Shepherd, R.E., et al., *Lactobionic and Gluconic Acid Complexes of Fe-I and Fe-II - Control of Oxidation Pathways by an Organ-Transplantation Preservant*. Journal of Inorganic Biochemistry, 1993. 49(1): p. 23-48.
94. Southard, J.H. and F.O. Belzer, *Organ Preservation*. Annual Review of Medicine, 1995. 46: p. 235-247.
95. Gerling, K.G. *Large scale production of lactobionic acid - Use and new applications*. in *Whey : Proceedings of the Second International Whey Conference*. 1998. Chicago, USA: International Dairy Federation.
96. Guo, R., et al., *Synthesis of glycoconjugated poly(amindoamine) dendrimers for targeting human liver cancer cells*. RSC Advances, 2012. 2(1): p. 99-102.
97. Lin, W.J., et al., *Synthesis of lactobionic acid-grafted-pegylated-chitosan with enhanced HepG2 cells transfection*. Carbohydrate Polymers, 2011. 83(2): p. 898-904.
98. Luo, Z., et al., *Mesoporous Silica Nanoparticles End-Capped with Collagen: Redox-Responsive Nanoreservoirs for Targeted Drug Delivery*. Angewandte Chemie-International Edition, 2011. 50(3): p. 640-643.
99. Kim, E.M., et al., *Asialoglycoprotein-receptor-targeted hepatocyte imaging using Tc-99m galactosylated chitosan*. Nuclear Medicine and Biology, 2006. 33(4): p. 529-534.
100. Rico-Lattes, I., et al., *Cationic sugar derived surfactants, polymers and dendrimers: from molecules to targeted self-organized systems*. Comptes Rendus Chimie, 2005. 8(5): p. 807-814.
101. Zhao, Q.H., et al., *Self-Assembled Virus-Like Particles from Rotavirus Structural Protein VP6 for Targeted Drug Delivery*. Bioconjugate Chemistry, 2011. 22(3): p. 346-352.
102. Choi, E.S., et al., *Water-Soluble Ultra-Small Manganese Oxide Surface Doped Gadolinium Oxide (Gd₂O₃)@MnO Nanoparticles for MRI Contrast Agent*. European Journal of Inorganic Chemistry, 2010(28): p. 4555-4560.
103. Bahadur K.C. R., et al., *Glycoconjugated chitosan stabilized iron oxide nanoparticles as a multifunctional nanoprobe*. Materials Science and Engineering: C, 2009. 29(5): p. 1668-1673.
104. Xiao, Q.F., et al., *Efficient Synthesis of PbTe Nanoparticle Networks*. Nano Research, 2010. 3(10): p. 685-693.
105. Green, B.A., R.J. Yu, and E.J. Van Scott, *Clinical and cosmeceutical uses of hydroxyacids*. Clinics in Dermatology, 2009. 27(5): p. 495-501.

106. Yu, R.J. and E.J. Van Scott, *Oligosaccharide Aldonic Acids and Their Topical Use*. Patent application number 20100099632. 2010.
107. Rivera, R., et al., *Bioavailability of Iron-Supplemented and Copper-Supplemented Milk for Mexican School-Children*. American Journal of Clinical Nutrition, 1982. 36(6): p. 1162-1169.
108. Nielsen, P.M., *Meat based food product comprising lactobionic acid*. US Patent 20090214752. 2009.
109. Oskarsson, H., et al., *Adsorption of novel alkylaminoamide sugar surfactants at tailor-made surfaces*. Journal of Surfactants and Detergents, 2007. 10(1): p. 41-52.
110. Ahamed, A. and P. Vermette, *Culture-based strategies to enhance cellulase enzyme production from Trichoderma reesei RUT-C30 in bioreactor culture conditions*. Biochemical Engineering Journal, 2008. 40(3): p. 399-407.
111. Frutos, A.A., et al., *Complex formation between D-lactobionate and bivalent metal ions. Studies in solution and in the solid state*. Canadian Journal of Chemistry-Revue Canadienne De Chimie, 1997. 75(4): p. 405-413.
112. Jain, N.K. and S.K. Jain, *Development and In Vitro Characterization of Galactosylated Low Molecular Weight Chitosan Nanoparticles Bearing Doxorubicin*. Aaps Pharmscitech, 2010. 11(2): p. 686-697.
113. Kim, I.S. and S.H. Kim, *Development of a polymeric nanoparticulate drug delivery system - In vitro characterization of nanoparticles based on sugar-containing conjugates*. International Journal of Pharmaceutics, 2002. 245(1-2): p. 67-73.
114. Merrill, R.K. and M. Singh, *Food ingredients and food products treated with an oxidoreductase and methods for preparing such food ingredients and food products*. EP 2 123 294 A1. 2009.
115. Yu, T., Y.X. Du, and B. Chen, *Evaluation of clarithromycin lactobionate as a novel chiral selector for enantiomeric separation of basic drugs in capillary electrophoresis*. Electrophoresis, 2011. 32(14): p. 1898-1905.
116. Chung, T.W., et al., *Preparation of alginate/galactosylated chitosan scaffold for hepatocyte attachment*. Biomaterials, 2002. 23(14): p. 2827-2834.
117. Kekkonen, V., et al., *Synthesis and characterization of biocompatible magnetic glyconanoparticles*. Journal of Magnetism and Magnetic Materials, 2009. 321(10): p. 1393-1396.
118. Peng, J.F., et al., *Identification of live liver cancer cells in a mixed cell system using galactose-conjugated fluorescent nanoparticles*. Talanta, 2007. 71(2): p. 833-840.
119. Colwell, N.S., M.J. Grupe, and D.M. Tollefsen, *Amino acid residues of heparin cofactor II required for stimulation of thrombin inhibition by sulphated polyanions*. Biochimica et Biophysica Acta (BBA) - Protein Structure and Molecular Enzymology, 1999. 1431(1): p. 148-156.
120. Raake, W., et al., *Anticoagulant and Antithrombotic Properties of Synthetic Sulfated Bis-Lactobionic Acid-Amides*. Thrombosis Research, 1989. 56(6): p. 719-730.
121. Klauser, R.J., *Interaction of the Sulfated Lactobionic Acid Amide Lw-10082 with Thrombin and Its Endogenous Inhibitors*. Thrombosis Research, 1991. 62(5): p. 557-565.
122. Ofosu, F.A., et al., *Inhibition of factor-X, factor-V and prothrombin activation by the bis(lactobionic acid amide) LW10082*. European Journal of Biochemistry, 1992. 203(1-2): p. 121-125.
123. Sugidachi, A., F. Asai, and H. Koike, *Anticoagulant and antiprotease activities of aprosulate sodium, a new synthetic polyanion, in human plasma and purified systems*. Blood Coagulation & Fibrinolysis, 1994. 5(5): p. 773-779.
124. Tasic-Kostov, M., et al., *Lactobionic acid in a natural alkylpolyglucoside-based vehicle: assessing safety and efficacy aspects in comparison to glycolic acid*. Journal of Cosmetic Dermatology, 2010. 9(1): p. 3-10.
125. Briden, M.E. and B. Green, *The next generation of hydroxy acids*, in *Cosmeceuticals*, Z.D. Draeos, Editor. 2005, Elsevier Saunders: New York. p. 205-211.
126. Green, B., et al., *Lactobionic acid: A bionic acid enhances skin clarity and provides skin plumping and firming effects*. Journal of the American Academy of Dermatology, 2006. 54(3): p. Ab37-Ab37.
127. Hatano, Y., et al., *Maintenance of an acidic stratum corneum prevents emergence of murine atopic dermatitis*. Journal of Investigative Dermatology, 2009. 129: p. 1824-1835.
128. Yu, R.J. and E.J. Van Scott, *Oligosaccharide aldonic acids and their topical use*. US Patent 7452545. 2008.
129. Van Scott, E.J. and R.J. Yu, *Hydroxyacids and their topical use in the elderly*, in *Skin Diseases in the Elderly*, L. Nall, G. Cauwenbergh, and P. Jacobs, Editors. 2004, Marcel Dekker: New York.
130. Il'ina, A.V. and V.P. Varlamov, *Galactosylated derivatives of low-molecular-weight chitosan: Obtaining and properties*. Applied Biochemistry and Microbiology, 2007. 43(1): p. 73-77.
131. Lu, B., et al., *Galactosyl conjugated N-succinyl-chitosan-graft-polyethylenimine for targeting gene transfer*. Molecular Biosystems, 2010. 6(12): p. 2529-2538.

132. Stannard, K.A., et al., *Galectin inhibitory disaccharides promote tumour immunity in a breast cancer model*. Cancer Letters, 2010. 299(2): p. 95-110.
133. Zhang, J., et al., *Fabrication of lactobionic-loaded chitosan microcapsules as potential drug carriers targeting the liver*. Acta Biomaterialia, 2011. 7(4): p. 1665-1673.
134. Rouquerol, J., et al., *Recommendations for the Characterization of Porous Solids*. Pure and Applied Chemistry, 1994. 66(8): p. 1739-1758.
135. Kresge, C.T., et al., *Ordered Mesoporous Molecular-Sieves Synthesized by a Liquid-Crystal Template Mechanism*. Nature, 1992. 359(6397): p. 710-712.
136. Beck, J.S., et al., *A New Family of Mesoporous Molecular-Sieves Prepared with Liquid-Crystal Templates*. Journal of the American Chemical Society, 1992. 114(27): p. 10834-10843.
137. Hoffmann, F., et al., *Silica-based mesoporous organic-inorganic hybrid materials*. Angewandte Chemie-International Edition, 2006. 45(20): p. 3216-3251.
138. Yang, P.P., S.L. Gai, and J. Lin, *Functionalized mesoporous silica materials for controlled drug delivery*. Chemical Society Reviews, 2012. 41(9): p. 3679-3698.
139. Fan, J., et al., *Cubic mesoporous silica with large controllable entrance sizes and advanced adsorption properties*. Angewandte Chemie-International Edition, 2003. 42(27): p. 3146-3150.
140. Tanev, P.T. and T.J. Pinnavaia, *Mesoporous silica molecular sieves prepared by ionic and neutral surfactant templating: A comparison of physical properties*. Chemistry of Materials, 1996. 8(8): p. 2068-2079.
141. Kim, J.Y., S.B. Yoon, and J. Yu, *Fabrication of a new mesostructured silica prepared by double replications from a MCM-48 silica*. Recent Advances in the Science and Technology of Zeolites and Related Materials, Pts a - C, 2004. 154: p. 380-385.
142. Chen, F.X., L.M. Huang, and Q.Z. Li, *Synthesis of MCM-48 using mixed cationic-anionic surfactants as templates*. Chemistry of Materials, 1997. 9(12): p. 2685-+.
143. Park, I., Z. Wang, and T.J. Pinnavaia, *Assembly of large-pore silica mesophases with wormhole framework structures from alpha,omega-diamine porogens*. Chemistry of Materials, 2005. 17(2): p. 383-386.
144. Zhao, D.Y., et al., *Nonionic triblock and star diblock copolymer and oligomeric surfactant syntheses of highly ordered, hydrothermally stable, mesoporous silica structures*. Journal of the American Chemical Society, 1998. 120(24): p. 6024-6036.
145. Zhao, D.Y., et al., *Triblock copolymer syntheses of mesoporous silica with periodic 50 to 300 angstrom pores*. Science, 1998. 279(5350): p. 548-552.
146. Gutiérrez, L.-F., S. Hamoudi, and K. Belkacemi, *Synthesis of Gold Catalysts Supported on Mesoporous Silica Materials: Recent Developments*. Catalysts, 2011. 1(1): p. 97-154.
147. Taguchi, A. and F. Schuth, *Ordered mesoporous materials in catalysis*. Microporous and Mesoporous Materials, 2005. 77(1): p. 1-45.
148. Yokoi, T., Y. Kubota, and T. Tatsumi, *Amino-functionalized mesoporous silica as base catalyst and adsorbent*. Applied Catalysis a-General, 2012. 421: p. 14-37.
149. Zhang, A.P., et al., *Mesoporous SBA-15 materials modified with PW or W active species as catalysts for the epoxidation of olefins with H2O2*. Research on Chemical Intermediates, 2011. 37(8): p. 975-984.
150. Ren, Y.H., et al., *Progress of the Application of Mesoporous Silica-Supported Heteropolyacids in Heterogeneous Catalysis and Preparation of Nanostructured Metal Oxides*. Materials, 2010. 3(2): p. 764-785.
151. Naik, B. and N.N. Ghosh, *A Review on Chemical Methodologies for Preparation of Mesoporous Silica and Alumina Based Materials*. Recent Patents on Nanotechnology, 2009. 3(3): p. 213-224.
152. Sun, J.M. and X.H. Bao, *Textural manipulation of mesoporous materials for hosting of metallic nanocatalysts*. Chemistry-a European Journal, 2008. 14(25): p. 7478-7488.
153. Hartmann, M., *Ordered mesoporous materials for bioadsorption and biocatalysis*. Chemistry of Materials, 2005. 17(18): p. 4577-4593.
154. Davis, M.E., *Ordered porous materials for emerging applications*. Nature, 2002. 417(6891): p. 813-821.
155. De Vos, D.E., et al., *Ordered mesoporous and microporous molecular sieves functionalized with transition metal complexes as catalysts for selective organic transformations*. Chemical Reviews, 2002. 102(10): p. 3615-3640.
156. Sayari, A. and S. Hamoudi, *Periodic mesoporous silica-based organic - Inorganic nanocomposite materials*. Chemistry of Materials, 2001. 13(10): p. 3151-3168.
157. Corma, A., *From microporous to mesoporous molecular sieve materials and their use in catalysis*. Chemical Reviews, 1997. 97(6): p. 2373-2419.
158. Van der Voort, P., et al., *Ordered mesoporous materials at the beginning of the third millennium: new strategies to create hybrid and non-siliceous variants*. Physical Chemistry Chemical Physics, 2008. 10(3): p. 347-360.

159. Meynen, V., P. Cool, and E.F. Vansant, *Verified syntheses of mesoporous materials*. *Microporous and Mesoporous Materials*, 2009. 125(3): p. 170-223.
160. Kruk, M., et al., *Characterization of the porous structure of SBA-15*. *Chemistry of Materials*, 2000. 12(7): p. 1961-1968.
161. Dai, Q.G., et al., *Direct synthesis of Cerium(III)-incorporated SBA-15 mesoporous molecular sieves by two-step synthesis method*. *Microporous and Mesoporous Materials*, 2007. 100(1-3): p. 268-275.
162. Cassiers, K., et al., *A detailed study of thermal, hydrothermal, and mechanical stabilities of a wide range of surfactant assembled mesoporous silicas*. *Chemistry of Materials*, 2002. 14(5): p. 2317-2324.
163. Janssen, A.H., et al., *A 3D-TEM study of the shape of mesopores in SBA-15 and modified SBA-15 materials*. *Chemical Communications*, 2002(15): p. 1632-1633.
164. Fan, J., et al., *Rapid and high-capacity immobilization of enzymes based on mesoporous silicas with controlled morphologies*. *Chemical Communications*, 2003(17): p. 2140-2141.
165. Sing, K.S.W., et al., *Reporting Physisorption Data for Gas Solid Systems with Special Reference to the Determination of Surface-Area and Porosity (Recommendations 1984)*. *Pure and Applied Chemistry*, 1985. 57(4): p. 603-619.
166. Hutchings, G.J., *Vapor-Phase Hydrochlorination of Acetylene - Correlation of Catalytic Activity of Supported Metal Chloride Catalysts*. *Journal of Catalysis*, 1985. 96(1): p. 292-295.
167. Haruta, M., et al., *Novel Gold Catalysts for the Oxidation of Carbon-Monoxide at a Temperature Far Below 0-Degrees-C*. *Chemistry Letters*, 1987(2): p. 405-408.
168. Della Pina, C., et al., *Selective oxidation using gold*. *Chemical Society Reviews*, 2008. 37(9): p. 2077-2095.
169. Claus, P., *Heterogeneously catalysed hydrogenation using gold catalysts*. *Applied Catalysis a-General*, 2005. 291(1-2): p. 222-229.
170. Corma, A. and P. Serna, *Chemoselective hydrogenation of nitro compounds with supported gold catalysts*. *Science*, 2006. 313(5785): p. 332-334.
171. Fu, Q., A. Weber, and M. Flytzani-Stephanopoulos, *Nanostructured Au-CeO₂ catalysts for low-temperature water-gas shift*. *Catalysis Letters*, 2001. 77(1-3): p. 87-95.
172. Idakiev, V., et al., *Gold nanoparticles supported on ceria-modified mesoporous-macroporous binary metal oxides as highly active catalysts for low-temperature water-gas shift reaction*. *Journal of Materials Science*, 2009. 44(24): p. 6637-6643.
173. Flytzani-Stephanopoulos, M., Q. Fu, and H. Saltsburg, *Active nonmetallic Au and Pt species on ceria-based water-gas shift catalysts*. *Science*, 2003. 301(5635): p. 935-938.
174. Nkosi, B., et al., *Hydrochlorination of Acetylene Using Gold Catalysts - a Study of Catalyst Deactivation*. *Journal of Catalysis*, 1991. 128(2): p. 366-377.
175. Conte, M., et al., *Hydrochlorination of acetylene using a supported gold catalyst: A study of the reaction mechanism*. *Journal of Catalysis*, 2007. 250(2): p. 231-239.
176. Edwards, J.K., et al., *Direct synthesis of hydrogen peroxide from H₂ and O₂ using TiO₂-supported Au-Pd catalysts*. *Journal of Catalysis*, 2005. 236(1): p. 69-79.
177. Ueda, A., T. Oshima, and M. Haruta, *Reduction of nitrogen monoxide with propene in the presence of oxygen and moisture over gold supported on metal oxides*. *Applied Catalysis B-Environmental*, 1997. 12(2-3): p. 81-93.
178. Nguyen, L.Q., C. Salim, and H. Hinode, *Roles of nano-sized Au in the reduction of NO(x) by propene over Au/TiO₂: An in situ DRIFTS study*. *Applied Catalysis B-Environmental*, 2010. 96(3-4): p. 299-306.
179. Teles, J.H., S. Brode, and M. Chabanas, *Cationic gold(I) complexes: Highly efficient catalysts for the addition of alcohols to alkynes*. *Angewandte Chemie-International Edition*, 1998. 37(10): p. 1415-1418.
180. Corma, A., S. Carrettin, and J. Guzman, *Supported gold catalyzes the homocoupling of phenylboronic acid with high conversion and selectivity*. *Angewandte Chemie-International Edition*, 2005. 44(15): p. 2242-2245.
181. Hashmi, A.S.K. and M. Rudolph, *Gold catalysis in total synthesis*. *Chemical Society Reviews*, 2008. 37(9): p. 1766-1775.
182. Haruta, M., *Catalysis of gold nanoparticles deposited on metal oxides*. *Cattech*, 2002. 6(3): p. 102-115.
183. Hashmi, A.S.K. and G.J. Hutchings, *Gold catalysis*. *Angewandte Chemie-International Edition*, 2006. 45(47): p. 7896-7936.
184. Daniel, M.C. and D. Astruc, *Gold nanoparticles: Assembly, supramolecular chemistry, quantum-size-related properties, and applications toward biology, catalysis, and nanotechnology*. *Chemical Reviews*, 2004. 104(1): p. 293-346.
185. Hutchings, G.J., M. Brust, and H. Schmidbaur, *Gold - an introductory perspective*. *Chemical Society Reviews*, 2008. 37(9): p. 1759-1765.

186. Hutchings, G.J. and M. Haruta, *A golden age of catalysis: A perspective*. Applied Catalysis a-General, 2005. 291(1-2): p. 2-5.
187. Thompson, D.T. and G.C. Bond, *Catalysis by gold*. Catalysis Reviews-Science and Engineering, 1999. 41(3-4): p. 319-388.
188. Hutchings, G.J., *Catalysis by gold*. Catalysis Today, 2005. 100(1-2): p. 55-61.
189. Gates, B.C. and J.C. Fierro-Gonzalez, *Catalysis by gold dispersed on supports: the importance of cationic gold*. Chemical Society Reviews, 2008. 37(9): p. 2127-2134.
190. Pyykko, P., *Theoretical chemistry of gold. III*. Chemical Society Reviews, 2008. 37(9): p. 1967-1997.
191. Jansen, M., *The chemistry of gold as an anion*. Chemical Society Reviews, 2008. 37(9): p. 1824-1835.
192. Corma, A. and H. Garcia, *Supported gold nanoparticles as catalysts for organic reactions*. Chemical Society Reviews, 2008. 37(9): p. 2096-2126.
193. Rossi, M., et al., *Selective oxidation using gold*. Chemical Society Reviews, 2008. 37(9): p. 2077-2095.
194. Haruta, M. and M. Date, *Advances in the catalysis of Au nanoparticles*. Applied Catalysis a-General, 2001. 222(1-2): p. 427-437.
195. Wang, A.Q., et al., *A novel efficient Au-Ag alloy catalyst system: preparation, activity, and characterization*. Journal of Catalysis, 2005. 233(1): p. 186-197.
196. Zheng, N.F. and G.D. Stucky, *A general synthetic strategy for oxide-supported metal nanoparticle catalysts*. Journal of the American Chemical Society, 2006. 128(44): p. 14278-14280.
197. Guzman, J. and B.C. Gates, *Catalysis by supported gold: Correlation between catalytic activity for CO oxidation and oxidation states of gold*. Journal of the American Chemical Society, 2004. 126(9): p. 2672-2673.
198. Haruta, M., et al., *Gold Catalysts Prepared by Coprecipitation for Low-Temperature Oxidation of Hydrogen and of Carbon-Monoxide*. Journal of Catalysis, 1989. 115(2): p. 301-309.
199. Ma, Z. and S. Dai, *Development of Novel Supported Gold Catalysts: A Materials Perspective*. Nano Research, 2011. 4(1): p. 3-32.
200. Ma, Z., S.H. Overbury, and S. Dai, *Gold nanoparticles as chemical catalysts*, in *Nanomaterials: Inorganic and Bioinorganic Perspectives*, C.M. Lukehart and R.A. Scott, Editors. 2008, John Wiley & Sons: Chichester. p. 247-266.
201. *Web of ScienceSM. Thomson Reuters. Citation Report. Topic: Gold Catalysts*. Web of Knowledge [cited 2011 November 23, 2011].
202. Glomm, W.R., et al., *Synthesis and characterization of gold nanoparticle-functionalized ordered mesoporous materials*. Journal of Dispersion Science and Technology, 2005. 26(6): p. 729-744.
203. Yang, C.M., et al., *Highly dispersed metal nanoparticles in functionalized SBA-15*. Chemistry of Materials, 2003. 15(1): p. 275-280.
204. Guari, Y., et al., *In situ formation of gold nanoparticles within thiol functionalized HMS-C-16 and SBA-15 type materials via an organometallic two-step approach*. Chemistry of Materials, 2003. 15(10): p. 2017-2024.
205. Zhu, H.G., et al., *Coassembly synthesis of ordered mesoporous silica materials containing Au nanoparticles*. Langmuir, 2003. 19(9): p. 3974-3980.
206. Zhu, H.G., et al., *Preparation of highly active silica-supported Au catalysts for CO oxidation by a solution-based technique*. Journal of Physical Chemistry B, 2006. 110(22): p. 10842-10848.
207. Okumura, M., et al., *Chemical vapor deposition of gold nanoparticles on MCM-41 and their catalytic activities for the low-temperature oxidation of CO and of H-2*. Chemistry Letters, 1998(4): p. 315-316.
208. Zhu, J., et al., *Encapsulation of metal (Au, Ag, Pt) nanoparticles into the mesoporous SBA-15 structure*. Langmuir, 2003. 19(10): p. 4396-4401.
209. Konya, Z., et al., *Synthetic insertion of gold nanoparticles into mesoporous silica*. Chemistry of Materials, 2003. 15(6): p. 1242-1248.
210. Yan, W.F., et al., *Effect of supporting surface layers on catalytic activities of gold nanoparticles in CO oxidation*. Journal of Physical Chemistry B, 2005. 109(32): p. 15489-15496.
211. Bandyopadhyay, M., et al., *Gold nano-particles stabilized in mesoporous MCM-48 as active CO-oxidation catalyst*. Microporous and Mesoporous Materials, 2006. 89(1-3): p. 158-163.
212. Alcaide, B., P. Almendros, and J.M. Alonso, *Gold-Catalyzed Cyclizations of Alkynol-Based Compounds: Synthesis of Natural Products and Derivatives*. Molecules, 2011. 16(9): p. 7815-7843.
213. Froba, M., et al., *Silica-based mesoporous organic-inorganic hybrid materials*. Angewandte Chemie-International Edition, 2006. 45(20): p. 3216-3251.
214. Kumar, R., et al., *Gold nanoparticles formed within ordered mesoporous silica and on amorphous silica*. Nanotechnology in Catalysis, Vols 1 and 2, 2004: p. 111-136.

215. Chi, Y.S., H.P. Lin, and C.Y. Mou, *CO oxidation over gold nanocatalyst confined in mesoporous silica*. Applied Catalysis a-General, 2005. 284(1-2): p. 199-206.
216. Gabaldon, J.P., M. Bore, and A.K. Datye, *Mesoporous silica supports for improved thermal stability in supported Au catalysts*. Topics in Catalysis, 2007. 44(1-2): p. 253-262.
217. Bore, M.T., et al., *The role of pore size and structure on the thermal stability of gold nanoparticles within mesoporous silica*. Journal of Physical Chemistry B, 2005. 109(7): p. 2873-2880.
218. Zhu, K.K., J.C. Hu, and R. Richards, *Aerobic oxidation of cyclohexane by gold nanoparticles immobilized upon mesoporous silica*. Catalysis Letters, 2005. 100(3-4): p. 195-199.
219. Yang, C.M., et al., *Gold nanoparticles in SBA-15 showing catalytic activity in CO oxidation*. Applied Catalysis a-General, 2003. 254(2): p. 289-296.
220. Ma, C.Y., et al., *Catalytic oxidation of benzyl alcohol on Au or Au-Pd nanoparticles confined in mesoporous silica*. Applied Catalysis B-Environmental, 2009. 92(1-2): p. 202-208.
221. Yang, Q.Y., et al., *Preparation and characterization of Au-In/APTMS-SBA-15 catalysts for chemoselective hydrogenation of crotonaldehyde to crotyl alcohol*. Applied Catalysis a-General, 2009. 369(1-2): p. 67-76.
222. Rombi, E., et al., *Modifications induced by pretreatments on Au/SBA-15 and their influence on the catalytic activity for low temperature CO oxidation*. Physical Chemistry Chemical Physics, 2009. 11(3): p. 593-602.
223. Wu, P.P., et al., *Au nanoparticles dispersed on functionalized mesoporous silica for selective oxidation of cyclohexane*. Catalysis Today, 2010. 158(3-4): p. 220-227.
224. Li, L., et al., *Cyclohexane Oxidation Over Size-Uniform Au Nanoparticles (SBA-15 hosted) in a Continuously Stirred Tank Reactor Under Mild Conditions*. Catalysis Letters, 2009. 129(3-4): p. 303-311.
225. Chen, L.F., J.C. Hu, and R.M. Richards, *Intercalation of aggregation-free and well-dispersed gold nanoparticles into the walls of mesoporous silica as a highly active catalyst for n-alkane and alcohols oxidation*. Abstracts of Papers of the American Chemical Society, 2009. 237.
226. Yang, Y.H., et al., *Mesostructured SBA-16 with excellent hydrothermal, thermal and mechanical stabilities: Modified synthesis and its catalytic application*. Journal of Colloid and Interface Science, 2009. 333(1): p. 317-323.
227. Cao, R., et al., *Stable gold nanoparticle encapsulated in silica-dendrimers organic-inorganic hybrid composite as recyclable catalyst for oxidation of alcohol*. Microporous and Mesoporous Materials, 2010. 136(1-3): p. 42-49.
228. Bai, Y., et al., *Gold nanoparticles-mesoporous silica composite used as an enzyme immobilization matrix for amperometric glucose biosensor construction*. Sensors and Actuators B-Chemical, 2007. 124(1): p. 179-186.
229. Xiao, F.S., et al., *Superior catalytic properties in aerobic oxidation of olefins over Au nanoparticles on pyrrolidone-modified SBA-15*. Journal of Catalysis, 2011. 281(1): p. 30-39.
230. Cutrufello, M.G., et al., *Synthesis, characterization and catalytic activity of Au supported on functionalized SBA-15 for low temperature CO oxidation*. Journal of Materials Science, 2009. 44(24): p. 6644-6653.
231. Lee, B., et al., *Influences of synthesis conditions and mesoporous structures on the gold nanoparticles supported on mesoporous silica hosts*. Microporous and Mesoporous Materials, 2009. 122(1-3): p. 160-167.
232. Liu, H.L., et al., *Dispersion of active Au nanoparticles on mesoporous SBA-15 materials*. Chinese Journal of Chemical Engineering, 2007. 15(4): p. 507-511.
233. Petkov, N., N. Stock, and T. Bein, *Gold electroless reduction in nanosized channels of thiol-modified SBA-15 material*. Journal of Physical Chemistry B, 2005. 109(21): p. 10737-10743.
234. Okubo, T., et al., *Microwave-induced synthesis of highly dispersed gold nanoparticles within the pore channels of mesoporous silica*. Journal of Solid State Chemistry, 2008. 181(4): p. 957-963.
235. Liu, Z.M., et al., *Nano-Au/silica composite synthesized using nitrated SBA-15 as a host*. Materials Letters, 2008. 62(8-9): p. 1197-1199.
236. Chao, K.J., et al., *Preparation and characterization of highly dispersed gold nanoparticles within channels of mesoporous silica*. Catalysis Today, 2004. 97(1): p. 49-53.
237. Richards, R., et al., *Size tunable gold nanorods evenly distributed in the channels of mesoporous silica*. ACS Nano, 2008. 2(6): p. 1205-1212.
238. Liu, P.H., et al., *The morphology and size of nanostructured Au in Au/SBA-15 affected by preparation conditions*. Materials Science & Engineering C-Biomimetic and Supramolecular Systems, 2006. 26(5-7): p. 1017-1022.
239. Cao, R., et al., *Monodisperse noble metal nanoparticles stabilized in SBA-15: Synthesis, characterization and application in microwave-assisted Suzuki-Miyaura coupling reaction*. Journal of Catalysis, 2010. 270(2): p. 268-274.

240. Zhang, T., et al., *Synthesis of Thermally Stable and Highly Active Bimetallic Au-Ag Nanoparticles on Inert Supports*. Chemistry of Materials, 2009. 21(2): p. 410-418.
241. Chen, Y.T., et al., *Solvent-free aerobic oxidation of benzyl alcohol over Pd monometallic and Au-Pd bimetallic catalysts supported on SBA-16 mesoporous molecular sieves*. Applied Catalysis a-General, 2010. 380(1-2): p. 55-65.
242. Mukherjee, P., et al., *Entrapment and catalytic activity of gold nanoparticles in amine-functionalized MCM-41 matrices synthesized by spontaneous reduction of aqueous chloroaurate ions*. Physchemcomm, 2001(5): p. art. no.-5.
243. Bore, M.T., et al., *Role of pore curvature on the thermal stability of gold nanoparticles in mesoporous silica*. Chemical Communications, 2004(22): p. 2620-2621.
244. Sen, T., et al., *Energy Transfer between Confined Dye and Surface Attached Au Nanoparticles of Mesoporous Silica*. Journal of Physical Chemistry C, 2010. 114(2): p. 707-714.
245. Wei, Q., et al., *Catalytically active gold nanoparticles confined in periodic mesoporous organosilica (PMOs) by a modified external passivation route*. Microporous and Mesoporous Materials, 2009. 117(1-2): p. 98-103.
246. Xie, J., et al., *Self-assembly preparation of Au/SiO₂ catalyst and its catalysis for cyclohexane oxidation with air*. Reaction Kinetics, Mechanisms and Catalysis, 2011. 102(1): p. 143-154.
247. Yu, J.J., et al., *Characterization of gold nanoparticles electrochemically deposited on amine-functioned mesoporous silica films and electrocatalytic oxidation of glucose*. Journal of Solid State Electrochemistry, 2007. 11(9): p. 1211-1219.
248. Zhao, L., et al., *A surface modification scheme for incorporation of nanocrystals in mesoporous silica matrix*. Journal of Solid State Chemistry, 2005. 178(10): p. 2980-2986.
249. Gu, J.L., et al., *Incorporation of highly dispersed gold nanoparticles into the pore channels of mesoporous silica thin films and their ultrafast nonlinear optical response*. Advanced Materials, 2005. 17(5): p. 557-560.
250. Yen, C.W., et al., *CO Oxidation Catalyzed by Au-Ag Bimetallic Nanoparticles Supported in Mesoporous Silica*. Journal of Physical Chemistry C, 2009. 113(41): p. 17831-17839.
251. Liu, X.Y., et al., *Au-Cu Alloy nanoparticles confined in SBA-15 as a highly efficient catalyst for CO oxidation*. Chemical Communications, 2008(27): p. 3187-3189.
252. Corriu, R.J.P., A. Mehdi, and C. Reye, *Molecular chemistry and nanosciences: on the way to interactive materials*. Journal of Materials Chemistry, 2005. 15(40): p. 4285-4294.
253. Jin, Y., et al., *Gold nanoparticles stabilized in a novel periodic mesoporous organosilica of SBA-15 for styrene epoxidation*. Microporous and Mesoporous Materials, 2008. 111(1-3): p. 569-576.
254. Ghosh, A., et al., *Preparation and stabilization of gold nanoparticles formed by in situ reduction of aqueous chloroaurate ions within surface-modified mesoporous silica*. Microporous and Mesoporous Materials, 2003. 58(3): p. 201-211.
255. Guari, Y., et al., *In situ formation of gold nanoparticles within functionalised ordered mesoporous silica via an organometallic 'chimie douce' approach*. Chemical Communications, 2001(15): p. 1374-1375.
256. Mehdi, A., et al., *New mesostructured organosilica with chiral sugar derived structures: nice host for gold nanoparticles stabilisation*. Dalton Transactions, 2011. 40(2): p. 446-451.
257. Zhuang, D.Y., et al., *Preparation and Catalytic Performance of Gold Nanoparticles Supported on Periodic Mesoporous Organosilica of SBA-15*. Chinese Journal of Catalysis, 2009. 30(9): p. 896-900.
258. Mehdi, A., et al., *Soft route for monodisperse gold nanoparticles confined within SH-functionalized walls of mesoporous silica*. Journal of Materials Chemistry, 2009. 19(27): p. 4746-4752.
259. Kumagi, H. and K. Yano, *Synthesis and Characterization of Au-Loaded Core/Shell Mesoporous Silica Spheres Containing Propyl Group in the Shell*. Chemistry of Materials, 2010. 22(17): p. 5112-5118.
260. Nakamura, T., Y. Yamada, and K. Yano, *Direct synthesis of monodispersed thiol-functionalized nanoporous silica spheres and their application to a colloidal crystal embedded with gold nanoparticles*. Journal of Materials Chemistry, 2007. 17(35): p. 3726-3732.
261. Hsu, Y.T., W.L. Chen, and C.M. Yang, *Co-Condensation Synthesis of Aminopropyl-Functionalized KIT-5 Mesophases Using Carboxy-Terminated Triblock Copolymer*. Journal of Physical Chemistry C, 2009. 113(7): p. 2777-2783.
262. Boullanger, A., et al., *Generic way for functionalised well-ordered cubic mesoporous silica via direct synthesis approach*. New Journal of Chemistry, 2010. 34(4): p. 738-743.
263. Rosenholm, J.M. and M. Linden, *Wet-chemical analysis of surface concentration of accessible groups on different amino-functionalized mesoporous SBA-15 silicas*. Chemistry of Materials, 2007. 19(20): p. 5023-5034.
264. Lu, G.M., et al., *A highly efficient catalyst Au/MCM-41 for selective oxidation cyclohexane using oxygen*. Catalysis Letters, 2004. 97(3-4): p. 115-118.

265. Lu, G.M., et al., *Gold nanoparticles in mesoporous materials showing catalytic selective oxidation cyclohexane using oxygen*. Applied Catalysis a-General, 2005. 280(2): p. 175-180.
266. Sobczak, I., et al., *The role of chlorine in the generation of catalytic active species located in Au-containing MCM-41 materials*. Journal of Catalysis, 2007. 245(2): p. 259-266.
267. Grams, J. and I. Sobczak, *Application of ToF-SIMS to the study of surfactant removal from AuNbMCM-41 and AuMCM-41 materials*. International Journal of Mass Spectrometry, 2010. 289(2-3): p. 138-143.
268. Sobczak, I., et al., *Novel AuNbMCM-41 catalyst for methanol oxidation*, in *Studies in Surface Science and Catalysis*, Z.G.J.C. Ruren Xu and Y. Wenfu, Editors. 2007, Elsevier. p. 1300-1306.
269. Akolekar, D.B., G. Foran, and S.K. Bhargava, *X-ray absorption spectroscopic studies on gold nanoparticles in mesoporous and microporous materials*. Journal of Synchrotron Radiation, 2004. 11: p. 284-290.
270. Akolekar, D.B. and S.K. Bhargava, *Investigations on gold nanoparticles in mesoporous and microporous materials*. Journal of Molecular Catalysis a-Chemical, 2005. 236(1-2): p. 77-86.
271. Wojtaszek, A., et al., *Gold Grafted to Mesoporous Silica Surfaces, a Molecular Picture*. Journal of Physical Chemistry C, 2009. 113(31): p. 13855-13859.
272. Mokhonoana, M.P., N.J. Coville, and A.K. Datye, *Small Au Nanoparticles Supported on MCM-41 Containing a Surfactant*. Catalysis Letters, 2010. 135(1-2): p. 1-9.
273. Sobczak, I., et al., *Gold, vanadium and niobium containing MCM-41 materials-Catalytic properties in methanol oxidation*. Catalysis Today, 2008. 139(3): p. 188-195.
274. Hagaman, E.W., et al., *C-13 NMR characterization of the organic constituents in ligand-modified hexagonal mesoporous silicas: Media for the synthesis of small, uniform-size gold nanoparticles*. Langmuir, 2004. 20(22): p. 9577-9584.
275. Overbury, S.H., et al., *Comparison of Au catalysts supported on mesoporous titania and silica: investigation of Au particle size effects and metal-support interactions*. Catalysis Letters, 2004. 95(3-4): p. 99-106.
276. Mou, C.Y., A.Q. Wang, and C.M. Chang, *Evolution of catalytic activity of Au-Ag bimetallic nanoparticles on mesoporous support for CO oxidation*. Journal of Physical Chemistry B, 2005. 109(40): p. 18860-18867.
277. Wu, P.P., et al., *Gold nanoparticles supported on functionalized mesoporous silica for selective oxidation of cyclohexane*. Microporous and Mesoporous Materials, 2011. 141(1-3): p. 222-230.
278. Zhao, R., et al., *A highly efficient oxidation of cyclohexane over Au/ZSM-5 molecular sieve catalyst with oxygen as oxidant*. Chemical Communications, 2004(7): p. 904-905.
279. Wu, P., et al., *Selective oxidation of cyclohexane over gold nanoparticles supported on mesoporous silica prepared in the presence of thioether functionality*. Catalysis Science & Technology, 2011. 1(2): p. 285-294.
280. Hu, J.C., et al., *Aerobic oxidation of alcohols catalyzed by gold nano-particles confined in the walls of mesoporous silica*. Catalysis Today, 2007. 122(3-4): p. 277-283.
281. Hu, J.C., L.F. Chen, and R. Richards, *Intercalation of Aggregation-Free and Well-Dispersed Gold Nanoparticles into the Walls of Mesoporous Silica as a Robust "Green" Catalyst for n-Alkane Oxidation*. Journal of the American Chemical Society, 2009. 131(3): p. 914-915.
282. Magureanu, M., et al., *Plasma-assisted catalysis total oxidation of trichloroethylene over gold nano-particles embedded in SBA-15 catalysts*. Applied Catalysis B-Environmental, 2007. 76(3-4): p. 275-281.
283. Piroi, D., et al. *Plasma-assisted catalysis for total oxidation of trichloroethylene over mesoporous Au-SBA catalysts*. in *28th ICPIG*. 2007. Prague, Czech Republic.
284. Budroni, G. and A. Corma, *Gold-organic-inorganic high-surface-area materials as precursors of highly active catalysts*. Angewandte Chemie-International Edition, 2006. 45(20): p. 3328-3331.
285. Gu, J.L., et al., *Thioether moiety functionalization of mesoporous silica films for the encapsulation of highly dispersed gold nanoparticles*. Journal of Solid State Chemistry, 2006. 179(4): p. 1060-1066.
286. Mou, C.Y., et al., *Catalytic nano-rattle of Au@hollow silica: towards a poison-resistant nanocatalyst*. Journal of Materials Chemistry, 2011. 21(3): p. 789-794.
287. Lee, B., et al., *Preparation of bicontinuous mesoporous silica and organosilica materials containing gold nanoparticles by co-synthesis method*. Microporous and Mesoporous Materials, 2004. 70(1-3): p. 71-80.
288. Block, B.P. and J.C. Bailar, *The Reaction of Gold(III) with Some Bidentate Coordinating Groups*. Journal of the American Chemical Society, 1951. 73(10): p. 4722-4725.
289. Beck, A., et al., *Formation and structure of Au/TiO₂ and Au/CeO₂ nanostructures in mesoporous SBA-15*. Catalysis Today, 2008. 139(3): p. 180-187.
290. Yin, H.F., et al., *Evidence for and mitigation of the encapsulation of gold nanoparticles within silica supports upon high-temperature treatment of Au/SiO₂ catalysts: Implication to catalyst deactivation*. Applied Catalysis a-General, 2010. 386(1-2): p. 147-156.

291. Guan, Y.J. and E.J.M. Hensen, *Ethanol dehydrogenation by gold catalysts: The effect of the gold particle size and the presence of oxygen*. Applied Catalysis a-General, 2009. 361(1-2): p. 49-56.
292. Parreira, L.A., et al., *Nanocrystalline gold supported on Fe-, Ti- and Ce-modified hexagonal mesoporous silica as a catalyst for the aerobic oxidative esterification of benzyl alcohol*. Applied Catalysis a-General, 2011. 397(1-2): p. 145-152.
293. Gutiérrez, L.-F., S. Hamoudi, and K. Belkacemi. *Selective oxidation of lactose to high value lactobionic acid over gold clusters supported on mesoporous silica decorated by ceria*. in NAM 22: 22nd Meeting Of The North American Catalysis Society. 2011. Detroit.
294. Dmowski, W., et al., *Atomic Structure of Au Nanoparticles on a Silica Support by an X-ray PDF Study*. Journal of Physical Chemistry C, 2010. 114(15): p. 6983-6988.
295. Wu, Z.L., et al., *DRIFTS-QMS Study of Room Temperature CO Oxidation on Au/SiO₂ Catalyst: Nature and Role of Different Au Species*. Journal of Physical Chemistry C, 2009. 113(9): p. 3726-3734.
296. Zanella, R., et al., *Gold nanoparticles: Support effects for the WGS reaction*. Journal of Molecular Catalysis a-Chemical, 2007. 278(1-2): p. 200-208.
297. Zhu, H.G., et al., *Low-temperature CO oxidation on Au/fumed SiO₂-based catalysts prepared from Au(en)(2)Cl-3 precursor*. Applied Catalysis a-General, 2007. 326(1): p. 89-99.
298. Zanella, R., et al., *New preparation method of gold nanoparticles on SiO₂*. Journal of Physical Chemistry B, 2006. 110(17): p. 8559-8565.
299. Yin, H.F., et al., *Promotion of Au(en)(2)Cl-3-derived Au/fumed SiO₂ by treatment with KMnO₄*. Journal of Physical Chemistry C, 2008. 112(22): p. 8349-8358.
300. Morales-Saavedra, O.G. and R. Zanella, *Structural and photophysical evaluation of Au-NPs/SiO₂-based inorganic-inorganic sonogel hybrid composites*. Materials Chemistry and Physics, 2010. 124(1): p. 816-830.
301. Reifsnnyder, S.N. and H.H. Lamb, *Characterization of silica-supported Pd-Au clusters by X-ray absorption spectroscopy*. Journal of Physical Chemistry B, 1999. 103(2): p. 321-329.
302. Yuan, G., et al., *Remarkable hydrodechlorination activity over silica supported nickel/gold catalysts*. Catalysis Communications, 2005. 6(8): p. 555-562.
303. Bauer, J.C., et al., *Synthesis of silica supported AuCu nanoparticle catalysts and the effects of pretreatment conditions for the CO oxidation reaction*. Physical Chemistry Chemical Physics, 2011. 13(7): p. 2571-2581.
304. Xu, Q., et al., *Bimetallic Au-Ni Nanoparticles Embedded in SiO(2) Nanospheres: Synergetic Catalysis in Hydrolytic Dehydrogenation of Ammonia Borane*. Chemistry-a European Journal, 2010. 16(10): p. 3132-3137.
305. Okumura, M., et al., *Deposition of gold nanoparticles on silica by CVD of gold acetylacetonate*, in *Studies in Surface Science and Catalysis*, P.A.J.R.M.J.A.M.P.G. B. Delmon and G. Poncelet, Editors. 1998, Elsevier. p. 277-284.
306. Okumura, M., S. Tsubota, and M. Haruta, *Preparation of supported gold catalysts by gas-phase grafting of gold acetylacetonate for low-temperature oxidation of CO and of H-2*. Journal of Molecular Catalysis a-Chemical, 2003. 199(1-2): p. 73-84.
307. Schimpf, S., et al., *Supported gold nanoparticles: in-depth catalyst characterization and application in hydrogenation and oxidation reactions*. Catalysis Today, 2002. 72(1-2): p. 63-78.
308. Okumura, M., et al., *The reactivities of dimethylgold(III)beta-diketone on the surface of TiO₂ - A novel preparation method for Au catalysts*. Solid State Ionics, 1997. 95(1-2): p. 143-149.
309. Araki, H., et al., *Template synthesis and characterization of gold nano-wires and -particles in mesoporous channels of FSM-16*. Journal of Molecular Catalysis a-Chemical, 2003. 199(1-2): p. 95-102.
310. Chou, J., et al., *Gas-phase catalysis by micelle derived Au nanoparticles on oxide supports*. Catalysis Letters, 2004. 95(3-4): p. 107-111.
311. Porta, F., et al., *Metal sols as a useful tool for heterogeneous gold catalyst preparation: reinvestigation of a liquid phase oxidation*. Catalysis Today, 2000. 61(1-4): p. 165-172.
312. Comotti, M., et al., *Support effect in high activity gold catalysts for CO oxidation*. Journal of the American Chemical Society, 2006. 128(3): p. 917-924.
313. Tsubota, S., et al., *Effect of calcination temperature on the catalytic activity of Au colloids mechanically mixed with TiO₂ powder for CO oxidation*. Catalysis Letters, 1998. 56(2-3): p. 131-135.
314. Pietron, J.J., R.M. Stroud, and D.R. Rolison, *Using three dimensions in catalytic mesoporous nanoarchitectures*. Nano Letters, 2002. 2(5): p. 545-549.
315. Xu, B.Q., et al., *Immobilized PVA-stabilized gold nanoparticles on silica show an unusual selectivity in the hydrogenation of cinnamaldehyde*. Catalysis Communications, 2008. 9(10): p. 1949-1954.
316. Pawelec, B., et al., *Factors influencing selectivity in naphthalene hydrogenation over Au- and Pt-Au-supported catalysts*. Applied Catalysis a-General, 2005. 283(1-2): p. 165-175.

317. Zheng, N. and G.D. Stucky, *Methods of Generating Supported Nanocatalysts and Compositions Thereof*. 2009.
318. Botella, P., A. Corma, and M.T. Navarro, *Single gold nanoparticles encapsulated in monodispersed regular spheres of mesostructured silica produced by pseudomorphic transformation*. *Chemistry of Materials*, 2007. 19(8): p. 1979-1983.
319. Grunwaldt, J.D., et al., *Preparation of supported gold catalysts for low-temperature CO oxidation via "size-controlled" gold colloids*. *Journal of Catalysis*, 1999. 181(2): p. 223-232.
320. Ma, G.C., et al., *Ordered Nanoporous Silica with Periodic 30-60 nm Pores as an Effective Support for Gold Nanoparticle Catalysts with Enhanced Lifetime*. *Journal of the American Chemical Society*, 2010. 132(28): p. 9596-9597.
321. Zheng, N., J. Fan, and G.D. Stucky, *One-step one-phase synthesis of monodisperse noble-metallic nanoparticles and their colloidal crystals*. *Journal of the American Chemical Society*, 2006. 128(20): p. 6550-6551.
322. Tai, Y., et al., *Composite formation of thiol-capped Au nanoparticles and mesoporous silica prepared by a sol-gel method*. *Journal of Materials Science*, 2007. 42(4): p. 1285-1292.
323. Brust, M., et al., *Synthesis of Thiol-Derivatized Gold Nanoparticles in a 2-Phase Liquid-Liquid System*. *Journal of the Chemical Society-Chemical Communications*, 1994(7): p. 801-802.
324. Anderson, M.L., et al., *Colloidal gold aerogels: Preparation, properties, and characterization*. *Langmuir*, 1999. 15(3): p. 674-681.
325. Konya, Z., et al., *Nanocrystal templating of silica mesopores with tunable pore sizes*. *Nano Letters*, 2002. 2(8): p. 907-910.
326. Lin, H.P., et al., *Direct synthesis of MCM-41 mesoporous aluminosilicates containing Au nanoparticles in aqueous solution*. *Chemistry Letters*, 2001(11): p. 1116-1117.
327. Aprile, C., et al., *Synthesis and catalytic activity of periodic mesoporous materials incorporating gold nanoparticles*. *Journal of Materials Chemistry*, 2005. 15(41): p. 4408-4413.
328. Rothenberg, G., et al., *Preventing sintering of Au and Ag nanoparticles in silica-based hybrid gels using phenyl spacer groups*. *Journal of Materials Chemistry*, 2010. 20(19): p. 3840-3847.
329. Ferrara, M.C., et al., *Synthesis and characterization of sol-gel silica films doped with size-selected gold nanoparticles*. *Nanotechnology*, 2008. 19(36).
330. Cheng, S., et al., *Facile synthesis of mesoporous gold-silica nanocomposite materials via sol-gel process with nonsurfactant templates*. *Chemistry of Materials*, 2003. 15(7): p. 1560-1566.
331. Bonnemann, H., et al., *An SiO₂-embedded nanoscopic Pd/Au alloy colloid*. *European Journal of Inorganic Chemistry*, 2000(5): p. 819-822.
332. Parvulescu, V.I., et al., *Characterization and catalytic-hydrogenation behavior of SiO₂-embedded nanoscopic Pd, Au, and Pd-Au alloy colloids*. *Chemistry-a European Journal*, 2006. 12(8): p. 2343-2357.
333. Mou, C.Y., et al., *Synergistic effect in an Au-Ag alloy nanocatalyst: CO oxidation*. *Journal of Physical Chemistry B*, 2005. 109(1): p. 40-43.
334. Hereijgers, B.P.C. and B.M. Weckhuysen, *Aerobic oxidation of cyclohexane by gold-based catalysts: New mechanistic insight by thorough product analysis*. *Journal of Catalysis*, 2010. 270(1): p. 16-25.
335. Tsukuda, T., et al., *Preparation of similar to 1 nm Gold Clusters Confined within Mesoporous Silica and Microwave-Assisted Catalytic Application for Alcohol Oxidation*. *Journal of Physical Chemistry C*, 2009. 113(31): p. 13457-13461.
336. Tsoncheva, T., et al., *Gold and iron nanoparticles in mesoporous silicas: Preparation and characterization*. *Catalysis Communications*, 2007. 8(11): p. 1573-1577.
337. Fukuoka, A., et al., *Template synthesis of nanoparticle arrays of gold, platinum and palladium in mesoporous silica films and powders*. *Journal of Materials Chemistry*, 2004. 14(4): p. 752-756.
338. Delannoy, L., et al., *Preparation of supported gold nanoparticles by a modified incipient wetness impregnation method*. *Journal of Physical Chemistry B*, 2006. 110(45): p. 22471-22478.
339. Damin, A., et al., *Gold Nanoparticle Aggregates Immobilized on High Surface Area Silica Substrate for Efficient and Clean SERS Applications*. *Journal of Physical Chemistry C*, 2010. 114(9): p. 3857-3862.
340. Shi, H.Z., L.D. Zhang, and W.P. Cai, *Preparation and optical absorption of gold nanoparticles within pores of mesoporous silica*. *Materials Research Bulletin*, 2000. 35(10): p. 1689-1695.
341. Cai, W.P., et al., *Optical properties of Ag and Au nanoparticles dispersed within the pores of monolithic mesoporous silica*. *Journal of Nanoparticle Research*, 2001. 3(5-6): p. 443-453.
342. Tsung, C.K., et al., *Shape- and orientation-controlled gold nanoparticles formed within mesoporous silica nanofibers*. *Advanced Functional Materials*, 2006. 16(17): p. 2225-2230.

343. Lotz, A.R. and M. Froba, *Synthesis and characterization of Au-55 clusters within mesoporous silica*. Zeitschrift Fur Anorganische Und Allgemeine Chemie, 2005. 631(13-14): p. 2800-2805.
344. Fukuoka, A., et al., *Template synthesis of nanoparticle arrays of gold and platinum in mesoporous silica films*. Nano Letters, 2002. 2(7): p. 793-795.
345. Venezia, A.M., et al., *Pd and PdAu on mesoporous silica for methane oxidation: Effect of SO₂*. Journal of Catalysis, 2007. 251(1): p. 94-102.
346. Cai, W.P., et al., *Synthesis and optical characterization of Pd-Au bimetallic nanoparticles dispersed within monolithic mesoporous silica*. Scripta Materialia, 2004. 50(12): p. 1481-1486.
347. Ma, Z. and F. Zaera, *Heterogeneous Catalysis by Metals*, in *Encyclopedia of Inorganic Chemistry*, R.B. King, Editor. 2005, Wiley: Chichester. p. 1768.
348. Gucci, L., A. Beck, and K. Frey, *Role of promoting oxide morphology dictating the activity of Au/SiO₂ catalyst in CO oxidation*. Gold Bulletin, 2009. 42(1): p. 5-12.
349. Kalvachev, Y.A., et al., *Selective partial oxidation of propylene to propylene oxide on Au/Ti-MCM catalysts in the presence of hydrogen and oxygen*. 3rd World Congress on Oxidation Catalysis, 1997. 110: p. 965-972.
350. Uphade, B.S., et al., *Effect of physical mixing of CsCl with Au/Ti-MCM-41 on the gas-phase epoxidation of propene using H-2 and O-2: Drastic depression of H-2 consumption*. Applied Catalysis a-General, 2000. 190(1-2): p. 43-50.
351. Qi, C.X., et al., *Effect of surface chemical properties and texture of mesoporous titanasilicates on direct vapor-phase epoxidation of propylene over Au catalysts at high reaction temperature*. Applied Catalysis a-General, 2003. 253(1): p. 75-89.
352. Sinha, A.K., et al., *Vapor-phase epoxidation of propene over Au/Ti-MCM-41 catalysts: influence of Ti content and Au content*. Catalysis Letters, 2003. 85(3-4): p. 223-228.
353. Uphade, B.S., et al., *Vapor-phase epoxidation of propene using H-2 and O-2 over Au/Ti-MCM-48*. Journal of Catalysis, 2002. 209(2): p. 331-340.
354. Sinha, A.K., et al., *Three-dimensional mesoporous titanasilicates prepared by modified sol-gel method: Ideal gold catalyst supports for enhanced propene epoxidation*. Journal of Physical Chemistry B, 2005. 109(9): p. 3956-3965.
355. Sinha, A.K., et al., *Catalysis by gold nanoparticles: epoxidation of propene*. Topics in Catalysis, 2004. 29(3-4): p. 95-102.
356. Qi, C., et al., *Vapor-phase epoxidation of propylene using H-2/O-2 mixture over gold catalysts supported on non-porous and mesoporous titania-silica: effect of preparation conditions and pretreatments prior to reaction*. Applied Catalysis a-General, 2004. 263(1): p. 19-26.
357. Sinha, A.K., et al., *A three-dimensional mesoporous titanasilicate support for gold nanoparticles: Vapor-phase epoxidation of propene with high conversion*. Angewandte Chemie-International Edition, 2004. 43(12): p. 1546-1548.
358. Haruta, M., et al., *Selective oxidation of propylene over gold deposited on titanium-based oxides*. Research on Chemical Intermediates, 1998. 24(3): p. 329-336.
359. Haruta, M., et al., *Trimethylamine as a gas-phase promoter: Highly efficient epoxidation of propylene over supported gold catalysts*. Angewandte Chemie-International Edition, 2006. 45(3): p. 412-415.
360. Hayashi, T., K. Tanaka, and M. Haruta, *Selective vapor-phase epoxidation of propylene over Au/TiO₂ catalysts in the presence of oxygen and hydrogen*. Journal of Catalysis, 1998. 178(2): p. 566-575.
361. Uphade, B.S., et al., *Vapor-phase epoxidation of propene using H₂ and O₂ over Au/Ti-MCM-41 and Au/Ti-MCM-48*, in *Studies in Surface Science and Catalysis*, F.V.M.S.M. Avelino Corma and G.F. José Luis, Editors. 2000, Elsevier. p. 833-838.
362. Datye, A.K., et al., *Synthesis and reactivity of gold nanoparticles supported on transition metal doped mesoporous silica*. Microporous and Mesoporous Materials, 2006. 95(1-3): p. 118-125.
363. Grunert, W., et al., *CO oxidation with Au/TiO₂ aggregates encapsulated in the mesopores of MCM-48: Model studies on activation, deactivation and metal-support interaction*. Applied Catalysis a-General, 2011. 391(1-2): p. 268-280.
364. Grunert, W., A. De Toni, and H. Gies, *The Impact of Water on CO Oxidation with Au/TiO₂ Catalysts: Poison or Promotor? A Study with an Au-TiO₂/MCM-48 Model Catalyst*. Catalysis Letters, 2011. 141(9): p. 1282-1287.
365. Ruszel, M., et al., *Au/Ti-SBA-15 catalysts in CO and preferential (PROX) CO oxidation*. Catalysis Communications, 2007. 8(8): p. 1284-1286.
366. Yan, W.F., et al., *Surface sol-gel modification of mesoporous silica materials with TiO₂ for the assembly of ultrasmall gold nanoparticles*. Journal of Physical Chemistry B, 2004. 108(9): p. 2793-2796.

367. Yan, W.F., et al., *Powder XRD analysis and catalysis characterization of ultra-small gold nanoparticles deposited on titania-modified SBA-15*. *Catalysis Communications*, 2005. 6(6): p. 404-408.
368. Chiang, C.W., et al., *High catalytic activity for CO oxidation of gold nanoparticles confined in acidic support Al-SBA-15 at low temperatures*. *Journal of Physical Chemistry B*, 2005. 109(38): p. 18042-18047.
369. Chiang, C.W., A.Q. Wang, and C.Y. Mou, *CO oxidation catalyzed by gold nanoparticles confined in mesoporous aluminosilicate Al-SBA-15: Pretreatment methods*. *Catalysis Today*, 2006. 117(1-3): p. 220-227.
370. Yan, W., S.H. Overbury, and S. Dai, *Gold Catalysts Supported on Nanostructured Materials: Support Effects*, in *Nanotechnology in Catalysis*, B. Zhou, et al., Editors. 2007, Springer - Verlag. p. 55-71.
371. Xu, X., et al., *Characterization and catalytic performance of Co/SBA-15 supported gold catalysts for CO oxidation*. *Materials Research Bulletin*, 2006. 41(2): p. 406-413.
372. Weckhuysen, B.M., et al., *Propene epoxidation over Au/Ti-SBA-15 catalysts*. *Journal of Catalysis*, 2007. 248(2): p. 235-248.
373. Schwartz, V., et al., *Structural investigation of au catalysts on TiO₂-SiO₂ supports: Nature of the local structure of ti and au atoms by EXAFS and XANES*. *Journal of Physical Chemistry C*, 2007. 111(46): p. 17322-17332.
374. Nava, R., et al., *Supported gold catalysts in SBA-15 modified with TiO₂ for oxidation of carbon monoxide*. *Applied Catalysis a-General*, 2010. 375(1): p. 37-48.
375. Weckhuysen, B.M., et al., *Understanding the effect of postsynthesis ammonium treatment on the catalytic activity of Au/Ti-SBA-15 catalysts for the oxidation of propene*. *Journal of Catalysis*, 2008. 259(1): p. 43-53.
376. Li, G., H.Y. Song, and X.S. Wang, *In situ synthesis of Au/Ti-HMS and its catalytic performance in oxidation of bulky sulfur compounds using in situ generated H₂O₂ in the presence of H₂/O₂*. *Microporous and Mesoporous Materials*, 2009. 120(3): p. 346-350.
377. Zepeda, T.A., et al., *Preferential CO oxidation in excess of hydrogen over Au/HMS catalysts modified by Ce, Fe and Ti oxides*. *Applied Catalysis B-Environmental*, 2010. 100(3-4): p. 450-462.
378. Li, G., et al., *Characterization and catalytic performance of Au/Ti-HMS for direct generation of H₂O₂ and in situ-H₂O₂-ODS from H₂ and O₂: An in situ-reduction synthesis and a recycle study of catalyst*. *Microporous and Mesoporous Materials*, 2011. 139(1-3): p. 104-109.
379. Perez-Cabero, M., et al., *Stable anchoring of dispersed gold nanoparticles on hierarchic porous silica-based materials*. *Journal of Materials Chemistry*, 2010. 20(32): p. 6780-6788.
380. Tai, Y. and K. Tajiri, *Preparation, thermal stability, and CO oxidation activity of highly loaded Au/titania-coated silica aerogel catalysts*. *Applied Catalysis a-General*, 2008. 342(1-2): p. 113-118.
381. Tai, Y., et al., *Structures and CO oxidation activities of size-selected Au nanoparticles in mesoporous titania-coated silica aerogels*. *Applied Catalysis a-General*, 2009. 364(1-2): p. 143-149.
382. Husing, N., et al., *Molecular approaches towards mixed metal oxides and their behaviour in mixed oxide support Au catalysts for CO oxidation*. *Dalton Transactions*, 2011. 40(13): p. 3269-3286.
383. Dai, S., et al., *Synthesis of ordered mixed titania and silica mesostructured monoliths for gold catalysts*. *Journal of Physical Chemistry B*, 2004. 108(52): p. 20038-20044.
384. Zepeda, T.A., et al., *Alternative bio-reduction synthesis method for the preparation of Au(AgAu)/SiO₂-Al₂O₃ catalysts: Oxidation and hydrogenation of CO*. *Applied Catalysis B-Environmental*, 2009. 90(1-2): p. 64-73.
385. Chatterjee, M., et al., *In situ synthesis of gold nanoparticles inside the pores of MCM-48 in supercritical carbon dioxide and its catalytic application*. *Advanced Synthesis & Catalysis*, 2006. 348(12-13): p. 1580-1590.
386. Gupta, G., et al., *Enhanced infusion of gold nanocrystals into mesoporous silica with supercritical carbon dioxide*. *Chemistry of Materials*, 2005. 17(26): p. 6728-6738.
387. Campelo, J.M., et al., *Microwave facile preparation of highly active and dispersed SBA-12 supported metal nanoparticles*. *Green Chemistry*, 2008. 10(8): p. 853-858.
388. Corma, A., et al., *New heterogenized gold(I)-heterocyclic carbene complexes as reusable catalysts in hydrogenation and cross-coupling reactions*. *Advanced Synthesis & Catalysis*, 2006. 348(14): p. 1899-1907.
389. Tsukuda, T., et al., *Size Effect of Silica-supported Gold Clusters in the Microwave-assisted Oxidation of Benzyl Alcohol with H₂O₂*. *Chemistry Letters*, 2010. 39(3): p. 159-161.
390. Asefa, T. and R.B. Lennox, *Synthesis of gold nanoparticles via electroless deposition in SBA-15*. *Chemistry of Materials*, 2005. 17(10): p. 2481-2483.
391. Gu, J.L., et al., *A new strategy to incorporate high density gold nanowires into the channels of mesoporous silica thin films by electroless deposition*. *Solid State Sciences*, 2004. 6(7): p. 747-752.
392. Chen, W., et al., *A convenient synthetic route to gold nanoparticles dispersed within mesoporous silica*. *Chemistry Letters*, 2001(2): p. 152-153.

393. Chen, W., J.Y. Zhang, and W.P. Cai, *Sonochemical preparation of Au, Ag, Pd/SiO₂ mesoporous nanocomposites*. Scripta Materialia, 2003. 48(8): p. 1061-1066.
394. Chen, W., et al., *Sonochemical processes and formation of gold nanoparticles within pores of mesoporous silica*. Journal of Colloid and Interface Science, 2001. 238(2): p. 291-295.
395. Chen, W., et al., *Structural change of mesoporous silica with sonochemically prepared gold nanoparticles in its pores*. Ultrasonics Sonochemistry, 2001. 8(4): p. 335-339.
396. Chen, W., et al., *Synthesis of gold nanoparticles dispersed within pores of mesoporous silica induced by ultrasonic irradiation and its characterization*. Materials Research Bulletin, 2001. 36(1-2): p. 335-342.
397. Sun, W., G. Fu, and W. Cai, *Ambient effect on optical absorption of Au nanoparticles dispersed within pores of mesoporous SiO₂*. Philosophical Magazine, 2007. 87(2): p. 337-353.
398. Jan, J.S., P.J. Chen, and Y.H. Ho, *Bioassisted synthesis of catalytic gold/silica nanotubes using layer-by-layer assembled polypeptide templates*. Journal of Colloid and Interface Science, 2011. 358(2): p. 409-415.
399. Zhao, D.Y., et al., *Multifunctional Mesoporous Composite Microspheres with Well-Designed Nanostructure: A Highly Integrated Catalyst System*. Journal of the American Chemical Society, 2010. 132(24): p. 8466-8473.
400. Lee, J., J.C. Park, and H. Song, *A nanoreactor framework of a Au@SiO₂ yolk/shell structure for catalytic reduction of p-nitrophenol*. Advanced Materials, 2008. 20(8): p. 1523-1528.
401. Berardesca, E., et al., *Alpha hydroxyacids modulate stratum corneum barrier function*. British Journal of Dermatology, 1997. 137(6): p. 934-938.
402. Toshiaki, S., et al., *Mineral absorption promoters containing lactobionic acid*. Japanese Patent 07277991. 1995.
403. Vlad, M.S.C., *Production of bioactive lactobionic acid using a novel catalytic method*. 2007, Université Laval. p. 116.
404. Besson, M. and P. Gallezot, *Selective oxidation of alcohols and aldehydes on metal catalysts*. Catalysis Today, 2000. 57(1-2): p. 127-141.
405. Mallat, T. and A. Baiker, *Catalyst Potential - a Key for Controlling Alcohol Oxidation in Multiphase Reactors*. Catalysis Today, 1995. 24(1-2): p. 143-150.
406. Haruta, M., *Size- and support-dependency in the catalysis of gold*. Catalysis Today, 1997. 36(1): p. 153-166.
407. Corti, C.W., R.J. Holliday, and D.T. Thompson, *Commercial aspects of gold catalysis*. Applied Catalysis a-General, 2005. 291(1-2): p. 253-261.
408. Barrett, E.P., L.G. Joyner, and P.P. Halenda, *The Determination of Pore Volume and Area Distributions in Porous Substances .1. Computations from Nitrogen Isotherms*. Journal of the American Chemical Society, 1951. 73(1): p. 373-380.
409. Moulder, J.F. and J.E. Chastain, *Handbook of X-ray photoelectron spectroscopy : a reference book of standard spectra for identification and interpretation of XPS data*. 1992, Eden Prairie, MN: Perkin-Elmer Corporation, Physical Electronics Division.
410. Lynch, J., *Physico-chemical analysis of industrial catalysts : a practical guide to characterisation*. Institut français du pétrole publications. 2003, Paris: Editions Technip. xiv, 305 p.
411. Choudhary, V.R., et al., *A green process for chlorine-free benzaldehyde from the solvent-free oxidation of benzyl alcohol with molecular oxygen over a supported nano-size gold catalyst*. Green Chemistry, 2005. 7(11): p. 768-770.
412. Liu, J., et al., *Hydrothermally stable thioether-bridged mesoporous materials with void defects in the pore walls*. Advanced Functional Materials, 2005. 15(8): p. 1297-1302.
413. Besson, E., et al., *Soft route for monodisperse gold nanoparticles confined within SH-functionalized walls of mesoporous silica*. Journal of Materials Chemistry, 2009. 19(27): p. 4746-4752.
414. Park, E.D. and J.S. Lee, *Effects of pretreatment conditions on CO oxidation over supported Au catalysts*. Journal of Catalysis, 1999. 186(1): p. 1-11.
415. Venezia, A.M., et al., *Relationship between structure and CO oxidation activity of ceria-supported gold catalysts*. Journal of Physical Chemistry B, 2005. 109(7): p. 2821-2827.
416. Casaletto, M.P., et al., *XPS study of supported gold catalysts: the role of Au-0 and Au+delta species as active sites*. Surface and Interface Analysis, 2006. 38(4): p. 215-218.
417. Abad, A., et al., *A collaborative effect between gold and a support induces the selective oxidation of alcohols*. Angewandte Chemie-International Edition, 2005. 44(26): p. 4066-4069.
418. Pestryakov, A.N. and V.V. Lunin, *Physicochemical study of active sites of metal catalysts for alcohol partial oxidation*. Journal of Molecular Catalysis a-Chemical, 2000. 158(1): p. 325-329.
419. Ishida, T., et al., *Influence of the Support and the Size of Gold Clusters on Catalytic Activity for Glucose Oxidation*. Angewandte Chemie-International Edition, 2008. 47(48): p. 9265-9268.

420. Simakova, O.A., et al., *Structure Sensitivity in L-Arabinose Oxidation over Au/Al₂O₃ Catalysts*. Journal of Physical Chemistry C, 2011. 115(4): p. 1036-1043.
421. Zanella, R., et al., *Crotonaldehyde hydrogenation by gold supported on TiO₂: structure sensitivity and mechanism*. Journal of Catalysis, 2004. 223(2): p. 328-339.
422. Hashmi, A.S.K., et al., *Gold catalysis: The benefits of N and N,O ligands*. Angewandte Chemie-International Edition, 2004. 43(47): p. 6545-6547.
423. Gonzalez-Arellano, C., et al., *Enantioselective hydrogenation of alkenes and imines by a gold catalyst*. Chemical Communications, 2005(27): p. 3451-3453.
424. Gonzalez-Arellano, C., et al., *Catalysis by gold(I) and gold(III): A parallelism between homo- and heterogeneous catalysts for copper-free Sonogashira cross-coupling reactions*. Angewandte Chemie-International Edition, 2007. 46(9): p. 1536-1538.
425. Corma, A., et al., *Heterogenized gold(I), gold(III), and Palladium(II) complexes for C-C bond reactions*. Synlett, 2007(11): p. 1771-1774.
426. Rudolph, M. and A.S.K. Hashmi, *Gold catalysis in total synthesis-an update*. Chemical Society Reviews, 2012. 41(6): p. 2448-2462.
427. Nkosi, B., et al., *Hydrochlorination of Acetylene Using Carbon-Supported Gold Catalysts - a Study of Catalyst Reactivation*. Journal of Catalysis, 1991. 128(2): p. 378-386.
428. Sekhar, A.C.S., et al., *A simple one pot synthesis of nano gold-mesoporous silica and its oxidation catalysis*. Catalysis Today, 2012. 198(1): p. 92-97.
429. Chen, L.F., et al., *Gold Nanoparticles Intercalated into the Walls of Mesoporous Silica as a Versatile Redox Catalyst*. Industrial & Engineering Chemistry Research, 2011. 50(24): p. 13642-13649.
430. Chen, Y.Y., et al., *Direct synthesis, characterization and catalytic activity of titanium-substituted SBA-15 mesoporous molecular sieves*. Applied Catalysis a-General, 2004. 273(1-2): p. 185-191.
431. Liu, J., et al., *Thioether-bridged mesoporous organosilicas: Mesophase transformations induced by the bridged organosilane precursor*. Advanced Functional Materials, 2007. 17(4): p. 569-576.
432. Davis, R.J., *All that glitters is not Au-0*. Science, 2003. 301(5635): p. 926-927.
433. Martra, G., et al., *Nanometer-sized gold particles supported on SiO₂ by deposition of gold sols from Au(PPh₃)₃Cl*. Journal of Physical Chemistry B, 2003. 107(23): p. 5453-5459.
434. Dekkers, M.A.P., M.J. Lippits, and B.E. Nieuwenhuys, *Supported gold/MO_x catalysts for NO/H₂ and CO/O₂ reactions*. Catalysis Today, 1999. 54(4): p. 381-390.
435. Mu, Z., et al., *Direct synthesis of lanthanide-containing SBA-15 under weak acidic conditions and its catalytic study*. Microporous and Mesoporous Materials, 2008. 113(1-3): p. 72-80.
436. Li, J.S., et al., *Direct synthesis of CeO₂/SiO₂ mesostructured composite materials via sol-gel process*. Microporous and Mesoporous Materials, 2009. 120(3): p. 421-425.
437. Aktas, O., et al., *Effect of Synthesis Conditions on the Structure and Catalytic Performance of V- and Ce-Incorporated SBA-15-like Materials in Propane Selective Oxidation*. Industrial & Engineering Chemistry Research, 2010. 49(15): p. 6790-6802.
438. Wang, X.Y., et al., *Highly Sensitive Fluorescence Probe Based on Functional SBA-15 for Selective Detection of Hg²⁺*. Nanoscale Research Letters, 2010. 5(9): p. 1468-1473.
439. Morey, M.S., et al., *Hydrothermal and postsynthesis surface modification of cubic, MCM-48, and ultralarge pore SBA-15 mesoporous silica with titanium*. Chemistry of Materials, 2000. 12(4): p. 898-911.
440. Concepcion, P., et al., *Chemoselective hydrogenation catalysts: Pt on mesostructured CeO₂ nanoparticles embedded within ultrathin layers of SiO₂ binder*. Journal of the American Chemical Society, 2004. 126(17): p. 5523-5532.
441. Bensalem, A., et al., *Preparation and Characterization of Highly Dispersed Silica-Supported Ceria*. Applied Catalysis a-General, 1995. 121(1): p. 81-93.
442. Carrettin, S., et al., *Nanocrystalline CeO₂ increases the activity of an for CO oxidation by two orders of magnitude*. Angewandte Chemie-International Edition, 2004. 43(19): p. 2538-2540.
443. Burroughs, P., et al., *Satellite Structure in X-Ray Photoelectron-Spectra of Some Binary and Mixed Oxides of Lanthanum and Cerium*. Journal of the Chemical Society-Dalton Transactions, 1976(17): p. 1686-1698.
444. Wang, A.Q., et al., *X-ray photoelectron spectroscopy study of electrodeposited nanostructured CeO₂ films*. Journal of Vacuum Science & Technology B, 2003. 21(3): p. 1169-1175.
445. Comotti, M., et al., *The catalytic activity of "Naked" gold particles*. Angewandte Chemie-International Edition, 2004. 43(43): p. 5812-5815.
446. Biella, S., L. Prati, and M. Rossi, *Selective oxidation of D-glucose on gold catalyst*. Journal of Catalysis, 2002. 206(2): p. 242-247.

447. Timofeeva, M.N., et al., *Ce-silica mesoporous SBA-15-type materials for oxidative catalysis: Synthesis, characterization, and catalytic application*. Applied Catalysis a-General, 2007. 317(1): p. 1-10.
448. Chen, G.Q., et al., *Preparation of Promoted Pt/SBA-15 and Effect of Cerium on the Catalytic Activity over Carbon Monoxide Oxidation Conversion Reaction*. Catalysis Letters, 2009. 133(3-4): p. 354-361.
449. Murzin, D.Y., et al., *Lactose Oxidation Kinetics with Oxygen in Catalyst-Solution-Gas Three-Phase System with Simultaneous Electrical Potential Measurement of Supported Gold Catalyst*. Russian Journal of Electrochemistry, 2009. 45(9): p. 1017-1026.
450. Leofanti, G., et al., *Surface area and pore texture of catalysts*. Catalysis Today, 1998. 41(1-3): p. 207-219.
451. Yu, N.Y., et al., *Gold nanoparticles supported on periodic mesoporous organosilicas for epoxidation of olefins: Effects of pore architecture and surface modification method of the supports*. Microporous and Mesoporous Materials, 2011. 143(2-3): p. 426-434.
452. Zope, B.N., et al., *Reactivity of the Gold/Water Interface During Selective Oxidation Catalysis*. Science, 2010. 330(6000): p. 74-78.
453. Zanella, R. and C. Louis, *Influence of the conditions of thermal treatments and of storage on the size of the gold particles in Au/TiO₂ samples*. Catalysis Today, 2005. 107-08: p. 768-777.
454. Simakova, O.A., et al., *Gold Catalysts for Selective Aerobic Oxidation of the Lignan Hydroxymatairesinol to Oxomatairesinol: Catalyst Deactivation and Regeneration*. Catalysis Letters, 2012. 142(8): p. 1011-1019.
455. Cuenya, B.R., et al., *Size- and support-dependent electronic and catalytic properties of Au-0/Au³⁺ nanoparticles synthesized from block copolymer micelles*. Journal of the American Chemical Society, 2003. 125(42): p. 12928-12934.
456. Jaime-Ferrer, J.S., et al., *Three-compartment bipolar membrane electrodialysis for splitting of sodium formate into formic acid and sodium hydroxide: Role of diffusion of molecular acid*. Journal of Membrane Science, 2008. 325(2): p. 528-536.
457. Bazinet, L., F. Lamarche, and D. Ippersiel, *Bipolar-membrane electrodialysis: Applications of electrodialysis in the food industry*. Trends in Food Science & Technology, 1998. 9(3): p. 107-113.
458. Pourcelly, G. and L. Bazinet, *Developments of Bipolar Membrane Technology in Food and Bio-Industries*, in *Handbook of Membrane Separations*. 2008, CRC Press. p. 581-657.
459. Pourcelly, G., *Electrodialysis with bipolar membranes: Principles, optimization, and applications*. Russian Journal of Electrochemistry, 2002. 38(8): p. 919-926.
460. Trivedi, G.S., et al., *Studies on bipolar membranes .2. Conversion of sodium acetate to acetic acid and sodium hydroxide*. Reactive & Functional Polymers, 1997. 32(2): p. 209-215.
461. Narebska, A., M. Kurantowicz, and H. Staniszewski, *Separation of fermentation products by membrane techniques. IV. Electrodialytic conversion of carboxylates to carboxylic acids*. Separation Science and Technology, 2001. 36(3): p. 443-455.
462. Yu, L.X., et al., *Large scale experiment on the preparation of vitamin C from sodium ascorbate using bipolar membrane electrodialysis*. Chemical Engineering Communications, 2002. 189(2): p. 237-246.
463. Novalic, S., T. Kongbangkerd, and K.D. Kulbe, *Recovery of organic acids with high molecular weight using a combined electrodialytic process*. Journal of Membrane Science, 2000. 166(1): p. 99-104.
464. Xu, T.W. and W.H. Yang, *Citric acid production by electrodialysis with bipolar membranes*. Chemical Engineering and Processing, 2002. 41(6): p. 519-524.
465. Xu, T.W. and W.H. Yang, *Effect of cell configurations on the performance of citric acid production by a bipolar membrane electrodialysis*. Journal of Membrane Science, 2002. 203(1-2): p. 145-153.
466. Iglinski, B., et al., *The production of citric acid using electrodialysis with bipolar membrane of sodium citrate solutions*. Polish Journal of Environmental Studies, 2006. 15(3): p. 411-417.
467. Buczkowski, R., B. Iglinski, and M. Cichosz, *Use of electrodialysis with a bipolar membrane for production of citric acid*. Przemysl Chemiczny, 2007. 86(11): p. 1051-1055.
468. Jaime-Ferrer, J.S., et al., *Two-compartment bipolar membrane electrodialysis for splitting of sodium formate into formic acid and sodium hydroxide: Modelling*. Journal of Membrane Science, 2009. 328(1-2): p. 75-80.
469. Ferrer, J.S.J., et al., *Formic acid regeneration by electromembrane processes*. Journal of Membrane Science, 2006. 280(1-2): p. 509-516.
470. Zhang, N., et al., *Simultaneous regeneration of formic acid and carbonic acid from oxalate discharge by using electrodialysis with bipolar membranes (EDBM)*. Journal of Membrane Science, 2008. 309(1-2): p. 56-63.
471. Molnar, E., N. Nemestothy, and K. Belafi-Bako, *Utilisation of bipolar electrodialysis for recovery of galacturonic acid*. Desalination, 2010. 250(3): p. 1128-1131.
472. Strathmann, H., *Ion-Exchange Membrane Separation Processes*. 2004, Amsterdam: Elsevier.

473. Lameloise, M.L. and R. Lewandowski, *Recovering L-malic acid from a beverage industry waste water: Experimental study of the conversion stage using bipolar membrane electrodialysis*. Journal of Membrane Science, 2012. 403: p. 196-202.
474. Yu, L.X., J. Su, and J. Wang, *Bipolar membrane-based process for the recycle of p-toluenesulfonic acid in D-(-)-p-hydroxyphenylglycine production*. Desalination, 2005. 177(1-3): p. 209-215.
475. Alvarez, F., et al., *Salicylic acid production by electrodialysis with bipolar membranes*. Journal of Membrane Science, 1997. 123(1): p. 61-69.
476. Zhang, F., C.H. Huang, and T.W. Xu, *Production of Sebacic Acid Using Two-Phase Bipolar Membrane Electrodialysis*. Industrial & Engineering Chemistry Research, 2009. 48(16): p. 7482-7488.
477. Zhang, K., et al., *The energy-saving production of tartaric acid using ion exchange resin-filling bipolar membrane electrodialysis*. Journal of Membrane Science, 2009. 341(1-2): p. 246-251.
478. Zhang, K., M. Wang, and C.J. Gao, *Ion conductive spacers for the energy-saving production of the tartaric acid in bipolar membrane electrodialysis*. Journal of Membrane Science, 2012. 387: p. 48-53.
479. Peretti, F.A., M.M. Silveira, and M. Zeni, *Use of electrodialysis technique for the separation of lactobionic acid produced by Zymomonas mobilis*. Desalination, 2009. 245(1-3): p. 626-630.
480. Bazinet, L., *Déminéralisation, enrichissement et stabilisation par procédés électromembranaires*, in *Concepts de génie alimentaire : Procédés associés et applications à la conservation des aliments*, T.e. Doc, Editor. 2011, Lavoisier: Paris. p. 527-568.
481. Aider, M., et al., *Electromigration behavior of a mixture of chitosan oligomers at different concentrations*. Journal of Agricultural and Food Chemistry, 2006. 54(26): p. 10170-10176.
482. Wang, Y.M., et al., *Production of monoprotic, diprotic, and triprotic organic acids by using electrodialysis with bipolar membranes: Effect of cell configurations*. Journal of Membrane Science, 2011. 385(1-2): p. 226-233.
483. Wei, Y.X., et al., *Treatment of simulated brominated butyl rubber wastewater by bipolar membrane electrodialysis*. Separation and Purification Technology, 2011. 80(2): p. 196-201.
484. Bazinet, L. and M. Araya-Farias, *Effect of calcium and carbonate concentrations on cationic membrane fouling during electrodialysis*. Journal of Colloid and Interface Science, 2005. 281(1): p. 188-196.
485. Cifuentes-Araya, N., G. Pourcelly, and L. Bazinet, *Impact of pulsed electric field on electrodialysis process performance and membrane fouling during consecutive demineralization of a model salt solution containing a high magnesium/calcium ratio*. Journal of Colloid and Interface Science, 2011. 361(1): p. 79-89.
486. Lteif, R., et al., *Conductivité électrique membranaire: étude de l'effet de la concentration, de la nature de l'électrolyte et de la structure membranaire*. European Polymer Journal, 1999. 35(7): p. 1187-1195.
487. Casademont, C., et al., *Electrodialysis of model salt solution containing whey proteins: Enhancement by pulsed electric field and modified cell configuration*. Journal of Membrane Science, 2009. 328(1-2): p. 238-245.
488. Wilhelm, F.G., et al., *Optimisation strategies for the preparation of bipolar membranes with reduced salt ion leakage in acid-base electrodialysis*. Journal of Membrane Science, 2001. 182(1-2): p. 13-28.
489. Saxena, A., G.S. Gohil, and V.K. Shahi, *Electrochemical membrane reactor: Single-step separation and ion substitution for the recovery of lactic acid from lactate salts*. Industrial & Engineering Chemistry Research, 2007. 46(4): p. 1270-1276.
490. Madzingaidzo, L., H. Danner, and R. Braun, *Process development and optimisation of lactic acid purification using electrodialysis*. Journal of Biotechnology, 2002. 96(3): p. 223-239.
491. Gutiérrez, L.-F., et al., *Production of lactobionic acid by means of a process comprising the catalytic oxidation of lactose and bipolar membrane electrodialysis*. Separation and Purification Technology, 2013. 109(0): p. 23-32.
492. Monteagudo, J.M. and M. Aldavero, *Production of L-lactic acid by Lactobacillus delbrueckii in chemostat culture using an ion exchange resins system*. Journal of Chemical Technology and Biotechnology, 1999. 74(7): p. 627-634.
493. Gonzalez, M.I., et al., *Purification of lactic acid from fermentation broths by ion-exchange resins*. Industrial & Engineering Chemistry Research, 2006. 45(9): p. 3243-3247.
494. Hamoudi, S., et al., *Adsorptive removal of nitrate and phosphate anions from aqueous solutions using functionalised SBA-15: Effects of the organic functional group*. The Canadian Journal of Chemical Engineering, 2012. 90(1): p. 34-40.
495. Boyd, G.E., A.W. Adamson, and L.S. Myers, *The Exchange Adsorption of Ions from Aqueous Solutions by Organic Zeolites. II. Kinetics*. Journal of the American Chemical Society, 1947. 69(11): p. 2836-2848.
496. Juang, R.S., H.C. Kao, and F.Y. Liu, *Ion exchange recovery of Ni(II) from simulated electroplating waste solutions containing anionic ligands*. Journal of Hazardous Materials, 2006. 128(1): p. 53-59.
497. Lin, L.C. and R.S. Juang, *Ion-exchange equilibria of Cu(II) and Zn(II) from aqueous solutions with Chelex 100 and Amberlite IRC 748 resins*. Chemical Engineering Journal, 2005. 112(1-3): p. 211-218.

498. Ribeiro, M.H.L. and I.A.C. Ribeiro, *Recovery of erythromycin from fermentation broth by adsorption onto neutral and ion-exchange resins*. Separation and Purification Technology, 2005. 45(3): p. 232-239.
499. Fernandez, A., M. Diaz, and A. Rodrigues, *Kinetic Mechanisms in Ion-Exchange Processes*. Chemical Engineering Journal and the Biochemical Engineering Journal, 1995. 57(1): p. 17-25.
500. Alguacil, F.J., I. Garcia-Diaz, and F. Lopez, *The removal of chromium (III) from aqueous solution by ion exchange on Amberlite 200 resin: batch and continuous ion exchange modelling*. Desalination and Water Treatment, 2012. 45(1-3): p. 55-60.
501. Lagergren, S., *Zur theorie der sogenannten adsorption gelöster stoffe*. Kungliga Svenska Vetenskapsakademiens. Handlingar, 1898. 24(4): p. 1-39.
502. Ho, Y.S. and G. McKay, *Pseudo-second order model for sorption processes*. Process Biochemistry, 1999. 34(5): p. 451-465.
503. Rahmati, A., A. Ghaemi, and M. Samadfam, *Kinetic and thermodynamic studies of uranium(VI) adsorption using Amberlite IRA-910 resin*. Annals of Nuclear Energy, 2012. 39(1): p. 42-48.
504. Erten-Kaya, Y. and F. Cakicioglu-Ozkan, *Effect of ultrasound on the kinetics of cation exchange in NaX zeolite*. Ultrasonics Sonochemistry, 2012. 19(3): p. 701-706.
505. Lin, L.C. and R.S. Juang, *Ion-exchange kinetics of Cu(II) and Zn(II) from aqueous solutions with two chelating resins*. Chemical Engineering Journal, 2007. 132(1-3): p. 205-213.
506. Weber, W.J. and J.C. Morris, *Kinetics of adsorption on carbon from solution*. J Sanit Eng Div Am Soc Civ Eng, 1963. 89: p. 31-60.
507. Ornek, A., M. Ozacar, and I.A. Sengil, *Adsorption of lead onto formaldehyde or sulphuric acid treated acorn waste: Equilibrium and kinetic studies*. Biochemical Engineering Journal, 2007. 37(2): p. 192-200.
508. Lee, I.H., Y.C. Kuan, and J.M. Chern, *Equilibrium and kinetics of heavy metal ion exchange*. Journal of the Chinese Institute of Chemical Engineers, 2007. 38(1): p. 71-84.
509. Shaltry, M., S. Phongikaroon, and M.F. Simpson, *Ion exchange kinetics of fission products between molten salt and zeolite-A*. Microporous and Mesoporous Materials, 2012. 152: p. 185-189.
510. Nollet, H., et al., *Removal of PCBs from wastewater using fly ash*. Chemosphere, 2003. 53(6): p. 655-665.

Appendix 1: List of contributions

Peer reviewed articles

1. **Luis-Felipe Gutiérrez**, Safia Hamoudi and Khaled Belkacemi. Selective production of lactobionic acid by aerobic oxidation of lactose over gold crystallites supported on mesoporous silica. *Applied Catalysis A: General*, 2011, 402 (1-2), 94-103. (See Chapter 3).
2. **Luis-Felipe Gutiérrez**, Safia Hamoudi and Khaled Belkacemi. Synthesis of gold catalysts supported on mesoporous silica materials: Recent developments. *Catalysts*, 2011, 1 (1), 97-154. (See Chapter 1).
3. **Luis-Felipe Gutiérrez**, Safia Hamoudi and Khaled Belkacemi. Effective gold catalyst supported on mesoporous silica decorated by ceria for the synthesis of high value lactobionic acid. *Applied Catalysis A: General*, 2012, 425-426, 213-223. (See Chapter 5).
4. **Luis-Felipe Gutiérrez**, Safia Hamoudi and Khaled Belkacemi. Lactobionic acid: A high value-added lactose derivative for food and pharmaceutical applications. *International Dairy Journal*, 2012, 26 (2), 103-111. (See Chapter 1).
5. **Luis-Felipe Gutiérrez**, Safia Hamoudi and Khaled Belkacemi. Synthesis of high value lactobionic acid by aerobic oxidation of lactose on Au/SiO₂ catalysts. *Catalysis Science & Technology*, submitted. (See Chapter 6).
6. **Luis-Felipe Gutiérrez**, Laurent Bazinet, Safia Hamoudi and Khaled Belkacemi. Production of lactobionic acid by means of a process comprising the catalytic oxidation of lactose and bipolar membrane electrodialysis. *Separation and Purification Technology*, 2013, 109, 23-32 (See Chapter 8).
7. **Luis-Felipe Gutiérrez**, Safia Hamoudi and Khaled Belkacemi. Production of lactobionic acid from sodium lactobionate solution by ion exchange on a commercial strong acid resin: Kinetic data and modeling. *Solvent Extraction and Ion Exchange*, submitted. (See Chapter 9).

8. **Luis-Felipe Gutiérrez**, Safia Hamoudi and Khaled Belkacemi. Characteristics and lactose oxidation activity of gold catalysts supported on mesoporous silica synthesized in the presence of thioether functional groups. *To be submitted.*

Conferences

1. **Luis-Felipe Gutiérrez**, Safia Hamoudi and Khaled Belkacemi. Selective lactose conversion to lactobionic acid via aerobic oxidation over gold-based mesostructured catalysts. *Oral presentation in: AIChE's 2010 Annual Meeting*, November 7-12, 2010, Salt Lake City, UT, USA.
2. **Luis-Felipe Gutiérrez**, Safia Hamoudi and Khaled Belkacemi. Selective oxidation of lactose to high value lactobionic acid on gold catalysts supported on mesoporous silica decorated by ceria. *Poster presentation in: 22nd North American Catalysis Society Meeting*, June 5-10, 2011, Detroit, MI, USA. (See Appendix 2).
3. **Luis-Felipe Gutiérrez**, Safia Hamoudi and Khaled Belkacemi. Gold supported on silica materials: Efficient catalysts for the synthesis of high value lactobionic acid from lactose. *Poster Presentation In: 22nd Canadian Symposium on Catalysis*, May 13-16, 2012, Quebec City, QC, Canada. (See Appendix 3).

Appendix 2: Poster presented at 22nd North American Catalysis Society Meeting (June 5-10, 2011, Detroit, MI, USA)

Selective Oxidation of Lactose to High Value Lactobionic Acid over Gold Clusters Supported on Mesoporous Silica Decorated by Ceria



Luis-Felipe Gutiérrez^{1,2}, Safia Hamoudi¹ and Khaled Belkacem¹

¹ Department of Soil Sciences and Food Engineering, ² Department of Food Sciences and Nutrition
Université Laval, Sainte-Foy, Québec, G1V 0A6, Canada



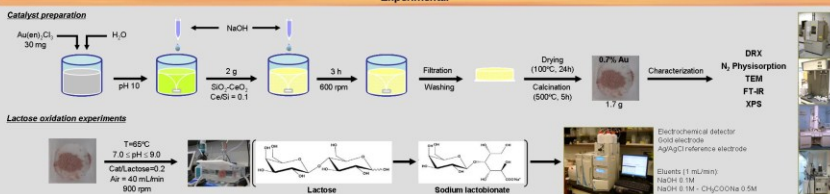
Introduction

Aerobic oxidation of glucose to gluconic acid over gold catalysts has been widely investigated since Biella et al. [1] reported high catalytic activity and selectivity of gold nanoparticles supported on activated carbon. However, lactose oxidation to lactobionic acid (LBA), a useful and high-value product for food and pharmaceutical applications, has been scarcely studied. Even though relatively high conversions and selectivities have been reached using gold nanoparticles supported on Al₂O₃, TiO₂, and CeO₂, and given that Pd and Pt catalysts promoted by Ia are very prone to deactivation by over-oxidation and/or poisoning as well as to metal leaching, the formulation of novel gold catalysts is highly desired.

The objectives of this work are to:

- Synthesize and characterize a novel gold catalyst supported on ordered mesoporous silica SBA-15 decorated by ceria.
- Evaluate the catalyst activity on the oxidation of lactose to LBA.

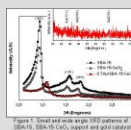
Catalyst preparation



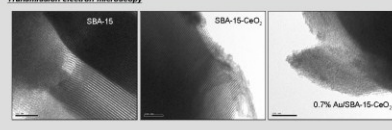
Results and discussion

X-ray diffraction

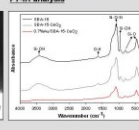
Small angle XRD patterns of SBA-15-CeO₂ showed three well-resolved diffraction peaks associated with $\sqrt{6}$ mm hexagonal symmetry, typical of the SBA-15 mesoporous materials. After impregnation, the intensity of the catalyst diffraction peaks was reduced, and the peaks shifted to a higher value, indicating some loss of symmetry.



Transmission electron microscopy

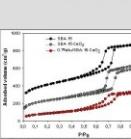


FT-IR analysis



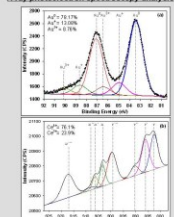
Nitrogen adsorption-desorption

Nitrogen adsorption-desorption isotherms of all samples exhibit the characteristic type IV according to IUPAC classification [2], and displayed a broad H1 type hysteresis loop characteristic of large pore mesoporous solids [3]. Table 1 shows the textural properties of SBA-15, SBA-15-CeO₂, and gold catalyst.



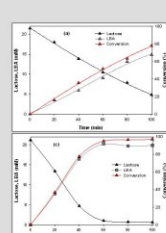
Material	BET surface area (m ² /g)	Pore diameter (nm)	Total pore volume (cm ³ /g)
SBA-15	831.2	6.8	1.260
SBA-15-CeO ₂	802.4	3.9 and 6.6	1.052
0.7% Au/SBA-15-CeO ₂	310	3.7 and 6.2	0.627

X-ray photoelectron spectroscopy analysis



Catalyst activity

The oxidation of lactose over gold catalyst is pH-dependent, as reported for the carbohydrates oxidation on metal catalysts [4-7]. As shown in Figure 4, the reaction rate was enhanced by increasing the pH value up to 9.0, which led to lactose conversion of nearly 100%, with 100% selectivity towards LBA, after only 60-100 min of reaction.



Conclusions

For the first time gold catalyst (0.7% Au nominal load) supported on mesoporous SBA-15-CeO₂ was synthesized via wet chemical process using a gold cationic complex precursor [Au(en)₃]³⁺ (en = ethylenediamine). This catalyst was successfully investigated for lactose oxidation using air as oxidizing agent. The catalyst was found highly active (100 % of conversion after only 60-100 min of reaction) and 100% selective towards LBA when it was added at a ratio of 0.2 catalyst/lactose under the reaction conditions of 65°C, pH of 9.0, air flow of 40 mL/min and agitation of 900 rpm. In comparison with the palladium or bimetal-promoted palladium supported catalysts normally used in carbohydrates oxidation, the reaction control using 0.7% Au/SBA-15-CeO₂ catalyst is easier because the control of oxygen flow, required to avoid the over oxidation of Pd and Bi-Pd catalysts, is not necessary.

Significance

Due to the rapid and simple method of synthesis and owing to its excellent catalytic performance, the 0.7% Au/SBA-15-CeO₂ can be regarded as an interesting catalyst for the industrial process of catalytic oxidation of lactose, as well as for the production of other aldonic acids, and for obtaining high value products via aerobic oxidation of organic compounds.



Acknowledgments

Funding for this work was provided by FORNT (Quebec).

References

- Biella, L., Pini, M., Basso, J. Catal. 2002, 24(2), 247.
- K. S. W. Cho, D.H. Eom, S.A.W. Hui, L. Mouco, R.A. Pinnell, J. Rouquerol, T. Stencel, Pure Appl Chem, 2008, 80, 1615.
- Leach, P. Characterization of industrial catalysts: a practical guide to characterization, Elsevier, 2008.
- Belkacem, K., Gao, S., Hamoudi, S., Gao, B., J. Catal. 2007, 248, 404-414.
- Belkacem, K., Hamoudi, S., J. Catal. 2007, 248, 127-141.
- Belkacem, K., Hamoudi, S., J. Catal. 2007, 248, 142-150.
- L.F. Gutiérrez, S. Hamoudi, K. Belkacem, Appl Catal A Gen. 2011, 40(10), 1016-1024.

Appendix 3: Poster presented at 22nd Canadian Symposium on Catalysis (May 13-16, 2012, Quebec City, QC, Canada)

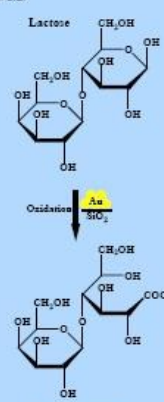
GOLD SUPPORTED ON SILICA MATERIALS: EFFICIENT CATALYSTS FOR THE SYNTHESIS OF HIGH VALUE LACTOBIONIC ACID FROM LACTOSE

Luis-Felipe Gutiérrez^{1,2,3}, Safia Hamoudi^{1,3} and Khaled Belkacemi^{1,3}

¹Department of Soil Sciences and Food Engineering, ²Department of Food Sciences and Nutrition, ³Centre de Recherche sur les Propriétés des Interfaces et la Catalyse (CERPIC) Université Laval, Quebec G1V0A6 (Canada)

ABSTRACT

Gold catalysts supported on silica with different structures (mesoporous SBA-15, mesoporous wormhole SiO₂ and amorphous fumed SiO₂) were synthesized and evaluated as catalysts for the synthesis of high value lactobionic acid (LBA) by aerobic oxidation of lactose. The catalysts were characterized by N₂ physisorption, XRD, FT-IR, TEM and XPS. Gold nanoparticles ranging between 6.0 and 7.0 nm were well dispersed and not aggregated in the synthesized samples. X-ray photoelectron spectroscopy analyses indicated the coexistence of metallic and oxidized species on the catalyst, with relative abundances of Au⁰ (~50%) > Au⁺ (~14%) > Au³⁺ (~5%). These Au/SiO₂ catalysts showed high activity (around 100%) and 100% selectivity towards LBA. The catalytic activity varied with the same order than the surface area for the three catalysts investigated. Lactose was almost depleted after 80-140 min of reaction under alkaline conditions (pH 9.0) and mild reaction temperature (65°C), when they were used at a catalyst/lactose ratio of 0.2.



Lactose $\xrightarrow[\text{SiO}_2]{\text{Au}}$ Lactobionic acid

INTRODUCTION

Carbohydrates have long time been used in the manufacture of bulk and fine chemicals, and they are currently viewed as renewable raw materials for the "green chemistry" of the future. The worldwide surplus and low cost of lactose, an important cheese and casein manufacturing by-product, has drawn the attention of researchers and industry to develop innovative processes for the production of value-added lactose derivatives, such as lactobionic acid, which is a high value product obtained from lactose oxidation, with valuable properties for food and pharmaceutical applications.¹ Because highly active Au/SiO₂ catalysts for lactose oxidation are very scarce, in this study we prepared and characterized Au/SBA-15, Au/mesoporous wormhole SiO₂ and Au/amorphous fumed silica (Cab-O-Sil) catalysts. The catalytic activity of these materials was evaluated in the selective production of LBA from lactose.

EXPERIMENTAL DETAILS

Synthesis of Au/SBA-15 and Au/Cab-O-Sil

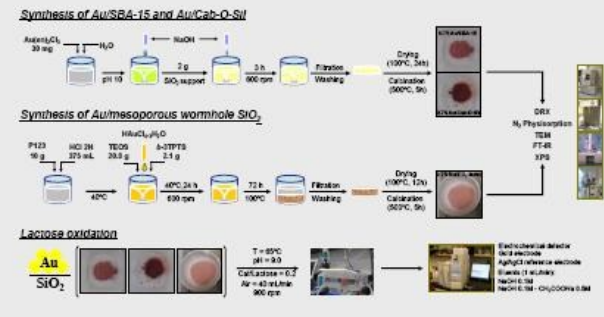
AuCl₃·3H₂O (30 mg), H₂O, NaOH, SiO₂ support (2 g), 3 h, 600 rpm, Filtration, Washing, Drying (100°C, 24h), Calcination (500°C, 9h)

Synthesis of Au/mesoporous wormhole SiO₂

P123 (10 g), HCl (3M, 375 mL), TEOS (28.5 g), A-OTFFS (2.4 g), 40°C, 24 h, 630 rpm, 72 h, 100°C, Filtration, Washing, Drying (100°C, 12h), Calcination (500°C, 9h)

Lactose oxidation

Au/SiO₂, T = 65°C, pH = 9.0, Catalyst/lactose = 0.2, Au: lactose = 1:100, Au: lactose = 1:100, Au: lactose = 1:100



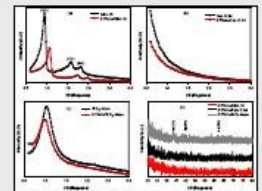
RESULTS AND DISCUSSION

Nitrogen physisorption

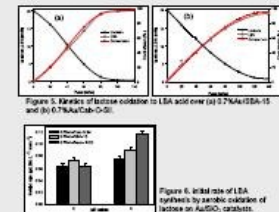
Material	BET surface area (m ² /g)	Pore diameter (nm)	Total pore volume (cm ³ /g)
SBA-15	931.2	6.8	1.260
Au/SBA-15	479.1	6.2	0.849
Cab-O-Sil	188.1	-	0.899
Au/Cab-O-Sil	190.4	-	0.713
SiO ₂ -meso	965.7	3.70 and 4.73	1.087
Au/SiO ₂ -meso	827.9	3.70	0.779

* Surface area measured at 25°C. Pore diameter (nm) is calculated from the maximum of the pore size distribution (PSD) curve. Total pore volume is calculated from the total volume of nitrogen adsorbed at P/P₀ = 0.95.

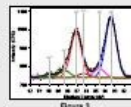
X-ray diffraction



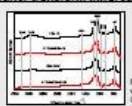
Catalytic activity



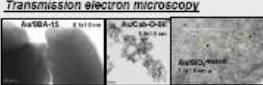
XPS analysis



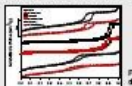
Fourier transform infrared spectroscopy (FT-IR)



Transmission electron microscopy



Marginal adsorption



GENERAL CONCLUSION

Gold supported on silica materials are efficient catalysts for the synthesis of high value LBA from lactose. Due to the rapid and simple method of synthesis, the use of the Au(en)₂Cl₂ can be regarded as a promising precursor for the synthesis of gold supported on mesoporous silicas for the oxidation of organic compounds in liquid phase.

REFERENCES

- L. F. Gutiérrez, S. Hamoudi and K. Belkacemi, *Appl. Catal. A: Gen.*, 2011, 402, 94-103.
- X. S. Wu, S. Q. Ji, D. Erweik, B. A. W. Hui, J. Mosen, B. A. Parris, G. Roper and T. G. S. Gnanaprakasam, *Pure Appl. Chem.*, 1992, 57, 805-816.
- J. Lynch, in *Physical-chemical analysis of industrial catalysts: A practical guide to characterization*, Elsevier Technol. Publ., 2003.
- G. Leclerc, M. Péroche, G. Toppet and B. Vanlerbeke, *Chem. Today*, 1989, 41, 207-214.